Towards Seamless Simulations of Polar Stratospheric Clouds and Ozone in the Polar Stratosphere with ICON-ART

Zur Erlangung des akademischen Grades eines
DOKTORS DER NATURWISSENSCHAFTEN (Dr. rer. nat.)
von der KIT-Fakultät für Physik des
Karlsruher Instituts für Technologie (KIT)

angenommene

DISSERTATION

von

M.Sc. Michael Weimer
aus Stuttgart

Tag der mündlichen Prüfung: 18.10.2019
1. Referent: Prof. Dr. Peter Braesicke
2. Korreferent: PD Dr. Michael Höpfner

Zusammenfassung

Seit der Entdeckung des Ozonlochs über der Antarktis vor einigen Jahrzehnten ist die Repräsentation von Ozon in seinen zentralen Rollen als Treibhausgas und UV-absorbierendes Molekül in Chemie-Klima-Modellen ein wesentliches Ziel. Dabei ist die realistische Darstellung von polaren Stratosphärenwolken (PSCs, von engl. "polar stratospheric clouds") unabdingbar, da diese in der Polarnacht eine Aktivierung von Chlorsubstanzen und irreversibles Ausfallen von stickstoffhaltigen Substanzen bewirken und damit den Ozonabbau im lokalen Frühling über der Antarktis erklären. Drei PSC-Typen werden anhand deren Zusammensetzung unterschieden: Salpetersäuretrihydrat-Partikel (NAT, von engl. "nitric acid trihydrate"), unterkühlte ternäre Lösungstropfen (STS, von engl. "supercooled ternary solution") und Eis-Partikel.

Globale Chemie-Klima-Modelle zur dekadischen Vorhersage von Ozon haben meist eine relativ grobe horizontale Auflösung von einigen hundert Kilometern. Dies hat zur Folge, dass Prozesse wie Schwerewellen hinter Gebirgen nicht aufgelöst werden können, da diese mit Wellenlängen von 100 km und weniger zu kleinräumig sind. Durch Leewellen entstandene PSCs haben jedoch einen signifikanten Einfluss auf die Ozonchemie, wodurch die Vorhersage des Ozonabbaus in diesen Regionen durch bisherige globale Chemie-Klima-Modelle eingeschränkt ist.

Das Modellsystem ICON-ART (ICON: ICOsahedral Non-hydrostatic, ART: Aerosols and Reactive Trace gases) bietet neben der Berechnung der atmosphärischen Zustandsvariablen in Skalen von einigen hundert Kilometern bis zu wenigen hundert Metern auch die Möglichkeit der lokalen Gitterverfeinerung mit Zwei-Wege-Interaktion. Dadurch können beispielsweise Regionen mit hoher Leewellenaktivität feiner aufgelöst werden, sodass in diesen Regionen die Leewelle direkt simuliert werden kann. Außerdem kann deren Effekt in die eigentlich zu grobe globale Auflösung zurückgeführt werden.

In dieser Arbeit wird ein neues Modul zur Mikrophysik von den bekannten drei PSC-Typen für ICON-ART erstellt und eingebaut. Die Ergebnisse des Moduls werden zunächst mit Reanalysedaten, Flugzeugmessungen und Satellitenmessungen verglichen. Es zeigt sich, dass mit der Implementierung des PSC-Schemas jetzt alle relevanten Prozesse im Modellsystem enthalten sind, um Ozon im Vergleich zu Satellitenmessungen realistisch zu repräsentieren.

Am Beispiel eines Leewellenereignisses im Juli 2008 an der Antarktischen Halbinsel wird gezeigt, dass sich im Modell große, Leewellen-induzierte PSC-Partikel bilden. Die Ergebnisse deuten darauf hin, dass durch die dadurch höhere Chloraktivierung in der Leewelle mehr Ozon abgebaut wird.

Daher wird mit dieser Arbeit die Lücke zwischen direkt aufgelösten Leewellen-induzierten PSCs und global gröber aufgelösten Langzeitsimulationen geschlossen, in denen dieser Effekt bisher nicht simuliert werden konnte. Dadurch wird es infolge dieser Arbeit möglich sein, die zukünftige Entwicklung von Ozon, auch in der Interaktion mit dem Klimawandel, besser vorherzusagen.

Abstract

Since the discovery of the ozone hole above Antarctica a few decades ago, the representation of ozone in its key role as greenhouse gas and UV radiation absorbing molecule is one of the central goals for chemistry climate models. In this context, the realistic treatment of polar stratospheric clouds (PSCs) is necessary because they lead to activation of chlorine species and irreversible removal of nitrogen-containing species that trigger the ozone depletion during local spring above Antarctica. Three PSC types are distinguished according to their composition: nitric acid trihydrate particles (NAT), supercooled ternary solution droplets (STS) and ice particles.

Global chemistry climate models for the decadal prediction of ozone mostly have relatively coarse horizontal resolutions in the order of a few hundred kilometres. As a consequence, processes like gravity waves in the lee of mountains cannot be resolved, because of their relatively small wavelengths in the order of 100 km and lower. However, mountain-wave induced PSCs are known to have a significant influence on the ozone chemistry. Thus, the prediction of ozone in these regions with current global chemistry climate models is limited.

The ICOsahedral Non-hydrostatic (ICON) modelling framework with the extension for Aerosols and Reactive Trace gases (ART) provides the possibility to calculate the atmospheric state variables on scales from hundreds of kilometres down to a few hundred metres as well as local grid refinement with two-way interaction. With this, regions with high mountain wave activity can be simulated for example with locally higher resolution so that the mountain wave and PSCs formed therein can be directly resolved. In addition, their effect can be transferred to the coarse global resolution.

In this thesis, a new module for microphysics of the three known PSC types is created and integrated into ICON-ART. At first, the results of the module are evaluated with reanalysis data, airborne and satellite measurements. It is shown that with the implementation of a PSC scheme in ICON-ART, all relevant processes for the realistic representation of ozone in comparison to satellite measurements are included in the modelling system.

It is demonstrated for an exemplary mountain wave event in July 2008 around the Antarctic Peninsula that large, directly resolved mountain-wave induced PSC particles are formed. The results indicate that due to the higher burden of activated chlorine by mountain-wave induced PSCs, more ozone is depleted in the model.

Thus, the gap between directly simulated mountain-wave induced PSCs and the coarser global resolution, where this process cannot be represented, is closed with this thesis. As a consequence, the thesis results enable more precise predictions of ozone in the future, especially with respect to its interaction with climate change.

Contents

1

Introduction

About one century ago, a layer with increased ozone concentrations in the atmosphere, essential for survival on the Earth, was discovered (e.g., Fabry and Buisson, 1921). It was found that ozone plays a key role in the atmosphere in many respects: in the stratosphere, ozone absorbs the skin cancer inducing ultra-violet (UV) radiation of the sun and leads to the characteristic temperature increase at this altitude (Chapman, 1930; Crutzen, 1970). In addition, it acts as greenhouse gas (Forster et al., 2007) and is important for air quality near the ground as first mentioned by Haagen-Smit et al. (1953).

Ozone interacts with the climate system in a non-linear way (e.g, Braesicke et al., 2018). As greenhouse gas, it influences the temperature and the dynamics in the atmosphere and therefore the climate system (e.g., Nowack et al., 2018). In addition, the ozone hole, discovered by Farman et al. (1985), induces regional climate change signals around the Antarctic Continent (e.g., Keeble et al., 2014). Thus, climate change and the ozone development are closely connected to each other and after the agreement of the Montreal Protocol in 1987 (UNEP, 1987), focus of current research is on the recovery of ozone in the future in a changing climate and with changing emissions of ozone depleting substances (Dhomse et al., 2018; Braesicke et al., 2018; Fang et al., 2019).

In this context, atmospheric chemistry modelling is an appropriate tool with which the processes influencing the ozone chemistry can be investigated separately as well as in their naturally non-linear interaction. With atmospheric chemistry modelling, the understanding of the atmospheric chemistry and its interaction with the climate system can be improved.

Ozone chemistry is driven by sunlight in the troposphere as well as in the stratosphere (Thornton et al., 2002; Seinfeld and Pandis, 2006). Photolytic reactions produce and destroy ozone in catalytic cycles. In addition, it was found that night-time processes also significantly contribute to the stratospheric ozone chemistry (Farman et al., 1985; Solomon et al., 1986). Chlorine and bromine species are activated on the surface of aerosols formed in the low temperatures of the polar night, today known as polar stratospheric clouds (PSCs). The activated species like molecular chlorine lead to springtime large ozone loss in the lower polar stratosphere as soon as the sun rises.

An extensive number of studies investigated the composition, formation and chemical processes of PSCs (see, e.g., Peter and Grooß, 2011, for an overview). Three types of PSCs are distinguished:

- Solid nitric acid trihydrate particles (NAT) consisting of nitric acid (HNO_3) and water
- Liquid supercooled ternary solution droplets (STS) originating from the stratospheric background sulphate aerosol and absorbing HNO_3 at low temperatures
- Solid ice clouds forming at the lowest temperatures

Nucleation processes of PSCs are still under debate (e.g., Voigt et al., 2018). The question if equilibrium or non-equilibrium processes are needed to describe the growth of PSCs is an issue of research (Zhu et al., 2015). In addition, it is also known that mountain waves can induce PSCs which have significant influence on the ozone chemistry (e.g., Hoffmann et al., 2017).

Polar stratospheric clouds were first seen as stationary clouds in mountain waves (e.g., Davison, 1886). Mountain waves can perturb the undisturbed temperature with fluctuations of ±10 K (Meilinger et al., 1995; Carslaw et al., 1998; Eckermann et al., 2009). Thus, PSCs can form within mountain waves although the temperature is too high in the undisturbed air. Mountain-wave induced PSCs are relevant for ozone depletion in the Arctic because of the generally higher temperatures in the Arctic than in the Antarctica. During most Arctic winters, denitrification is closely related to mountain wave activity since large NAT particles in the Arctic can mainly form in mountain waves (e.g., Tabazadeh et al., 2000). On the other hand, Antarctic PSCs can also be driven by mountain waves. Höpfner et al. (2006a) detected Antarctic mountain-wave induced NAT PSCs for the first time with a corresponding NAT belt around the Antarctica. McDonald et al. (2009) concluded that in the early winter when temperatures are close to NAT formation 40 % of PSCs come from mountain waves. Alexander et al. (2011) found that about 30 % of southern hemispheric PSCs can be related to mountain waves.

One of the hot spots for mountain wave activity around the South Pole is the Antarctic Peninsula (Bacmeister, 1993; Bacmeister et al., 1994; McDonald et al., 2009; Alexander et al., 2011; Hoffmann et al., 2017). As a mountain range in north-south direction, it blocks the usually westerly winds in this region so that mountain waves are generated downstream of the mountains. Measurements show that mountain wave activity varies from year to year. The year 2008 was a year with higher activity than the other years with mountain wave events lasting for more than 10 consecutive days (Kohma and Sato, 2011; Noel and Pitts, 2012; Hoffmann et al., 2017).

Although it is well-known that mountain waves play an important role for PSC development and hence for the ozone depletion, it is still a challenge how to represent mountain-wave induced PSCs in global atmospheric chemistry models: the horizontal resolution of global chemistry climate models is too coarse to represent the underlying orography sufficiently in order to generate mountain waves. After first two-dimensional idealised studies (Dhaniyala et al., 2002), Fueglistaler et al. (2003) presented an approach where they calculated mountain-wave induced PSCs with a meso-scale model. However, they calculated trajectories around mountains from a meteorological model and then derived PSCs as post-processing. Other studies transferred Lagrangian model results to an offline chemistry transport model (Mann et al., 2005). Eckermann et al. (2006) performed forecasts of mountain-wave induced PSCs using global input and simulated the temperature perturbations with three different models that are higher resolved. They used a temperature threshold for forecasting mountain-wave induced PSC development since mountain waves were not resolved in their model. Parametrisations of mountain waves as well as non-resolved mountain waves were also limitations to recent studies like by Orr et al. (2015) and Zhu et al. (2017).

This thesis aims to develop a module for PSCs in the ICOsahedral Non-hydrostatic modelling framework (ICON, Zängl et al., 2015) combined with the extension for Aerosols and Reactive Trace gases (ART, Rieger et al., 2015; Schröter et al., 2018). With ICON-ART, it is possible to bridge the gap between directly simulated mountain waves and long-term simulations with coarse resolution where mountain waves cannot be resolved. By using the property of local grid refinement with two-way interaction, ICON-ART is able to simulate mountain waves in a refined region including a feedback to the global domain within one simulation. With this, mountain-wave induced PSCs can be represented in ICON-ART in a realistic manner, in the refined region as well as in the coarser global resolution.

After providing the theoretical background of the thesis in Chapter 2, the ICON-ART modelling framework is described in Chapter 3 including the scheme for PSCs developed in the scope of this thesis. The new PSC scheme is evaluated using different types of simulations and reference data which are pointed out in Chapter 4. Chapter 5 shows results of different sensitivity studies with the PSC scheme in ICON-ART and its general evaluation with various satellite datasets for the year 2008. In Chapter 6, it is demonstrated that with the two-way nesting in ICON-ART, mountain-wave induced PSCs can be directly simulated with a feedback to the coarse global resolution where it cannot be simulated otherwise. Concluding remarks can be found in Chapter 7.

2

Theoretical Background

This chapter provides the theoretical basis for the investigation of mountain-wave induced PSCs. This includes a general introduction to atmospheric motion in Sect. 2.1, to gravity waves and especially to mountain waves in Sect. 2.2. This is followed by an introduction to atmospheric chemistry and aerosols in Sect. 2.3 which is applied to a general description of the stratospheric ozone chemistry in Sect. 2.4. Finally, the properties and microphysics of PSCs as well as the heterogeneous chemistry on their surfaces are discussed in Sect. 2.5.

2.1 The Atmosphere as a Dynamical System

The Earth's atmosphere is a dynamical system following the principles of physics, including momentum, mass and energy conservation. It is characterised by variables that apply to a continuum: velocity, density, temperature and pressure. This is complemented by chemical processes in the atmosphere which themselves influence the atmospheric dynamics and therefore the climate system (e.g., Seinfeld and Pandis, 2006).

As a consequence of these dynamical and chemical processes, the Earth's atmosphere is divided in different vertical layers, see Fig. 2.1. In the troposphere, the lowermost atmospheric layer up to an altitude of about 10 to 16 km dependent on the latitude, the temperature structure is driven by the vertical transport of air parcels. In these air parcels, diabatic processes like evaporation and condensation of water vapour lead to a redistribution of energy and to an average vertical temperature gradient of (see Fig. 2.1(a) and NASA, 1976):

$$\frac{\mathrm{d}T}{\mathrm{d}z} = -0.0065\,\mathrm{K\,m^{-1}} \tag{2.1}$$

In this equation, T and z stand for air temperature and geometric altitude, respectively. All symbols used in this thesis are also summarised in the list of symbols and abbreviations on page 139. In the stratosphere at altitudes from about 20 to 50 km, photochemical processes especially including

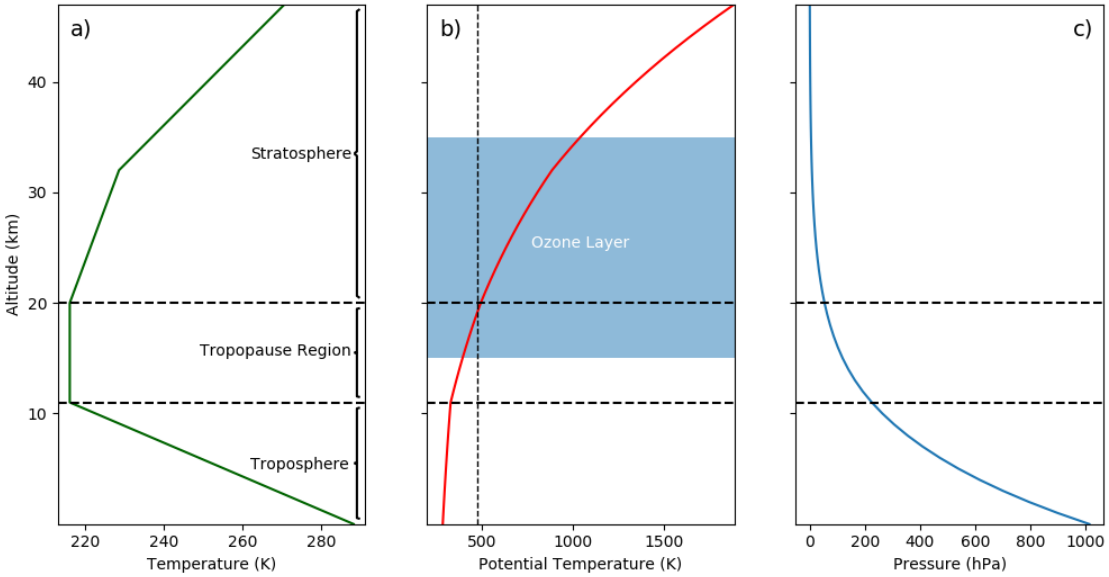

Figure 2.1: Layering of the atmosphere with typical altitude range of the ozone layer. Temperature data (left panel) from the US standard atmosphere (NASA, 1976). Pressure (right panel) is calculated by assuming hydrostatic equilibrium, see Eq. (2.7), with a surface pressure of 1013.25 hPa. The vertical line in the middle panel corresponds to a potential temperature value of $\theta = 475$ K.

ozone result in an increase of the temperature with height. In between, a layer with nearly constant temperature occurs which is called the tropopause. The US standard atmosphere treats the tropopause as a region between 11 and 20 km, see Fig. 2.1. In reality, the tropopause is thinner and its altitude depends on the latitude.

Derived from momentum, mass and energy conservation, atmospheric motion can be described in a comprehensive form by the following equations which are called Navier-Stokes equations, continuity equation, prognostic temperature equation and equation of state of an ideal gas:

$$\frac{\mathrm{d}\mathbf{v}}{\mathrm{d}t} = \mathbf{f} \tag{2.2}$$

$$\frac{\partial \rho}{\partial t} + \nabla \cdot (\rho \mathbf{v}) = 0 \tag{2.3}$$

$$\frac{\mathrm{d}T}{\mathrm{d}t} = Q_w + Q_I \tag{2.4}$$

$$p = \rho R_\mathrm{d} T \tag{2.5}$$

In these equations, $\mathbf{v}$, ρ and p stand for the air velocity, air density and air pressure, respectively, whereas R_d is the gas constant of dry air assuming air as an ideal gas. The terms Q_w and Q_I denote temperature changes due to water phase changes and radiation of the sun and Earth in an abbreviated form. Air acceleration in the rotating Earth system is driven by external forces $\mathbf{f}$ which consist of pressure gradient force, gravity force, Coriolis force and friction force due to interaction with the Earth's surface or turbulence:

$$\mathbf{f} = -\frac{1}{\rho}\nabla p - g\,\mathbf{k} - 2\,\boldsymbol{\Omega} \times \mathbf{v} - \mathbf{f}_{\mathrm{F}} \tag{2.6}$$

Here, g is the gravitational acceleration on Earth, $\mathbf{k}$ is the vertical unity vector, $\boldsymbol{\Omega}$ is the Earth's angular velocity and $\mathbf{f}_{\mathrm{F}}$ are the frictional forces. Centrifugal forces are included in terms of the geopotential combined with the gravitational force.

In large-scale flow of the order of 1000 km, vertical wind acceleration can be neglected because of the dominant pressure gradient and gravitational forces. By this, the hydrostatic approximation results from the vertical component of Eq. (2.2):

$$\frac{\mathrm{d}p}{\mathrm{d}z} = -\rho g \tag{2.7}$$

On smaller scales, however, the vertical acceleration is significantly higher and can not be neglected. Therefore, high resolution models have to solve the non-hydrostatic equation set with explicit vertical wind acceleration (e.g., Zängl et al., 2015).

Another important variable in the atmosphere is the potential temperature θ which is constant for adiabatic processes, i.e. for processes where neither mass nor energy is exchanged with the environment. It is defined as

$$\theta = T\left(\frac{p_{00}}{p}\right)^{\left(\frac{R_{\mathrm{d}}}{c_{\mathrm{pd}}}\right)} \tag{2.8}$$

where p_{00} is the standard pressure for the potential temperature of 1000 hPa and c_{pd} denotes the specific heat capacity of dry air for constant pressure. If the potential temperature decreases with height, the atmosphere is unstably stratified and vertical acceleration of an air parcel is enhanced by the ambient conditions. If the potential temperature is constant with height, vertical acceleration of an air parcel is zero. On the other hand, if the potential temperature increases with height, the atmosphere is stably stratified and an air parcel's vertical acceleration gets negative.

As can be seen in Fig. 2.1(b), the average atmosphere is stably stratified in the stratosphere as well as in tropopause and troposphere. Locally, however, the troposphere can be unstably stratified, e.g. in thunderstorms. Due to the stably stratified tropopause, this layer is a transport barrier for vertical exchange between the troposphere and the stratosphere.

In the stratosphere, the atmospheric motion is dominated by a global stratospheric circulation, called the Brewer-Dobson circulation (Brewer, 1949; Dobson et al., 1929; Newell, 1963), see Fig. 2.2. This circulation is mainly driven by planetary and gravity waves in the troposphere propagating upwards into the stratosphere (Bönisch et al., 2011). A summary of gravity waves follows in the next section. The Brewer-Dobson circulation is a meridional circulation transporting air masses in the stratosphere from the tropics to the poles. During the polar night, the air temperature in the lower stratosphere decreases to values of $T < 195$ K due to the missing absorption of UV-radiation by ozone. Moreover, this results in an enclosed area characterised by only minor exchange with lower latitudes as well as a large-scale downwelling (see Schoeberl and Hartmann, 1991). This encapsulated region is known as the polar vortex which most stably occurs above the South Pole in

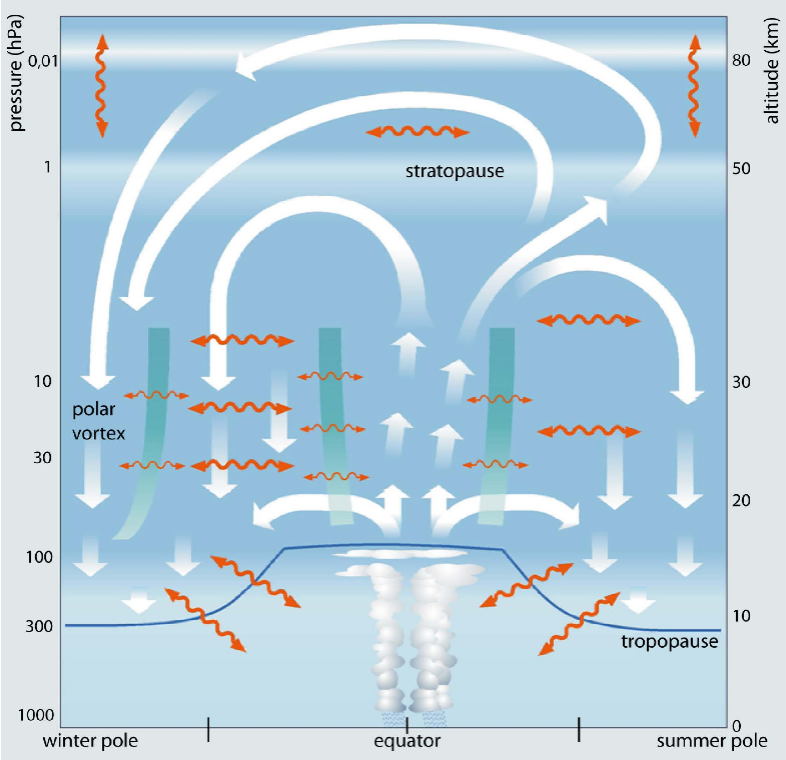

Figure 2.2: Schematic of the Brewer-Dobson circulation. Air masses are transported large-scale diabatic ascent or by tropical storms from the troposphere into the stratosphere (e.g., Stohl et al., 2003). White arrows depict the air tranport pathways in the stratosphere and mesosphere. Mixing barriers hinder the horizontal transport in the stratosphere (green thick lines). Two-way mixing is indicated by the red arrows. In total, the Brewer-Dobson circulation transports air masses from the tropics to the poles and is driven by waves in the atmosphere, such as gravity waves. Figure is taken from Bönisch et al. (2011) (CC-BY 3.0 license).

contrast to the North Pole where mid-latitudinal mountains lead to meridional displacements and subsequently to a warming of the northern polar regions.

A quantity that is conserved for the intrinsic (i.e. adiabatic and mass conserving) motion of an air parcel is the potential vorticity PV (e.g., Hoskins, 2014):

$$PV = \frac{\boldsymbol{\zeta} + 2\boldsymbol{\Omega}}{\rho} \cdot \nabla\theta \tag{2.9}$$

where $\boldsymbol{\zeta}$ is the three-dimensional relative vorticity of the air:

$$\boldsymbol{\zeta} = \nabla \times \mathbf{v} \tag{2.10}$$

The potential vorticity combines dynamical and thermodynamic quantities and can be used to distinguish air masses of different properties. On a global perspective (and neglecting the relative

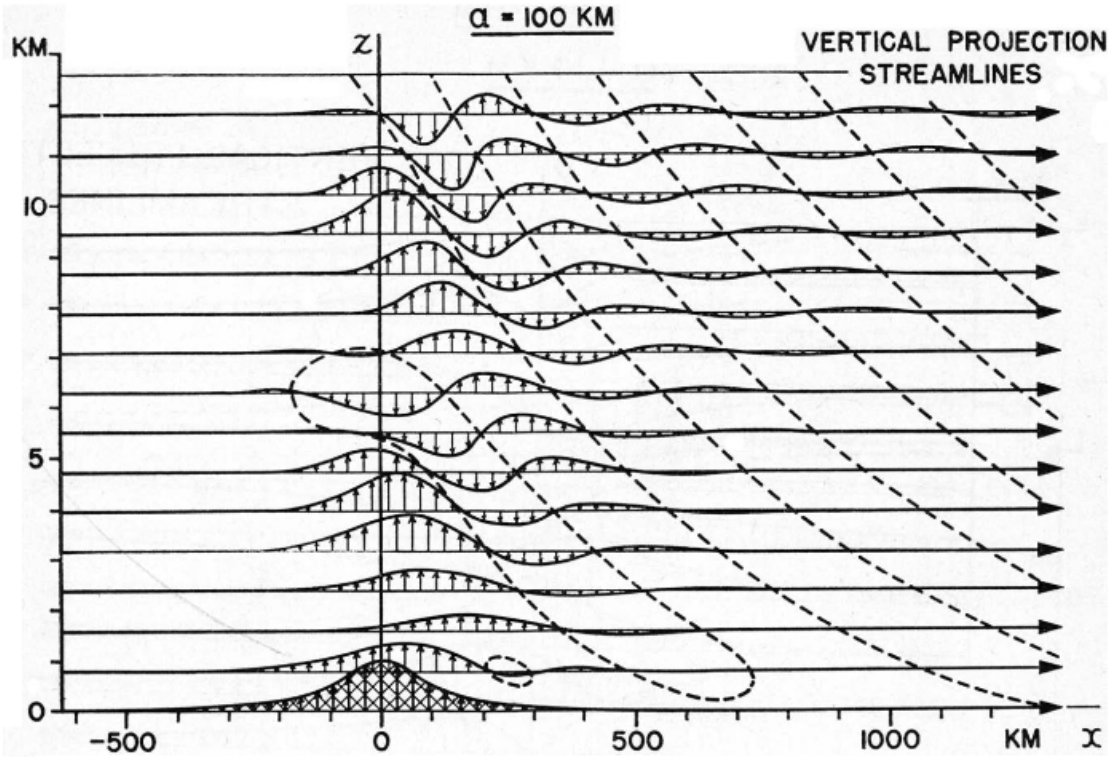

Figure 2.3: Schematic of vertical (orographic) gravity wave propagation. An unlimited uniform stratified flow is assumed. Arrows show the displacement of the stream lines due to the mountain. From Queney (1948).

vorticity), it changes its sign at the equator and is negative (positive) in the southern (northern) hemisphere. Unit of the PV is 1 PVU = 10^{-6} K m^2 kg^{-1} s^{-1}.

2.2 Gravity Waves

Gravity waves in the atmosphere are important because they transport momentum and energy from low altitudes up to the stratosphere and mesosphere (e.g., Fritts and Alexander, 2003). Thus, gravity waves influence the dynamical structure and the temperature distribution in the stratosphere and above. Therefore, it is essential that they are considered in atmospheric models. They can be initiated by a variety of sources, such as topography, convection and wind shear as well as frontal systems. Gravity waves induced by topography are called orographic gravity waves or mountain waves and are characterised by a zero horizontal phase speed, i.e. they are stationary. In contrast to this, gravity waves of nonorographic origin additionally propagate horizontally and are not localised around mountains.

Due to the variety of sources, atmospheric gravity waves have a wide range of wavelengths. Horizontally, the wavelengths of gravity waves are in the order of 10 to 1000 km (Orr et al., 2010; Dörnbrack et al., 2017). Vertically, they have wavelengths of a few kilometres (Orr et al., 2010).

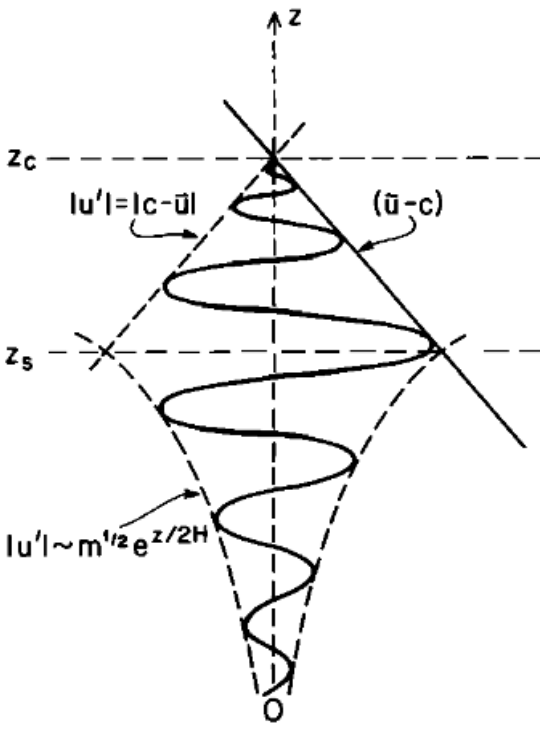

Figure 2.4: Gravity wave saturation and exchange with the background flow. Derived from linearised theory of gravity wave description. Saturation of the wave arises from convective instability. Below the saturation altitude z_s the horizontal velocity perturbation u' induced by the mountain increases exponentially with height, dependent on the vertical wave number m and the local atmospheric scale height H. Above z_s, u' decreases linearly and returns its energy and momentum to the background flow with velocity $\overline{u}$. The phase speed of the wave is denoted by c. From Fritts (1984), published with permission of John Wiley & Sons.

As indicated by Fig. 2.3, gravity waves can propagate upwards (e.g., Wright et al., 2017), depending on the stratification of the atmosphere which is expressed by the Brunt-Väisälä frequency ν_B:

$$\nu_B^2 = \frac{g}{\theta}\frac{d\theta}{dz} \tag{2.11}$$

In this equation, g and θ stand for gravitational accelaration and potential temperature, respectively. The generation of gravity waves requires a stably stratified atmosphere, i.e. $d\theta/dz > 0$ in Eq. (2.11). An initial vertical displacement in this case leads to adiabatic cooling of the air parcel. The resulting difference between parcel and ambient air potential temperature induces a negative buoyancy to the air parcel so that the gravity wave develops. In a stably stratified atmosphere, the Brunt-Väisälä frequency is real, as well as the wave numbers in all space directions, and the gravity wave can propagate upwards (Fritts and Alexander, 2003).

From linearised analyses, it can be derived that the amplitude of horizontal velocity within gravity waves increases exponentially with height due to the decrease of air density with height (e.g., Fritts, 1984). As soon as the amplitude exceeds the horizontal phase speed of the wave, it becomes convectively instable and the wave breaks at a certain level, see Fig. 2.4. This process is called

saturation of the gravity wave. At higher altitudes, the wave dissipates producing turbulent kinetic energy for the background flow (Fritts and Alexander, 2003). This accelerates the mean background flow which explains the importance of gravity waves for the thermodynamic structure of the stratosphere and mesosphere (e.g. Alexander et al., 2010). As a consequence, temperature and vertical wind fluctuations can be used to detect gravity waves (e.g., Innis and Klekociuk, 2006; Alexander et al., 2011; Hoffmann et al., 2017). The dissipation of gravity waves and its influence on the background flow is also called gravity wave drag (Kim et al., 2003).

Gravity waves have to be parametrised in atmospheric general circulation models because of their wide range of horizontal and vertical wavelengths and their importance for the dynamics (e.g., Hines, 1997; Lott and Miller, 1997; McLandress and Scinocca, 2005; Orr et al., 2010; Xu et al., 2017). These parametrisations can be used to to adjust the circulation as well as the polar temperatures in the models (Alexander et al., 2010).

2.3 Atmospheric Chemistry and Aerosols

Trace gases can transfer the tropopause and reach the stratosphere especially in the tropics (cf. Fig. 2.2). This region is also known as the tropical pipe (Plumb, 1996). The high-energy UV radiation reaches the stratosphere and is mainly absorbed by trace gases therein. Thus, the time until a trace gas is depleted can be significantly different between the troposphere and the stratosphere.

The existence time of trace gases in the atmosphere is limited by chemical depletion or photolysis. The efficiency of a unimolecular reaction, i.e. the splitting-up of an artificial molecule Y by photolysis or radioactive decay forming the artificial molecules O and P

$$\mathrm{Y} \longrightarrow \mathrm{O} + \mathrm{P} \tag{R2.1}$$

is expressed by the reaction rate constant k (in s^{-1}):

$$\frac{\mathrm{d}N_\mathrm{Y}}{\mathrm{d}t} = -k\,N_\mathrm{Y} \tag{2.12}$$

In these equations, N_Y denote the number concentration of the artificial compound Y and t is the time. Assuming k to be constant in time this leads to an exponential decrease of Y when integrating Eq. (2.12):

$$N_\mathrm{Y} = N_{\mathrm{Y},0}\exp(-kt) \tag{2.13}$$

The characteristic time length in this equation $\tau = 1/k$ is called lifetime of the gas Y. Thus, the lifetime of a trace gas corresponds to the time when its number concentration decreases to $1/e$ of its initial value. This property can also be generalised for time dependent reaction rate constants k. For photolysis, k in Eqs. (2.12) and (2.13) is usually denoted by J. In chemical equations, photolysis is depicted by hν with h the Planck's constant and ν the radiation frequency:

$$\mathrm{Y} + \mathrm{h}\nu \longrightarrow \mathrm{O} + \mathrm{P} \tag{R2.2}$$

In the case of a bimolecular chemical reaction like

$$\mathrm{Y} + \mathrm{Z} \longrightarrow \mathrm{O} + \mathrm{P} \tag{R2.3}$$

the concentration evolution depends on the concentrations of the artificial compounds Y and Z:

$$\frac{\mathrm{d}N_\mathrm{Y}}{\mathrm{d}t} = -k\, N_\mathrm{Y}\, N_\mathrm{Z} \tag{2.14}$$

The rate constant k (in units of $\mathrm{cm}^3\ \mathrm{s}^{-1}$) depends on the temperature following the Arrhenius equation (Arrhenius, 1889):

$$k(T) = A \exp\left(-\frac{\hat{E}}{R^* T}\right) \tag{2.15}$$

where T is the temperature, R^* is the universal gas constant and A and $\hat{E}$ are parameters to be determined experimentally for each reaction (e.g., Sander et al., 2011b). Usually, the parameter $E = \hat{E}/R^*$ is used to determine the temperature dependence in Eq. (2.15).

Termolecular reactions are most improbable under atmospheric conditions because in this case three different reactants have to collide at the same time (Seinfeld and Pandis, 2006). However, an air molecule can be involved in a reaction by transferring energy from a produced energy-rich molecule immediately after its reaction which is then denoted by:

$$\mathrm{Y} + \mathrm{Z} + \mathrm{M} \longrightarrow \mathrm{YZ} + \mathrm{M} \tag{R2.4}$$

The compound M stands for either molecular nitrogen (N_2) or oxygen (O_2) whose mixing ratios are almost constant in the troposphere and stratosphere. The rate constant of a termolecular reaction non-linearly depends on temperature and pressure (Sander et al., 2011b).

Radicals, i.e. atoms or molecules with at least one unpaired electron, are highly reactive in the atmosphere and are mainly responsible for the oxidising capacity of the atmosphere (e.g., Seinfeld and Pandis, 2006). The lifetime of radicals in the atmosphere usually is in the order of 1 s or less (Lelieveld et al., 2016). Thus, their abundance is small. This lifetime is by some orders of magnitude lower than typical model time steps so that radicals do not need to be transported in atmospheric chemistry models. Atomic oxygen in the atmosphere exists in two different states (e.g., Hancock and Tyley, 2001): the ground state ($\mathrm{O}(^3\mathrm{P})$) and the energy-rich excited state ($\mathrm{O}(^1\mathrm{D})$), see Appendix C for an explanation.

In addition to the atmospheric chemistry, aerosols are another relevant component interacting with the climate system. Aerosols are the liquid and solid particles existing in the atmosphere. On the one hand, aerosols have a direct effect on the climate because they are able to reflect the sunlight back to space (e.g., Kremser et al., 2016). On the other hand, aerosols have an indirect effect on the climate since they serve as water and ice nuclei. In the absence of radiation, chemical processes can additionally be more efficient on aerosol particles.

Junge et al. (1961) found that a sulphate aerosol layer covers the globe in the lower stratosphere, i.e. at altitudes from 15 to 25 km (see also Kremser et al., 2016). Correlations between global temperature and the thickness of the so-called "Junge layer" have shown the direct effect of this layer on the climate system. The stratospheric aerosol particles are influenced by the dynamics in the atmosphere since they originate from tropospheric precursors such as sulphur dioxide, dimethyl sulphide and carbonyl sulphide. These precursors are injected into the stratosphere by volcanic eruptions (Hofmann et al., 1975; Deshler et al., 2003) or are emitted at the surface.

In the atmosphere, aerosol particles exist in a large range of sizes from nearly molecular scale up to visible objects like pollen. Therefore, aerosols are usually captured by size distributions. For aerosols in the atmosphere, it was shown that lognormal distributed aerosols fit well to observed size distribtions (e.g., Grainger et al., 1995; Hervig and Deshler, 1998; Höpfner et al., 2002; Seinfeld and Pandis, 2006):

$$N(D_c) = \frac{N_\mathrm{t}}{\sqrt{2\pi} D_c \ln \sigma_\mathrm{g}} \exp\left(-\frac{(\ln D_c - \ln D_\mathrm{g})^2}{2 \ln^2 \sigma_\mathrm{g}}\right) \tag{2.16}$$

Here, parameters to be determined are the total aerosol number concentration N_t, the median diameter D_g and the standard deviation of the distribution σ_g. Bimodal lognormal size distributions combine two size distributions of the form as in Eq. (2.16) with two different parameter sets and sum them up, see e.g., Grainger et al. (1995). Particle concentrations of aerosols are usually given as particle number concentration N_c, particle surface concentration S_c or particle volume concentration V_c. Assuming spherical particles, they are calculated as follows:

$$N_c = \int_0^\infty N(D_c) D_c \mathrm{d}D_c \tag{2.17}$$

$$S_c = \int_0^\infty N(D_c) \pi D_c^2 \mathrm{d}D_c \tag{2.18}$$

$$V_c = \int_0^\infty N(D_c) \frac{\pi}{6} D_c^3 \mathrm{d}D_c \tag{2.19}$$

In these equations, D_c is the diameter and $N(D_c)$ is the particle number concentration in the diameter range between D_c and $D_c + \mathrm{d}D_c$.

Depending on their effective diameter D_c compared to the mean free path λ_mfp of air molecules, aerosols are categorised into different regimes (Seinfeld and Pandis, 2006). For this, the Knudsen number is introduced which is the ratio between the mean free path of air molecules and the size of the particle:

$$\mathrm{Kn} = \frac{\lambda_\mathrm{mfp}}{r_c} = \frac{2\lambda_\mathrm{mfp}}{D_c} \tag{2.20}$$

In the kinetic regime (Kn $\gg$ 1) the aerosol particles can be considered as gas-like with respect to their dynamics. In contrast, the fluid for aerosols in the continuum regime (Kn $\ll$ 1) can be seen as a continuum. For Kn $\approx$ 1, slip flow corrections are applied (Cunningham, 1910).

Aerosol particles experience a variety of processes, such as nucleation, coagulation, condensation, evaporation and sedimentation which are briefly described in the following. Further details can be found e.g. in Seinfeld and Pandis (2006) and Kremser et al. (2016).

(a) *Nucleation:*

Aerosols are initially formed either by clustering of molecules directly from gaseous phase (homogeneous nucleation) or the molecules are collected on a foreign pre-existing nucleus (heterogeneous nucleation). Nucleation requires a supersaturation of the gaseous phase with respect to the condensed phase, i.e. the partial pressure of the gaseous phase p_i must be higher than the saturation pressure $p_{\mathrm{sat},i}$:

$$p_i > p_{\mathrm{sat},i} \tag{2.21}$$

The partial pressure p_i of a gas i in a mixture of gases is the pressure it would exert if the other gases were removed. Thus, the sum of all partial pressures yields the total pressure p of the mixture, called Dalton's law (Dalton, 1802):

$$p = \sum_i p_i \tag{2.22}$$

According to classical nucleation theory (Köhler, 1936), two contraverse effects determine the growth of a particle: On the one hand, due to dissolved foreign species the saturation vapour pressure over the assumed spherical particle is decreased which is called the Raoult effect (Raoult, 1886). On the other hand, the surface tension of a sphere is higher than on a plane which enhances the saturation vapour pressure especially for small particles which is called the Kelvin effect (Thomson, 1871). In total, a critical supersaturation is needed beyond which the particle can grow to large sizes. If this critical supersaturation is reached, it can be assumed that the total supersaturated amount of the species nucleates on the particle.

Homogeneous nucleation usually requires a higher supersaturation with respect to the gaseous phase than heterogeneous nucleation.

(b) *Condensation and Evaporation:*

Condensation is a special case of nucleation where the condensed phase already exists in the atmosphere. The condensation and evaporation of a vapour on a particle is determined by the difference of ambient vapour pressure and the saturation vapour pressure with respect to the particle. In case of supersaturation, the vapour condenses onto the particle whereas in case of undersaturation mass is transferred from the solid or liquid phase back to the gaseous phase. The time evolution of the particle mass can be described by (Seinfeld and Pandis, 2006):

$$\frac{\mathrm{d}m_c}{\mathrm{d}t} = \frac{2\pi D_c d_i M_i}{R^* T} f(\mathrm{Kn}, \alpha)(p_i - p_{\mathrm{sat},i}) \tag{2.23}$$

where m_c is the particle mass of particle type c, D_c is the particle diameter and d_i, M_i, p_i and $p_{\mathrm{sat},i}$ are diffusion coefficient, molar mass and vapour and saturation vapour pressure of the gaseous species i, respectively. The function $f(\mathrm{Kn}, \alpha)$ connects the continuum with the kinetic regime and R^* and T are universal gas constant and air temperature, respectively.

(c) *Coagulation:*

Aerosols of various sizes can collide and stick together forming larger aggregates. This process is called coagulation. Since particle number concentrations of polar stratospheric clouds generally are relatively small this process is not very likely for these particles (Hamill and Toon, 1991; Zhu et al., 2015).

(d) *Sedimentation:*

Aerosols of substantial mass experience a gravitational descent, i.e. sedimentation. Sedimentation is an irreversible process in the atmosphere and especially for large particles it can result in a significant redistribution of the aerosol constituents.

The sedimentation velocity is usually expressed as terminal sedimentation velocity which is reached after initial acceleration. This initial acceleration lasts only a fraction of a second for particles smaller than 50 µm and can therefore be neglected for these particles (Seinfeld and Pandis, 2006). As a result of equilibrium between gravitational and drag force, the sedimentation velocity $v_{\mathrm{t},c}$ of a non-accelerating rigid ball in an incompressible fluid with negligible buoyancy and inertial forces can be described by Stokes' law (Stokes, 1851):

$$v_{\mathrm{t},c} = \frac{\rho_c \, D_c^2 \, g \, C_\mathrm{C}}{18 \, \eta} \tag{2.24}$$

where ρ_c and D_c are density and diameter of the aerosol particle c, respectively. g stands for the gravity acceleration and η is the dynamic viscosity of the fluid calculated by Sutherland's equation (Sutherland, 1893):

$$\eta = 1.458 \times 10^{-6} \, \frac{T^{\frac{3}{2}}}{T + 110.4} \tag{2.25}$$

Here, T has to be given in K to get η in $\mathrm{kg\,m^{-1}\,s^{-1}}$. The Cunningham slip flow correction factor C_C ensures the transition between kinetic and continuum regime (Cunningham, 1910).

2.4 The Ozone Chemistry in the Stratosphere

Ozone in the stratosphere is mainly formed by the photolysis of oxygen at wavelengths λ smaller than 242 nm which produces oxygen atoms ($\mathrm{O}(^3\mathrm{P})$). Atomic oxygen can react with molecular oxygen to form ozone (Chapman, 1930):

$$O_2 + h\nu \longrightarrow O(^3P) + O(^3P) \quad (\lambda \leq 242\,\text{nm}) \tag{R2.5}$$

$$2\left[O(^3P) + O_2 + M \longrightarrow O_3 + M\right] \tag{R2.6}$$

$$\text{Net: } 3\,O_2 + h\nu \longrightarrow 2\,O_3$$

According to Chapman (1930), this is compensated by a depletion of ozone via photolysis at wavelengths lower than 1140 nm which produces atomic oxygen ($O(^3P)$):

$$O_3 + h\nu \longrightarrow O(^3P) + O_2 \quad (\lambda \leq 1140\,\text{nm}) \tag{R2.7}$$

$$O(^3P) + O_3 \longrightarrow 2\,O_2 \tag{R2.8}$$

$$\text{Net: } 2\,O_3 + h\nu \longrightarrow 3\,O_2$$

This overestimates the stratospheric ozone concentration. Crutzen (1970) concluded that ozone is also depleted by catalytic cycles of HO_x (i.e. OH and HO_2) and NO_x (i.e. NO and NO_2) which can be summarised as follows (Bates and Nicolet, 1965; Crutzen, 1971; Cariolle, 1983):

$$X + O_3 \longrightarrow XO + O_2 \tag{R2.9}$$

$$O_3 + h\nu \longrightarrow O(^3P) + O_2 \quad (\lambda \leq 1140\,\text{nm}) \tag{R2.10}$$

$$XO + O(^3P) \longrightarrow X + O_2 \tag{R2.11}$$

$$\text{Net: } 2\,O_3 + h\nu \longrightarrow 3\,O_2$$

In this cycle, X stands for either NO or OH (Crutzen, 1970). These reactions are most relevant in the upper stratosphere. In the lower and middle stratosphere, Cl and Br radicals are mainly responsible to deplete ozone by the same catalytic cycles of Reacts. (R2.9) to (R2.11) (Molina and Rowland, 1974; Wofsy et al., 1975). Although the abundance of total bromine is by an order of magnitude lower than that of total chlorine, the reactivity of the bromine cycles is larger and therefore more efficient than that of chlorine (Wofsy et al., 1975). This is why the bromine cycles are important for the stratospheric ozone chemistry, too.

Additionally to the mentioned catalytic cycle of Reacts. (R2.9) to (R2.11), it was shown that also the catalytic cycle including chlorine peroxide (Cl_2O_2) is important for ozone depletion in the stratosphere (Molina and Molina, 1987; Horný et al., 2016). After reaction of Cl with ozone, chlorine monoxide (ClO) is formed which combines in a self-reaction to Cl_2O_2. This is destroyed by photolysis, subsequently:

$$2\left[\mathrm{Cl} + \mathrm{O_3} \longrightarrow \mathrm{ClO} + \mathrm{O_2}\right] \quad \text{(R2.12)}$$

$$\mathrm{ClO} + \mathrm{ClO} + \mathrm{M} \longrightarrow \mathrm{Cl_2O_2} + \mathrm{M} \quad \text{(R2.13)}$$

$$\mathrm{Cl_2O_2} + \mathrm{h}\nu \longrightarrow 2\,\mathrm{Cl} + \mathrm{O_2} \quad (\lambda \leq 400\,\mathrm{nm}) \quad \text{(R2.14)}$$

$$\text{Net: } 2\,\mathrm{O_3} + \mathrm{h}\nu \longrightarrow 3\,\mathrm{O_2}$$

In addition to chlorine and bromine cycles, catalytic cycles involving combinations of them can deplete ozone (McElroy et al., 1986; Barton et al., 1984; Beckert et al., 2003):

$$\mathrm{BrO} + \mathrm{ClO} \longrightarrow \mathrm{Br} + \mathrm{Cl} + \mathrm{O_2} \quad \text{(R2.15)}$$

$$\mathrm{BrO} + \mathrm{ClO} \longrightarrow \mathrm{BrCl} + \mathrm{O_2} \quad \text{(R2.16)}$$

$$\mathrm{BrO} + \mathrm{ClO} \longrightarrow \mathrm{Br} + \mathrm{OClO} \quad \text{(R2.17)}$$

$$\mathrm{BrCl} + \mathrm{h}\nu \longrightarrow \mathrm{Br} + \mathrm{Cl} \quad (\lambda \leq 554\,\mathrm{nm}) \quad \text{(R2.18)}$$

$$\mathrm{OClO} + \mathrm{h}\nu \longrightarrow \mathrm{Cl} + \mathrm{O_2} \quad (\lambda \leq 480\,\mathrm{nm}) \quad \text{(R2.19)}$$

$$3\left[\mathrm{Br} + \mathrm{O_3} \longrightarrow \mathrm{BrO} + \mathrm{O_2}\right] \quad \text{(R2.20)}$$

$$3\left[\mathrm{Cl} + \mathrm{O_3} \longrightarrow \mathrm{ClO} + \mathrm{O_2}\right] \quad \text{(R2.21)}$$

$$\text{Net: } 6\,\mathrm{O_3} + \mathrm{h}\nu \longrightarrow 9\,\mathrm{O_2}$$

As indicated by the photolytic reactions in all the cycles described above, these reaction systems require radiation within a specific wavelength range to form or destroy ozone. This is why these reactions cannot explain why the ozone loss is larger over Antarctica during spring than at other places.

After the discovery of the ozone hole by Farman et al. (1985), the scientific attention focussed on the processes that result in the ozone depletion during early spring over the Antarctica. The ozone depletion begins with the emissions of chlorofluorocarbons (CFCs) which was first suggested by Molina and Rowland (1974), see Fig. 2.5. In the troposphere, they are chemically inert with lifetimes of several decades (Molina and Rowland, 1974; Seinfeld and Pandis, 2006). Thus, concentrations of CFCs increase with continued emissions and they are almost uniformly distributed within the troposphere all over the globe. In the tropical pipe, CFCs can cross the tropopause layer and reach the stratosphere, see Fig. 2.5. In the stratosphere, CFCs are photolysed by the UV radiation, here as example for trichlorofluoromethane ($\mathrm{CFCl_3}$, CFC-11, Lyman et al., 1997):

$$\mathrm{CFCl_3} + \mathrm{h}\nu \longrightarrow 3\,\mathrm{Cl} + \text{Products} \quad (\lambda \leq 200\,\mathrm{nm}) \quad \text{(R2.22)}$$

$$\mathrm{Cl} + \mathrm{CH_4} \longrightarrow \mathrm{HCl} + \mathrm{CH_3} \quad \text{(R2.23)}$$

$$\mathrm{ClO} + \mathrm{NO_2} + \mathrm{M} \longrightarrow \mathrm{ClONO_2} + \mathrm{M} \quad \text{(R2.24)}$$

This photolytic reaction results in the formation of chlorine radicals which subsequently react to form the compounds HCl and $\mathrm{ClONO_2}$. Their lifetime is in the order of several weeks for

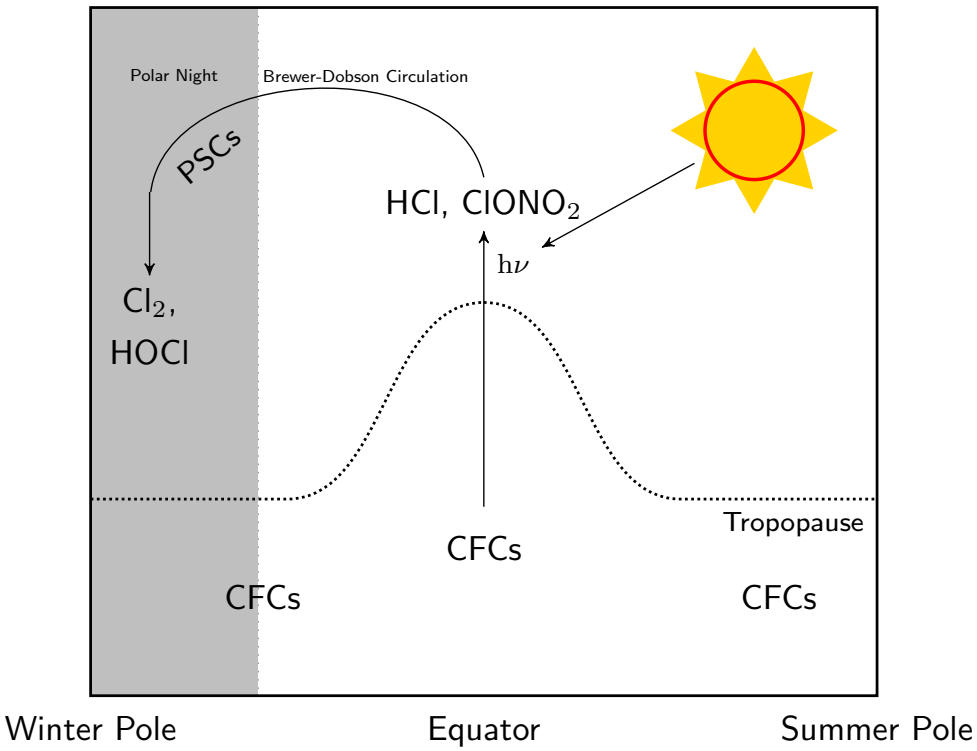

Figure 2.5: Schematic of the chlorine pathway in the atmosphere. Chlorofluorocarbons (CFCs) are emitted at the Earth's surface and distributed all over the troposphere. Due to their long tropospheric lifetime they reach the stratosphere in tropical latitudes where they are photolysed to form hydrochloric acid (HCl) and chlorine nitrate ($ClONO_2$) eventually. They are transported to the poles with the Brewer-Dobson circulation (see Fig. 2.2) where they are converted to chlorine (Cl_2) and hypochloric acid (HOCl) on the surface of polar stratospheric clouds (PSCs) during the polar night.

stratospheric conditions (Seinfeld and Pandis, 2006). Therefore, HCl and $ClONO_2$ are called reservoir gases.

In the low polar temperatures, the reservoir species are activated on the surface of polar stratospheric clouds forming reactive species like Cl_2 or HOCl (PSCs, see Reacts. (R2.29) to (R2.39) in Sect. 2.5). These processes are summarised as "chlorine activation". Similar activation mechanisms were found for bromine containing reservoir gases, like $BrONO_2$ and HBr forming the activated species Br_2 and HOBr. Since chlorine and bromine activation take place in the polar night, the activated species can be accumulated, which explains the yearly large ozone losses above the Antarctica. As soon as the sun rises during local spring, the activated species are split up by photolysis, forming Cl and Br radicals:

$$Cl_2 + h\nu \longrightarrow 2\,Cl \quad (\lambda \leq 400\,nm) \tag{R2.25}$$

$$Br_2 + h\nu \longrightarrow 2\,Br \quad (\lambda \leq 550\,nm) \tag{R2.26}$$

$$HOCl + h\nu \longrightarrow OH + Cl \quad (\lambda \leq 310\,nm) \tag{R2.27}$$

$$HOBr + h\nu \longrightarrow OH + Br \quad (\lambda \leq 500\,nm) \tag{R2.28}$$

The wavelength limits originate from Ganske et al. (1992), Finlayson-Pitts and Pitts (2000), Molina et al. (1980), and Ingham et al. (1998), respectively. The radicals then lead to the catalytic ozone depletion described above and with this to the so-called ozone hole. The ozone hole usually is defined as area where the ozone column is lower than 220 DU (Newman et al., 2004; Chipperfield et al., 2015; Ivy et al., 2017), see also Appendix A for the conversion to Dobson units.

The catalytic cycles can be stopped by the reaction of the radicals with NO_2 or CH_4, forming reservoir species, as already discussed in Reactions (R2.23) and (R2.24).

As indicated by Fig. 2.5, the whole process leading to the ozone hole can only be explained with the existence of PSCs. In the following, the properties of PSCs and the heterogeneous chemistry on their surface are described in detail.

2.5 Polar Stratospheric Clouds and Heterogeneous Chemistry

Polar stratospheric clouds (PSCs) were first seen as iridescendent clouds occurring before dawn and after sunset at the end of the 19th century (e.g., Davison, 1886; Piazzi-Smyth, 1886; Stevenson, 1886; Størmer, 1929). About 100 years later and one year after the discovery of the ozone hole by Farman et al. (1985), these clouds came back into the focus of scientific interest. Solomon et al. (1986) first suggested that heterogeneous reactions on the surface of PSCs are able to explain the large ozone loss occurring over the Antarctica. Since then, an extensive number of studies was conducted investigating the composition of PSCs and the heterogeneous reactions on their surfaces. They form at altitudes between about 15 to 30 km (Tabazadeh et al., 2001; Bevilacqua et al., 2002; Pitts et al., 2018) at temperatures lower than about 195 K (e.g., Hanson and Mauersberger, 1988) and with vertical extends in the order of 100 m and more (Carslaw et al., 1998). Chemical composition and state of the different PSC types are summarised in Table 2.1. Equilibrium temperatures for the existence of PSCs are depicted in Fig. 2.6.

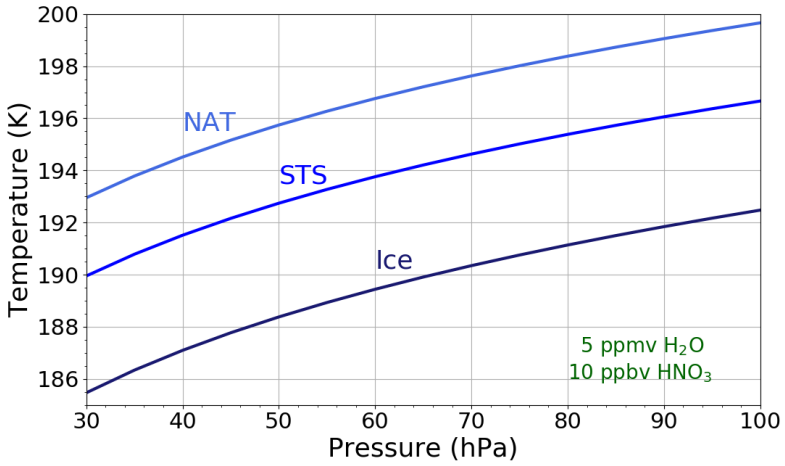

Figure 2.6: Equilibrium temperatures for NAT, STS and ice polar stratospheric clouds. The equilibrium temperature for NAT is derived from Hanson and Mauersberger (1988). The STS equilibrium temperature is estimated as 3 K below that of NAT, cf. Carslaw et al. (1994) and Fig. 3.12. The ice equilibrium temperature comes from Marti and Mauersberger (1993). Adapted from Diekmann (2017).

Table 2.1: State and composition of the different PSC types. STS = supercooled ternary solution droplets; NAT = nitric acid trihydrate.

PSC Type	State	Chemical Composition
STS	Liquid	H_2O / HNO_3 / H_2SO_4
NAT	Solid	$HNO_3(H_2O)_3$
Ice	Solid	H_2O

Composition and Microphysics of PSCs

Airborne remote sensing measurements already in early times suggested that PSCs consist of different types, composed of water (H_2O), nitric acid (HNO_3) and sulphuric acid (H_2SO_4) (e.g., Poole and McCormick, 1988). Verified by satellite measurements, PSCs can be classified into three major classes (Toon et al., 1990; Biele et al., 2001; Höpfner et al., 2006b; Peter and Grooß, 2011): (1) nitric acid trihydrate particles ($HNO_3(H_2O)_3$, NAT), (2) supercooled ternary solution droplets (STS) and (3) ice clouds.

Close after the discovery of heterogeneous processes Toon et al. (1986) found that the background sulphate aerosols of the Junge layer can grow by absorbing HNO_3 under stratospheric conditions. For temperatures lower than about 192 K, the background sulphate aerosol particles of the Junge layer can take up significant amount of HNO_3 so that their volume increases and a ternary solution droplet forms (Arnold, 1992; Dye et al., 1992; Carslaw et al., 1994; Peter, 1997). STS particles grow to sizes as large as 0.5 µm (Carslaw et al., 1994; Tabazadeh et al., 2000). Comprehensive theoretical studies for determining the equilibrium states of the ternary solution system were conducted which are still widely accepted in the community (Carslaw et al., 1995a). Nucleation and growth of STS particles can be explained by processes in equilibrium (Carslaw et al., 1995b). Non-equilibrium processes may be important for the background sulphate aerosol, only (Zhu et al., 2015). As particles of sizes smaller than 1 µm, sedimentation is negligible for STS particles (Considine et al., 2000; Tabazadeh et al., 2000).

Since STS particles are generated from the background sulphate aerosol it was found that they are mainly responsible for chlorine activation (e.g., Peter, 1997; Kirner et al., 2015b). Even supercooled binary sulphate droplets are efficient in activating the chlorine species (Wohltmann et al., 2013).

The fact that HNO_3 can be taken up by PSC particles was already suggested by Toon et al. (1986) but the composition of these particles was under debate. In laboratory studies, Hanson and Mauersberger (1988) found that nitric acid trihydrate forms stable crystals under stratospheric conditions at temperatures up to 7 K above the frost point, see Fig. 2.6. The existence of other hydrates, such as nitric acid dihydrate (NAD), is verified by laboratory experiments (Worsnop et al., 1993; Tabazadeh et al., 2002; Möhler et al., 2006) but not supported by measurements in the polar regions so far (Höpfner et al., 2006b). In contrast, the existence of NAT particles is verfied by a variety of atmospheric measurements (e.g., Fahey et al., 1989; Voigt et al., 2000; Fahey et al., 2001; Molleker et al., 2014; Woiwode et al., 2016).

The crystalline structure of NAT particles consists of independent plates so that other substances like HCl can be absorbed by the particles (Turco et al., 1989). NAT particles have been measured over Antarctic and Arctic regions as well as in the tropical upper troposphere where cirrus clouds can also take up HNO_3 (Romakkaniemi et al., 2006; Voigt et al., 2008). In the Arctic, wide-spread

NAT particles can only occur when the polar vortex is concentric and therefore temperatures can decrease below the existence temperature for NAT (Mann et al., 2002).

The nucleation of NAT particles is still under debate: on the one hand, homogeneous nucleation is assumed to be unlikely (Koop et al., 1995). In the other hand, a supersaturation with respect to the gaseous phase was found to best describe NAT formation which supports the assumption of homogeneous nucleation of NAT (Peter et al., 1991; Considine et al., 2000; Grooß et al., 2002). Heterogeneous nucleation on nuclei such as STS (Peter and Grooß, 2011), ice (Iannarelli and Rossi, 2015) or meteoric dust coming from space (Hoyle et al., 2013; James et al., 2018) have been suggested as possible processes for NAT formation.

NAT particles can grow to diameters up to 20 µm (Fahey et al., 2001). In rare events, NAT particles as large as 40 µm have been observed (Molleker et al., 2014). Carslaw et al. (2002) found that NAT particles larger than 10 µm cannot be in thermodynamic equilibrium with the gaseous phase and developed a parametrisation for non-equilibrium growth of NAT particles based on Eq. (2.23) (see Sect. 3.5.2). Especially, this is the case for fast meso-scale temperature fluctuations because the particle growth is inert and cannot totally follow these changes (Murphy and Gary, 1995).

Comprehensive knowledge of growth and particle size of NAT particles is essential. The uptake and sedimentation of HNO_3 on PSCs can extend the ozone loss, today known as "denitrification" as first mentioned by Crutzen and Arnold (1986) and Toon et al. (1986). Salawitch et al. (1989) confirmed these statements by combining measured sizes of NAT particles with their typical sedimentation velocities. Due to sedimentation of NAT particles, HNO_3 is irreversibly removed from the region with Cl- and Br-catalysed ozone depletion. Therefore, the interruption of the catalytic cycles by React. (R2.24) is prevented and the ozone depletion can last for a longer time. NAT particles have to exist for at least some days to lead to significant denitrification because of their sedimentation velocity in the order of a few cm s^{-1} (Tabazadeh et al., 2000; Flentje et al., 2002; Yu, 2004). However, it was found that large NAT particles are aspherical and most probably non-compact so that the assumed sedimentation velocity of a spherical particle has to be reduced to fit to observations (Woiwode et al., 2014, 2016).

As a third component, ice particles can form in the polar stratosphere at temperatures below the frost point, usually around 188 K (see Fig. 2.6). An extrapolation of the saturation vapour pressure over ice for stratospheric conditions was shown by Marti and Mauersberger (1993). The nucleation of ice is discussed to be initiated by either STS, NAT or meteoric particles serving as nuclei (Koop et al., 2000; Engel et al., 2013; Voigt et al., 2018). Similar to NAT particles, ice PSCs can grow to large sizes and lead to significant dehydration of the lower polar stratosphere (Kelly et al., 1989; Vömel et al., 1995; Nedoluha et al., 2000; Engel et al., 2014). Thus, sedimentation of ice particles influences the formation of the other PSC types and the ozone depletion. Widespread dehydration can be found in the Antarctica due to the lower temperatures but it can also be large over the Arctic regions as shown by Khaykin et al. (2013) and references therein.

In mountain waves, the formation processes and composition of PSCs slightly differ from synoptic-scale PSCs. Box model simulations showed that STS formation in mountain waves considerably differs from thermodynamic equilibrium and the fraction of HNO_3 is increased (Meilinger et al., 1995; Bertram et al., 2000; Salcedo et al., 2001). Additionally, STS particles in mountain waves can exist at temperatures lower than the ice frost point as shown in measurements by Schreiner et al. (2002). NAT particles can grow to large sizes in mountain waves and then significantly contribute to denitrification (Carslaw et al., 1998). Within mountain waves, so-called "mother clouds" can

be formed (Mann et al., 2005): ice clouds are formed in the wave where then small NAT particles can be adhered. These larger particles sediment faster, subsequently. In addition, mountain-wave induced PSCs can enhance or disturb synoptic-scale PSCs (Bevilacqua et al., 2002).

Heterogeneous Reactions on the Surface of PSCs

Solomon et al. (1986) first showed that the observed ozone loss can only be explained by heterogeneous processes on the surface of PSCs. They suggested two reactions involving $ClONO_2$ that may be fast on aerosol surfaces. This was confirmed by Molina and Molina (1987) and Tolbert et al. (1988) who showed that HCl can be adsorbed by ice particles in the atmosphere. In addition, Tolbert et al. (1988) showed that N_2O_5 can react heterogeneously on the surfaces of PSCs. During the late 1980s, it was found that also HOCl is able to react with HCl when HCl is adsorbed by condensed surfaces (e.g., Elliott et al., 1994). Heterogeneous reactions of bromine-containing compounds were also found to be efficient on PSCs (Danilin and McConnell, 1995; Hanson and Ravishankara, 1995).

In summary, the following heterogeneous reactions on PSCs are described (e.g, Solomon, 1999):

$$ClONO_{2(g)} + H_2O_{(a)} \longrightarrow HNO_{3(a)} + HOCl_{(g)} \quad \text{(R2.29)}$$
$$ClONO_{2(g)} + HBr_{(a)} \longrightarrow HNO_{3(a)} + BrCl_{(g)} \quad \text{(R2.30)}$$
$$ClONO_{2(g)} + HCl_{(a)} \longrightarrow HNO_{3(a)} + Cl_{2(g)} \quad \text{(R2.31)}$$
$$BrONO_{2(g)} + H_2O_{(a)} \longrightarrow HNO_{3(a)} + HOBr_{(g)} \quad \text{(R2.32)}$$
$$BrONO_{2(g)} + HCl_{(a)} \longrightarrow HNO_{3(a)} + BrCl_{(g)} \quad \text{(R2.33)}$$
$$HOCl_{(g)} + HCl_{(a)} \longrightarrow H_2O_{(a)} + Cl_{2(g)} \quad \text{(R2.34)}$$
$$HOCl_{(g)} + HBr_{(a)} \longrightarrow H_2O_{(a)} + BrCl_{(g)} \quad \text{(R2.35)}$$
$$HOBr_{(g)} + HCl_{(a)} \longrightarrow H_2O_{(a)} + BrCl_{(g)} \quad \text{(R2.36)}$$
$$HOBr_{(g)} + HBr_{(a)} \longrightarrow H_2O_{(a)} + Br_{2(g)} \quad \text{(R2.37)}$$
$$N_2O_{5(g)} + H_2O_{(a)} \longrightarrow 2\,HNO_{3(a)} \quad \text{(R2.38)}$$
$$N_2O_{5(g)} + HCl_{(a)} \longrightarrow HNO_{3(a)} + ClONO_{(g)} \quad \text{(R2.39)}$$

The subscript "a" in these reactions stands for the species adsorbed in PSCs whereas species with "g" are in gaseous phase.

The heterogeneous reaction rate constant, $k_{\mathrm{het},r}$, of reaction r on solid and liquid particles can be derived from mass transfer and flux analyses (e.g., Turco et al., 1989, and references therein). Here, it is assumed that the equilibrium vapour concentration of the gaseous species is zero, meaning that the surface reaction is infinitely fast (Drdla et al., 1993). Expressing the resulting reaction rate constant as an equivalent bimolecular gas phase reaction rate constant, this leads to:

$$k_{\mathrm{het},r,c} = \frac{\gamma_{r,c}\pi r_c^2 \overline{v}_{i(r)} N_c}{N_{j(r)}\left(1 + \frac{3\gamma_{r,c}}{4\mathrm{Kn}}\right)} \quad (2.26)$$

with the Knudsen number Kn, see Eq. (2.20). Equation (2.26) is simplified from Fuchs and Sutugin (1971) for relatively small Knudsen numbers. It accounts for adsorption of the reactants on the particles by the uptake coefficient $\gamma_{r,c}$ on the assumed spherical particle with radius r_c. Here, c stands for the particle, i.e. ice, NAT or STS. N_c is the particle number concentration whereas $N_{j(r)}$ denotes the number concentration of the reactant adsorbed on the particle surface, i.e. $j(r)$ is either H_2O, HCl or HBr (Drdla et al., 1993). The mean thermal velocity $\overline{v}_{i(r)}$ of the gaseous reactant is another input parameter for Eq. (2.26), where $i(r)$ is then either N_2O_5, $ClONO_2$, $BrONO_2$, HOCl or HOBr. The thermal velocity of a molecule i can be described by the expected value of Maxwell-Boltzmann-distributed thermal velocities:

$$\overline{v}_i = \sqrt{\frac{8\,R^*\,T}{\pi\,M_i}} \tag{2.27}$$

In this equation, R^*, M_i and T are universal constant of an ideal gas, molar mass of i and air temperature, respectively.

In addition, the free mean path λ_{mfp} of the gaseous reactant in air has to be accounted for in the Knudsen number of Eq. (2.26). Thus, λ_{mfp} should principally depend on the gaseous reactant c. The mean free path λ_{mfp} is calculated as follows (see Kennard, 1938):

$$\lambda_{\mathrm{mfp}} = \frac{R^*\,T}{\sqrt{2}\pi p N_{\mathrm{A}} D_{\mathrm{c}}^2} \tag{2.28}$$

Here, R^* and N_{A} are universal constant of an ideal gas and Avogadro's constant whereas T and p stand for temperature and pressure, respectively. Due to uncertainties in the collision diameters D_{c} of the gaseous reactants in the heterogeneous reactions, the collision diameter of air molecules of $D_{\mathrm{c}} = 3.7$ Å is used for Eq. (2.26) (Kennard, 1938).

In contrast to ice and NAT particles, STS particles are considerably smaller. Therefore, the Knudsen number becomes large compared to the uptake coefficient $\gamma_{r,c}$ in Eq. (2.26) and this term can be neglected for STS particles (e.g., Lovejoy and Hanson, 1995; Hanson et al., 1996; Shi et al., 2001). Expressed in terms of the particle surface concentration S_{STS} instead of the radius and particle number concentration, the heterogeneous reaction rate constant for STS yields:

$$k_{\mathrm{het},r,\mathrm{STS}} = \frac{\gamma_{r,\mathrm{STS}}\overline{v}_{i(r)}S_{\mathrm{STS}}}{4N_{j(r)}} \tag{2.29}$$

3

The Modelling Framework ICON-ART

The ICOsahedral Non-hydrostatic modelling framework (ICON) is a next-generation model of the atmosphere uniquely allowing for modelling across scales. Combined with the extension for Aerosols and Reactive Trace gases (ART), large-scale transport and chemistry of trace gases as well as small-scale processes, such as chemical processes in mountain waves, can be modelled simultaneously with two-way interaction. Thus, the modelling framework ICON-ART gives the unique possibility to investigate polar stratospheric clouds in mountain waves and their representation in long-term simulations with coarse global resolution.

After a general overview of ICON-ART (Sect. 3.1), the local grid refinement with two-way interaction (Sect. 3.2) and the parametrisation of subgrid-scale gravity waves in the model are described (Sect. 3.3). Then, the gas phase chemistry mechanism is described (Sect. 3.4). Finally, the PSC scheme in ICON-ART is pointed out which was developed in the scope of this thesis (Sect. 3.5).

3.1 General Overview

3.1.1 The ICON Model

The ICON model is a joint development of German Weather Service (DWD) and Max-Planck-Institute for Meteorology (MPI-M). It is designed for applications like large-eddy simulations (LES, Dipankar et al., 2015), numerical weather prediction (NWP, Zängl et al., 2015) and up to climate projections for Earth system modelling (Giorgetta et al., 2018). To achieve the large variety of space and time scales with grid spacings from 100 m up to more than 100 km the governing equations in ICON are formulated as non-hydrostatic equations with local mass conservation (Zängl et al., 2015).

Horizontal discretisation is performed on an icosahedral-triangular C grid (e.g., Staniforth and Thuburn, 2012). Refinement of the icosahedron covering the globe (red in Fig. 3.1(a)) is done by dividing it into several parts, called root division (Rn). The resulting triangles are then refined via bisections (Bk). For projection on the Earth's surface, the original equilateral triangles are enlarged.

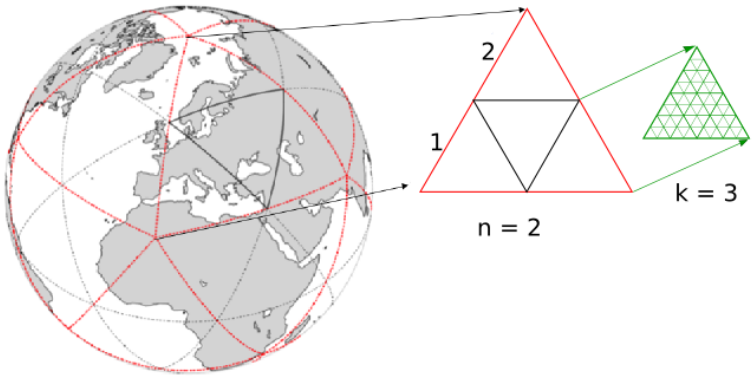

(a) Horizontal grid

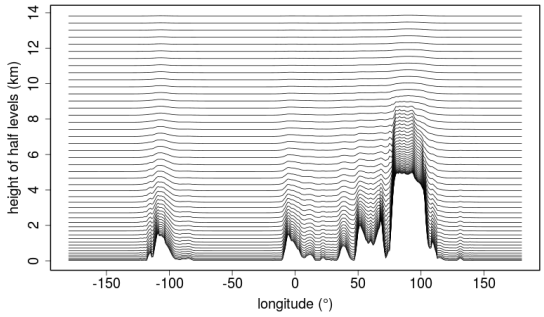

(b) Vertical grid

Figure 3.1: Horizontal and vertical grid of ICON. (a) Schematic illustration for refining the horizontal grid (red: original icosahedron). Example is shown for the resolution of R2B03. Figure from Weimer (2015). The globe in panel (a) was e.g. published in Fig. 1a of Borchert et al. (2019) (CC-BY 3.0 license). (b) Lowest model layers at the latitude of the Himalayas. Figure from Weimer et al. (2017).

Table 3.1: Horizontal resolutions used in this thesis. The grid spacing Δx is approximated from $\Delta x = \sqrt{\pi/5}\ R/(n\,2^k)$ with R as Earth's radius, n number of root divisions and k number of triangle bisections.

Nest	Resolution	approx. Δx (km)	Number of Cells
Global	R2B04	160	20480
Antarctica	R2B05	80	15008
Antarctic Peninsula	R2B06	40	6172

Thus, a spring dynamics optimisation is applied to the triangles in order to get triangles of nearly the same size (Tomita et al., 2001; Zängl et al., 2015). An example for the refinement process of the resolution R2B03 can be found in Fig. 3.1(a). The horizontal resolutions used in this thesis are summarised in Table 3.1. A description of the nesting technique in ICON-ART follows in Sect. 3.2.

Vertically, generalised terrain following coordinates are used according to Schär et al. (2002) and Leuenberger et al. (2010). Figure 3.1(b) shows the height of the lowest model layers at the latitude of the Himalayas.

The dynamical core of ICON solves the Navier Stokes equations, the continuity equation and the first law of thermodynamics. They are expressed as equations for the prognostic variables horizontal wind perpendicular to the triangle edge v_n, vertical wind w, air density ρ and virtual potential temperature θ_v (Zängl et al., 2015):

$$\frac{\partial v_\mathrm{n}}{\partial t} + \frac{\partial K_\mathrm{h}}{\partial n} + (\zeta + f)v_\mathrm{t} + w\frac{\partial v_\mathrm{n}}{\partial z} = -c_\mathrm{pd}\theta_\mathrm{v}\frac{\partial \pi}{\partial n} + f_\mathrm{F}(v_\mathrm{n}) \tag{3.1}$$

$$\frac{\partial w}{\partial t} + \mathbf{v}_\mathrm{h}\cdot\nabla w + w\frac{\partial w}{\partial z} = -c_\mathrm{pd}\theta_\mathrm{v}\frac{\partial \pi}{\partial z} - g \tag{3.2}$$

$$\frac{\partial \rho}{\partial t} + \nabla\cdot(\mathbf{v}\rho) = 0 \tag{3.3}$$

$$\frac{\partial \pi}{\partial t} + \frac{R_\mathrm{d}}{c_\mathrm{vd}}\frac{\pi}{\rho\theta_\mathrm{v}}\nabla\cdot(\mathbf{v}\rho\theta_\mathrm{v}) = Q \tag{3.4}$$

with π as Exner function:

$$\pi = \left(\frac{R_\mathrm{d}}{p_{00}}\rho\theta_\mathrm{v}\right)^{\frac{R_\mathrm{d}}{c_\mathrm{vd}}} \tag{3.5}$$

In these equations, the indices n and t stand for the direction perpendicular and tangential to the triangle edge, respectively, and the index h depicts the horizontal component. K_h denotes the horizontal kinetic energy. Constants in the equations are the specific heat capacities of dry air for constant volume c_vd and constant pressure c_pd, the gas constant of dry air R_d, the gravitational acceleration g and the reference pressure of $p_{00} = 1000\,\mathrm{hPa}$. $f_\mathrm{F}(v_\mathrm{n})$ is a source and sink term for momentum, e.g. due to frictional forces at the surface and turbulence in the atmosphere. The diabatic heating Q is a source and sink term for temperature. The external source and sink terms f_F and Q are subject of the physics parametrisations in ICON. In addition, the physics parametrisations include the microphysics schemes for generation of clouds and precipitation. A two-time-level predictor corrector method is used to solve the non-hydrostatic equation system above, with special treatment of vertically propagating sound waves. Further details can be found in Zängl et al. (2015).

Tracers in ICON, such as hydrometeors, are transported as barycentric averaged mass specific variables, such as mixing ratios. This ensures the correct treatment of parametrised turbulence for the tracers (see Schröter, 2018). Tracer transport is calculated by a flux-form semi-Lagrangian method (further details see Miura, 2007; Wan et al., 2013).

For applying the model to the whole variety of space and time scales mentioned above the parametrised physics have to be adapted. For instance, convection has to be treated differently

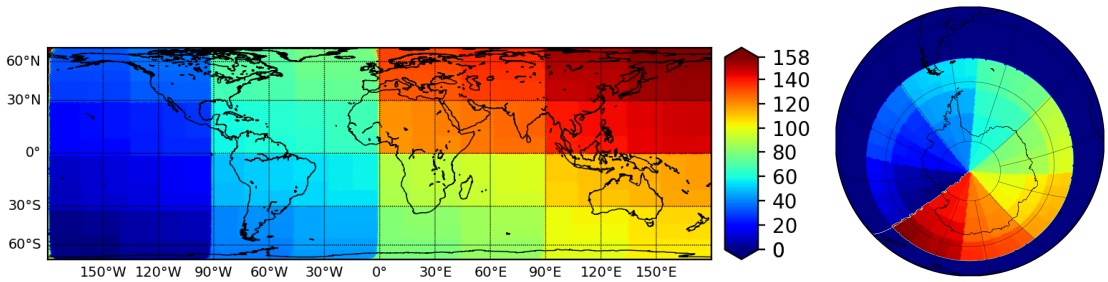

(a) Global Domain (b) Nest over Antarctica

Figure 3.2: Distribution of MPI processes on (a) global domain and (b) nested over Antarctica. The example is shown for 159 computing MPI processes (not used for I/O).

for a grid spacing of Δx = 100 m, 10 km or 100 km. At a resolution of 100 m, convection can be directly resolved, at 10 km it can be partly resolved whereas for a grid spacing of 100 km it has to be parametrised completely. In ICON, three different physics parametrisations can be chosen: LES, NWP and climate configurations. This thesis focusses on ICON used in NWP and climate configurations. Their microphysics schemes will be further discussed in Sect. 3.5.

ICON as a next-generation model is parallelised for hybrid architectures and especially using the Message Passing Interface (MPI, MPI Forum, 2015). Each MPI process calculates a specific limited area of the Earth and communicates its boundaries to its neighbours. The distribution of the MPI processes in the global domain for 159 computing MPI processes is shown in Fig. 3.2(a). For an optimal load balance, all MPI processes are also distributed in the nested domain. Figure 3.2(b) shows a circular nest around the South Pole and the distribution of the same 159 MPI processes.

3.1.2 The ART Extension

The extension for Aerosols and Reactive Trace gases (ART) has been developed for incorporating aerosols and the atmospheric chemistry into ICON. The ART module can be coupled to ICON in NWP (Rieger et al., 2015) and climate configuration (Schröter et al., 2018).

Trace gases in ICON-ART (called tracers hereafter) are transported as mixing ratios using the same methods as for ICON tracers. The applicability of ICON-ART for small-scale as well as long-term simulations provokes the need of a flexible tracer framework where tracers can be added without changes in the code. In ICON-ART, this is realised via XML files where tracers can easily be added to the model including meta information (Schröter et al., 2018).

Three chemistry modes are available in ICON-ART:

1. the lifetime-based chemistry where tracers are depleted by a constant lifetime (see Rieger et al., 2015)
2. the simplified steady-state OH chemistry for depletion of tracers reacting with OH (Weimer et al., 2017)
3. the gas phase chemistry (Schröter et al., 2018)

Lifetime-based chemistry and simplified OH chemistry can be complemented by linearised schemes for ozone (Stassen, 2015) and NO_y (Diekmann, 2017). Gas phase chemistry is calculated with the Module Efficiently Calculating the Chemistry of the Atmosphere (MECCA, Sander et al., 2011a), as described in Schröter et al. (2018), see Sect. 3.4.

In addition, ICON-ART contains a module for adding emissions from external data sources, as pointed out by Weimer et al. (2017). Photolysis rates are computed with the CloudJ module (Prather, 2015).

The ART extension is applied at DWD to predict specific dust events in Europe. Recent work with ICON-ART included the investigation of several trace gases such as acetone (Weimer et al., 2017), ammonia (Ullwer, 2018) and methane (Guggenberger, 2018). Diekmann (2017) investigated the polar upper troposphere and lowermost stratosphere with ICON-ART, focussing on N_2O and NO_y. These studies included long-term simulations as well as comparisons to local measurement campaigns. Schröter et al. (2018) investigated the climate impact of ozone and water vapour due to a feedback on radiation. Eckstein et al. (2018) presented the module for investigation of isotopologues with ICON-ART and compared it with ground station data. Gruber (2019) examined the influence of Arctic cirrus clouds on the climate. Schröter (2018) showed the first application of ICON-ART using chemistry with local grid refinement which is described in the following section.

3.2 Local Grid Refinement with Two-way Interaction

In order to improve the weather prediction skill at a specific region of the Earth, the general procedure up to now was as follows: a simulation with a global model and low resolution was conducted where many physical processes had to be parametrised. This model provided the boundary conditions for a regional model with higher resolution and more realistic physics which resulted in the weather prediction of that region[1]. Since these were different models and because of the successive execution of the simulations a feedback to the global model was not possible.

With the grid structure of ICON-ART and the straight-forward procedure to refine the grid (Fig. 3.1(a)) it is now possible to locally refine the grid and provide boundary conditions for the better resolved regions consistently within the same model. In addition, since global and refined grid are computed simultaneously information can be transferred from the refined grid back to the global domain. Since the two-way grid refinement (nesting) is applicable to any pair of grids with resolutions RnBk and RnB($k+1$) (see Table 3.1) the coarser grid is referred to as parent domain and the refined grid as child domain. The technical realisation, as shown by Reinert et al. (2019), and the configuration used in this thesis is discussed in the following.

External data such as orography has to be configured for each domain separately. For this, the ExtPar package is used in its most recent version (Smiatek et al., 2008, extended for application in ICON-ART). In the configuration of this thesis, the prognostic variables in the child domain are initialised by the parent domain. This requires the child domain to start a few time steps after the parent domain, set to $\Delta t_{\text{start}} = 24$ min in this thesis.

The feedback from child to parent domain is a relaxation based method (Reinert et al., 2019). Firstly, the prognostic variables are upscaled to the parent domain, i.e. interpolated. The four child triangles

[1] This can be nested, so that the second model initialises a third one with even higher resolution and so on.

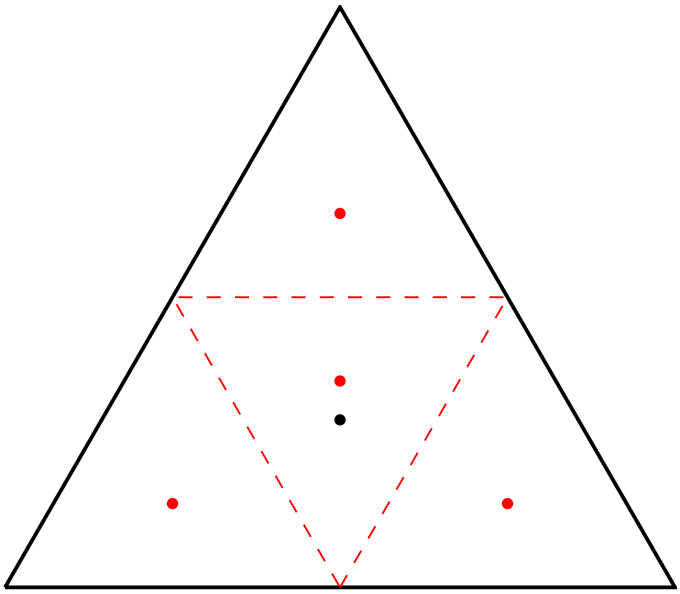

Figure 3.3: Illustration of one triangle in the parent domain, refined by bisection in the child domain. This is a schematic figure since the triangles in the model have to be optimised in their size to fit on the Earth's sphere. Therefore, the triangles are not exactly equilateral triangles (cf. Fig. 3.1(a)). The points refer to the centres of the circumscribed circle of each triangle. The four red points are used for the feedback to the black point in the parent domain.

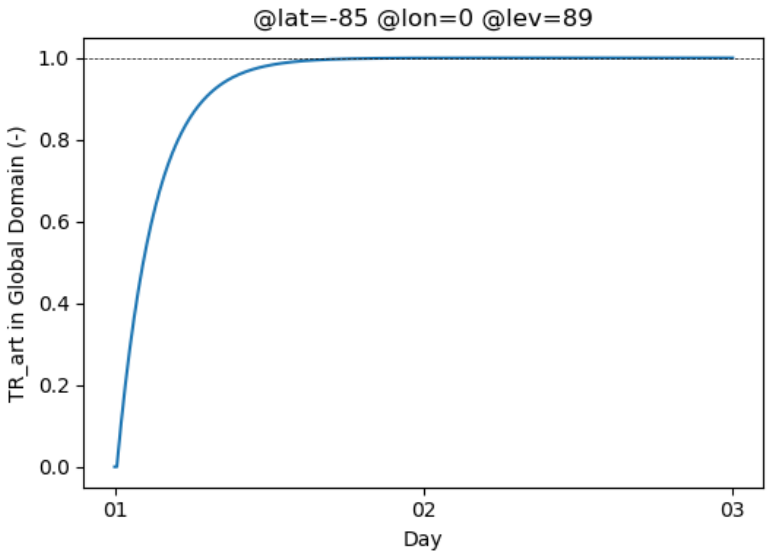

Figure 3.4: Test of relaxation for two-way nesting in ICON-ART. The concentration change of an artificial ART tracer in the global domain is shown for one grid point where the tracer is initialised with one in the nest and zero in the global domain. The latitude is chosen to ensure negligible influence by the edge of the nest.

contribute to the value for the parent domain, see Fig. 3.3. Then, the variables in the parent domain are relaxed towards the values in the child domain. A relaxation time scale can be chosen by the user and is set to 3 h in this thesis. After this time scale the parent domain has been relaxed towards the child domain exponentially. This can be seen in Fig. 3.4 where a test is performed for an artificial ICON-ART tracer initialised with 0 in the global domain and with 1 in the nested domain. A time series of the tracer value in the centre of the nest is shown which should not be influenced by boundary processes too much. After 3 h, the tracer has a value of 0.63 which corresponds to $1 - 1/e$. Then, it approximates the value of 1 which is the initialisation value of the child domain.

3.3 Parametrisation of Gravity Waves

The goal of this thesis is the investigation of PSCs in directly simulated mountain waves. Nevertheless, subgrid scale gravity waves have to be parametrised. The parametrisation of subgrid-scale mountain waves and nonorographic gravity waves is briefly described in this section. The representation of gravity waves depends on the resolved physics in the model and therefore on the chosen physics package. In both, NWP and climate configurations, the scheme of Lott and Miller (1997) is applied for subgrid-scale mountain waves (Sect. 3.3.1). The parametrisation of nonorographic gravity waves differs within the two physics packages (Sect. 3.3.2).

3.3.1 Subgrid-scale Mountain Waves

In the scheme for subgrid-scale orographic gravity waves in ICON-ART, the gravity wave drag is calculated by standard deviation, anisotropy, slope, orientation, minimum, maximum, and mean elevation of the mountains (Lott and Miller, 1997; Lott, 1999)[2]. In ICON-ART, these parameters are derived from the high-resolution data set GLOBE (GLOBE Task Team, 1999) using the ExtPar package (Smiatek et al., 2008). The concept is based on elliptically shaped mountains where the flow is either blocked or lifted by the mountain. Blocking in this context means that the flow passes the mountain at the flanks at levels below the mountain's top. Subsequently, this concept is modified for a realistic representation of subgrid-scale orography by using the seven parameters mentioned above. The parametrisation assumes Boussinesq and hydrostatic approximations in the layers up to the mountain height.

3.3.2 Nonorographic Gravity Waves

NWP Configuration

Nonorographic gravity waves in NWP configuration are based on the implementation within the ECMWF Integrated Forecast System (IFS, Simmons et al., 1989; Scinocca, 2003; Orr et al., 2010). This scheme uses a hydrostatic formulation for gravity waves and assumes that they are non-rotational. The wave spectra are launched at a specific level with an initial momentum flux and are then propagated upwards. As soon as the amplitude of the wave exceeds a defined saturation

[2] Lott and Miller (1997) describe only four parameters whereas Lott (1999) indicates the seven parameters mentioned in the text, but referencing to Lott and Miller (1997).

threshold the excess momentum flux is deposited to the background flow. At the model top, mass conservation is ensured by transferring the remaining momentum flux to the background flow.

One of the tuning parameters of this scheme is the initial momentum flux. This quantity depends on the horizontal resolution of the model because double counting of resolved and parametrised gravity waves has to be avoided. The actual value of the initial momentum flux is an issue of research (Orr et al., 2010). In the configuration of this thesis, it is set to the ICON-ART default value of 2.5×10^{-3} which is also used in the operational setup at DWD with an approximate horizontal resolution of 13 km.

Climate Configuration

Hines (1997) provides a parametrisation of nonorographic gravity waves based on the Doppler-spread theory. Advective processes lead to nonlinear interaction between waves in the propagating spectrum and hence to a Doppler shift and an increase of the wave amplitude. Similar to Orr et al. (2010), the gravity waves are released at an initial height (680 hPa in ICON-ART, Giorgetta et al., 2018) and dissipate for vertical wavelengths larger than a cut-off wavelength (126 km in ICON-ART). The overshooting momentum flux, kinetic and intrinsic energy is then deposited to the background flow. Further details can be found in Giorgetta et al. (2018).

3.4 Gas Phase Chemistry

The gas phase chemistry module MECCA (Sander et al., 2011a) has been incorporated in ICON-ART by Schröter et al. (2018) and is used to calculate the non-linear system of ordinary differential equations (ODEs) of chemical mechanisms in the model. The chemistry module MECCA uses the Kinetic PreProcessor (KPP, Sandu and Sander, 2006), with which the chemistry mechanism can be chosen by the user.

The KPP preprocessor provides a variety of solvers for the non-linear ODE system, see e.g. Sandu et al. (1997), Damian et al. (2002), and Sandu and Sander (2006). In this thesis, the third-order Rosenbrock ODE solver RODAS-3 is used (within the KPP solver file "rosenbrock_mz"), see Sandu et al. (1997). Third-order solvers generally compute the stiff system of ODEs with sufficient precision for atmospheric conditions (Sander et al., 2011a).

In this thesis, a system of 141 chemical reactions including 37 photolytic and 11 heterogeneous reactions is used. The full mechanism can be found in Appendix C. It includes a comprehensive ozone and NO_y chemistry as well as chemistry of the halogens Cl and Br. The heterogeneous reaction rate constants on PSCs are provided by the PSC scheme in ICON-ART (see Sect. 3.5.4) and are input for the MECCA module.

Deposition of sulphate aerosols is one the main sinks for H_2SO_4 in the atmosphere. Since this is not included in the current stage of ICON-ART the H_2SO_4 tracer is prescribed by a climatology based on SAGE-II satellite measurements combined with model simulations for the CMIP5 project (Thomason et al., 2008; SPARC, 2013). Technically, the prescribing is performed by a module developed in the scope of this thesis. It combines the ideas of the emission module by Weimer et al. (2017) and the vertical interpolation for initialisation of chemical species mentioned in Schröter et al. (2018).

Table 3.2: Emission datasets for chemical species used in this thesis. The external datasets are interpolated to the ICON grid and included in ICON-ART as described in Weimer et al. (2017). They are downloaded from the ECCAD database.

Species	GEIA[a]	MACCity[b]	MEGAN-MACC[c]	GFED3[d]	EDGARv4.2[e]
$CFCl_3$	✓	–	–	–	–
CH_4	–	✓	✓	✓	–
CO	–	✓	✓	–	✓
CO_2	–	–	–	✓	✓
N_2O	–	–	–	✓	✓
SO_2	–	✓	–	✓	–

[a] Cunnold et al. (1994)
[b] van der Werf et al. (2006), Lamarque et al. (2010), Granier et al. (2011), and Diehl et al. (2012)
[c] Sindelarova et al. (2014)
[d] van der Werf et al. (2010)
[e] Janssens-Maenhout et al. (2011, 2013)

For emissions of the chemical tracers, external datasets provide global surface emission mass flux densities with a grid spacing of 0.5° × 0.5° or 1° × 1°. The time resolution is either monthly or yearly. They have been downloaded from the database of Emissions of atmospheric Compounds & Compilation of Ancillary Data[3] (ECCAD). The emissions are converted to volume mixing ratio, interpolated to the simulation time and added to the respective tracer as described by Weimer et al. (2017). The used emission datasets are summarised in Table 3.2.

3.5 The Scheme for Polar Stratospheric Clouds

In this section, the PSC scheme in ICON-ART as implemented in the scope of this thesis is described. This includes the formation and sedimentation of PSCs as well as the heterogeneous chemistry on PSCs. The general work flow can be found in Fig. 3.5. In the first step ice clouds are calculated within the ICON microphysics, then NAT and STS particles are formed in the model. Finally, the heterogeneous reaction rate constants on PSCs and the NAT sedimentation are computed before the call of the gas phase chemistry.

In the following, the formation of the three PSC types is described (stratospheric ice in Sect. 3.5.1, NAT and its sedimentation in Sect. 3.5.2 and STS in Sect. 3.5.3). This is followed by the heterogeneous chemistry on PSCs (Sect. 3.5.4).

3.5.1 Ice Formation in the Stratosphere

Current atmospheric chemistry models such as EMAC (ECHAM/MESSy Atmospheric Chemistry, Jöckel et al., 2006) or GMI 3-D (Global Modeling Initiative, Considine et al., 2000) form ice PSCs by using the parametrisation of the saturation vapour pressure over ice by Marti and Mauersberger (1993):

[3] https://eccad.aeris-data.fr/

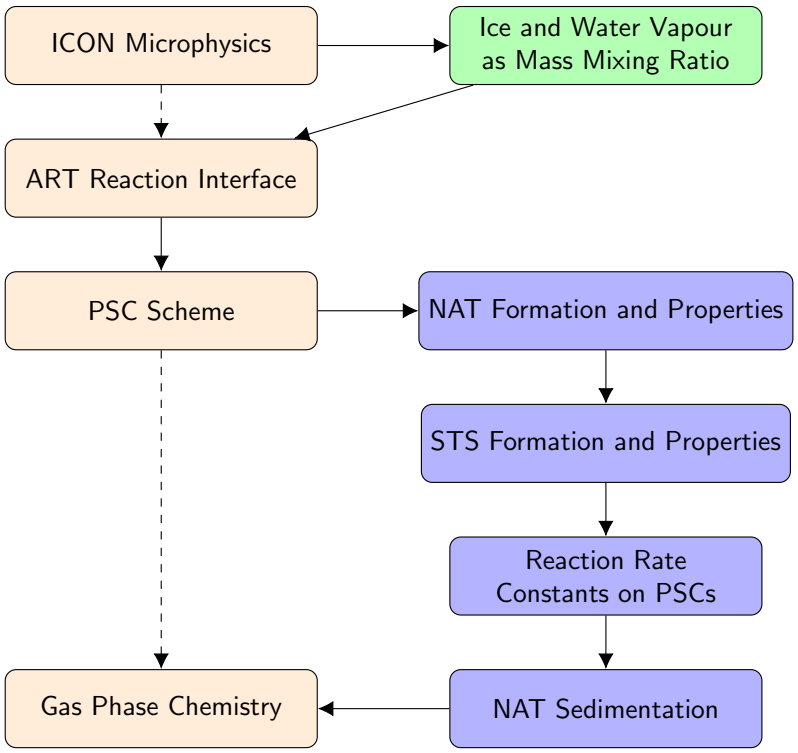

Figure 3.5: General work flow of the PSC scheme. The ice and water vapour mass mixing ratios are calculated by the ICON microphysics. The PSC scheme is called in the reaction interface of ICON-ART before the gas phase chemistry. With this, the heterogeneous reaction rate constants on PSCs are updated directly before the call of the gas phase chemistry.

$$\log_{10}(p_{\mathrm{sat,ice}}) = \frac{A_{\mathrm{ice}}}{T} + B_{\mathrm{ice}} \tag{3.6}$$

with $A_{\mathrm{ice}} = -2663.5 \pm 0.8$ and $B_{\mathrm{ice}} = 12.537 \pm 0.011$. In this equation, T is the temperature in K and $p_{\mathrm{sat,ice}}$ is the saturation vapour pressure over ice in Pa. Equation (3.6) is based on measurements and verified within the temperature range from 170 to 250 K. As a diagnostic parametrisation, ice forms, chemistry is calculated and ice sublimates again within the same time step.

If the water vapour pressure exceeds the saturation vapour pressure of Eq. (3.6) the ice volume mixing ratio ($X_{\mathrm{H_2O(ice)}}$) is calculated by the difference of partial water vapour pressure $p_{\mathrm{H_2O}}$ and saturation vapour pressure over ice $p_{\mathrm{sat,ice}}$ divided by the ambient pressure p (e.g., Kirner et al., 2011):

$$X_{\mathrm{H_2O(ice)}} = \frac{p_{\mathrm{H_2O}} - p_{\mathrm{sat,ice}}}{p}, \quad p_{\mathrm{H_2O}} > p_{\mathrm{sat,ice}} \tag{3.7}$$

This parametrisation assumes that the complete supersaturated amount of water vapour immediately resublimates. Therefore, it presumes heterogeneous nucleation with a sufficient number of ice nuclei in the lower stratosphere (around 7.5 $\mathrm{cm^{-3}}$, Hoyle et al., 2013).

Calculation of Ice Formation in NWP Configuration

For the purpose of numerical weather prediction with ICON, the ice formation is calculated operationally by a one-moment scheme described by Doms et al. (2011). In the operational setup, five different hydrometeor classes are distinguished:

- water vapour
- cloud water
- cloud ice
- rain
- snow

The scheme calculates conversions among all the classes in a consistent way. With respect to cloud ice, conversions such as accretion, freezing, deposition, riming, melting and evaporation of the ice particles are taken care of. As part of a one-moment scheme, either size distribution or mass of cloud ice particles have to be prescribed. In ICON, the particle number concentration of ice particles (in $\mathrm{m^{-3}}$) is parametrised dependent on temperature T in K (Cooper, 1986):

$$N_{\mathrm{ice}}(T) = \min\left(5 \exp[0.304\,(273.15 - T)], 250 \times 10^3\right) \tag{3.8}$$

Thus, the cloud ice particle number concentration saturates at a value of 250 000 $\mathrm{m^{-3}}$. This corresponds to a temperature of $T \approx 239$ K, see Fig. 3.6. Therefore, the number concentration is constant for temperatures around formation of PSCs (dashed line in Fig. 3.6). The particle number concentration of 250 000 $\mathrm{m^{-3}}$ is by factor of about ten larger than the observed concentrations in the stratosphere (see, e.g., Buchholz, 2005, and references therein). In order to keep the consistency

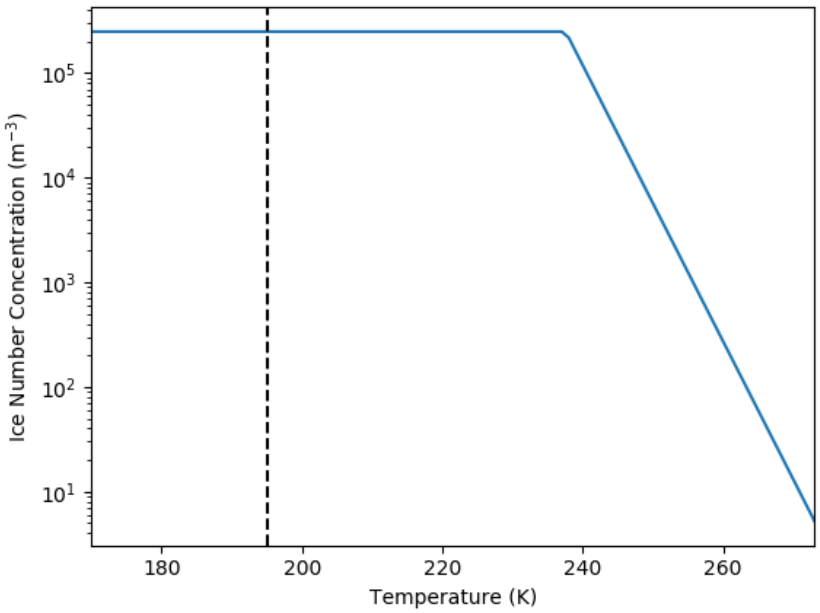

Figure 3.6: The particle number concentration of ice particles as implemented in the one-moment scheme in NWP configuration. The ice number concentration is calculated by Eq. (3.8), based on Cooper (1986). It saturates at a value of 250 000 m^{-3} which corresponds to $T \approx 239$ K. The temperature below which PSCs usually form (195 K) is depicted by the black dashed line.

with the microphysical scheme in NWP configuration, this value is used for stratospheric conditions. The one-moment scheme also accounts for sedimentation of ice particles.

In the operational setup at DWD, the one-moment scheme is applied up to a specific altitude. For the purpose of operational weather forecasts at DWD, this altitude[4] is set to $h_{\text{top}} = 22.5$ km (approx. 20 hPa). Since PSCs also occur below this altitude they have to be parametrised differently below and above h_{top}. Above h_{top}, the parametrisation by Marti and Mauersberger (1993) (Eq. (3.6)) should be applied whereas the one-moment scheme of ICON would be calculated below h_{top}. Thus, ice formation would be computed by different parametrisations above and below h_{top} and an inconsistency arises at this threshold altitude. This is indicated by Fig. 3.7(d) where the operational setup is illustrated including the vertical range where PSCs are expected to form. Therefore, the handling of h_{top} will be discussed in the following.

The top altitude of the microphysics h_{top} must not get lower than the tropopause all over the globe to ensure the microphysics and convection to be applied in the whole troposphere. That is why five possibilities can be taken into account how to proceed with ice PSCs in ICON-ART (see Fig. 3.7). All of them have advantages and disadvantages.

(a) h_{top} *as function of the tropopause height*:

From a physical point of view, it seems reasonable to set h_{top} equal to the tropopause height since the ICON one-moment scheme mainly fits for tropospheric conditions (see Fig. 3.7(a)).

[4]Here, it is referred to h_{top} as both the ICON parameters `htop_moist_proc` and `hbot_qvsubstep` where `htop_moist_proc` is the top height for calculation of microphysics and `hbot_qvsubstep` is the height above which water vapour is calculated with a sub-stepping.

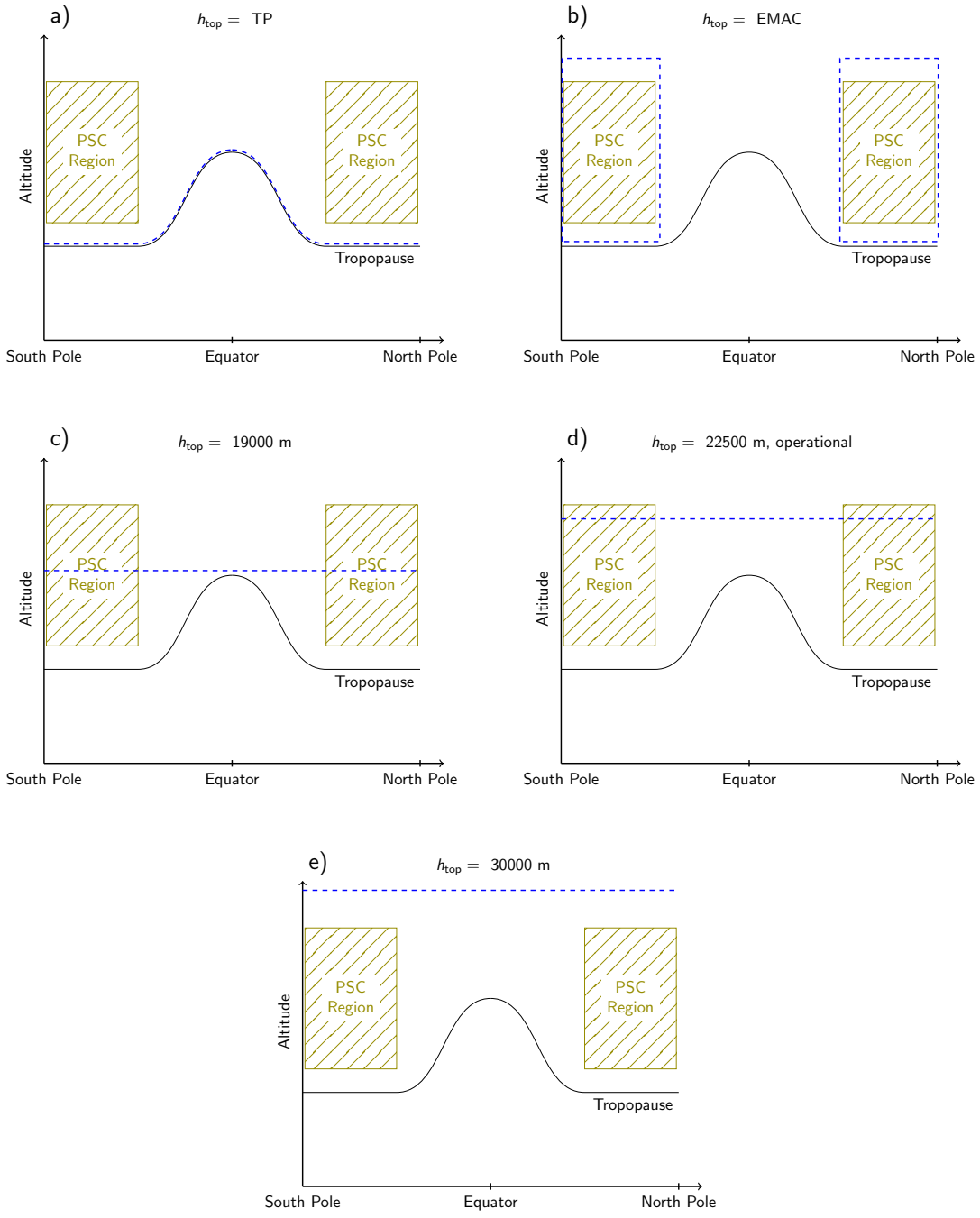

Figure 3.7: Schematic illustration of the different possibilities for h_{top}. (a) h_{top} follows the tropopause height, (b) height and latitude range where ice PSCs are parametrised, (c) to (e) several constant values for h_{top}.

In this case, ice PSCs are calculated with the parametrisation by Marti and Mauersberger (1993). The tropopause height, though, depends on the latitude. Thus, from a technical point of view, this option means a lot of changes within one of the core modules of ICON since all loops within the code have to be rearranged, making it quite inefficient.

(b) *Defined region with PSC formation:*

In the atmospheric chemistry model EMAC, the formation of PSCs is computed at specific altitude and latitude regions around South and North Poles (see Fig. 3.7(b)). The diagnostic parametrisation by Marti and Mauersberger (1993) is applied in this region and the standard module of the cloud microphysics outside. This ansatz, however, has the same disadvantage as in (a): h_{top} depends on the location in this case. In addition, overlapping regions to the standard procedure of ice formation are possible and have to be avoided.

(c) *Decrease h_{top}:*

Another possibility could be to decrease h_{top} to 19 km (approx. 60 hPa). This value is an attempt to separate the tropospheric microphysics from the stratospheric parametrisation by Marti and Mauersberger (1993). However, the tropopause height varies with latitude (see Fig. 3.7(c) and e.g. Weimer et al., 2017). The tropopause height is lower above the poles than above the tropics. Therefore, the initial problem of the inconsistency of ice PSC parametrisation still holds for lower values of h_{top}. It is just shifted to a lower altitude.

(d) *Keep h_{top} as it is:*

With this option, the problems have already been discussed above: The value of h_{top} is within the height range where PSCs are expected to exist. Thus, ice PSCs have to be calculated with different parametrisations above and below this altitude (see Fig. 3.7(d)).

(e) *Increase h_{top} above PSC region:*

Polar stratospheric clouds have been measured up to an altitude of about 27 km (Zhu et al., 2017; Pitts et al., 2018). Thus, setting h_{top} = 30 km (approx. 10 hPa) ensures the ICON one-moment scheme to be applied also for ice PSCs, i.e. in the lower stratosphere, see Fig. 3.7(e). The diagnostic ice parametrisation by Marti and Mauersberger (1993) is completely left out in this case.

The most natural way to proceed with ice formation in the stratosphere is to increase h_{top} in order to ensure that ice is formed consistently by the one-moment scheme in the whole troposphere and stratosphere. However, this option also raises the following questions:

1. When changing h_{top}, the water cycle and with this the dynamics in the model are changed. Therefore, the question is: What is the influence on the dynamics when increasing h_{top}?
2. Does the one-moment scheme produce realistic ice clouds in the stratosphere and how do both parametrisations compare to each other?
3. What is the influence on other processes in the model such as convection?

These questions will be addressed in Sect. 5.3.1.

Radius of Ice Particles in NWP Configuration

Radius and particle number concentration are essential parameters for calculation of the heterogeneous reaction rate constants on PSCs (see Sect. 2.5). With Eq. (3.8), the mass of ice particles can be derived by:

$$m_{\text{ice}} = \frac{\rho W_{\text{ice}}}{N_{\text{ice}}} \tag{3.9}$$

where ρ and W_{ice} stand for air density and water mass mixing ratio in cloud ice, respectively. The particle number concentration is set to 250 000 m^{-3} according to Eq. 3.8 for low temperatures. By assuming the ice particles to have an aspect ratio of 0.2 and an ice density of 500 kg m^{-3} (Doms et al., 2011)[5], the radius of the ice particles is calculated as follows:

$$r_{\text{ice}} = \frac{1}{2}\sqrt[3]{\frac{m_{\text{ice}}}{130}} \tag{3.10}$$

where the particle mass has to be given in kg to get the effective radius in m.

Calculation of Ice Formation in Climate Configuration

ICON-ART can be used in NWP (Rieger et al., 2015) as well as in climate configuration (Schröter et al., 2018). This also holds for the PSC scheme. As described above it requires the ice concentration as external input which was discussed for the NWP configuration so far, only.

The microphysics in the model in climate configuration (Giorgetta et al., 2018) are based on Lohmann and Roeckner (1996) and Giorgetta et al. (2013) of the ECHAM model. It accounts for three hydrometeor classes:

- water vapour
- cloud water
- cloud ice

The treatment of the microphysics is generally similar as in NWP configuration: conversions in terms of tendencies are computed for the different hydrometeor classes and added or subtracted from them. The microphysics of ice in climate configuration accounts for advection, sedimentation, sublimation, turbulent fluxes, melting, freezing, aggregation and accretion. In contrast to the NWP microphysics, no particle number concentration of ice is prescribed in the scheme. The growth of the particle is rather based on assumptions of relative humidity and cloudiness. A start level for calculation of the microphysics can be specified by the user and is set initially to the level corresponding to 30 km in the 47 level configuration (level 15).

[5] The ice density is declared as 5×10^{-2} kg m^{-3} but most probably has to be 500 kg m^{-3}.

Radius and Particle Number Concentration in Climate Configuration

In the climate configuration of ICON, the calculation of the radius of ice particles described in the following and is based on Giorgetta et al. (2013). In a first step, the effective radius is calculated as:

$$r_{\text{eff,ice}} = 83.8\left(10^3 \rho q_{\text{ice}}\right)^{0.216} \tag{3.11}$$

In this equation, the air density ρ and q_{ice} have to be given in kg m^{-3} and kg kg^{-1}, respectively, to get $r_{\text{eff,ice}}$ in µm. Subsequently, the volume radius of ice particles is derived from the effective radius:

$$r_{\text{ice}} = 10^{-6}\left(\sqrt{2809\, r_{\text{eff,ice}}^3 + 5113188} - 2216\right)^{\frac{1}{3}} \tag{3.12}$$

As indicated in this equation, r_{ice} is used as radius of the ice particles in the climate configuration, where the effective radius has to be given in µm to get r_{ice} in m.

The deposition of ice particles in the climate configuration is calculated based on Eq. (2.23) and no size distribution of the particles is assumed. Thus, it is set to the value of 10^4 m^{-3} which correponds to the typical ice particle number concentration in the stratosphere (e.g., Considine et al., 2000; Buchholz, 2005).

3.5.2 Nitric Acid Trihydrate Particles

In ICON-ART, two parametrisations for NAT particles have been implemented in the scope of this thesis (cf. Kirner et al., 2011). The work flow of these two approaches is shown in Fig. 3.8. The diagnostic thermodynamic parametrisation is described in the following section. In the kinetic approach NAT particles are categorised into different size bins to improve the size distribution of the particles. As briefly mentioned in Chapter 2, sedimentation is the essential process corresponding to NAT particles since it leads to denitrification and a slower recovery of ozone after its depletion in early spring. Sedimentation will be discussed in the end of this section.

Thermodynamic NAT Parametrisation

The thermodynamic NAT parametrisation is based on Hanson and Mauersberger (1988). The difference between HNO_3 vapour pressure and its saturation vapour pressure over NAT determines the amount of NAT phase HNO_3 that is formed. According to Hanson and Mauersberger (1988), the saturation vapour pressure over NAT depends on temperature and the partial pressure of water:

$$\log_{10}(p_{\text{sat,HNO}_3}) = a_{\text{NAT}}(T)\, \log_{10}(p_{\text{H}_2\text{O}}) + b_{\text{NAT}}(T) \tag{3.13}$$

with

$$a_{\text{NAT}}(T) = -2.7836 - 0.00088\, T \tag{3.14}$$

$$b_{\text{NAT}}(T) = 38.9855 - \frac{11397.0}{T} + 0.009179\, T \tag{3.15}$$

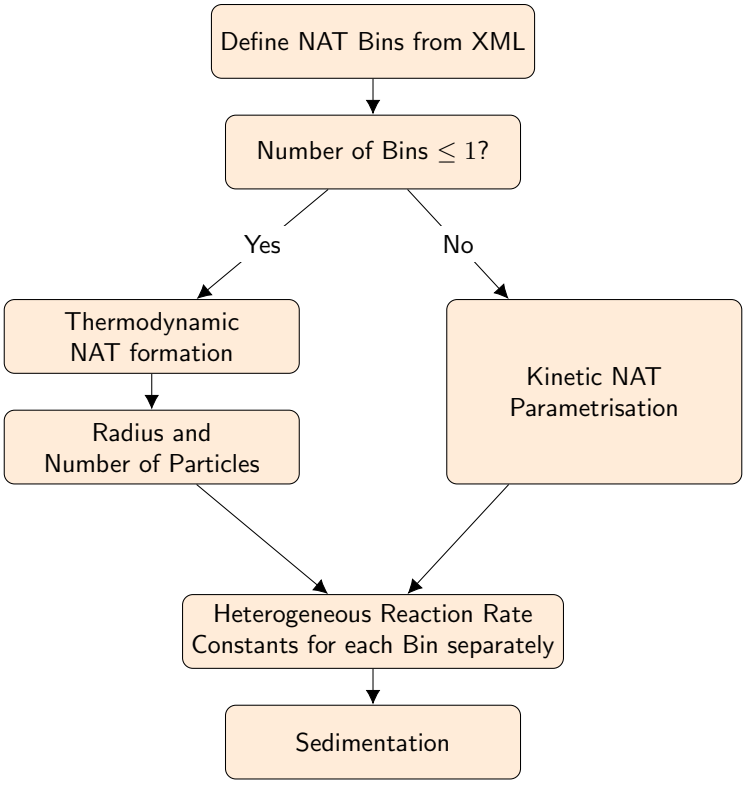

Figure 3.8: Work flow of the NAT scheme. The number of size bins in the corresponding XML file decides about the NAT parametrisation that is used. If the number of size bins is one or lower the thermodynamic NAT parametrisation is applied where radius and particle number concentrations have to be calculated separately. If the number of size bins is larger, the kinetic approach is applied. Then, the properties for the heterogeneous chemistry and sedimentation are calculated for both parametrisations.

In these equations, the water vapour pressure p_{H_2O} has to be given in torr, the temperature T in K, to get the saturation vapour pressure of HNO_3 over NAT p_{sat,HNO_3} in torr. The proposed parametrisation is valid within the temperature range 180 K < T < 200 K with a precision of 1 % based on measurements under stratospheric conditions (Hanson and Mauersberger, 1988). For temperatures lower than 180 K, the saturation vapour pressure over NAT in ICON-ART is calculated with T = 180 K.

Analogously to Eq. (3.7) for ice, the volume mixing ratio of NAT phase HNO_3 in the air is then calculated with the difference of vapour pressure and saturation vapour pressure:

$$X_{HNO_3(NAT)} = \frac{p_{HNO_3} - p_{sat,\,HNO_3}}{p}, \quad p_{HNO_3} > p_{sat,\,HNO_3} \tag{3.16}$$

Similar to the diagnostic ice parametrisation of Eq. (3.7), the thermodynamic NAT parametrisation assumes heterogeneous nucleation because the total supersaturated fraction of HNO_3 is treated as

NAT. This fraction is removed from gaseous nitric acid, directly sedimented as described below and finally sublimated within the same time step.

Radius and particle number concentration of NAT particles have to be derived from the volume mixing ratio of HNO_3 in NAT ($X_{HNO_3(NAT)}$). For this, a minimum radius of $r_{min} = 0.1\,\mu m$ is assumed as well as a maximum particle number concentration of $N_{NAT,max} = 2.3 \times 10^{-4}\,cm^{-3}$ based on airborne observations in the Arctic winter 1999/2000 by Fahey et al. (2001).

In this parametrisation, it is assumed that NAT particles have a radius of r_{min} if the particle number concentration of NAT is smaller than the maximum. The calculation of radius and particle number concentration consists of two steps. First, the particle number concentration assuming spherical particles of radius r_{min} is calculated:

$$N_{NAT,cur} = \frac{3\, X_{HNO_3(NAT)}\, M_{NAT}\, \rho}{4\,\pi\, r_{min}^3\, \rho_{NAT}\, M_{air}} \tag{3.17}$$

With this, the particle number concentration of the NAT particles can be calculated as follows:

$$N_{NAT} = \min(N_{NAT,cur}, N_{NAT,max}) \tag{3.18}$$

The radius of NAT particles is r_{min} if the NAT number concentration is lower than the maximum value. If the particle number concentration is larger than $N_{NAT,max}$ the radius is calculated from the ratio between particle number concentration and maximum particle number concentration:

$$r_{NAT} = \begin{cases} r_{min}, & N_{NAT,cur} < N_{NAT,max} \\ \left(\frac{N_{NAT,cur}}{N_{NAT,max}}\right)^{\frac{1}{3}} r_{min}, & N_{NAT,cur} \geq N_{NAT,max} \end{cases} \tag{3.19}$$

The same assumption for particle number concentration and radius is applied in EMAC (Buchholz, 2005; Kirner et al., 2011).

Kinetic NAT Parametrisation

In the thermodynamic parametrisation described above, assumptions about the size distribution of NAT particles have to be made to calculate their sedimentation velocity. Due to that issue, Carslaw et al. (2002) developed a parametrisation where NAT particles are separated in different size bins. The transfer of this parametrisation to Eulerian models was firstly published by van den Broek et al. (2004). This parametrisation is applied in various Lagrangian and Eulerian models (Davies et al., 2002, 2005; Grooß et al., 2005; Mann et al., 2005; Wohltmann et al., 2010; Kirner et al., 2011). Apart from some constraints described below, the particles of a specific size bin can grow and sediment independently of the other bins so that sedimentation of the NAT particles is calculated in a more realistic manner than in the thermodynamic parametrisation. This independent growth of the particles shows that this approach is a non-equilibrium approach: only a part of the total supersaturated amount of nitric acid resublimates on the particles in contrast to the thermodynamic

parametrisation, Eq. (3.16). The sublimation and resublimation is rather determined by diffusive fluxes on the surface of the particles.

The implementation in ICON-ART benefits from the flexible tracer concept where tracers and corresponding meta information can easily be added via XML files (Schröter et al., 2018). Each bin is represented by a separate tracer called "TRNAT_bin[01..99]" where the numbers in squared brackets stand for a two digit number between 01 and 99. Two additional meta information have to be given for each tracer: the minimum radius of the bin $r_{\mathrm{min},b}$ and the maximum particle number concentration $N_{\mathrm{NAT,max},b}$ that is allowed in the bin b (details see below). The minimum radius of the next greater size bin is handled as upper boundary of the bin and the mean radius of the bin is calculated as arithmetic average of the boundaries.

In the following, the kinetic NAT parametrisation as integrated in ICON-ART is described. The process of NAT formation begins like in the thermodynamic case with the difference of vapour pressure and saturation vapour pressure of HNO_3 over NAT (Eq. 3.13). However, Peter et al. (1991) demonstrated that for the initial nucleation of NAT particles a sufficient supersaturation must exist, due to different nucleation conditions in the experiments of Hanson and Mauersberger (1988) and in the atmosphere. NAT particles of a certain size nucleate heterogeneously so that the saturation vapour pressure by Hanson and Mauersberger (1988) can be used directly to form NAT particles in the model. According to the measurements shown by Peter et al. (1991), smaller NAT particles grow by homogeneous nucleation. This is why Peter et al. (1991) and Grooß et al. (2002) introduced a temperature threshold of 3 K for the initial formation of NAT which is also applied in terms of supersaturation by Considine et al. (2000). In the configuration of ICON-ART, this temperature threshold is also applied. NAT is formed initially in the first size bin if

$$p_{\mathrm{HNO_3}} > p_{\mathrm{sat,HNO_3}}(T + 3\,\mathrm{K}) \tag{3.20}$$

The difference between $p_{\mathrm{HNO_3}}$ and $p_{\mathrm{sat,HNO_3}}(T)$ determines the size change of the particles in size bin b, see also Eq. (2.23). It is expressed as a growth factor G_b (Carslaw et al., 2002):

$$G_b = \frac{d^*_{\mathrm{HNO_3},b}\, M_{\mathrm{NAT}}}{\rho_{\mathrm{NAT}}\, R^*\, T}\left(p_{\mathrm{HNO_3}} - p_{\mathrm{sat,HNO_3}}(T)\right) \tag{3.21}$$

The diffusive particle growth is inversely proportional to the particle radius r_b:

$$\frac{\mathrm{d}r_b}{\mathrm{d}t} = \frac{G_b}{r_b} \tag{3.22}$$

In these equations, M_{NAT} is the NAT molar mass of 117 g mol^{-1}, R^* is the universal constant of an ideal gas (~8.31 J mol^{-1} K^{-1}) and T is the temperature in K. The NAT crystal mass density ρ_{NAT} has a value of 1.626×10^6 g m^{-3} (Drdla et al., 1993; van den Broek et al., 2004). $d^*_{\mathrm{HNO_3}}$ is the diffusion coefficient of HNO_3 molecules in air accounting for non-continuum effects (Carslaw et al., 2002):

$$d^*_{\mathrm{HNO_3},b} = \frac{d_{\mathrm{HNO_3}}}{1 + 4\, d_{\mathrm{HNO_3}}/(\bar{v}_{\mathrm{HNO_3}}\, r_b)} \tag{3.23}$$

with $\overline{v}_{HNO_3}$ as expected value of Maxwell-Boltzmann-distributed thermal velocities of HNO_3 molecules, see Eq. (2.27), and d_{HNO_3} as diffusion coefficient of HNO_3 parametrised according to Hall and Pruppacher (1976) for H_2O and transferred to HNO_3 (see Appendix B):

$$d_{HNO_3} = 0.466 \times 0.22 \times 10^{-4} \left(\frac{T}{273.15} \right)^{1.94} \frac{101325}{p} \tag{3.24}$$

In this equation, T and p have to be given in K and Pa, respectively, to get the diffusion coefficient in $m^2\,s^{-1}$.

By assuming that G_b does not vary within one advective model time step Δt, Eq. (3.22) can be integrated analytically:

$$r_b^2(t + \Delta t) = r_b^2(t) + 2\,G_b\,\Delta t \tag{3.25}$$

This assumption will be further analysed in Sect. 5.3.5.

In the implementation in ICON-ART, the particle dynamics follow the "FixedRad" approach by van den Broek et al. (2004): any change in the radius due to Eq. (3.25) is immediately converted to an increased or decreased NAT number concentration in the respective size bin. The maximum particle number concentration has to be specified for each bin as described above in order to get realistic size distributions. To keep the size distribution of NAT particles as close to the observations as possible the sum of the bin maximum number concentrations has to be the maximum observed particle number concentration (Fahey et al., 2001, see also above in the thermodynamic NAT parametrisation):

$$\sum_{b=1}^{n_{bin}} N_{NAT,max,b} \stackrel{!}{=} 2.3 \times 10^{-4}\,cm^{-3} \tag{3.26}$$

If the maximum particle number concentration of the bin $N_{NAT,max,b}$ is exceeded after the growth of the particle according to Eq. (3.25) the excess mass is transferred to the next greater size bin.

As mentioned above, the formula for saturation vapour pressure over NAT of Eq. (3.13) is valid for the temperature range 180 K < T < 200 K, only. Therefore, the formula for G_b by Carslaw et al. (2002) is adapted in the case of ICON-ART:

$$G_b = \begin{cases} -\dfrac{r_b^2(t)}{2\,\Delta t}, & T \geq 200\,K \\ \dfrac{d^*_{HNO_3,b}(T)\,M_{NAT}}{\rho_{NAT}\,R^*\,T}\,(p_{HNO_3} - p_{sat,HNO_3}(T)), & 180\,K < T < 200\,K \\ \dfrac{d^*_{HNO_3,b}(T)\,M_{NAT}}{\rho_{NAT}\,R^*\,T}\,(p_{HNO_3} - p_{sat,HNO_3}(180\,K)), & T \leq 180\,K \end{cases} \tag{3.27}$$

For $T \geq 200$ K it is assumed that NAT particles cannot exist anymore and the new radius is set to zero by setting $G = -r_b^2/(2\,\Delta t)$ for Eq. (3.25). For $T \leq 180$ K, which is rather rare in the lower stratosphere, p_{sat,HNO_3} is calculated with $T = 180$ K. The diffusion coefficient is calculated with the ambient temperature.

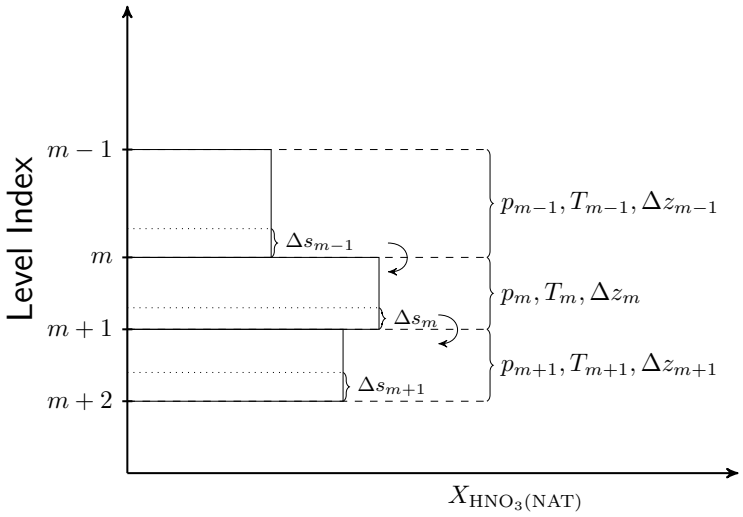

Figure 3.9: Sedimentation with simple upwind scheme. The fraction of moles of NAT is sedimented which corresponds to the distance Δ*s* of a NAT particle within one time step. It has to be considered that the model levels underlie different atmospheric conditions. This figure is inspired by Buchholz (2005).

Sedimentation of NAT Particles

Both thermodynamic and kinetic parametrisations compute the sedimentation velocity of NAT particles similarly. For sedimentation, the thermodynamic parametrisation is treated as a special case of the kinetic parametrisation with number of size bins $n_{\mathrm{bin}} = 1$. The radius of the NAT particles is calculated by Eq. (3.19) in case of the thermodynamic NAT parametrisation.

The sedimentation velocity of the NAT particles is calculated via Stokes' law, see Eq. (2.24), expressed for the radius of the NAT particle in the size bin b and at the vertical level m:

$$v_{b,m} = \frac{2\,\rho_{\mathrm{NAT}}\,r_b^2\,g\,C_{\mathrm{C},b}}{9\,\eta_m} \tag{3.28}$$

The Cunningham factor in this equation is parametrised according to Pruppacher and Klett (1997) and Carslaw et al. (2002):

$$C_{\mathrm{C},b} = 1 + \frac{\lambda_{\mathrm{mfp}}}{r_b}\left[1.257 + 0.4\,\exp\left(\frac{-1.1\,r_b}{\lambda_{\mathrm{mfp}}}\right)\right] \tag{3.29}$$

The mean free path λ_{mfp} in this equation is calculated by Eq. (2.28) with the collision diameter D_{c} of HNO_3 of 4.2 Å (Liu et al., 2007). The assumption of spherical particles instead of a shape dependent sedimentation velocity in Eq. (3.28) induces an uncertainty of about 10 % (Carslaw et al., 2002).

The sedimentation of NAT particles is then calculated by a simple upwind scheme. In the following, the index $m + 1$ stands for the index of the lower model layer where the sedimented particles

come into. The index m describes the model layer above where NAT particles are removed. In the following, the bin index b is omitted. As indicated by Fig. 3.9, the sedimenting number of moles of HNO_3 molecules in NAT in one model layer ($n_{\text{falling},m}$) can be described by the ratio of model layer height Δz_m and the vertical distance $\Delta s_{\text{NAT},m}$ of the sedimenting particle:

$$n_{\text{falling},m} = -\Delta n_{\text{NAT},m} = \Delta n_{\text{NAT},m+1} = X_{\text{HNO}_3(\text{NAT}),m} \frac{\Delta s_{\text{NAT},m}}{\Delta z_m} n_{\text{air},m} \tag{3.30}$$

where n are the number moles of HNO_3 in NAT or in air, respectively, $X_{\text{HNO}_3(\text{NAT}),m}$ is the volume mixing ratio of HNO_3 in NAT and the vertical distance of the sedimenting particles $\Delta s_{\text{NAT},m}$ is calculated according to

$$\Delta s_{\text{NAT},m} = v_m \, \Delta t \tag{3.31}$$

Here, v_m is calculated by Eq. (3.28). By replacing $n_{\text{air},m}$ using the equation for an ideal gas, one gets:

$$n_{\text{falling},m} = X_{\text{HNO}_3(\text{NAT}),m} \frac{\Delta s_{\text{NAT},m}}{\Delta z_m} \frac{p_m \Delta A \Delta z_m}{R^* T_m} = X_{\text{HNO}_3(\text{NAT}),m} \Delta s_{\text{NAT},m} \frac{p_m \Delta A}{R^* T_m} \tag{3.32}$$

with the cell base area ΔA, temperature T_m, pressure p_m and universal gas constant R^*. As indicated in Eq. (3.30), the falling number of molecules must be equal for the upper and lower model level. Therefore, the NAT volume mixing ratio that is removed from the upper level is derived by dividing Eq. (3.30) by $n_{\text{air},m}$:

$$\Delta X_{\text{HNO}_3(\text{NAT}),m} = -X_{\text{HNO}_3(\text{NAT}),m} \frac{\Delta s_{\text{NAT},m}}{\Delta z_m} \tag{3.33}$$

The volume mixing ratio that is added to the level underneath is derived by dividing Eq. (3.32) by $n_{\text{air},m+1}$ which yields:

$$\Delta X_{\text{HNO}_3(\text{NAT}),m+1} = \frac{\Delta n_{\text{NAT},m+1}}{n_{\text{air},m+1}} = X_{\text{HNO}_3(\text{NAT}),m} \frac{p_m}{p_{m+1}} \frac{T_m}{T_{m+1}} \frac{\Delta s_{\text{NAT},m}}{\Delta z_{m+1}} \tag{3.34}$$

The process of sedimentation of NAT particles is mass conserving for grid boxes with differing temperature and pressure. The conservation of the sedimented mass is shown in Fig. 3.10. A detailed description of the simulation behind this figure can be found in Sect. 4.1. The relative difference of all columns and all size bins does not exceed 10^{-15}. This is close to computation precision.

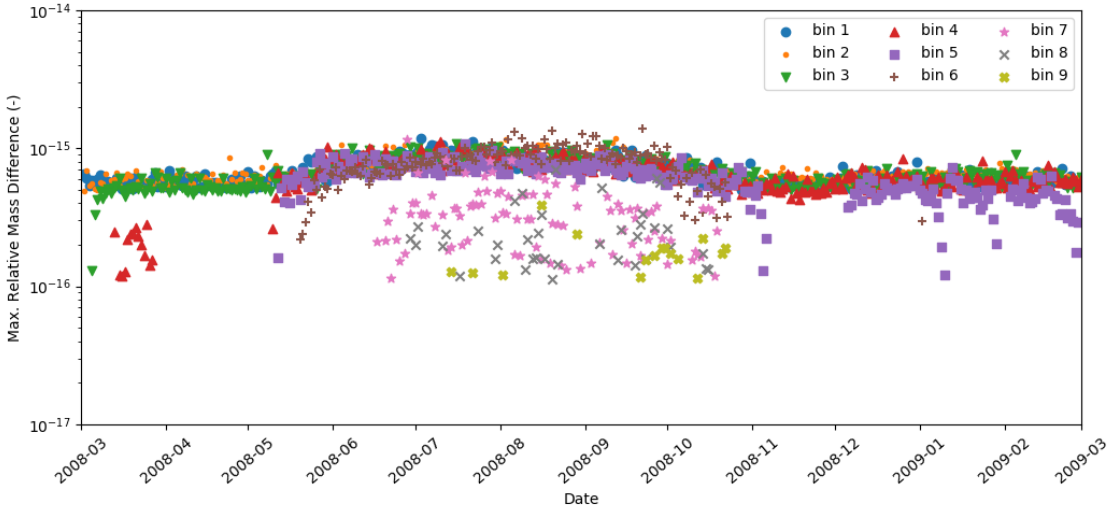

Figure 3.10: Global maximum relative difference between sedimenting NAT mass before and after sedimentation integrated over the column. It is shown for each size bin of the kinetic NAT parametrisation. The relative difference is calculated according to 2(after − before)/(after + before) in each grid box. The global maximum absolute value is shown. A description of the used KinPar simulation can be found in Sect. 4.1.

3.5.3 The Formation of Supercooled Ternary Solution Droplets

A module for the calculation of supercooled ternary solution droplets (STS) and the corresponding heterogeneous reaction rate constants is described in Carslaw et al. (1995b). This is the standard module for calculation of STS, used e.g. in KASIMA (Kouker et al., 1999; Ruhnke et al., 1999), CLaMS (McKenna et al., 2002), GMI (Considine et al., 2000), EMAC (Kirner et al., 2011) and COSMO-ART (Eckstein, 2013). The module can be used within the temperature range $\max(T_{\text{ice}} - 3\,\text{K}, 185\,\text{K}) < T < 240\,\text{K}$. If the temperature decreases below the minimum, it is set internally to this value (see also Buchholz, 2005). Furthermore, the suggestions by Eckstein (2013) are integrated which decrease the validity range of the module to avoid NaN values produced by the module.

Zhu et al. (2015) implemented a more complex STS model into WACCM based on a size bin approach similar to the kinetic NAT parametrisation described above. It accounts for non-equilibrium processes in the growth of STS particles. This, though, would lead to highly increased number of tracers in the model. In the model by Zhu et al. (2015), STS particles are represented by 40 tracers. They conclude that non-equilibrium processes are important for STS particles with a particle surface concentration lower than 4 $\mu m^2\ cm^{-3}$ and therefore for the background sulfate aerosol. Since the heterogeneous chemistry is most efficient on large STS particles (Drdla et al., 1993), which are close to equilibrium (Zhu et al., 2015), the module by Carslaw et al. (1995b) has been integrated in the scope of this thesis.

In contrast to NAT and ice particles, STS particles are supercooled liquid droplets and consist of three main components: water, nitric acid and sulphuric acid. To describe the STS formation, the complex three-component system in liquid and gaseous phase has to be accounted for which includes iterative processes (Carslaw et al., 1995a). Carslaw et al. (1995b) simplified the physics to an analytic approach with relatively small differences with respect to the iterative approach usually up

to 4 %. At temperatures lower than about 192 K the binary H_2O-H_2SO_4 background sulfate aerosol droplets begin to absorb HNO_3 and form supercooled ternary H_2SO_4-HNO_3-H_2O solution (STS) droplets (Carslaw et al., 1994).

In the module by Carslaw et al. (1995b), the ternary solution is derived from a polynomial fit of assumed independent binary H_2SO_4-water and HNO_3-water solutions. Each binary solution is calculated for the case of thermodynamic equilibrium dependent on temperature and component concentrations. Supersaturation over the liquid solution yields growing of the particle.

While H_2SO_4 and HNO_3 both mainly contribute to the size of the droplets, the module also computes the partitioning of minor substances such as HCl, HOCl and HOBr based on literature descriptions (Huthwelker et al., 1995; Luo et al., 1994; Hanson and Ravishankara, 1995). As a result, the module computes the reaction probabilities of the heterogeneous reactions on STS according to Hanson and Ravishankara (1994) and Hanson et al. (1996) and others.

The second result of the module are liquid surface concentration and mean radius of the particles. In the original code by Carslaw et al. (1995b) the particle number concentration is set to the fixed value of 10 cm^{-3}. The radius is calculated for the case of lognormal distributed STS particles.

In order to improve the fixed aerosol number concentration, Grainger et al. (1995) suggest the following relationships between liquid surface concentration S_{STS} (in $\mu m^2\,cm^{-3}$), mean particle radius $r_{STS,mean}$ (in μm) and liquid volume concentration V_{STS} (in $\mu m^3\,cm^{-3}$). They assume a bimodal lognormal size distribution for sulfate aerosols:

$$S_{STS} = a_{SV}\,(V_{STS})^{b_{SV}} \tag{3.35}$$

$$r_{STS,mean} = \frac{3\,V_{STS}}{S_{STS}} \tag{3.36}$$

The power law parameters a_{SV} and b_{SV} to connect V_{STS} with S_{STS} by Grainger et al. (1995) are only measured for sulphate aerosols of the Junge layer, and not for STS particles. It is expected that the STS particles get larger than the sulphate aerosols for low temperatures where the aerosols can take up HNO_3 (e.g., Dye et al., 1992; Peter, 1997).

Hervig and Deshler (1998) compared measurements of different satellite instruments and derived relationships between the absorption or extinction coefficient $\beta(\lambda)$ and S_{STS} and V_{STS} for PSC particles, respectively:

$$V_{STS} = a_V\,(\beta(\lambda))^{b_V} \tag{3.37}$$

$$S_{STS} = a_S\,(\beta(\lambda))^{b_S} \tag{3.38}$$

Here, β is the absorption or extinction coefficient measured at wavelength λ. A lognormal size distribution of the STS droplets is assumed based on balloon-borne measurements over the Antarctica. By eliminating β in Eq. (3.37) and Eq. (3.38), a relationship between V_{STS} and S_{STS} can be established which can be derived from the original parameters of Hervig and Deshler (1998):

$$S_{STS} = a^*\,(V_{STS})^{b^*}, \quad a^* = a_S \cdot (a_V)^{\frac{b_S}{b_V}}, \quad b^* = \frac{b_S}{b_V} \tag{3.39}$$

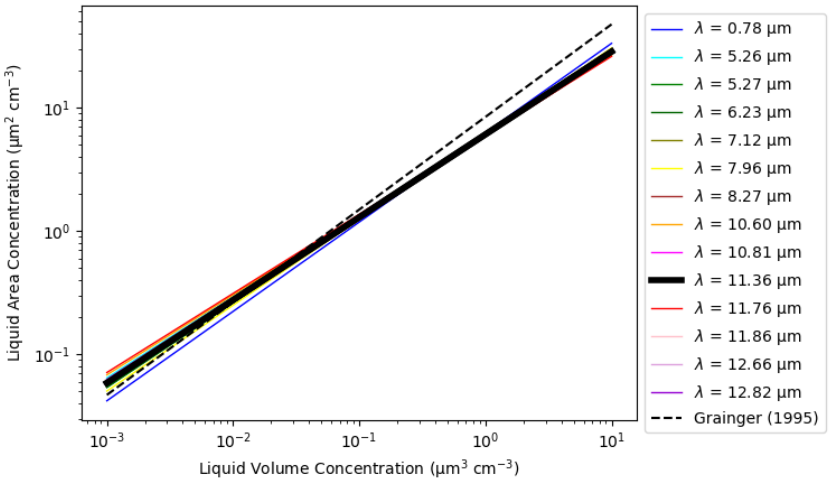

Figure 3.11: Comparison of the STS surface concentration of Grainger et al. (1995) (black dashed) and the 14 measurements by Hervig and Deshler (1998). The parameters for the measurements by Hervig and Deshler (1998) are derived from the original values by Eq. (3.39). The thick black line corresponds to the average of all measurements.

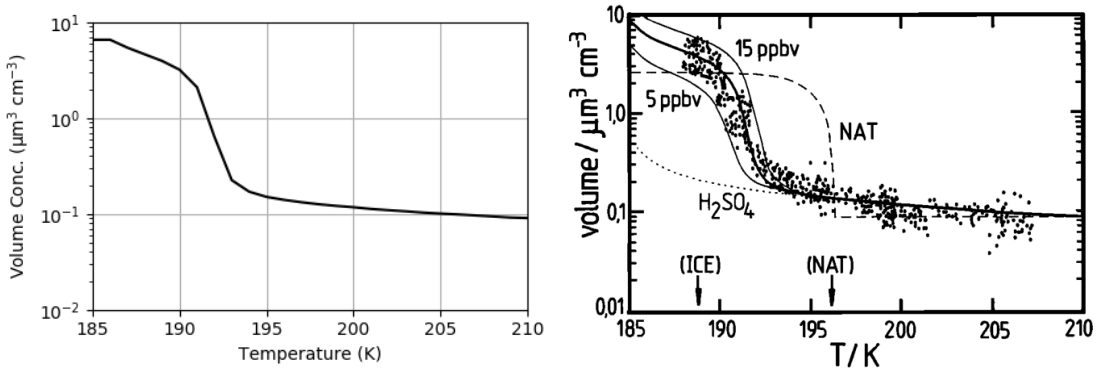

(a) ICON-ART (b) Carslaw et al. (1994)

Figure 3.12: STS volume concentrations of (a) ICON-ART and (b) original implementation by Carslaw et al. (1994). Input parameters are the same as in Carslaw et al. (1994): p = 55 hPa, X_{H_2O} = 5 ppmv, X_{HNO_3} = 10 ppbv. The H_2SO_4 volume mixing ratio is not mentioned in Carslaw et al. (1994) and is set to 0.33 ppbv in this figure. Figure by Carslaw et al. (1994) published with permission of John Wiley & Sons.

In this equation, the liquid volume concentration has to be given in $\mu m^3\ cm^{-3}$ to get the particle surface concentration in $\mu m^2\ cm^{-3}$. The mean radius (approximated as the effective radius of the size distribution) is calculated according to Eq. (3.36).

Figure 3.11 shows the different parametrisations derived from all the wavelengths used by Hervig and Deshler (1998), as well as the parametrisation by Grainger et al. (1995). The measurements by Hervig and Deshler (1998) were measured by the cryogenic limb array etalon spectrometer (CLAES, Roche et al., 1993; Massie et al., 1996). As S_{STS} and V_{STS} are related by a power law in every case, all the parametrisations are represented by a straight line in the double logarithmic diagram. Especially for high particle volume concentrations above $0.1\ \mu m^3\ cm^{-3}$, the parametrisations by Hervig and Deshler (1998) result in a lower particle surface concentration which means larger particles (cf. Eq. (3.36)). This indicates that the parametrisation by Hervig and Deshler (1998) is really derived for STS particles and not for the background aerosol.

The thick black line in Fig. 3.11 corresponds to the measurement at a wavelength of $\lambda = 11.36\ \mu m$. This measurement coincides with the average of all measurements with a maximum deviation of 1 ‰. Therefore, the parameters of this measurement are applied to Eq. (3.39). This results in the following formula for the calculation of S_{STS} in ICON-ART:

$$S_{STS} = 6.068\,(V_{STS})^{0.671} \tag{3.40}$$

The STS volume concentration for Eq. (3.40) is derived from the particle mass concentration in the liquid phase

$$W_{STS,tot} = \frac{p}{R^* T}\left(X_{HNO_3(STS)} M_{HNO_3} + X_{H_2SO_4(STS)} M_{H_2SO_4} + X_{H_2O(STS)} M_{H_2O}\right) \tag{3.41}$$

and the density of the liquid solution ρ_{STS}, calculated according to Luo et al. (1996):

$$V_{STS} = \frac{W_{STS,tot}}{\rho_{STS}} \tag{3.42}$$

No sedimentation is considered for STS since the droplets generally have too low diameters to significantly contribute to denitrification as described in Sect. 2.5.

The comparison of this STS module with the original output by Carslaw et al. (1994) is shown in Fig. 3.12. The same input parameters as in the original publication for H_2O, HNO_3, H_2SO_4, temperature and pressure are used, which can be found in the figure caption. As can be seen, the module accounts for the sulfate background aerosol at temperature values higher than about 192 K. For decreasing temperatures, gaseous HNO_3 is absorbed by the particles so that their particle volume concentration increases. Both implementations in Fig. 3.12 agree well. Differences occur only for temperatures lower than 186 K where the STS volume concentration in ICON-ART gets lower than that by Carslaw et al. (1994). This is a result of the different size distributions used in the modules. Since the values by Dye et al. (1992), included as dots in Fig. 3.12(b), have been measured for temperatures down to approx. 188 K, the differences between both modules are negligible.

3.5.4 Heterogeneous Chemistry on the Surface of Polar Stratospheric Clouds

The primary goals of any PSC scheme is the representation of denitrification and dehydration as well as chlorine and bromine activation on the surface of PSCs. They are implemented according to Eq. (2.26) for all the known heterogeneous reactions, see Reactions (R2.29) to (R2.39). The corresponding reaction rate constants include the uptake coefficient as one parameter. The used values are summarised in Table 3.3.

For ice particles, radius and particle number concentration are determined by Eq. (3.8) and Eq. (3.10) or by Eq. (3.12), dependent on the chosen physics parametrisation, respectively. Then, Equation (2.26) is used to calculate the heterogeneous reaction rate constant.

For NAT particles, the heterogeneous reaction rate constant is calculated by Eq. (2.26) for each size bin and summed up to get the total heterogeneous reaction rate constant on the NAT particle in one grid box. In case of the thermodynamic NAT parametrisation, particle number concentration and radius are calculated by Eq. (3.18) and Eq. (3.19), respectively.

For STS particles, the heterogeneous reaction rate constant, simplified for small particles by Eq. (2.29) is used, including the STS surface concentration.

Finally, the total heterogeneous reaction rate constant for a heterogeneous reaction r is the sum of ice, NAT and STS:

$$k_{\text{het},r,\text{total}} = k_{\text{het},r,\text{ice}} + k_{\text{het},r,\text{NAT}} + k_{\text{het},r,\text{STS}} \tag{3.43}$$

Table 3.3: Uptake coefficients (reaction probabilities) for the heterogeneous reactions on PSCs in this thesis. Where not stated differently, the values come from Sander et al. (2011b).

Reaction	γ_{STS}	γ_{NAT}	γ_{ice}
$ClONO_{2(g)} + H_2O_{(a)}$	*(a)*	0.004	0.3
$ClONO_{2(g)} + HBr_{(a)}$	*(a)*	0.3	0.3
$ClONO_{2(g)} + HCl_{(a)}$	*(a)*	0.2	0.3
$BrONO_{2(g)} + H_2O_{(a)}$	*(a)*	0.001*(b)*	0.26
$BrONO_{2(g)} + HCl_{(a)}$	*(a)*	0.3*(b)*	0.26
$HOCl_{(g)} + HCl_{(a)}$	*(a)*	0.1	0.2
$HOCl_{(g)} + HBr_{(a)}$	*(a)*	0.3*(b)*	0.3*(c)*
$HOBr_{(g)} + HCl_{(a)}$	*(a)*	0.1*(b)*	0.3
$HOBr_{(g)} + HBr_{(a)}$	*(a)*	0.1*(b)*	0.1
$N_2O_{5(g)} + H_2O_{(a)}$	*(a)*	0.0004	0.027
$N_2O_{5(g)} + HCl_{(a)}$	*(a)*	0.003	0.03

(a) Parametrised according to Carslaw et al. (1995b)
(b) In analogy to similar reactions, coming from Carslaw et al. (1995b)
(c) In analogy to HOBr + HCl

4

Simulation Setup and Reference Datasets

ICON-ART as a next-generation atmospheric chemistry model is able to cover a variety of space and time scales which is demonstrated in this chapter. The example year is 2008 where the mountain wave activity around the Antarctica was higher than in other years (Kohma and Sato, 2011; Hoffmann et al., 2017). Moreover, a mountain wave event around the Antarctic Peninsula lasting for more than 10 consecutive days occurred in July 2008 (Noel and Pitts, 2012). In addition, PSC observing satellites such as Envisat, CALIPSO and Aura operated in this year so that an evaluation with all of them is possible in the year 2008.

Four types of simulations are performed for the investigation of PSCs in ICON-ART and for the comparison with reference data:

1. A multi-year simulation with repeated boundary conditions of 2008 is performed in order to evaluate the long-term dynamics of the model (Sect. 4.1)
2. A simulation in the configuration like the Atmospheric Model Intercomparison Project (AMIP) demonstrates that PSCs can be simulated with the climate configuration of ICON-ART (Sect. 4.2)
3. Ensemble simulations of 2008 with perturbed initial states provide uncertainty ranges for the simulated trace gases and their comparison to measurements (Sect. 4.3)
4. A simulation with locally refined grids around the Antarctic Peninsula is used for the detailed investigation of mountain-wave induced PSCs in this region (Sect. 4.4)

Table 4.1 summarises the setup of the different simulations, including some additional sensitivity simulations which are also described in the following sections. This demonstrates that ICON-ART can be used for long-term simulations as well as for detailed comparisons of specific events.

The reference datasets that are used for evaluation of the simulations are described in the last sections of this chapter. This includes the recent reanalysis datasets ERA5 by ECMWF (Sect. 4.5) and MERRA by NASA (Sect. 4.6). Moreover, the PSC scheme in ICON-ART is evaluated with the satellite instruments MIPAS, CALIOP, MLS and OMI, which are described in Sect. 4.7 accompanied by the illustration of the interpolation of the ICON-ART simulations to the satellite locations.

Table 4.1: Simulation summary. Global horizontal resolution is R2B04 (in the nests R2B05 and R2B06 as shown in Table 3.1). If not stated differently, the simulations start in March and end in April of the next year. The AMIP-like simulation includes 47 vertical levels whereas all other simulation have 90 vertical levels. The used NAT parametrisation is abbreviated: th stands for thermodynamic NAT parametrisation and ki denotes the kinetic NAT parametrisation.

Simulation	Physics	Chemistry	Δt (min)	NAT	Time Range
Time Slice	NWP	Lifetime/LINOZ	6	th	2008 – 2037[a]
KinPar	NWP	Lifetime/LINOZ	6	ki	2008[b]
Size Bins	NWP	Lifetime/LINOZ	6	ki	15 June 2008 – 18 June 2008[c]
AMIP	Climate	Lifetime/LINOZ	10	th	2008
Ensemble	NWP	Stratospheric	6	ki	2008[d]
without PSCs	NWP	Stratospheric	6	ki	2008
Nest	NWP	Stratospheric	6	ki	01 May 2008 – 29 July 2008[e]

[a] Repeated boundary conditions of 2008
[b] Same as Time Slice but with kinetic NAT parametrisation
[c] Three simulations with different number of size bins in kinetic NAT parametrisation
[d] 30 simulations with perturbed initial conditions
[e] Reinitialised meteorology every second day until 20 July, then including the Antarctica and Antarctic Peninsula nests

4.1 Simulations with Lifetime-based Chemistry

Time Slice Simulation

In Sect. 3.5.1, the different possibilities were discussed how to calculate ice PSCs in combination with the ICON microphysics which are calculated operationally up to an altitude of $h_{\text{top}} = 22.5\,\text{km}$. This is in the altitude range where ice PSCs are expected to exist so that a sensitivity study with two values of h_{top} is performed which are summarised in the term of "time slice simulation": (1) with $h_{\text{top}} = 22\,500\,\text{m}$ and (2) with $h_{\text{top}} = 30\,000\,\text{m}$ (see Sect. 3.5.1). Boundary conditions such as sea surface temperature (SST), sea ice cover (SIC) and trace gas emissions are repeated for the year 2008. Sea surface temperature and sea ice cover are monthly prescribed, interpolated to the actual simulation day and originate from AMIP (Taylor et al., 2000). In total, the year 2008 is repeated 30 times in free-running simulations. The dynamical variables are initialised by the ECMWF Reanalysis ERA-Interim on 01 March 2008 (Dee et al., 2011).

Horizontally, a resolution of R2B04 is used (approx. 160 km, see Table 3.1) in combination with the same 90 vertical levels up to an altitude of 75 km as in the operational setup at DWD. The advective model time step is 6 min. Apart from these parameters, the operational setup as used at DWD is used.

For chemistry, the lifetime-based chemistry is applied accompanied by the PSC scheme with thermodynamic NAT parametrisation. Tracers are CO, CO_2, CH_4 (which feeds back to water vapour), O_3, HNO_3 and H_2SO_4. HNO_3 is used as a passive tracer, each year reinitialised with its three-dimensional field of 01 March 2008 before the southern polar vortex develops. H_2SO_4 is prescribed as described in Sect. 3.4. Apart from H_2SO_4, the chemical tracers are initialised at the beginning of the simulation from an EMAC simulation which included tropospheric as well as stratospheric chemistry similar to Jöckel et al. (2010). For ozone, the linearised ozone scheme (LINOZ, Hsu

and Prather, 2009) including a term for depletion of ozone due to heterogeneous chemistry is used (see Schröter et al., 2018). Ozone for radiation feedback is used from the Global and regional Earth-system (Atmosphere) Monitoring using Satellite and in-situ data (GEMS, Hollingsworth et al., 2008). In addition to this, a passive O_3 tracer is included in the simulation which is a proxy for ozone depletion in combination with the active tracer, see Sect. 5.6. The passive O_3 tracer is reinitialised every year with the value of ozone on 01 May and 01 December.

KinPar Simulation

A simulation in the same setup as the time slice experiment with $h_{\text{top}} = 30\,\text{km}$ is conducted for the year 2008 starting on 01 March but using the kinetic NAT parametrisation instead of the thermodynamic parametrisation. With this, the differences between thermodynamic and kinetic NAT parametrisation can be investigated.

The used NAT size distribution is based on Fahey et al. (2001) and van den Broek et al. (2004), summarised in Table 4.2 and visualised in Fig. 4.1. It consists of nine size bins up to minimum radii of 20 µm and equally distributed maximum number densities. The width of the bins increases with larger radius.

Table 4.2: Size bins for the kinetic NAT parametrisation. Based on Fahey et al. (2001) and van den Broek et al. (2004). The values of the maximum particle number density are rounded to two digits. A visualisation of the size distribution can be found in Fig. 4.1.

Bin	1	2	3	4	5	6	7	8	9
$r_{\text{min},b}$ (µm)	0.0	0.2	1.0	2.0	6.0	9.0	12.0	16.0	20.0
$[\text{NAT}]_{\text{max},b}$ (10^{-5} cm^{-3})	3.29	3.29	3.29	3.29	3.29	3.29	1.64	1.64	1.64

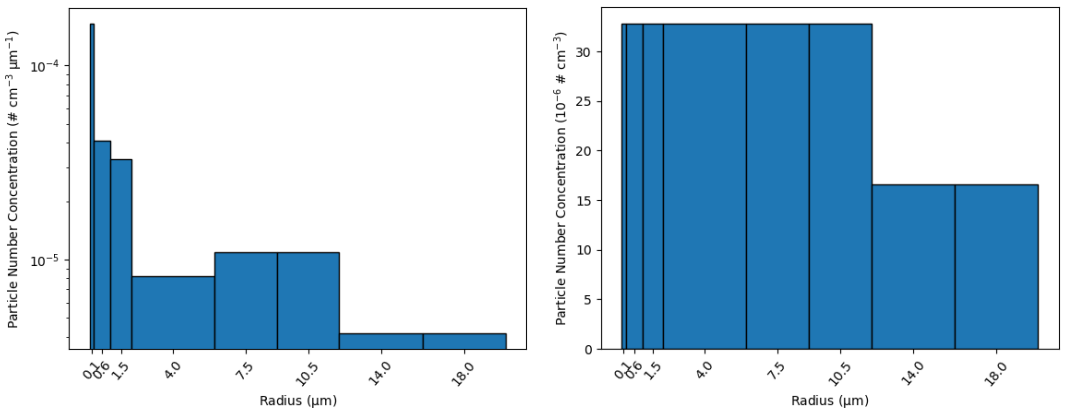

(a) normalised size distribution

(b) non-normalised size distribution

Figure 4.1: NAT size distribution (a) normalised with the bin width and (b) non-normalised. The size distribution of Table 4.2 is visualised.

Size Bins Simulation

The kinetic NAT parametrisation is a non-equilibrium approach where particles in each size bin grow independently. Thus, the growth of the particles could be different if the same experiment is executed with different number of size bins. This is investigated with the two additional sensitivity simulations with larger number of size bins. A discussion how the same experiment is performed with different size bins as well as the used size distributions can be found in Sect. 5.3.4.

The setup bases on that of the KinPar experiment. Three simulations are conducted with different size bins in the kinetic NAT parametrisation. The simulated days are 15 June 2008 to 18 June 2008 (i.e. 800 time steps of 360 s). During June, the temperature gets low enough so that PSCs can develop. To ensure supersaturation of gaseous HNO_3 with respect to NAT it set initially to a global value of 1 ppbv.

4.2 AMIP-like Simulation with Polar Stratospheric Clouds

In order to investigate the development of PSCs with climate configuration, a free-running simulation in a configuration like in AMIP (Gates et al., 1999) is conducted. The boundary conditions in this simulation have already been mentioned by Schröter (2018) and can be found in Table 4.3. It is a one-year simulation starting on 01 March 2008 with dynamics initialised by ERA-Interim and chemistry from the same EMAC simulation used for the time slice experiment. As indicated in Table 4.1, the chemistry configuration is the same as for the time slice experiment of Sect. 4.1. The PSC scheme is used with the thermodynamic NAT parametrisation.

Horizontal resolution is R2B04 and vertically 47 model levels are used up to an altitude of 80 km. The advective model time step is 10 min.

4.3 Global Simulations with Stratospheric Chemistry

Ensemble Simulation

Deterministic free-running simulations have a limited predictive skill up to a few weeks (Zhang et al., 2019). Thus, the evaluation of single free-running simulations with measurements is only possible within this time period.

Table 4.3: Boundary conditions for the AMIP-like simulation with ICON-ART. Taken from Schröter (2018).

Variable	Reference
SST/SIC	Taylor et al. (2000)
Spectral solar irradiation	Lean et al. (2005)
Greenhouse gases RCP 8.5	Riahi et al. (2007)
O_3 concentration	Cionni et al. (2011)
Tropospheric aerosol	Stenchikov et al. (1998, 2004, 2009)
Stratospheric aerosol	Stenchikov et al. (1998, 2004, 2009)

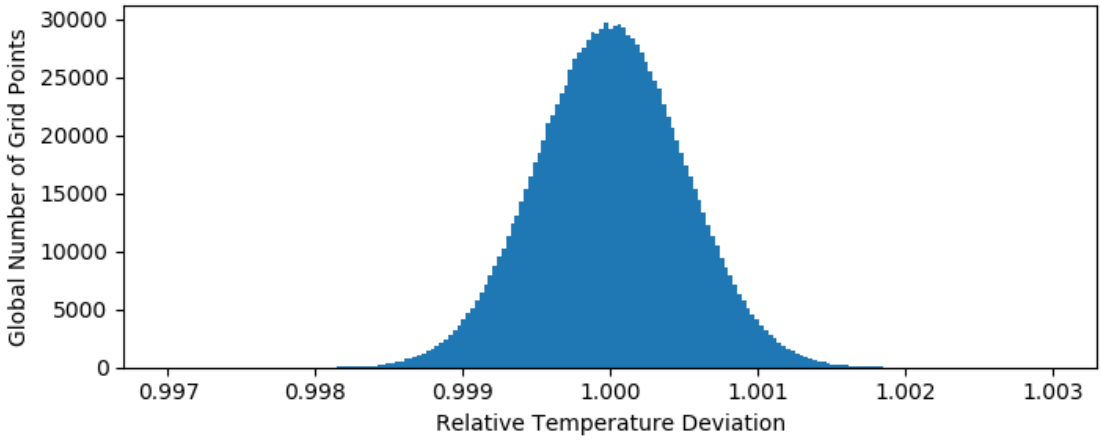

Figure 4.2: Gaussian perturbation of temperature in the ensemble simulation. The quotient of the temperature values in first ensemble initialisation and original ERA-Interim initialisation is shown. This perturbation is applied to temperature, three-dimensional wind, surface pressure, geopotential and the three water phases of the initial state for the simulations.

On the other hand, the simulations can be compared to measurements on a statistical basis by creating an ensemble of simulations with perturbed initial states. In the simulation conducted for the comparison to satellites in this thesis, the intial dynamical variables are perturbed by Gaussian noise, see Fig. 4.2. This is done by multiplying them by the factor generated by Gaussian random number. The width of the distribution is chosen in the way that the perturbation is up to 1 ‰ with the probability of 99.99 %. This value is similar to the perturbation Lorenz (1963) applied to his data to provoke chaotic behaviour. However, the global average of the perturbed values is not changed since the expected value of the distribution is 1, see Fig. 4.2.

The perturbation is applied to temperature, three-dimensional wind, surface pressure, geopotential and the three water phases of the ERA-Interim data on 01 March 2008. With this method, 30 ensemble members are generated which enables a statistical analysis of the simulations. Additionally, a simulation with the original ERA-Interim initialisation is conducted which is called "base run" hereafter. Horizontal resolution is R2B04 and each ensemble member covers the time range from 01 March 2008 to 30 April 2009. The 90 model levels, the model time step as well as the NWP configuration are the same as for the time slice experiment.

For chemistry, the stratospheric chemistry mechanism is used as shown in Appendix C and mentioned in Sect. 3.4. The PSC scheme is applied with the kinetic NAT parametrisation and the size bins described in Table 4.2. The simulated ozone is used for radiation feedback in this simulation. The chemical variables are initialised from the same EMAC simulation as in the simulations described above.

Simulation without PSCs

As another sensitivity study, the simulation setup of the ensemble simulation including stratospheric gas phase chemistry and photolytic reactions is taken, but with PSCs switched off. With this, the result can be investigated if the heterogeneous chemistry in the atmosphere is missing.

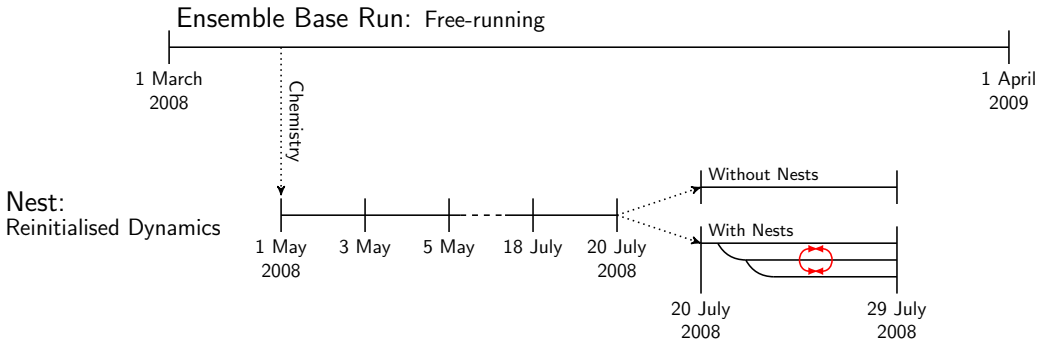

Figure 4.3: Configuration of the Nest simulation. The chemical species are used from the ensemble base run on 1 May 2008. The dynamics are reinitialised every second day until 20 July 2008. The chemical species are free-running, but transported with the updated dynamics. On 20 July 2008, one simulation without nests is started, free-running until 29 July 2008. Another simulation includes the nests, which is initialised from the parent domain 24 min after the parent domain's start date. This simulation includes two-way nesting (red arrows).

4.4 Simulation with Nested Region around the Antarctic Peninsula

In order to avoid the divergence of the model's dynamics from reality after a few weeks, one possibility is the nudging of the model's dynamics towards external reanalysis data (e.g., Jeuken et al., 1996). In ICON-ART, this is realised by the feature of reinitialising the model's dynamics and microphysics while keeping the state of the chemical tracers in the model, first mentioned by Diekmann (2017). In order to be able to compute ice PSCs continuously, this has been extended for cloud ice in the model in this thesis.

In order to evaluate the single event of mountain-wave induced PSCs at the end of July 2008 with satellite data the dynamics have to be realistic. Especially the development of the polar vortex has to be realistically represented in the model because of the high gradients of photolytically active species at the edge of the vortex. Therefore, the meteorology is reinitialised every second day from 01 May 2008 when the polar vortex and the heterogeneous chemistry are not active yet. The initial data for chemical species is derived from the ensemble base run. With this, a spin-up of the chemistry of two months ensures consistency within the ICON-ART model. The general setup of the simulation is the same as in the ensemble simulation. A schematic illustration of this simulation can be found in Fig. 4.3.

After approaching the mountain wave event beginning on 20 July 2008 (Noel and Pitts, 2012), the simulation runs freely until end of July 2008 with two nests included as shown in Fig. 4.4. Global horizontal resolution is R2B04 (approx. 160 km) and the corresponding nests have resolutions of R2B05 (approx. 80 km, called Antarctica nest) and R2B06 (approx. 40 km, called Antarctic Peninsula nest), see also Table 3.1. Vertically, the configuration is the same as in the ensemble simulation. The nests are initialised four time steps after the next higher one so that after 8 time steps (i.e. 48 min) all the nests are active including two-way interaction.

Another simulation is conducted in the same configuration but without the nests after 20 July

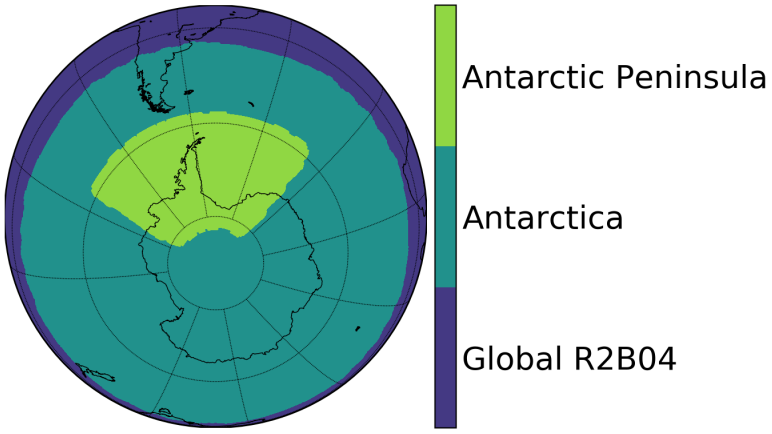

Figure 4.4: Visualisation of the used nests around Antarctic Peninsula. Resolutions are R2B04 in the global domain and R2B05 and R2B06 in the nests.

2008.

4.5 The ERA5 Reanalysis Dataset

The ECMWF Reanalysis 5 (ERA5, Hersbach et al., 2018) is the successive operational reanalysis dataset of ERA-Interim (Dee et al., 2011). The following brief description of ERA5 is based on Hersbach et al. (2018).

In the reanalysis, observations and model data are combined by optimal interpolation methods. In case of ERA5, this includes an ensemble 4-dimensional assimilation system where the model simulation is corrected by a variety of measurements within a time window of 12 h. Assimilated observations include measurements by more than 30 satellites as well as ground-based measurements. The model bases on the IFS model (Simmons et al., 1989) which is operational at ECMWF and which is accompanied by a land surface scheme and a submodel for ocean waves. The assimilation ensemble is generated by adding random zero-mean gaussian perturbations to the observational and model data.

The ensemble data assimilation enables ERA5 to provide uncertainty estimates of the reanalysis dataset. Compared to ERA-Interim, ERA5 has a higher spatial (31 km x 137 levels up to 1 Pa) and temporal resolution (hourly output interval) and more output variables. In addition, more observation datasets are assimilated. A comparison of ERA5 and ERA-Interim can be found in Hoffmann et al. (2019). ERA5 will cover the time period beginning from 1950 until now with monthly updates. It is available via the Climate Data Storage[1].

In this thesis, the potential vorticity of ERA5 in the pressure range between 100 and 30 hPa is used to investigate the development of the polar vortex in comparison to the ICON-ART simulations (see Sect. 5.1). Data of every even day in the respective month of the period 2004 to 2016 is selected.

[1] https://cds.climate.copernicus.eu

4.6 The MERRA Reanalysis Dataset

The Modern-Era Retrospective analysis for Research and Applications (MERRA, Rienecker et al., 2011), provided by NASA, is a reanalysis product for weather and climate applications covering the satellite period from 1979 until 2015. After this, it was replaced by version 2 of the reanalysis (MERRA2, Gelaro et al., 2017) where more observational data is assimilated (but not used in this thesis). The following description of the MERRA reanalysis is based on Rienecker et al. (2011).

The MERRA reanalysis is based on the Goddard Earth Observing System atmospheric model version 5 (GEOS5) which includes boundary conditions and parametrisations for all relevant variables for the application in weather and climate. Horizontal resolution of the model for the data assimilation system is 0.5° in latitude and 0.66° in longitude. Vertically, 72 levels cover altitudes from the Earth's surface up to 0.01 hPa. A three-dimensional variational data assimilation system is applied which combines the observational and modelled data every 6 h. The used observations include various satellite datasets, ground based stations data and radiosonde profiles.

In this thesis, the southern hemispheric minimum temperature from MERRA is used for the comparison with the ICON-ART simulations. It is published via website[2] and provides daily minimum temperature data for one specific year as well as minimum and maximum values for the whole period that was covered by MERRA.

4.7 Satellite Measurement Data

The simulations are evaluated with different satellite datasets which are described in the following. The MIPAS instrument on the Envisat satellite is described first (Sect. 4.7.1). Then, a description of the CALIOP instrument aboard the CALIPSO satellite follows (Sect. 4.7.2). The MLS and OMI instruments on the Aura satellite are pointed out in Sect. 4.7.3. In the last subsection, the method to interpolate the ICON-ART simulation data to the satellite orbits is described (Sect. 4.7.4).

The CALIPSO and Aura satellites are part of the A-train constellation (Stephens et al., 2002) where six satellites share an orbit with 98° inclination and the satellites moving polewards up to a latitude of 82°N/S with a time lag in the order of minutes. By this, the same atmospheric air masses can be investigated by a multiplicity of different instruments.

There are two major viewing geometries for Earth observing satellite instruments: limb and nadir, see Fig. 4.5. In limb view the instrument measures along the horizon. Due to the increase of air density at lower altitudes and the long pathlength in the tangent layer, the major signal in this geometry comes from the tangent point, i.e. the point closest to the ground. Profiles can be retrieved by varying the viewing angle. In nadir geometry, the instrument's view is downwards to the ground. Profiles can be retrieved either by pulsing the actively emitted light beam or by pressure broadening of the spectral lines.

[2] https://ozonewatch.gsfc.nasa.gov/meteorology/figures/merra/temperature

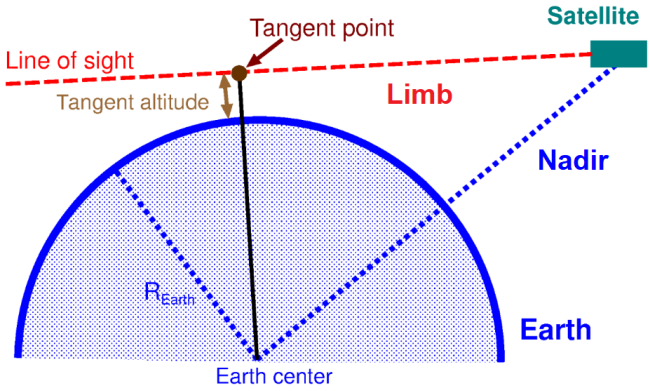

Figure 4.5: Limb and Nadir geometries of satellite instruments. Limb: The satellite scans the horizon. By this, most of the signal comes from the tangent point, i.e. the point closest to the ground. Nadir: The satellite scans the atmosphere downwards in direction of the Earth's radius. Adapted from Ern et al. (2018) (CC-BY 4.0 license).

4.7.1 MIPAS on Envisat

The Environmental Satellite (Envisat) of the European Space Agency (ESA) was launched in 2002 and operated until 2012 in a sun-synchronous polar orbit with 98° inclination at an altitude[3] of 800 km (Höpfner et al., 2018). The satellite repeated its orbit in 35 d. Envisat reached latitudes up to 81.45°N/S and was equipped with 10 instruments scanning the Earth's environment.

The Michelson Interferometer for Passive Atmospheric Sounding (MIPAS) on Envisat was a Fourier transform spectrometer in the mid-infrared in the wavelength range from 4.15 to 14.6 µm with a spectral resolution of 0.0625 cm^{-1} in 2008 (Fischer et al., 2008; Höpfner et al., 2018). The MIPAS instrument sounded the atmosphere in limb geometry, i.e. in horizontal direction, see Fig. 4.5, which led to a high vertical resolution and trace gases with low volume mixing ratios could be detected by MIPAS. With this, more than 25 atmospheric trace gases (Fischer et al., 2008) as well as cloud properties of PSCs (Höpfner et al., 2006b) could be retrieved at altitudes from the upper troposphere up to the mesosphere. In addition, the limb geometry caused MIPAS to be able to take profiles down to latitudes of 87.5°S, thus very close to the South Pole.

Höpfner et al. (2018) recently compiled a climatology of PSC measurements for the whole MIPAS/Envisat period for latitudes around the poles (40° to 90°N/S) and for the respective winter periods. With MIPAS, PSCs are detected by assuming refractive indices for the different PSC types within four different spectral windows where the spectrum is not disturbed by other species too much. The dataset contains two profiles of the PSC volume concentration with different assumptions: the first profile assumes small particles which is a maximum assumption for the particle volume concentration. The second profile assumes particles with a radius of 3 µm which is the minimum assumption for the particle volume concentration (Höpfner et al., 2018).

[3] see also official ESA website: https://earth.esa.int/web/eoportal/satellite-missions/e/envisat

4.7.2 CALIOP on CALIPSO

The primary instrument onboard the Cloud-Aerosol Lidar and Infrared Pathfinder Satellite Observation (CALIPSO) is the Cloud-Aerosol Lidar with Orthogonal Polarisation (CALIOP, Pitts et al., 2009; Höpfner et al., 2009; Pitts et al., 2018). The CALIPSO satellite was launched on 28 April 2006 (Winker et al., 2007). As part of the A-train constellation, the satellite flew in an orbit with 98° inclination at an altitude of 705 km and coming down to latitudes of 82°S with a repeat cycle of 16 d (Stephens et al., 2002; Pitts et al., 2018). In February 2018, it was moved to a lower orbit[4] with an altitude of about 688 km.

The CALIOP instrument is a light detecting and ranging (Lidar) instrument which actively scans the atmosphere by light beams at wavelengths of 532 and 1064 nm including two polarisations for both channels (Winker et al., 2007). The instrument is set up in nadir geometry, i.e. looking downwards to the ground, see Fig. 4.5. In the altitude range from 8.4 to 30 km, the vertical resolution is 180 m or higher and the light beam has a diameter of about 100 m at the ground (Höpfner et al., 2009; Pitts et al., 2018).

Polar stratospheric clouds are detected by CALIOP using the ratio of the total backscatter coefficient and the molecular backscatter coefficient R_{532} as well as the backscatter coefficient at perpendicular polarisation $\beta_{\perp,532}$ at 532 nm. Discrimination of the PSC types can be established in the $1/R_{532}$ vs. $\beta_{\perp,532}$ figures where different regions represent the different PSC types (Pitts et al., 2009, 2018). Thus, the types can be inferred from the CALIOP data but a quantitative comparison of concentration is more difficult, which is further discussed in Sect. 5.7.1. The data distinguishes between no cloud, STS and ice clouds. In addition, ice in mountain waves is a PSC class in CALIOP. For NAT, three mixture types between STS and NAT are distinguished which are called Mix1, Mix2 and Mix-enh according to different assumptions of number concentrations of the two types. In the comparison with ICON-ART, the STS and NAT classes are summarised and called STS+NAT.

The data used in the scope of this thesis originate from the PSC climatology by Pitts et al. (2018) and are the version 2 and level 1B data, which have been averaged with a window of 5 km along the satellite flight path. In addition, the data is restricted to night-time data since the backscattered sunlight leads to higher noise levels (Pitts et al., 2018). Data between 50°S and 82°S from 01 May to 31 October 2008 is selected for the comparison with ICON-ART.

4.7.3 MLS and OMI on Aura

The Aura satellite finishes the A-train constellation (see CALIPSO description above) and was launched on 15 July 2004 (Schoeberl et al., 2006). The satellite is equipped with four instruments whereof two are used in the scope of this thesis for evaluation studies: the Microwave Limb Sounder (MLS, Waters et al., 2006) and the Ozone Monitoring Instrument (OMI, Levelt et al., 2006b).

The MLS instrument passively measures the thermal emission of about 20 trace gases and cloud properties in the atmosphere in limb geometry and at wavelengths in millimetre to submillimetre range (Waters, 1989; Waters et al., 2006). Advantages of this measurement technique are for instance that it is not affected by clouds and that measurements can be performed during daytime as well as during the night. Limb scans are measured every 25 s with a nearly global coverage from 82°N

[4] see https://atrain.nasa.gov/

Table 4.4: Pressure ranges and quality check of MLS data. The values originate from the documentation of the version 4 level 2 data, see text and foot note 5. Data where the quality flag is higher than the given threshold and data where the convergence flag is lower than the given threshold are used.

Compound	Pressure range (hPa)	Quality Threshold	Convergence Threshold
HNO_3	215 – 1.50	-	-
N_2O	46 – 4.60[a]	1.0	2.00
H_2O	316 – 0.10	0.7	2.00
ClO	147 – 1.00	1.3	1.05
HCl	100 – 0.32	1.2	1.05

[a] Due to biases up to 100 % at other altitudes, this pressure range is chosen for N_2O which differs from the recommended range in the documentation.

to 82°S. The instrument consists of five spectrometers sounding at defined wavelength ranges and measuring various species and properties of the atmosphere (Waters et al., 2006).

Nitric acid is detected by the MLS radiometer at a wavelength of about 1.5 mm (= 190 GHz). The vertical resolution of the data is 3 to 4 km (Waters et al., 2006). The dataset used in this thesis is the version 4 level 2 HNO_3 data for the complete year 2008 and the latitude band from 75°S to 82°S. The pressure range to be used in the data is 215 to 1.5 hPa, according to the documentation of the dataset[5]. In addition, the data provides flags when the retrieved HNO_3 lacks precision. These data points are cancelled from the MLS data for comparison with ICON-ART. The same data screening with different pressure ranges and precision thresholds is applied to N_2O, H_2O, ClO and HCl. The values are summarised in Table 4.4. In addition, remaining profiles with negative volume mixing ratio within the recommended pressure range of Table 4.4 are cancelled. This mostly affects ClO where 2 ‰ of the profiles can be used, only.

The history of the OMI instrument goes back to 1979 when the predecessor Total Ozone Mapping Spectrometer (TOMS) was integrated in previous satellites (Levelt et al., 2006b). The OMI instrument on the Aura satellite consists of a nadir solar backscatter spectrometer for ultra-violet to visible wavelengths from 270 to 500 nm. As a passive nadir sounder, the instrument covers the latitudes of the satellite from 82°S to 82°N. The ozone column is retrieved by algorithms that already have been used for the TOMS instrument so that comparability to the early measurements is ensured (Levelt et al., 2006a).

The data used in this thesis are the southern hemispheric minimum ozone columns which are downloaded from https://ozonewatch.gsfc.nasa.gov/meteorology/SH.html. It provides the minimum and maximum of the whole measurement period from 1979 until 2017 as well as time series of the minimum ozone column for a specific year.

4.7.4 Interpolation of the ICON-ART Data to the Satellite Orbits

For the comparison with MIPAS, CALIOP and MLS, the ICON-ART data have to be interpolated to the measurement space of each satellite. The three-step procedure is described here. First, the three triangle grid points closest to the observation longitude and latitude are searched for each

[5] see https://mls.jpl.nasa.gov/data/v4-2_data_quality_document.pdf

measurement point for horizontal interpolation. Interpolation is performed by a inverse-distance-weighted average of the three neighbours:

$$\psi_{\text{hor}}(z,t) = \frac{\sum_{p=1}^{3} \frac{\psi(\lambda_p,\varphi_p,z,t)}{s_p^2}}{\sum_{p=1}^{3} \frac{1}{s_p^2}} \tag{4.1}$$

where ψ is the ICON-ART variable to be interpolated to the satellite and s_p is the distance to the neighbour grid point with index p. In addition, λ_p and φ_p stand for the grid point longitude and latitude, respectively. Then, the variable is interpolated linearly between the two neighboured (daily) output time steps of ICON-ART:

$$\psi_{\text{time}}(z) = \psi_{\text{hor}}(z,t_0) + \frac{t_{\text{satellite}} - t_0}{t_1 - t_0}\left(\psi_{\text{hor}}(z,t_1) - \psi_{\text{hor}}(z,t_0)\right) \tag{4.2}$$

where $t_{\text{satellite}}$, t_0 and t_1 are the dates of the satellite observation as well as the previous and next ICON-ART output time step, respectively.

Finally, the data are interpolated linearly to the given vertical coordinate ε of the satellites (geometric altitude for MIPAS and CALIOP, pressure for MLS):

$$\psi_{\text{satellite}} = \psi_{\text{time}}(\varepsilon_0) + \frac{\varepsilon_{\text{satellite}} - \varepsilon_0}{\varepsilon_1 - \varepsilon_0}\left(\psi_{\text{time}}(\varepsilon_1) - \psi_{\text{time}}(\varepsilon_0)\right) \tag{4.3}$$

For MIPAS, ψ refers to the particle volume concentrations of the different PSC types and the temperature in ICON-ART. For CALIOP, the particle surface and volume concentrations are used, see next section for a discussion. For MLS, ψ stands for the volume mixing ratio of the compounds used for comparison: X_{HNO_3}, X_{N_2O}, X_{H_2O}, X_{ClO} and X_{HCl}.

For comparison to OMI, the southern hemispheric minimum ozone values are calculated within the same latitude band of 40°S to 90°S as in the measurements after converting the ozone volume mixing ratios to DU as demonstrated in Appendix A.1.

5

Evaluation and Sensitivity Studies with the PSC Scheme in ICON-ART

The major goal of this thesis is the investigation of the interaction between PSCs and mountain waves. To achieve this goal, the PSC scheme is generally evaluated with reference data, such as reanalysis data and satellite measurements in this chapter. In addition, sensitivity studies with the PSC scheme provide insights in the parametrisations of the different PSC types.

First, the dynamics of the polar vortex, a measure for the size of the ozone hole, is investigated including all simulations of this thesis (Sect. 5.1). Then, it is shown that PSCs can be simulated using ICON-ART in climate configuration and generally with the thermodynamic NAT parametrisation (Sect. 5.2). Some sensitivity studies with the PSC scheme follow in Sect. 5.3. This includes the investigation of the impact of changing the top height of the ICON microphysics (Sect. 5.3.1) in order to calculate ice PSCs. After this discussion of ice PSCs in the model, it is examined if the STS box model shown in Fig. 3.12 can also be reproduced in the simulations with ICON-ART (Sect. 5.3.2). Supercooled ternary solution droplets are also part of the discussion of the comparison between thermodynamic and kinetic NAT parametrisations that follows in Sect. 5.3.3. The kinetic NAT parametrisation is further investigated in Sect. 5.3.4 and Sect. 5.3.5 where the dependency of the NAT size distribution on the number of size bins and the dependency of the growth factor of Eq. (3.27) on the radius are examined, respectively.

After this general investigation of the PSC scheme itself, it is demonstrated that denitrification is included in the model by the comparison of NO_y and N_2O to flight measurements (Sect. 5.4). Then, it is shown that chlorine and bromine activation are consistently integrated in ICON-ART (Sect. 5.5). The impact on ozone is demonstrated in Sect. 5.6 where the linearised ozone scheme is compared to the ozone development as part of the gas phase chemistry.

Finally, the PSC scheme is compared to four satellite measurement datasets in Sect. 5.7: MIPAS, CALIOP, MLS and OMI. It is shown in this section that denitrification, dehydration and chlorine activation occur in the correct time spans and altitude ranges. Thus, with the introduction of the PSC scheme in ICON-ART, it is now possible to represent ozone in the gas phase chemistry in a realistic manner.

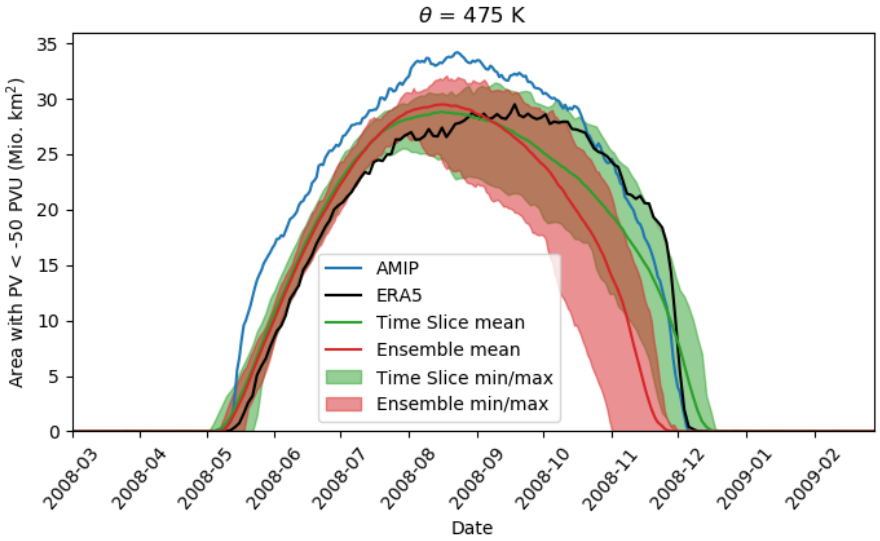

Figure 5.1: Area of the polar vortex in all global simulations with ICON-ART compared to ERA5 reanalysis. The area on Earth where the potential vorticity is lower than −50 PVU is shown, after linearly interpolated to the potential temperature surface of 475 K. The AMIP experiment uses the climate configuration of ICON-ART with AMIP boundary conditions for the year 2008. The time slice experiment consists of 30 years with repeated boundary conditions of the year 2008. The ensemble experiment consists of 31 free-running simulations of 2008 with zero-mean Gaussian perturbed initial conditions.

5.1 Dynamics of the Polar Vortex

Due to the low temperatures within the polar vortex it determines the area where ozone depletion takes place during local spring and it is therefore a measure for the size of the ozone hole. In the operational setup at the Climate Prediction Center of the U.S. National Weather Service[1], the size of the polar vortex is analysed by the potential vorticity, see Eq. (2.9), at a specific surface with constant potential temperature θ. Here, the surface with the potential temperature $\theta = 475$ K is used, i.e. an altitude of about 21 km. The potential vorticity depends on altitude which is why a threshold of −50 PVU defines the vortex edge in this thesis, which is based on, e.g., Braathen and Proffitt (2000) and Serra et al. (2017). The potential vorticity in ICON-ART is calculated as described by Selz (2019). As a reference, the recent ECMWF reanalysis ERA5 is used in this section, see Sect. 4.5.

Figure 5.1 shows the time series of the area where $PV < -50$ PVU for ERA5 (black) and all realisations of the year 2008 of ICON-ART. The potential vorticity of ICON-ART and ERA5 are linearly vertically interpolated to the 475 K surface. Then, the area of the polar vortex is calculated as sum of the triangle areas where $PV < -50$ PVU. For the time slice and the ensemble simulations, the minimum and maximum area for each day is illustrated by the green and red ranges in Fig. 5.1, respectively. The AMIP-like simulation is represented by the blue line in the figure.

The polar vortex in ERA5 starts to develop in mid of May which is consistently represented in all simulations with ICON-ART. Both the time slice and ensemble simulations are able to capture the growth of the polar vortex in ERA5 until begin of August where the uncertainty ranges of the simulations is in the order of 5 days. The AMIP-like simulation overestimates the area of the polar

[1] https://www.cpc.ncep.noaa.gov/products/stratosphere/polar/polar.shtml

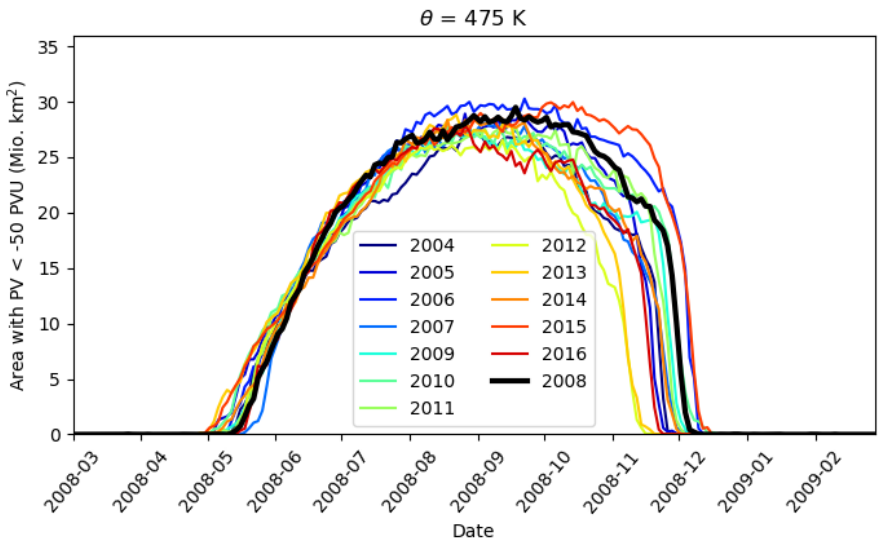

Figure 5.2: Area of the polar vortex in ERA5 for the years 2004 to 2016. The algorithm to calculate and interpolate the *PV* on the θ = 475 K surface is the same as in Fig. 5.1. The year 2008 is the black thick line which is also shown in the previous figure.

vortex by up to 5 Mio. km^2 in this time period. At the maximum size of the polar vortex in mid of August, this difference rises to up to 10 Mio. km^2.

During the reduction of the polar vortex, the uncertainty ranges of both time slice and ensemble simulations increase to up to one month indicating that the variability in the decrease of is larger than for the growth of the polar vortex. While the area of the polar vortex in ERA5 is within the uncertainty range of the time slice experiment over the whole time period, the polar vortex decreases by at least 10 days faster than in the reanalysis. In the AMIP-like simulation, the decrease of the polar vortex is also captured compared to ERA5.

The main difference between the AMIP, time slice and the ensemble simulations is the treatment of ozone in the model. In the ensemble simulation, ozone is computed as part of the gas phase chemistry with feedback to radiation whereas climatologies of ozone are used for the radiation feedback in the other simulations. This could explain the different development of the polar vortex in the simulations. In addition, the physics and vertical resolution of the AMIP-like simulation differ from the time slice and ensemble simulations which could explain the overestimation of the size of the polar vortex.

Figure 5.2 illustrates the polar vortex in ERA5 of 2008 in the context of the years 2004 to 2016. The year 2008 is pointed out by the thick black line. Especially at the end of the vortex development, the year 2008 is an exceptional year with a vortex area of more than 20 Mio. km^2 in December and a late decrease of the vortex area afterwards compared to the other years.

Single free-running simulations may not capture this long continuing polar vortex. However, there are members of the time slice experiment which can reflect this feature of this specific year. Thus, Figure 5.1 demonstrates the usefulness of conducting a variety of simulations where the state at the beginning of the season in March 2008 is perturbed but where the other boundary conditions are conserved.

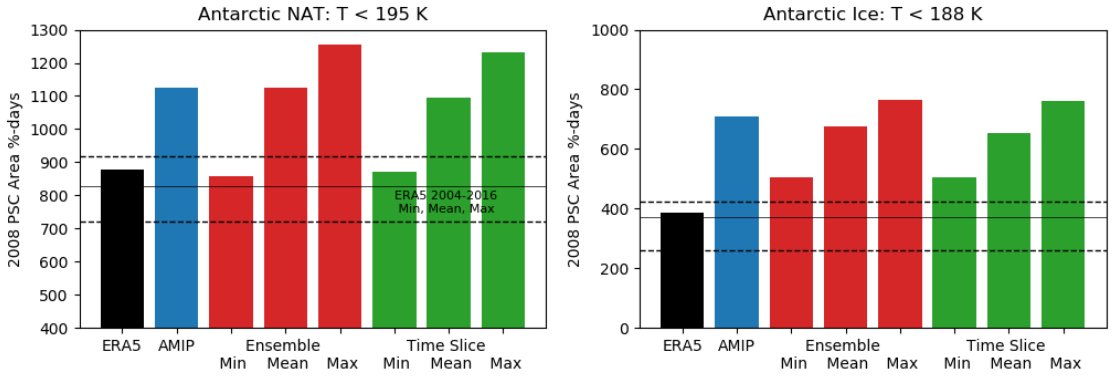

Figure 5.3: Area of NAT and ice PSCs based on temperature thresholds at an altitude of 50 hPa. This corresponds to a geometric altitude of about 20 km, similar to the 475 K surface used in Fig. 5.1. The simulation data are linearly interpolated to 50 hPa. The algorithm to derive the southern hemispheric PSC area is the same as mentioned in Butchart and Charlton-Perez (2010), details see text. Please note the different vertical axes which correspond to that by Butchart and Charlton-Perez (2010). The horizontal lines correspond to minimum, mean and maximum of the ERA5 period from 2004 to 2016.

Comparing the different types of ICON-ART simulations with each other, the initial variability in May is larger in the time slice experiment than in the ensemble simulation. This is a result how the initial state is perturbed in the different simulations. In the time slice experiment, the second member is generated by the state after the first year of simulation. Therefore, the average difference to the first initial state is most probably larger than the second member in the ensemble simulation which has been perturbed by up to 1 ‰. At the final stage of the polar vortex during November, the variability of the vortex area is comparable in both simulations.

A quantity that is connected to the size of the polar vortex is the area covered by PSCs. In the fifth SPARC report (Butchart and Charlton-Perez, 2010), this area is derived from temperature thresholds for a variety of models at an altitude of 50 hPa. The algorithm is based on Pawson et al. (1999) and Austin et al. (2003) and described in the following.

As proxies for NAT and ice PSCs at this altitude, the area south of 50°S is calculated where temperatures are lower than 195 K and 188 K, respectively, for each output time step. This is multiplied by the output interval, divided by the total area of the hemisphere and summed up for the period from 1 July to 30 September. This a proxy for the total amount of PSCs that are present during the whole season. The resulting relative accumulated area is shown in Fig. 5.3 for ERA5 and the simulations already used in the discussion of the polar vortex. A value of 800 %-days means that a total area eight times of the southern hemisphere was covered by temperatures lower than the threshold during this season. The vertical axes correspond to Fig. 4.15 in Butchart and Charlton-Perez (2010). In addition, the average, minimum and maximum values for the ERA5 period from 2004 to 2016 is illustrated as black line in the panels of Fig. 5.3 as a measure for a realistic variability of this quantity.

For the ice threshold of 188 K (right panel of Fig. 5.3), the area in ERA5 is significantly smaller then in all simulations and members. The averages of all simulations agree within a few tens of %-days but are by a factor of 1.8 larger than that of ERA5 for 2008. No simulation is within the range of the total shown period of ERA5 from 2004 to 2016 thus showing that the area with potential for ice PSCs is too large in the model.

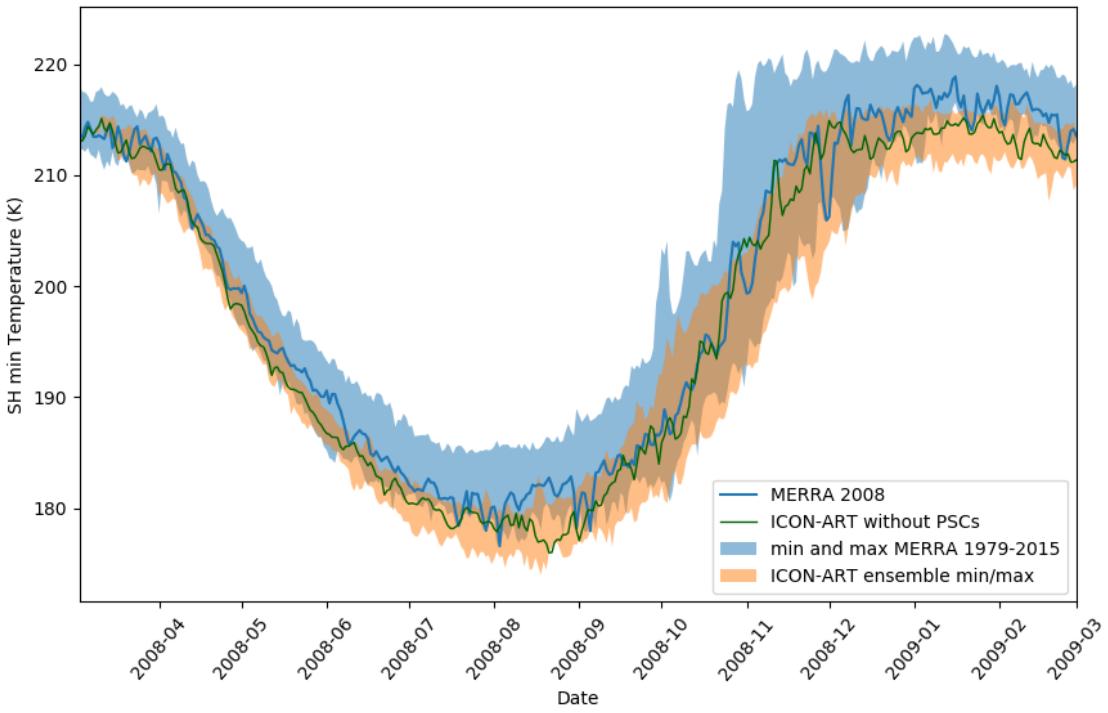

Figure 5.4: Southern hemispheric minimum temperature at 50 hPa in the MERRA reanalysis and ICON-ART simulations. The blue line corresponds to the MERRA minimum temperature of 2008, the green line depicts the minimum ozone in the simulation without PSCs. The blue range illustrates the range of southern hemispheric minimum temperature between 1979 to 2017. The orange range corresponds to the range of the ensemble simulation. The minimum is taken for latitudes south of 50°S.

The left panel of Fig. 5.3 demonstrates that the PSC areas in the mean of all realisations of the year 2008 agree for NAT PSCs (left panel) with values around 1130 %-days and deviation of about 20 %-days in spite of the differences in the size of the polar vortex. These values are by 250 %-days larger than in ERA5 of the year 2008. Thus, the area where PSCs can exist in the model is overestimated. Nevertheless, there are members of both ensemble and time slice experiments that can reflect the conditions of ERA5. Thus, this demonstrates again the usefulness of knowing the variability and error of the model simulations so that statements about the uncertainty of both reference data and model data can be derived.

In addition to the threshold temperatures for PSCs, the southern hemispheric minimum temperature is analysed in comparison to the MERRA reanalysis data. Figure 5.4 shows the timeseries of the minimum temperature of the reanalysis (blue) as well as the range of the reanalysis from 1979 until 2015 (blue shaded). The range of the ensemble simulation of ICON-ART is depicted as orange shaded range. In addition, the simulation without PSCs is illustrated as green line in the figure.

Due to the polar night, the minimum temperature decreases from 215 K in April to 180 K in August. This is in correspondence with the size of the polar vortex, see Fig. 5.1. After this, the temperature increases again to its initial value.

This general structure of the temperature development is represented in both simulations of ICON-ART. The temperatures at the beginning of the simulation on 1 March 2008 coincide with the

measured ones in the first weeks. During July to September, the temperature in the model simulations is lower than in MERRA but with an overlap of at least 2 K to the historical range of MERRA. This underestimation during the maximum size of the polar vortex is in accordance with the findings above where the temperature-based PSC area was shown to be larger than in ERA5. During the increase of the temperature between October and November, the MERRA temperature of 2008 is within the range of the ensemble simulation. Thus, this shows that the dynamics of the southern hemispheric minimum temperature is realistically represented in the model.

The PSC scheme in ICON-ART has an indirect feedback to the dynamics via the radiation feedback of ozone. Therefore, the temperature in the simulation without PSCs is within the ensemble range with PSCs during the whole year.

Concluding, the temperature development agrees with MERRA apart from underestimations during the period from July to September.

5.2 Polar Stratospheric Clouds with the Thermodynamic NAT Parametrisation

In this section, the development of PSCs within the polar vortex as defined above is demonstrated in the AMIP-like simulation using the climate configuration as well as in the first year of the time slice experiment. Both simulations use the thermodynamic NAT parametrisation and the general formation of PSCs using this parametrisation is investigated. Figure 5.5 shows time series of all PSC types in the upper three panel as vortex average (ice and NAT) and minimum and maximum values (STS) occurring within the polar vortex on the 475 K surface. The time period covers the whole life cycle of the polar vortex from May to December 2008.

Both simulations shown in Fig. 5.5 agree in the formation and development of PSCs. NAT particles are formed first with particle volume concentrations up to 0.35 $\mu m^3\,cm^{-3}$. The NAT particles are calculated by the thermodynamic parametrisation which leads to large denitrification in the model, i.e. to a removal of gaseous HNO_3 from this layer. In both simulations, HNO_3 descreases to values lower than 1 ppbv. Whereas the sedimentation of HNO_3 takes a few days in the time slice experiment, the dentrification is slower in the AMIP experiment either due to smaller NAT particles or due to the input of HNO_3 from higher altitudes.

Because of the fast denitrification in the model, no ternary solution droplets can be formed. Only binary sulphate solution droplets exist with particle volume concentrations of 1 $\mu m^3\,cm^{-3}$ in the maximum. This will be further discussed in Sect. 5.3.3. The particle volume concentration of the background sulphate aerosol is larger than zero in the polar vortex during the whole time period, because it can exist all over the year.

Ice particles are formed the latest in the polar vortex because the temperature has to decrease to the lowest values for the formation of ice clouds (see e.g., Fig. 2.6). The ice volume concentration is in an order of magnitude that has been measured by in-situ balloon observations (see Höpfner et al., 2018, and references therein). The ice volume concentrations between AMIP and time slice simulations agree in the vortex-averaged values. On the other hand, the ice number concentration should fit to the microphysics in the model in order to be consistently applied.

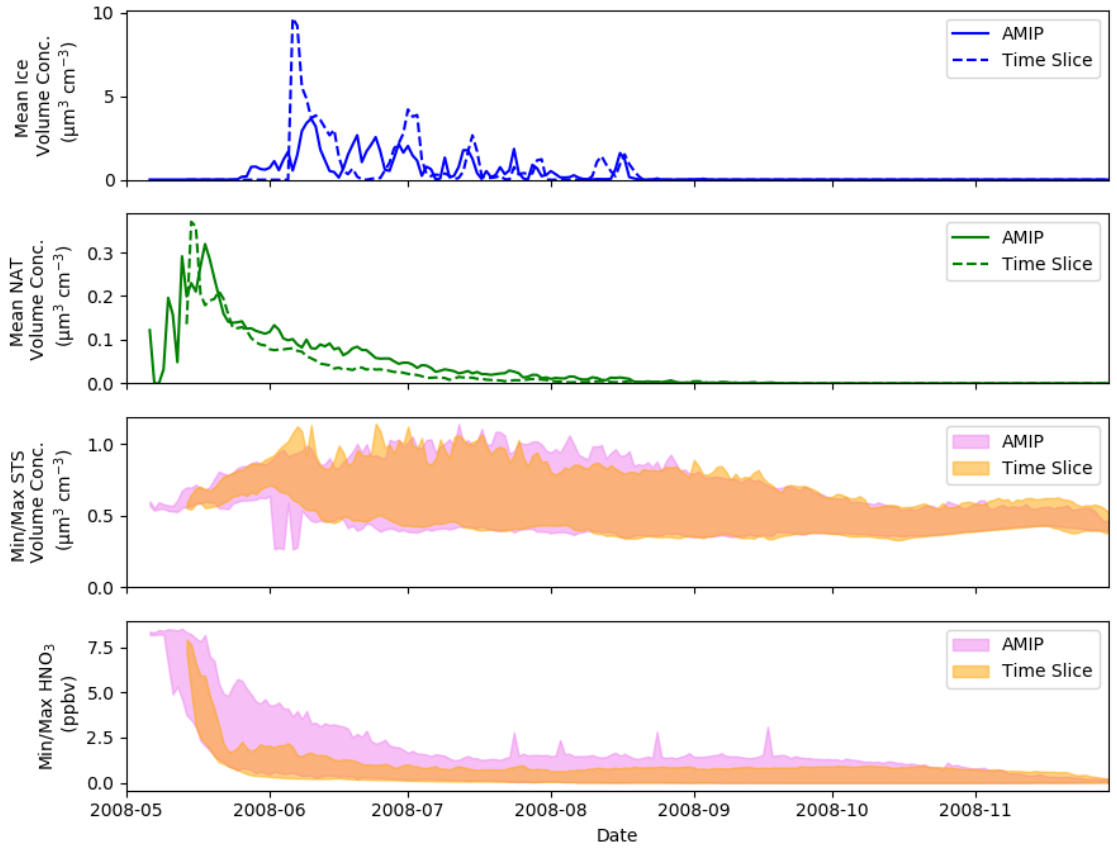

Figure 5.5: Polar stratospheric cloud development with the thermodynamic NAT parametrisation. Results of the AMIP simulation (solid lines and violet) and the first year of the time slice simulation (dashed lines and orange) are shown. The time series show the vortex-averaged PSC volume concentration of ice and NAT in the first two panels, and vortex minimum and maximum of STS in the third panel. The minimum and maximum of HNO_3 in the vortex is shown in last panel. This is shown for the AMIP-like simulation in climate configuration and for the time slice experiment in NWP configuration. The simulations are interpolated on the 475 K surface of potential temperature. The polar vortex is defined by $PV < -50$ PVU on the 475 K surface.

Since there is an uncertainty about the particle number concentration of ice particles in the climate configuration, as already discussed in Sect. 3.5.1, and because of the overestimation of the area of the polar vortex in the AMIP simulation, the NWP configuration is used in the remaining part of this thesis.

5.3 Sensitivity Studies with the PSC Scheme

In this section, the three types of PSCs are examined using ICON-ART in NWP configuration. It begins with ice PSCs in Sect. 5.3.1 where the impact of changing the top altitude of the microphysics is further investigated. Then, the development of STS in the ensemble simulation is pointed out by comparisons to box model results in Sect. 5.3.2. In Sect. 5.3.3, the kinetic and the thermodynamic NAT parametrisations are compared to each other. The last two subsections include sensitivity

studies on changing the size distribution of NAT in Sect. 5.3.4 and the investigation of the radius dependency of the growth factor used for the growth of NAT, see Sect. 5.3.5.

5.3.1 Impact of Changing the Top Height of the Microphysics

In section 3.5.1, different possibilities how to calculate ice PSCs in the NWP configuration of ICON-ART were discussed. The impact of increasing the top height h_{top} of the NWP microphysics to 30 km instead of the operationally used 22.5 km is investigated in the following in more detail. The impact on the dynamics of the model is investigated by the changes in temperature and the tropopause height. Then, the two ice parametrisations by the ICON microphysics and Marti and Mauersberger (1993), as mentioned in Sect. 3.5.1, are compared with each other, followed by the influence of the h_{top} change on convection in the model.

Influence on the Model Dynamics

Due to the radiation feedback of water vapour, an increased value of h_{top} leads to different dynamics globally in the model compared to the operational setup at DWD. Therefore, both temperature and tropopause height are analysed for the complete time range of the time slice experiment.

The temperature in Fig. 5.6 is averaged globally and for southern high latitudes (60°S to 90°S) and linearly interpolated to different lower stratospheric pressure surfaces (5, 10 and 50 hPa). It is shown for both values of h_{top} which are the different panels in Fig. 5.6(a) and Fig. 5.6(b), respectively. Generally, the temperature decreases in the stratosphere with decreasing pressure (see, e.g., Fig. 2.1) and the yearly cycle is amplified for lower pressure values. In the lower stratosphere at 50 hPa (green dotted/dashed lines), the temperature time series for both h_{top} values show an oscillation with period of six months in the global mean (Fig. 5.6(a)). Most probably, this is a result of the different temperature structures during summer and winter in both hemispheres of the Earth.

In the southern high latitudes in Fig. 5.6(b), the yearly oscillation has a mean amplitude up to $\Delta T = 60$ K, by a factor of about 12 larger than in the global average due to the seasonal cycle around the South Pole. During the winter months May to September, the temperatures decrease to values below 195 K on the pressure surfaces of 10 and 50 hPa. Thus, the formation of PSCs is possible over the Antarctica although the simulation runs freely for both values of h_{top} which was already demonstrated for 50 hPa in Sect. 5.1.

Figure 5.7 shows the differences between the time series with different top height of the NWP microphysics of Fig. 5.6(a) and Fig. 5.6(b), respectively. It is calculated as difference between the time series with $h_{\text{top}} = 30$ km and 22.5 km. In the upper panel of this figure comparing the global time series, the differences are mostly below 1 K and thus a factor of 3 lower than the amplitude of the original time series. A yearly pattern in the temperature differences indicates that the increase and decrease in temperature differ between the time series. In addition, there is a trend in the difference in the order of 1 K within the 27 years of the time slice experiment.

This trend is also analysed in the time series themselves by linear regressions. The respective slopes and offsets are denoted on the right hand side of the panels in Fig. 5.6. The slope is given in K yr^{-1} and the offset in K. The largest slopes in the global time series occur at the pressure values 10 and 5 hPa where the linear trend is in order of $-0.03\ \text{K yr}^{-1}$ when using $h_{\text{top}} = 22.5$ km in the upper

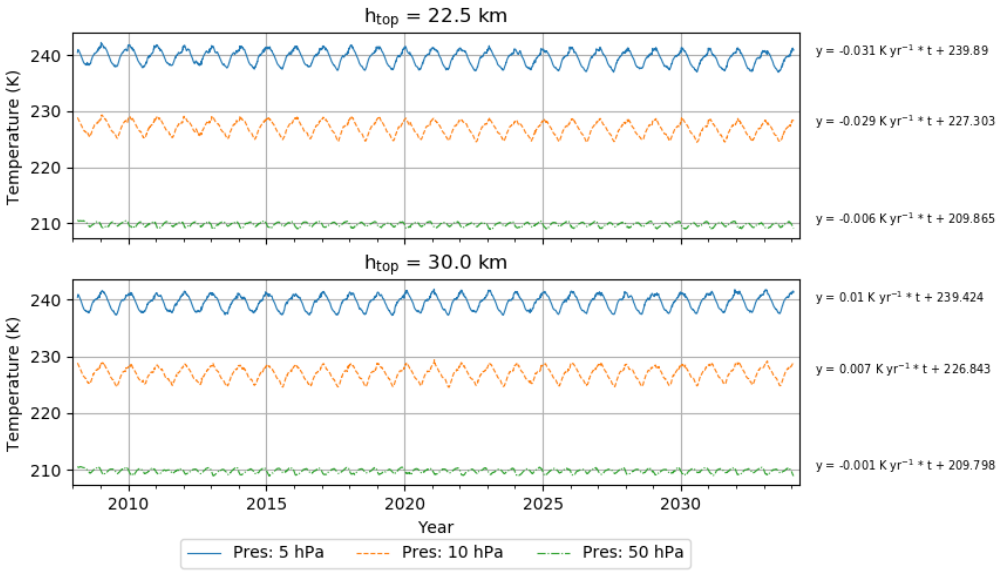

(a) Latitude: 90°S to 90°N

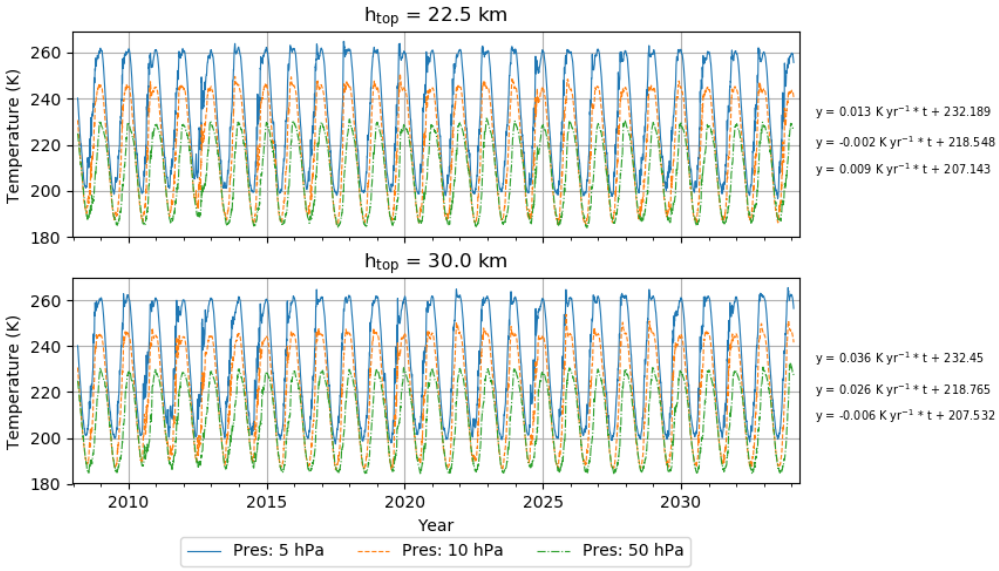

(b) Latitude: 90°S to 60°S

Figure 5.6: Stratospheric temperature time series in ICON-ART (a) globally and (b) at southern high latitudes. The temperature is averaged for different latitude bands and interpolated to specific pressure surfaces in the lower stratosphere as denoted in the figures. The respective upper panels include a value of h_{top} = 22.5 km whereas the lower panels correspond to h_{top} = 30 km. The notes on the right hand side of the panels show the linear trend in the time series where the slope is given in K yr^{-1} and the offset is given in K. Results of the time slice experiment are shown.

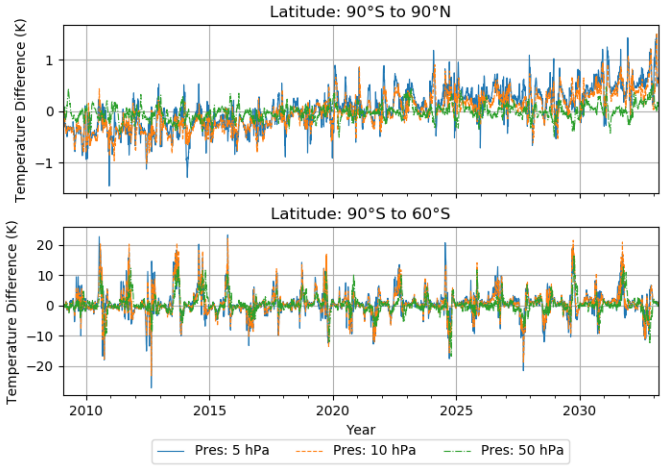

Figure 5.7: Difference of the time series of Fig. 5.6. The panels show the different latitude bands.

panel of Fig. 5.6(a). In contrast to this, the trend is positive and in the order of 0.01 K yr^{-1} for h_{top} = 30 km, i.e. in the lower panel of Fig. 5.6(a). Thus, the trend in the time series is decreased when using a value for the NWP microphysics top height of h_{top} = 30 km instead of 22.5 km.

In the southern high latitudes, the trend is negligible compared to the order of magnitude of the yearly cycle. In the lower panel of Fig. 5.7, the difference between the temperature time series peaks at ±20 K which shows that the oscillation differs between the southern time series. Especially, during the time of increasing and decreasing temperature small variations lead to a large difference between the time series. The general development of the temperature, though, is similar between the two values of h_{top}.

The tropopause height is also a result of the dynamical structure and thus sensitive to the value of h_{top}. In Figure 5.8, the maximum tropopause altitude is shown which is calculated according to the thermal definition by World Meteorological Organization (WMO, 1957). The panel 5.8(a) illustrates the time series for h_{top} = 22.5 km for the same latitude bands as in the temperature time series and Fig. 5.8(b) shows the same for h_{top} = 30 km. The differences between the tropopause time series are illustrated in Fig. 5.9.

Like in the temperature time series, the amplitude of the global maximum tropopause altitude is lower than that in southern high latitudes. Globally, it varies between 15 and 20 km with some exceptions whereas the tropopause altitude ranges from 11 to 22 km in the southern high latitudes. This is a result of the seasonal cycle of the temperature and general dynamics around the South Pole. Minimum tropopause heights in the southern high latitudes occur during winter which is a result of the low stratospheric temperature and has been observed (e.g., Rieckh et al., 2014).

On the other hand, the differences in Fig. 5.9 are in the order of the variations in the time series themselves. Since the differences again show a yearly cycle and no trend, this originates from differences in the yearly cycle when using h_{top} = 30 km instead of 22.5 km. As the general structure of the tropopause altitude is conserved for both values of h_{top} the differences are reasonable.

Concluding, the trend in the temperature that occurs in NWP microphysics in the stratosphere could be improved by increasing the top altitude of the NWP microphoysics to h_{top} = 30 km. Differences between the time series of temperature and tropopause altitude can be explained by different

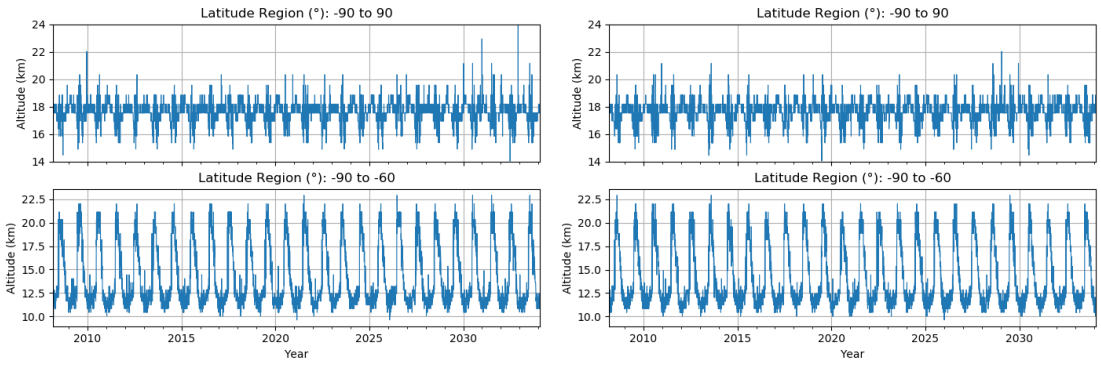

(a) h_{top} = 22 500 m (b) h_{top} = 30 000 m

Figure 5.8: Time series of maximum tropopause altitude in ICON-ART for a h_{top} value of (a) 22 500 m and (b) 30 000 m. Definition of the thermal tropopause according to WMO (1957). Maximum is taken from the latitude bands shown in the figures. Results of the time slice experiment is shown.

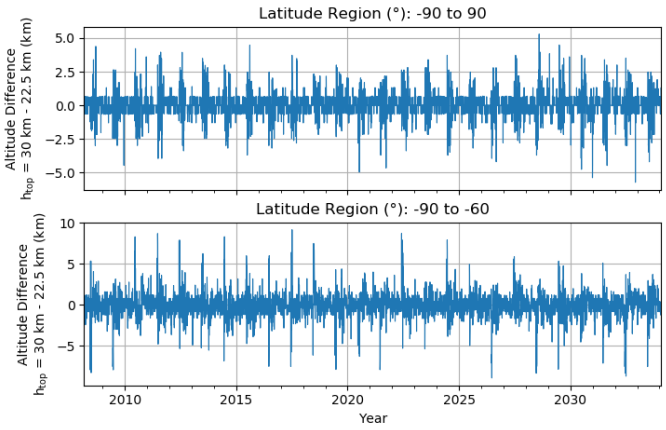

Figure 5.9: Difference of the time series of Fig. 5.8. The panels show the different latitude bands.

dynamics especially in the yearly cycle. Thus, increasing the top altitude of the microphysics leads to reasonable results and the general response of the model in terms of dynamics is negligible.

Comparison of the Two Ice Parametrisations

The parametrisations by Marti and Mauersberger (1993) and Doms et al. (2011) both parametrise ice on different ways. In Figure 5.10, time series of ice for both parametrisations are shown averaged for southern high latitudes (60°S to 90°S) and calculated within the same simulation and with the same water vapour mixing ratio as input. The microphysics are computed in the operational setup but up to h_{top} = 30 km. The same patterns for both parametrisations occur during the whole simulated year which demonstrates that they represent the same process and lead to similar quantitative results.

The parametrisation by Marti and Mauersberger (1993) starts to form ice about 10 days earlier than in the microphysics of ICON-ART. Since the parametrisation by Marti and Mauersberger

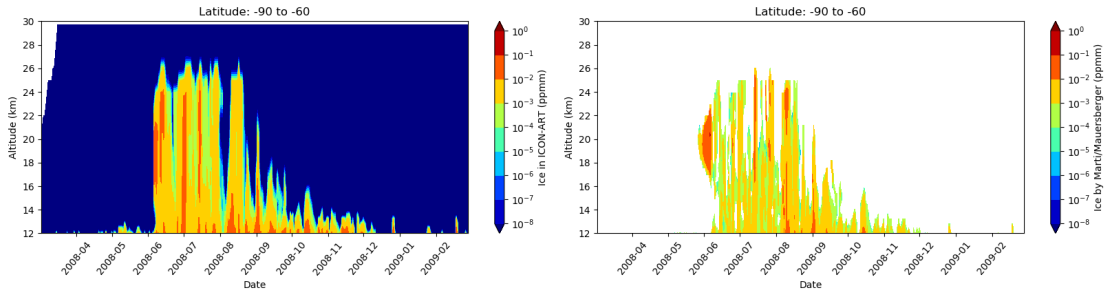

(a) Ice in ICON-ART (b) Ice due to Marti and Mauersberger (1993)

Figure 5.10: Ice mass mixing ratio with h_{top} = 30 km in (a) ICON-ART and (b) parametrisation of Eq. (3.6). The mass mixing ratio is averaged in southern high latitudes (90°S to 60°S). The parametrisation by Marti and Mauersberger (1993) produces zeros when temperatures are too high for ice formation, thus leading to white space in panel (b). Results of the first year in the time slice experiment are shown.

(1993) is a diagnostic parametrisation, no sedimentation is included whereas in the microphysics of ICON-ART ice particles sediment and irreversibly remove water vapour from the altitudes where ice forms. This explains the initial values up to 0.1 ppmm in the parametrisation of Marti and Mauersberger (1993), see Fig. 5.10(b). In addition, the parametrisation of the microphysics includes more processes for the transformation of ice particles which explains the differences.

Since the absolute values are in the same order of magnitude and the dates when ice forms agree between the two parametrisations, ice formation can be used from the microphysics of ICON-ART also for the stratosphere. With this, ice is consistently calculated in the whole atmosphere. In addition, the integration of the diagnostic parametrisation by Marti and Mauersberger (1993) would lead to technical problems with respect to its connection to the other hydrometeors in the model.

Influence on Convection in the Model

Changing h_{top} could additionally influence especially convection in the model which could then also be computed up to this altitude. To investigate the influence on convection in the model the convective tendencies of the hydrometeors are analysed along with the thermal tropopause altitude (WMO, 1957). Figure 5.11 shows the global maximum altitude up to which the convective tendencies of water vapour, cloud water and cloud ice are non-zero for the first year of the time slice experiment using h_{top} = 22.5 km. The tropopause height is displayed at the grid point where the maximum altitude of non-zero cloud ice tendency occurs.

The tendency of cloud water becomes zero in a maximum altitude of about 11 km which is about 5 km below the tropopause height. The altitudes of water vapour and cloud ice tendencies coincide with each other and are closely connected to the tropopause height at this grid point. The tendencies of water vapour and cloud ice are about 2 km higher than the thermal tropopause altitude because of the overshooting of the tropopause in tropical storms. In the maximum, these tendencies do not overshoot above 19 km which demonstrates that the cut-off of the hydrometeor convective tendencies is at least by 3.5 km lower than h_{top} (black line). A similar behaviour can be seen for h_{top} = 30 km (not shown). Thus, convection is not affected by the value of h_{top} as long as h_{top} is not decreased below 19 km.

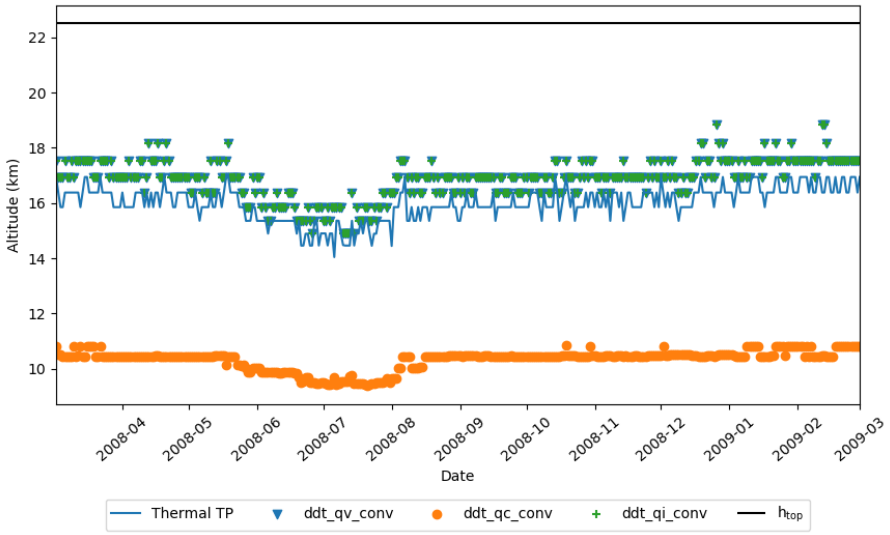

Figure 5.11: Maximum altitude of non-zero convective tendency for water vapour, cloud water and cloud ice. The convective tendencies are denoted by ddt_qv_conv for water vapour, ddt_qc_conv for cloud water and ddt_qi_conv for cloud ice. The thermal tropopause height is shown as blue line at the respective grid point where the maximum altiude for cloud ice occurs. The h_{top} altitude is shown as black line for a value of 22 500 m.

Conclusion

Altogether, it was shown in this section that

(1) the influence on the dynamics is negligible when h_{top} is increased to 30 km. Trends in the order of $-0.03\,\mathrm{K\,yr^{-1}}$ could be decreased to close to zero by increasing h_{top}.

(2) the parametrisations of Marti and Mauersberger (1993) and Doms et al. (2011) lead to similar results although they parametrise ice clouds differently

(3) convection is not affected by the change in the top height of the NWP microphysics.

In conclusion, ice PSCs can be computed with ICON-ART in the lower stratosphere using the NWP microphysics increased up to 30 km.

5.3.2 From STS Box Model to Three-Dimensional Simulation

STS particles play a key role in the heterogeneous chemistry since the major part of chlorine activation can be explained by heterogeneous reactions on STS particles (e.g., Wohltmann et al., 2013). In Figure 3.12, it was shown that the STS module in ICON-ART compares well with the original publication by Carslaw et al. (1994). Here, it is analysed if these box model results can also be found in the three-dimensional simulations in ICON-ART. For this, the base run of the ensemble simulation is used. It is rather unlikely that the exact input value tuples of $(T, p, H_2O, HNO_3, H_2SO_4)$ can be found in the model. This is why the input variables for the box model are slightly adapted in this section: $p = 55\,\mathrm{hPa}$, $X_{H_2O} = 4.7\,\mathrm{ppmv}$, $X_{HNO_3} = 7\,\mathrm{ppbv}$ and $X_{H_2SO_4} = 250\,\mathrm{pptv}$, see Fig. 5.12. The ICON-ART output is selected within the ranges of:

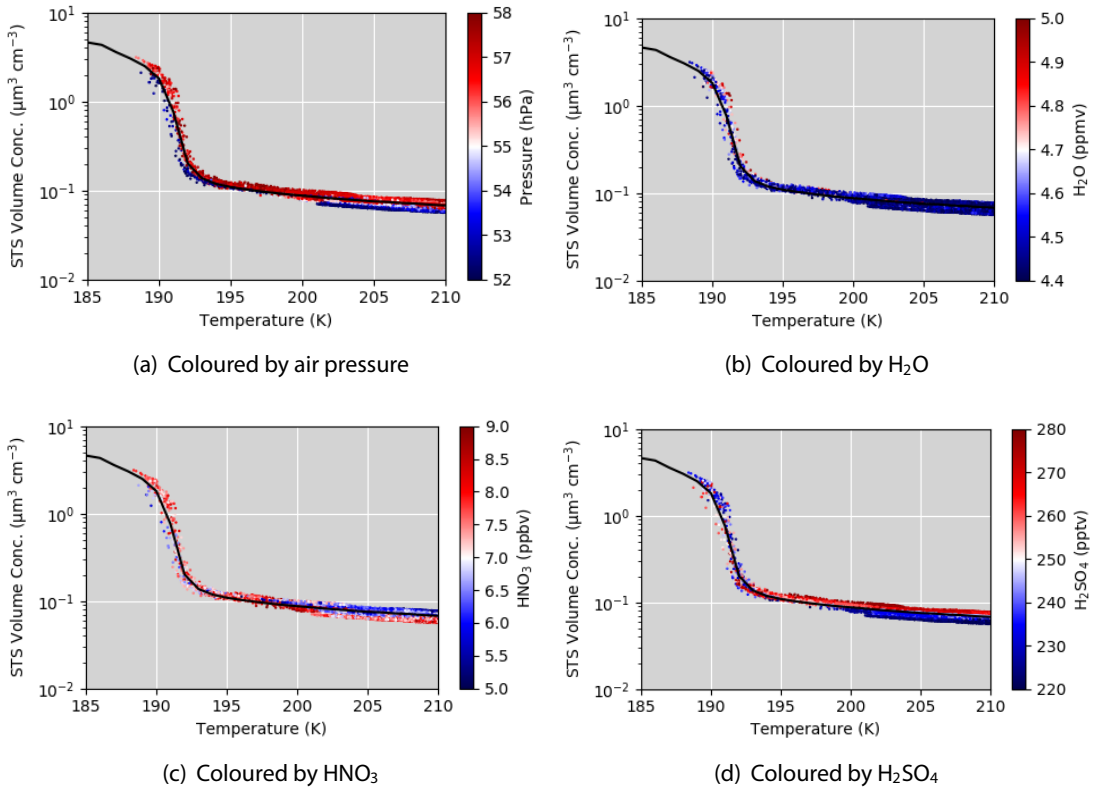

(a) Coloured by air pressure

(b) Coloured by H_2O

(c) Coloured by HNO_3

(d) Coloured by H_2SO_4

Figure 5.12: Comparison of STS box model with three-dimensional simulation in ICON-ART. Input parameters for the box model (black line) are: p = 55 hPa, H_2O = 4.7 ppmv, HNO_3 = 7 ppbv and H_2SO_4 = 250 pptv. The different ICON-ART input variables for STS in the model are colour-coded with (a) air pressure, (b) H_2O, (c) HNO_3 and (d) H_2SO_4 by values symmetrically around the box model values. White points correspond to the box model values. The ensemble base run is chosen and only value tuples within the ranges of the colour bars are shown.

$$T \in [185\,\mathrm{K}, 210\,\mathrm{K}] \tag{5.1}$$

$$p \in [52\,\mathrm{hPa}, 58\,\mathrm{hPa}] \tag{5.2}$$

$$X_{\mathrm{H_2O}} \in [4.4\,\mathrm{ppmv}, 5\,\mathrm{ppmv}] \tag{5.3}$$

$$X_{\mathrm{HNO_3}} \in [5\,\mathrm{ppbv}, 9\,\mathrm{ppbv}] \tag{5.4}$$

$$X_{\mathrm{H_2SO_4}} \in [220\,\mathrm{pptv}, 280\,\mathrm{pptv}] \tag{5.5}$$

In Figure 5.12, the box model result is depicted as black line whereas the model output of the ensemble base run simulation is colour-coded by the different input variables. White points in the figures correspond to the values of the box model. Figure 5.12(a) demonstrates the pressure dependence of the STS module. The black line separates the red from the blue points in the whole temperature range, so that lower (higher) pressure values also lead to a decreased (increased) STS volume concentration compared to the box model case.

The figure with H_2O colour-coded has to be separated into two regions, see Fig. 5.12(b): For binary solution droplets, i.e. for temperatures larger than 195 K, the STS volume concentration does not

depend on the H_2O volume mixing ratio. The H_2O mixing ratios are lower than the box model value regardless if the STS volume concentration is higher or lower than the box model's one. On the other hand, for the tenary solution droplet at temperatures lower than 195 K, mixing ratios higher than in the box model occur that also lead to an increased STS volume concentration.

This separation can also be seen in the other two panels for colour-coded HNO_3, Fig. 5.12(c), and H_2SO_4, Fig. 5.12(d). The binary sulphate aerosol droplets mainly consist of H_2SO_4 and water so that the aerosol volume concentration does not depend on the HNO_3 volume mixing ratio. In this case, mixing ratios of HNO_3 nearly equal to the box model values as well as lower and higher ones can be found above and below the black box model line. On the other hand, the binary aerosol volume concentration in Fig. 5.12(d) with colour-coded H_2SO_4 is separated by the black line with higher (lower) particle volume concentration for higher (lower) H_2SO_4 volume mixing ratio for temperatures larger than 195 K.

In contrast to this, the ternary solution particle volume concentration for temperatures lower than 195 K is dominated by the HNO_3 volume mixing ratio. At these temperatures, the binary solution droplets begin to absorb HNO_3 (Carslaw et al., 1995b) which is reflected in Fig. 5.12(c) where the black line again separates the HNO_3 volume mixing ratios that are beyond the box model ones'. Sulphuric acid, on the other hand, is less important for the STS volume concentration at these temperatures.

Altogether and in combination with the discussion of Fig. 3.12, this demonstrates that STS particles are not only formed in a physically consistent way in the box model but also in the three-dimensional ICON-ART model: binary solution droplets are dominated by the content of H_2SO_4 whereas ternary solution droplets are dominated by the absorption of HNO_3.

5.3.3 Comparison of Thermodynamic and Kinetic NAT Parametrisations

As mentioned in the previous section, STS particles are important for the heterogeneous chemistry, i.e. for chlorine activation. On the other hand, NAT particles denitrify the stratosphere by sedimentation which prolongs the ozone depletion. Both NAT and STS compete against the amount of gaseous HNO_3 in the stratosphere which is investigated in this section by comparing the thermodynamic and kinetic NAT parametrisations in this respect.

For this, the first year of the time slice simulation is used together with the simulation using the kinetic NAT parametrisation instead of the thermodynamic NAT parametrisation. The results are shown in Fig. 5.13 for the southern hemispheric high latitudes from 75°S to 90°S and within the altitude range from 15 to 20 km.

As soon as the temperature decreases below the typical NAT formation temperature threshold of 195 K in the mid of May (upper panel), NAT is formed by the thermodynamic parametrisation with average particle volume concentrations of more than 0.4 $\mu m^3\ cm^{-3}$ (third panel). In these simulations, HNO_3 is treated as passive tracer so that it is only transported but does not experience chemical reactions. Since NAT PSCs are also formed at higher altitudes, HNO_3 is sedimented from these altitudes into the depicted volume which enhances the HNO_3 volume mixing ratio from initially 7 to up to 14 ppbv in the maximum (lowermost panel). In the following month, the maximum HNO_3 volume mixing ratio decreases to values around 1 ppbv due to the sedimentation of NAT particles. Thus, on the one hand, this demonstrates that denitrification is included in the

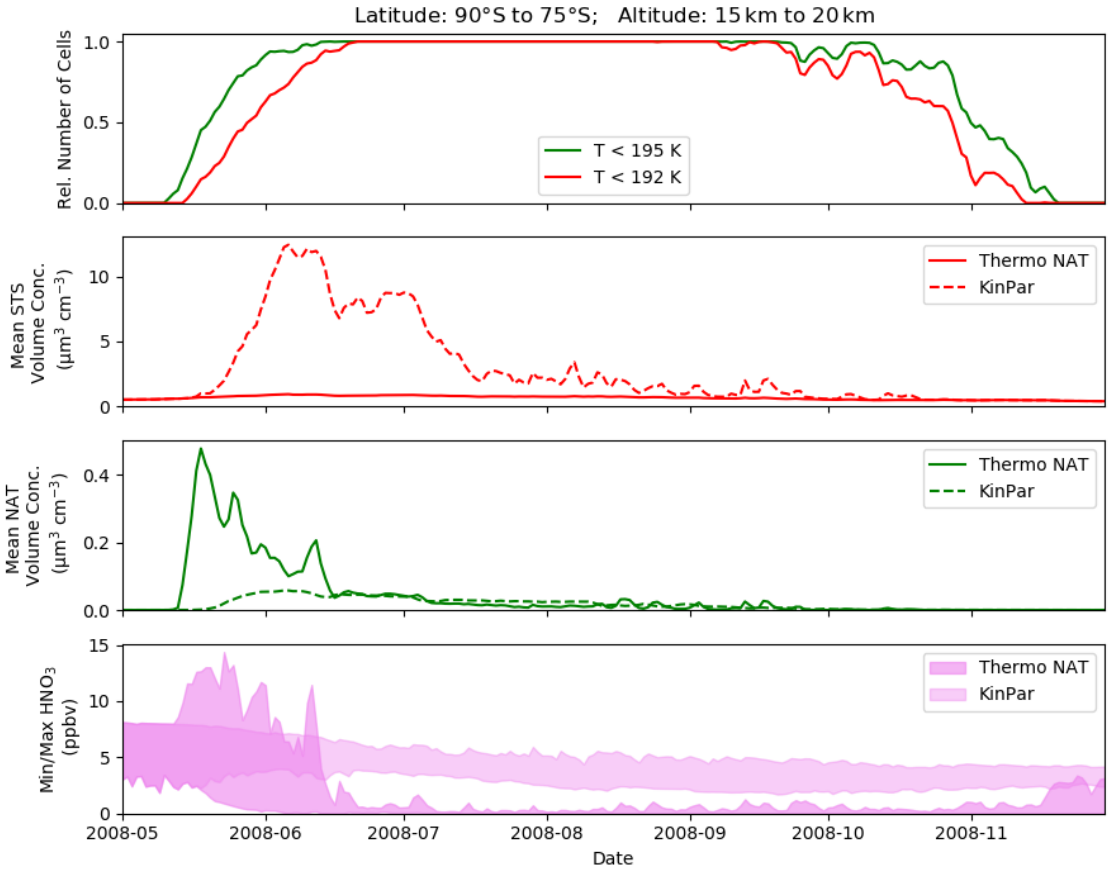

Figure 5.13: Comparison of thermodynamic and kinetic NAT parametrisations. Results of the first year of the time slice simulation (Thermo NAT in the figure) and the KinPar simulation are shown. The time series are calculated for the latitude region from 75°S to 90°S and within the altitude range from 15 to 20 km. The uppermost panel shows the relative number of cells that are below the typical STS and NAT formation temperature thresholds 192 and 195 K. The two middle panels show the average STS and NAT volume concentrations, respectively. The lowermost panel depicts the minimum and maximum HNO_3 volume mixing ratio.

case of the thermodynamic NAT parametrisation. On the other hand, no ternary solution droplets can form due to the denitrification and the lower temperatures that are needed for the formation of STS particles. However, the formation of STS particles has been observed in the stratosphere (e.g., Dye et al., 1992). Thus, the NAT particles most probably are too large which leads to an overestimation of the sedimentation velocities of NAT particles using the thermodynamic NAT parametrisation.

In case of the kinetic instead of the thermodynamic NAT parametrisation, STS particles can form with an average particle volume concentration up to 12 $\mu m^3\ cm^{-3}$ at the beginning of June. The formation of NAT with the kinetic approach starts later than in the thermodynamic NAT parametrisation and the particle volume concentration increases to values around 0.05 $\mu m^3\ cm^{-3}$, i.e. by a factor of 8 smaller than in the thermodynamic NAT parametrisation. Correspondingly, the denitrification is weaker for the kinetic NAT parametrisation because of the smaller particles. The general lower particle volume concentration of NAT compared to STS has already been simulated

in previous studies with other models (e.g., Khosrawi et al., 2018).

Because both STS and NAT particles can be simulated simultaneously by using the kinetic NAT parametrisation, this parametrisation is used for the simulations using stratospheric gas phase chemistry. These simulations are used for the comparison with satellites at the end of this chapter. The kinetic NAT parametrisation is further investigated in the next sections where its dependency on the number of size bins and the radius dependency of the growth factor are examined.

5.3.4 Dependency of the Kinetic NAT Parametrisation on the Number of Size Bins

The kinetic NAT parametrisation is a non-equilibrium approach where particles grow according to microphysical properties of the particles as well as atmospheric conditions (van den Broek et al., 2004). Since every single particle grows independently the method by van den Broek et al. (2004) could depend on the number of size bins that are specified by the user. If more size bins are (partly) filled with particles, they also could grow faster than with fewer number of size bins.

To evaluate this, the same experiment has to be conducted with larger number of size bins. Therefore, the question is how the maximum particle number concentration of each new size bin has to be chosen so that the experiment is the same as for fewer number of size bins. In the first part of this section, a system of five variables is derived for splitting one size bin into two. The respective notations are summarised in Fig. 5.14.

When splitting a size bin into two, the number of molecules must not be changed, i.e. the total mass of NAT has to be conserved. The particle mass per volume can be described by the particle number concentration multiplied by the mass of one particle which can be expressed by the NAT density and the particle volume:

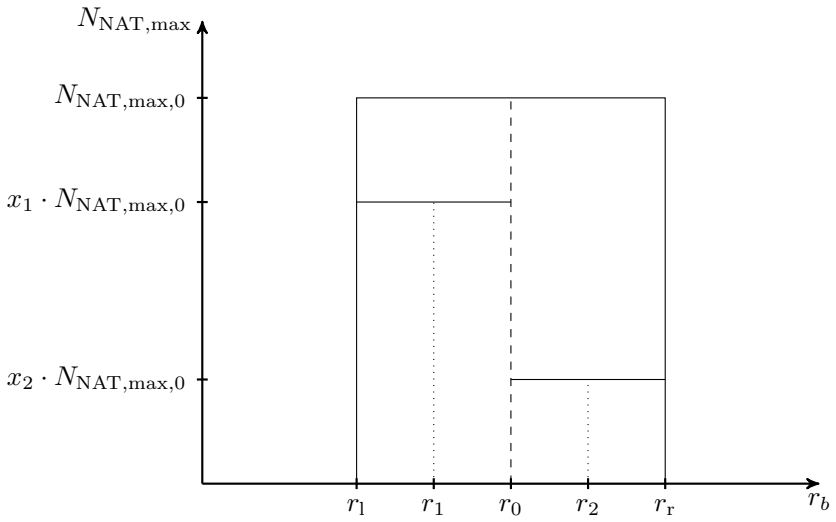

Figure 5.14: Definition of the maximum particle number concentration and radii when splitting a size bin into two. r_l and r_r mark the boundary radii of the broader size bin with average radius r_0. The average radii of the new thinner size bins are denoted by r_1 and r_2. x_1 and x_2 are the fractions of the new maximum particle number concentration compared to that of the broader size bin.

$$W_0 = n_{\max,0}\, m_{\mathrm{NAT}} = N_{\mathrm{NAT},\max,0}\, \rho_{\mathrm{NAT}}\, \frac{4}{3}\pi r_0^3 \tag{5.6}$$

The sum of the particle mass concentration of both size bins has to be conserved which leads to the following equation:

$$W_1 + W_2 = W_0 \tag{5.7}$$

$$\Longleftrightarrow N_{\mathrm{NAT},\max,1}\, r_1^3 + N_{\mathrm{NAT},\max,2}\, r_2^3 = N_{\mathrm{NAT},\max,0}\, r_0^3 \tag{5.8}$$

$$\Longleftrightarrow x_1\, r_1^3 + x_2\, r_2^3 = r_0^3 \tag{5.9}$$

The following expressions hold for the radii of the broader and splitted size bins:

$$r_0 = \frac{1}{2}(r_\mathrm{l} + r_\mathrm{r}) \tag{5.10}$$

$$r_1 = \frac{1}{2}(r_\mathrm{l} + r_0) \tag{5.11}$$

$$r_2 = \frac{1}{2}(r_0 + r_\mathrm{r}) \tag{5.12}$$

With Equations (5.10), (5.11) and (5.12) all radii can be described by the boundaries of the original size bin r_l and r_r:

$$r_1 = \frac{3}{4}r_\mathrm{l} + \frac{1}{4}r_\mathrm{r} \tag{5.13}$$

$$r_2 = \frac{1}{4}r_\mathrm{l} + \frac{3}{4}r_\mathrm{r} \tag{5.14}$$

After including the radii in Eq. (5.9), there is still a degree of freedom how to calculate the maximum particle number concentration for the new bins. There are two possible scenarios that are considered in this section: either the number of particles within the size bin could be conserved, too, or the number concentrations of the new size bins could be equal. Both approaches will be discussed in the following.

Conserved Maximum Particle Number Concentrations

In the original size distribution (blue in Fig. 5.15) the maximum particle number concentrations of each bin are fixed. Therefore, it seems reasonable to close the system by assuming the sum of the new bins to equal the original one:

$$x_1 + x_2 = 1 \tag{5.15}$$

Inserting x_1 of Eq. (5.15) and the equations for the radii in Eq. (5.9) yields:

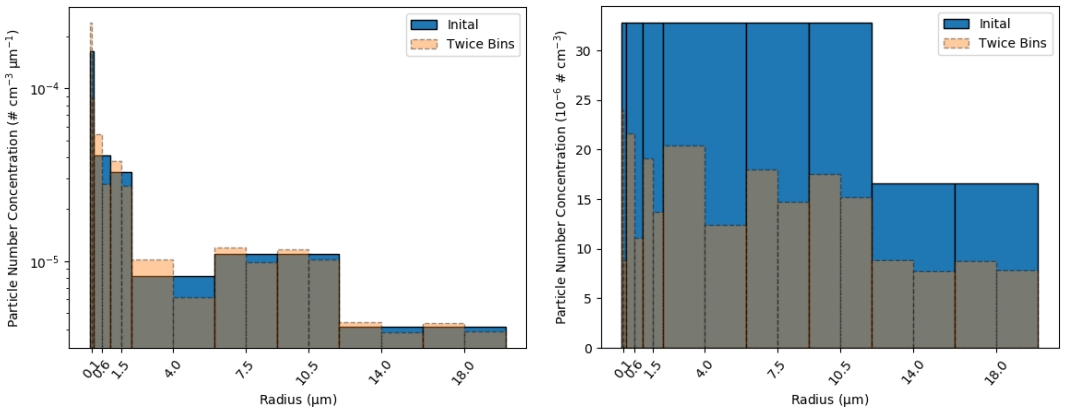

(a) normalised size distribution (b) non-normalised size distribution

Figure 5.15: Same figure as Fig. 4.1 but including a second size distribution with double number of size bins conserving the maximum particle number concentrations. The second size distribution is transparently overlaid on top of the original size distribution and merges to brown colours between 0 and the minimum of both values.

$$x_2 = \frac{8(r_\mathrm{l} + r_\mathrm{r})^3 - (3r_\mathrm{l} + r_\mathrm{r})^3}{(r_\mathrm{l} + 3r_\mathrm{r})^3 - (3r_\mathrm{l} + r_\mathrm{r})^3} \tag{5.16}$$

$$x_1 = 1 - x_2 \tag{5.17}$$

The resulting size distribution can be found in Fig. 5.15 in two different ways: the size distribution normalised by the width of the size bin and not normalised. In case of the not normalised distribution, the new maximum number concentrations (orange, dashed) are around half of the original maximum particle number concentration. For the normalised size distributions, the new ones vary around the original maximum particle number concentrations. In addition, the particle number concentration of the new bins with smaller radii generally have a higher maximum particle number concentration than the larger ones.

Equal Maximum Particle Number Concentrations

Another possibility to ensure the experiment as equal as possible to the original one could be to equal x_1 and x_2:

$$x_1 = x_2 \tag{5.18}$$

Inserting this equation into Eq. (5.9) results in a different equation for both particle number concentrations:

$$x_1 = x_2 = \frac{8(r_\mathrm{l} + r_\mathrm{r})^3}{(r_\mathrm{l} + 3r_\mathrm{r})^3 + (3r_\mathrm{l} + r_\mathrm{r})^3} \tag{5.19}$$

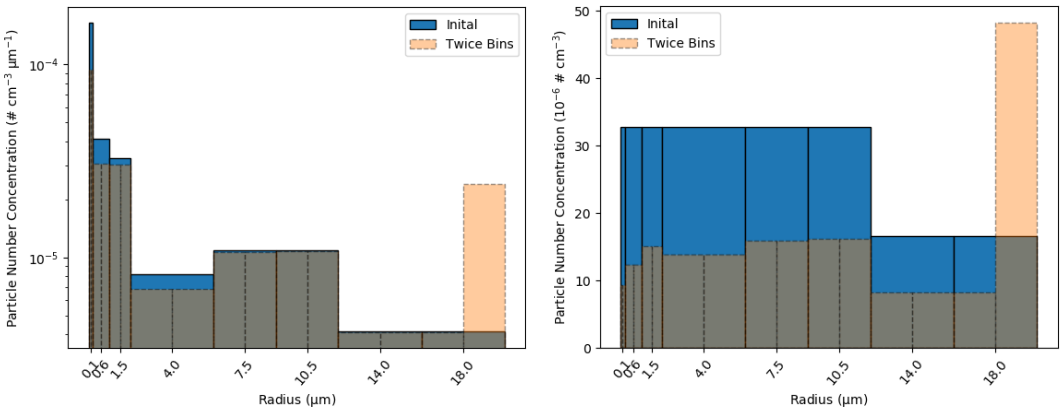

(a) normalised size distribution (b) non-normalised size distribution

Figure 5.16: Same as Fig. 5.15 but by assuming equal maximum particle number concentration. The higher value in the largest size bin is a result of satisfying the condition in Eq. (3.26) because the number concentrations are explicitly not conserved in this case.

As can be seen in Fig. 5.16(a), this approach improves the conservation of normalised maximum particle number concentration for larger size bins. However, the number concentrations for size bins with radius smaller than 7.5 µm are underestimated.

With Fig. 5.16(b), the intention of this approach gets clear: The new maximum number concentrations are close to half of the original ones for the large size bins so that this could be a good estimate of the original experiment.

Sensitivity Simulation

In order to evaluate the sensitivity to the number of size bins three ICON-ART simulations are conducted using the three NAT size distributions mentioned above: the original (blue in Fig. 5.15), conserved maximum number concentrations (orange in Fig. 5.15) and equal maximum number concentrations (orange in Fig. 5.16). The resulting global HNO_3 moles in NAT can be found in Fig. 5.17. In the simulations, the initial gaseous HNO_3 is set to the global value of 1 ppbv to ensure a wide-spread supersaturation of HNO_3 with respect to NAT. The dynamical variables are initialised with the IFS analysis on 15 June 2008 where temperatures in the polar vortex already are low enough for NAT formation.

As can be seen in Fig. 5.17, the number of moles of HNO_3 in NAT differs between the experiments at the beginning of the simulation. With the original distribution, it is twice as large as for the experiment with double number of size bins and equal maximum number concentrations and it is four times larger than in the experiment with conserving maximum number concentrations. This is a result of slower initial growth of NAT particles if the smallest size bin is splitted into two. The size bin with smallest radius has to be filled before larger particles can be formed. Since the smallest size bin in the original size distribution is twice as wide as in the other two cases the initial growth of NAT particles is faster.

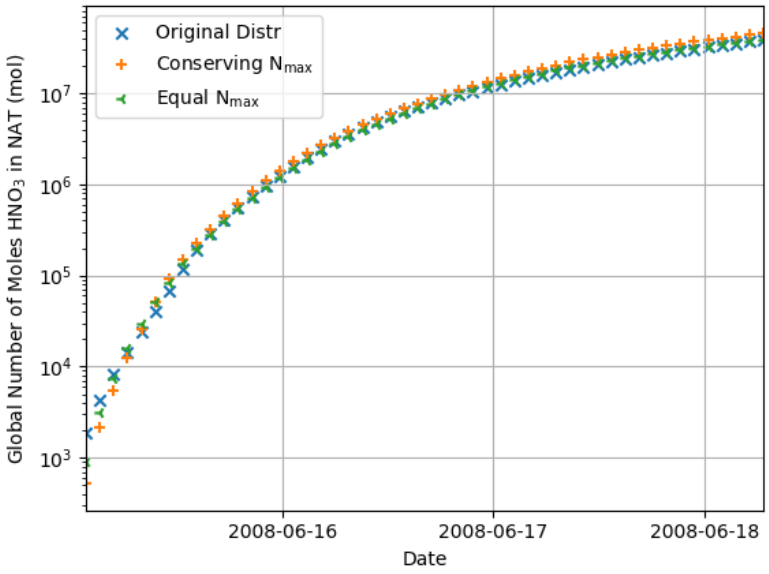

Figure 5.17: Global number of moles of HNO_3 in NAT for different size distributions. The size distributions are shown in Figs. 5.15 and 5.16

These differences decrease within the first day of the simulation and get negligible after this. Thus, it can be stated that for NAT particles existing for more than one day the method to derive NAT particles with the kinetic approach is insensitive to the number of size bins.

5.3.5 Impact of Radius Dependence in the Growth Factor

The particle growth according to Eq. (3.22) is integrated by assuming a growth factor that does not depend on the radius (Carslaw et al., 2002). However, Equation (3.27) indicates that the growth factor by itself depends on the radius. The differential equation (3.22) which does not neglect the radius dependence of the growth factor is:

$$\frac{\mathrm{d}r_b}{\mathrm{d}t} = \frac{G_b(r_b)}{r_b} \tag{5.20}$$

$$= \frac{d^*_{\mathrm{HNO_3}}(r_b)}{r_b} \frac{M_{\mathrm{HNO_3}}}{\rho_{\mathrm{NAT}} R^* T} \left(p_{\mathrm{HNO_3}} - p_{\mathrm{sat,NAT}}\right) \tag{5.21}$$

$$= \frac{1}{r_b + \frac{4 d_{\mathrm{HNO_3}}}{\bar{\nu}_{\mathrm{HNO_3}}}} x \tag{5.22}$$

with x as the part that does not depend on the radius:

$$x = \frac{d_{\mathrm{HNO_3}} M_{\mathrm{HNO_3}}}{\rho_{\mathrm{NAT}} R^* T} \left(p_{\mathrm{HNO_3}} - p_{\mathrm{sat,NAT}}\right) \tag{5.23}$$

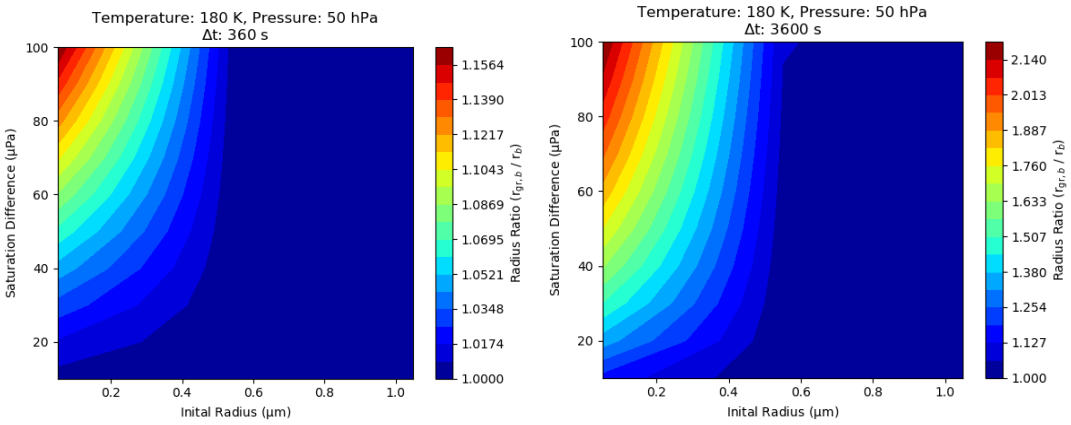

(a) Δt = 360 s (b) Δt = 3600 s

Figure 5.18: Impact on using corrected equation for growth factor in kinetic NAT parametrisation. The ratio between $r_{gr,b}$ and r_b at $t + \Delta t$ is shown for fixed temperature T = 180 K and pressure p = 50 hPa and for Δt of (a) 360 s and (b) 3600 s. Please note the different colour bars of the two figures.

Separating the variables in Eq. (5.22) yields:

$$\int_{r_b}^{r_{gr,b}} \left(r + \frac{4 d_{HNO_3}}{\overline{\nu}_{HNO_3}} \right) \mathrm{d}r = \int_0^{\Delta t} x \, \mathrm{d}t \tag{5.24}$$

Assuming only the radius to be time dependent, the integration then leads to a quadratic equation for the radius after growth of the particle $r_{gr,b}$. The solution (neglecting the negative one) is then:

$$r_{gr,b} = -\frac{4 d_{HNO_3}}{\overline{\nu}_{HNO_3}} + \sqrt{\left(\frac{4 d_{HNO_3}}{\overline{\nu}_{HNO_3}} + r_b \right)^2 + 2x\Delta t} \tag{5.25}$$

Like in Equation (3.25), the radius according to Eq. (5.25) increases in case of supersaturation and decreases in case of undersaturation. In both equations, the radius essentially depends on five parameters: temperature T, pressure p, saturation difference $\Delta p_{sat} = p_{HNO_3} - p_{sat,NAT}$, time step Δt and initial radius r_b. The saturation difference is set in the order of 10^{-5} Pa based on ICON-ART simulations and due to the lack of literature values.

The influence on using Eq. (5.25) is tested by varying the parameters within the following intervals:

$$T \in [171\,\mathrm{K}, 195\,\mathrm{K}] \tag{5.26}$$
$$p \in [10\,\mathrm{hPa}, 210\,\mathrm{hPa}] \tag{5.27}$$
$$\Delta p_{sat} \in [10^{-5}\,\mathrm{Pa}, 10^{-4}\,\mathrm{Pa}] \tag{5.28}$$
$$r_b \in [0.05\,\mu\mathrm{m}, 1.1\,\mu\mathrm{m}] \tag{5.29}$$
$$\Delta t = 360\,\mathrm{s} \text{ or } 3600\,\mathrm{s} \tag{5.30}$$

Figure 5.18 shows the ratio between $r_{\mathrm{gr},b}$ of Eq. (5.25) and the originally grown radius by Eq. (3.25) for fixed temperature and pressure values and two different time steps of 360 s and 3600 s. Using Eq. (5.25) generally yields larger particles than Eq. (3.25) since 1 is the lower limit in the figures. The relative difference between the radii is larger than 1 % for radii lower than 0.5 µm. For saturation differences higher than 9×10^{-5} Pa, the particles can grow to sizes up to 15 % larger than in the original case. In contrast to this, the difference between the two growth mechanisms is negligible for particles with an initial radius larger than 0.5 µm. In this case, the radius ratio decreases to values lower than 1 ‰.

5.4 Denitrification and Renitrification in the Model

In order to quantify the denitrification of a PSC scheme, Waibel et al. (1999) suggested a method that is based on measurements by Loewenstein et al. (1993) and Rinsland et al. (1996). Waibel et al. (1999) combined the measurements by Loewenstein et al. (1993) and Rinsland et al. (1996) at a threshold of $X_{\mathrm{N_2O}} = 120$ ppbv. Rinsland et al. (1996) found that NO_y and $\mathrm{N_2O}$ are highly correlated without denitrification during a Space Shuttle campaign during November 1994 at the time period of the sunrise in latitudes between 64.5°S and 72.4°S. The filled black circles in Fig. 5.19(a) are measured outside the polar vortex and demonstrate the correlation between NO_y and $\mathrm{N_2O}$ in the ambient air. Within the polar vortex, the NO_y values significantly decrease below these values which is shown as open circles in Fig. 5.19(a).

In the right panel of Fig. 5.19, the corresponding ICON-ART result of the ensemble base run is

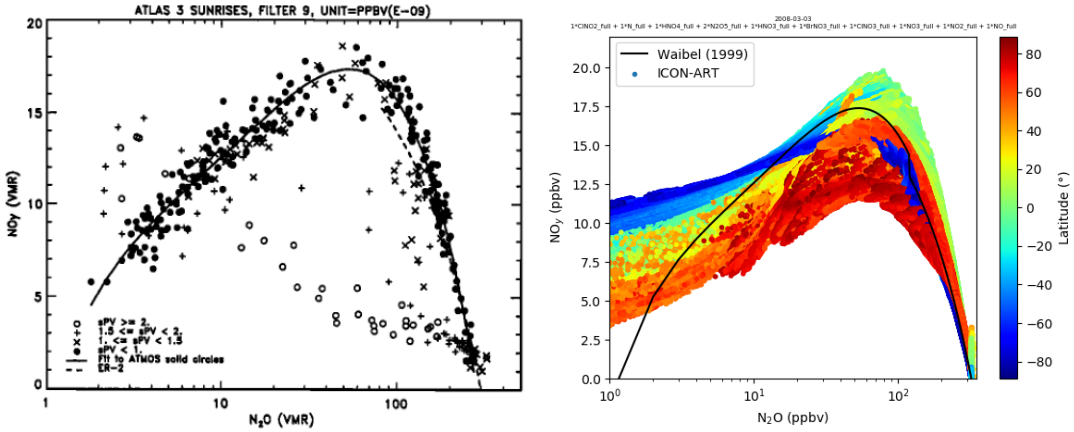

(a) Rinsland et al. (1996) (b) ICON-ART

Figure 5.19: NO_y-$\mathrm{N_2O}$ correlations (a) as originally measured and (b) as simulated in ICON-ART. For the measurements, the tracer values are given as ppbv. For ICON-ART, it is an example at 2 days after initialisation of the ensemble base run in ICON-ART. The higher NO_y values at high $\mathrm{N_2O}$ values originate from the initialisation with EMAC and its emissions at the ground, see also Table 3.2. The latitude of each grid point is colour-coded in the ICON-ART figure. The black lines show (a) the polynomial fit to the measurements in ambient air outside the polar vortex and (b) the correlation for ambient air by the method of Waibel et al. (1999) which coincides with the left panel's black line up to $X_{\mathrm{N_2O}} = 120$ ppbv. Graphic by Rinsland et al. (1996) published with permission of John Wiley & Sons.

shown with the correlation of NO_y and N_2O as suggested by Waibel et al. (1999) (black line in Fig. 5.19(b)). In addition, the values are colour-coded according to the grid point latitude: blue colours stand for high southern latitude, green coloured points are close to the Equator and red colours show high northern latitudinal grid points. The ICON-ART panel shows the NO_y-N_2O correlation at an early stage of the simulation on 03 March 2008, two days after its initialisation with EMAC. Rinsland et al. (1996) calculated NO_y as the sum of all gaseous nitrogen-containing species they could measure apart from N_2 and N_2O. In accordance to this, NO_y in ICON-ART is calculated as the nitrogen-weighted sum of all gaseous nitrogen-containing species apart from N_2 and N_2O:

$$X_{NO_y} = X_{ClNO_2} + X_N + X_{HNO_4} + 2X_{N_2O_5} + X_{HNO_3} + X_{BrONO_2} + X_{ClONO_2} + X_{NO_3} + X_{NO_2} + X_{NO} \quad (5.31)$$

At this early stage of the simulation, no polar vortex appears in the simulation neither in the northern nor in the southern hemisphere. Therefore, the conditions outside the polar vortex can be applied globally and all simulated NO_y-N_2O values are close to the measured correlation.

In accordance to this, the general shape of the measurements can be reproduced in all grid points of the ICON-ART simulation (Fig. 5.19(b)). A maximum occurs at each latitude around X_{N_2O} = 80 ppbv which was also measured by Rinsland et al. (1996) around the southern polar vortex. The NO_y values are generally lower on the northern hemisphere than on the southern hemisphere at the corresponding N_2O values. Best agreement with the measurements can be found at N_2O values higher than 200 ppbv where the difference between measurements and simulated values is smaller than 5 %.

On the other hand, the simulation differs in slope and offset to the measurements for N_2O values lower than 10 ppbv. All grid points in this sector overshoot the measured values. One possible reason for this is that Rinsland et al. (1996) only measured NO_y-N_2O pairs for values of $X_{N_2O} > 3$ ppbv, see Fig. 5.19(a). Thus, the black line in Fig. 5.19(b) at lower N_2O values is an extrapolation of the measurements and not necessarily realistic. In addition, the measurements rely on one Space Shuttle campaign and might be only representative for the polar vortex conditions during November 1994 (Rinsland et al., 1996).

In the same way as Fig. 5.19(b), the NO_y-N_2O correlation is evaluated for each month of the simulation as snapshots, see Fig. 5.20. The panels show the total number of grid points with their NO_y and N_2O values, colour-coded by the latitude. As indicated by the open circles of Fig. 5.19(a), a measure for denitrification are values that are significantly lower than the line of air outside the polar vortex.

During the first two months, i.e. during March and April 2008, no NAT particles are formed so that the general shape does not vary significantly from the beginning of the simulation. Some lower values at high northern latitudes (red colours) could indicate local NAT particles around the North Pole leading to denitrification in the high northern latitudes.

As already shown in Fig. 5.1, the southern polar vortex starts to develop in the simulation in June. This is reflected in Fig. 5.20 where NAT particles begin to form in the low temperatures within the southern polar vortex in June 2008 (Fig. 5.20(d)). This is demonstrated by the blue coloured points in June 2008 that differ from the black measured line. In July, the starting denitrification is extended with NO_y values down to 6 ppbv. This accumulates during the following months until

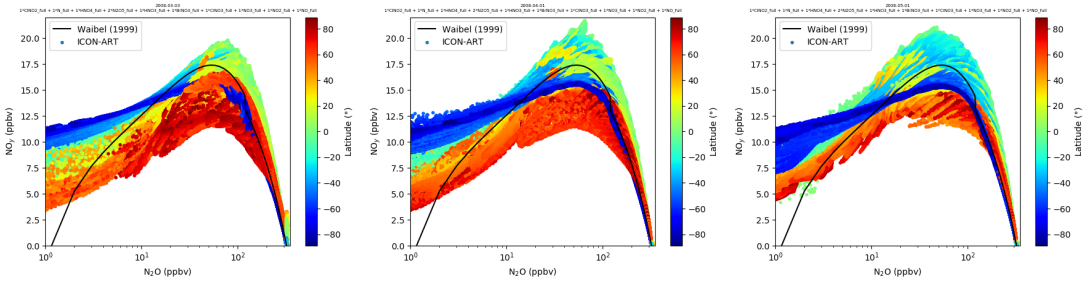

(a) 03 March 2008 (b) 01 April 2008 (c) 01 May 2008

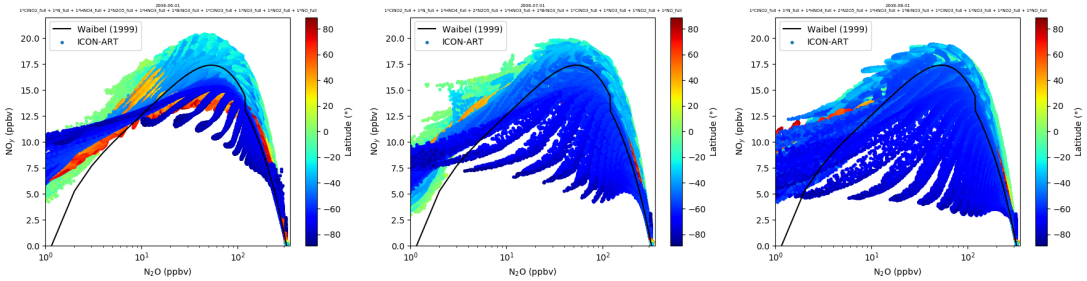

(d) 01 June 2008 (e) 01 July 2008 (f) 01 August 2008

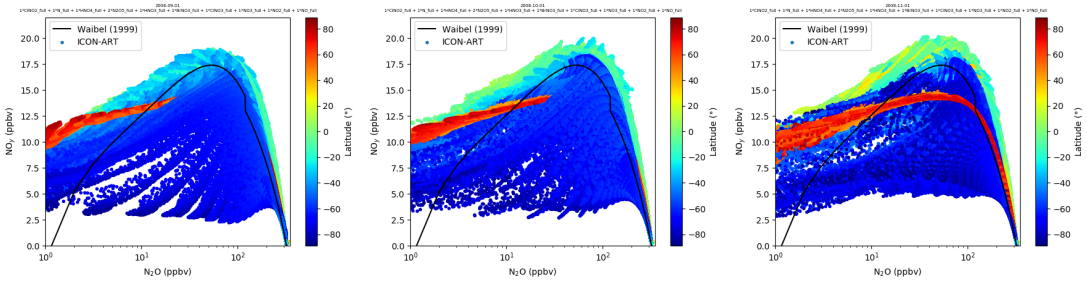

(g) 01 September 2008 (h) 01 October 2008 (i) 01 November 2008

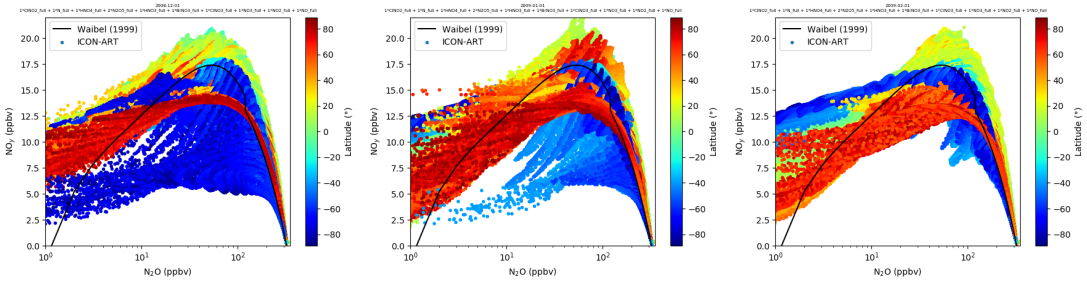

(j) 01 December 2008 (k) 01 January 2009 (l) 01 February 2009

Figure 5.20: Monthly snapshots of NO_y-N_2O correlations. Results of the ensemble base run are shown. The latitude of each grid point is colour-coded in the figures.

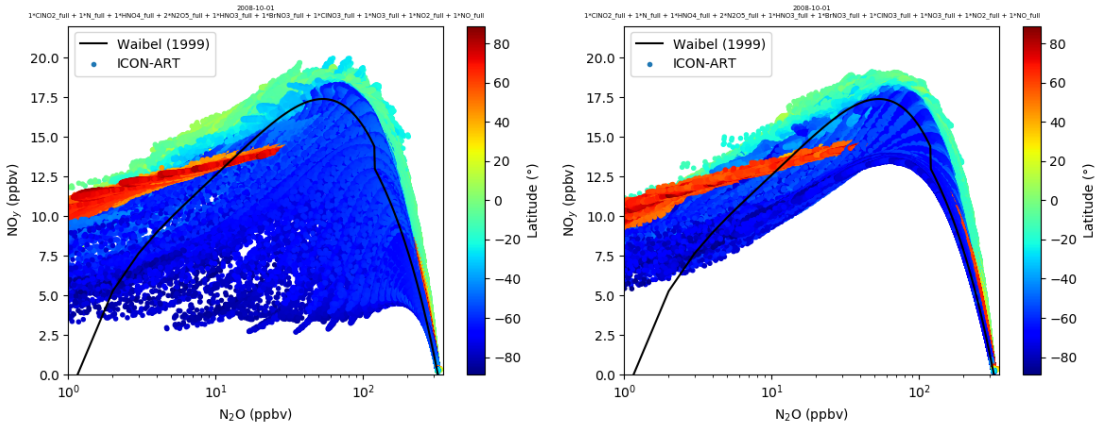

Figure 5.21: Comparison of denitrification between simulations with and without PSCs. Panel (a) is the same as Fig. 5.20(h), i.e. for 01 October 2008, panel (b) is the figure for the same date but for the simulation without PSCs.

the peak of denitrification is reached during September to November where also the polar vortex is at the maximum of extent. At this stage, the NO_y values decrease to 3 ppbv which coincides with the original measurements by Rinsland et al. (1996) of Fig. 5.19(a).

After November, the area of the polar vortex decreases again and ambient warmer air is mixed into the high latitudes. Thus, the denitrified air is mixed with air that did not experience denitrification so that step by step the NO_y values increase again. During January (Fig. 5.20(k)), some remnants of the southern polar vortex can be identified for $X_{N_2O} > 20$ ppbv which vanish until February (Fig. 5.20(l)). In addition to that, January and February values of the northern hemisphere are decreased with respect to previous months which could indicate denitrification on the northern hemisphere but weaker than on the southern hemisphere.

Waibel et al. (1999) and Rinsland et al. (1996) stated that this decrease of NO_y originates from sedimenting NAT particles. This is verified by the simulations with ICON-ART. Figure 5.21 shows the N_2O-NO_y correlation plot for the ensemble base run (Fig. 5.21(a)) and for the simulation without PSCs (Fig. 5.21(b)), exemplarily for 01 October 2008 when the denitrification peaks in the model. Without PSCs, the NO_y values do not decrease to values below 5 ppbv in high latitudes which occurs in the ensemble base run within the whole range of 1 to 300 ppbv N_2O shown in the figures. Similar results can be seen during the whole year (not shown). Thus, there is evidence that the low NO_y values come from denitrification in the model.

Another feature of this analysis is the quantification of renitrification at lower altitudes. This is demonstrated as an example for June 2008 in Fig. 5.22. The volume mixing ratio of N_2O as a long-lived tropospheric source gas is an indicator for altitude: low values mean high altitudes where N_2O is photolysed and high values occur in lower altitudes in the troposphere. The feature of renitrification can be emphasised by linearising the horizontal axis in Fig. 5.20(d). At N_2O values higher than 200 ppbv the NO_y values are increased compared to the measured line for high southern latitudes (blue colours). Therefore, the denitrified air at higher altitudes (low N_2O) corresponds to renitrified air at lower altitudes.

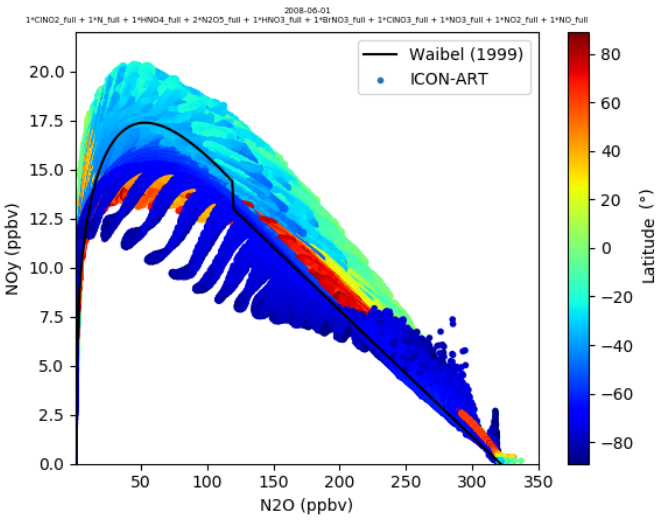

Figure 5.22: Renitrification in June 2008. This figure is the same as Fig. 5.20(d) but with linear horizontal axis.

5.5 Chlorine and Bromine Activation in the Model

Apart from denitrification, the activation of chlorine and bromine is another major effect of PSCs in the polar night. During this period, the reservoir compounds $ClONO_2$ and HCl are converted to the active species which are summarised in the ClO_x group. In this thesis, the chlorine volume mixing ratio of the ClO_x family is determined by the sum of all active chlorine compounds weighted by their content of Cl atoms:

$$X_{ClO_x} = X_{ClNO_2} + 2\,X_{Cl_2O_2} + X_{OClO} + 2\,X_{Cl_2} + X_{BrCl} + X_{HOCl} + X_{Cl} + X_{ClO} \tag{5.32}$$

In the simulations of this thesis, all species are transported separately. Time series of the reservoir species as well as of the active chlorine species can be found in Fig. 5.23. The values are averaged between 75°S and 82°S to be comparable to the comparison to the satellites in Sect. 5.7.2. As reservoir species, that can exist for a relatively long time in the atmosphere, HCl and $ClONO_2$ have the highest volume mixing ratios during the polar day. Due to the lower reactivity of HCl compared to that of $ClONO_2$ its mixing ratio is generally higher in the stratosphere than that of $ClONO_2$, see Appendix C. $ClONO_2$ is depleted by reactions with $O(^3P)$ as well as with Cl and is photolysed whereas HCl is depleted by reaction with OH, only.

During the polar night between May and October, the reservoir species are converted into the reactive ClO_x species by heterogeneous processes on the surface of PSCs by Reacts. (R2.29) to (R2.39). This is shown in the lowermost panel of Fig. 5.23 where ClO_x is enhanced during this time period.

As soon as the sun rises in the mid of September, the active species are destroyed again and are converted back into $ClONO_2$ by a larger fraction before the conditions are similar to the beginning of the simulation again after mid of October.

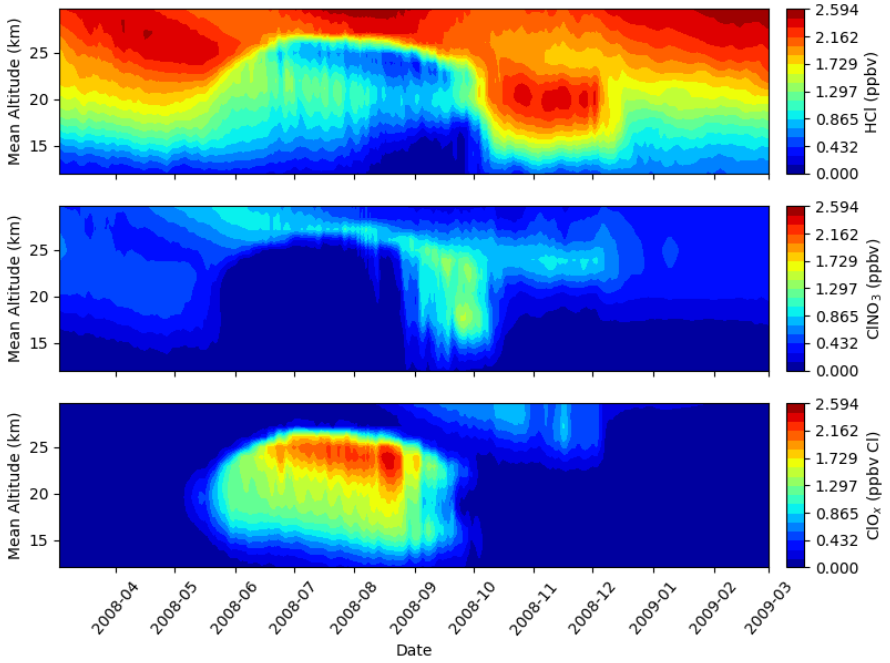

Figure 5.23: Chlorine activation in ICON-ART. Results of the ensemble base run are shown. Time series of HCl, $ClONO_2$ and ClO_x (see Eq. (5.32)) are shown. The values are averaged between 75°S and 82°S.

A similar analysis can be made with bromine species. Here, the mechanism is principally similar but the velocity of chemical reactions differs from that of the chlorine mechanism. This is why the BrO_x group volume mixing ratio is defined as follows:

$$X_{\mathrm{BrO}_x} = 2\,X_{\mathrm{Br}_2} + X_{\mathrm{BrO}} + X_{\mathrm{Br}} \tag{5.33}$$

As mentioned above, all species are transported separately neglecting their family membership. Time series of all relevant bromine species are illustrated in Fig. 5.24. The volume mixing ratio of the bromine species are by a factor of about 100 lower than that of the chlorine species above due to higher reactivity. In addition, the abundance of HBr is much less dominant than for HCl in comparison to the other species because of the higher reaction rate with OH, the main sink of HBr. During the polar day, the largest volume mixing ratio in the lower stratosphere up to 25 km is in $BrONO_2$ with values up to 17 pptv. When the sun elevation goes down (lowermost panel in Fig. 5.24) the photolysis rates decrease, PSCs form and the reaction rates of other reactions get dominant. As example, the production rate of HOBr due to React. (R2.32) is shown in the second to last panel of Fig. 5.24 which is calculated according to:

$$P_{\mathrm{het,HOBr}} = \frac{\mathrm{d}N_{\mathrm{HOBr}}}{\mathrm{d}t} = k_{\mathrm{het,(R2.32),total}}\, N_{\mathrm{BrONO_2}}\, N_{\mathrm{H_2O}} \tag{5.34}$$

The number concentrations of the compounds in this equation are given in molec cm^{-3} s^{-1}. These heterogeneous reactions lead to a decrease of $BrONO_2$ as well as BrO_x and an increase in HOBr with values up to the sum of all Br species.

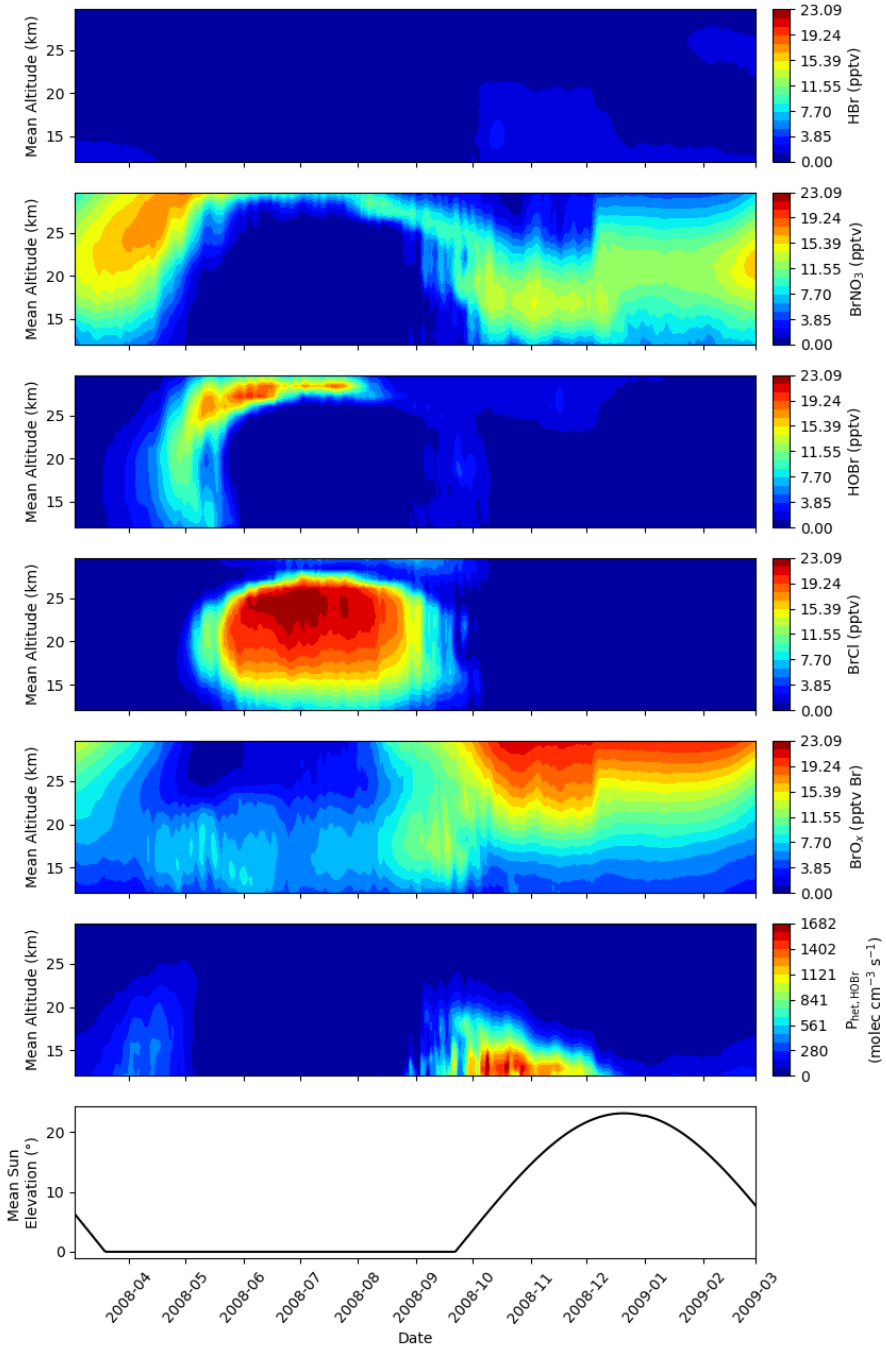

Figure 5.24: Bromine activation in ICON-ART. Results of the ensemble base run are shown. Time series of HBr, $BrONO_2$, HOBr, BrCl and BrO_x (see Eq. (5.33)) are shown, together with the heterogeneous production rate of HOBr due to React. (R2.32) (see Eq. (5.34)) and the mean solar elevation angle. The values are averaged between 75°S and 82°S.

During the polar night, HOBr is further activated on the surface of PSCs. As can be seen in the heterogeneous reactions, especially Reacts. (R2.30), (R2.33), (R2.35) and (R2.36), the product of the heterogeneous bromine chemistry is BrCl. The reaction rate of HOBr + HBr is negligible because of the low abundance of HBr. Thus, BrCl is increased up to the sum of all bromine species during the polar night. Significant fractions also remain in the other BrO_x species which are not photolysed during the night, especially at altitudes below 20 km.

As soon as the sun rises, the activated BrCl is photolysed which leads to an increase of both BrO_x and HOBr and finally of $BrONO_2$ during October and afterwards. The amount of atomic Br due to the photolysis of BrCl suffices that HBr is produced with mean values around 5 pptv. At altitudes above 25 km, BrO_x has the largest abundance due to higher photolysis rates and thus higher reactivity of $BrONO_2$.

Altogether, this section showed that chlorine and bromine activation are consistently present in the model which are closely connected to the presence of PSCs. Therefore, it was shown that the direct impact of PSCs on the chemistry is integrated in ICON-ART in a consistent way. The impact of these developments on ozone are investigated in the following section.

5.6 Comparison of Linearised Ozone and Heterogeneous Chemistry

In previous versions of ICON-ART, ozone had to be represented by a linearised scheme, which is called the LINOZ scheme (see Schröter et al., 2018). By integrating a PSC scheme in ICON-ART, all processes that are relevant for the interactive representation of ozone are now implemented in the model: emissions of trace gases such as CFCs (Weimer et al., 2017), a gas phase chemistry scheme solving the set of non-linear ordinary differential equations with a module for photolysis rates (Schröter, 2018) and the heterogeneous chemistry on the surface of PSCs. In this section, the linearised ozone scheme is compared to the interactively calculated ozone within the polar vortex as defined in Sect. 5.1.

In accordance to the explanations of the differences between kinetic and thermodynamic NAT parametrisation of Sect. 5.3.3, the development of PSCs is different in both simulations. Nevertheless, the time ranges when the PSCs exist are similar so that the two simulations are comparable in this respect.

The intrinsic problem of a diagnostic ozone parametrisation is the time shift between activation of chlorine species on PSCs and the actual ozone depletion. In ICON-ART, this is realised by assuming that the ozone depletion is connected to the occurrence of PSCs based on the temperature threshold of 195 K and a solar zenith angle lower than 92.5°, i.e. it has to be dark (Schröter et al., 2018). As soon as the temperature and solar zenith angle decrease below these thresholds ozone is depleted assuming a lifetime of 10 days.

This is shown in Fig. 5.25 for the time slice simulation where timeseries of minimum passive and LINOZ ozone volume mixing ratio in the polar vortex are depicted in the uppermost panel. The vortex is defined as horizontal region where $PV < -50$ PVU at $\theta = 475$ K. The ranges relate to the minimum and maximum values during all years of the time slice experiment. In addition, the figure shows time series of the area within the vortex with temperature lower than 195 K. The total PSC volume concentration is shown in the third panel as vortex average. The last panel shows the minimum and maximum sun elevation angle in the vortex. The same time series are shown in

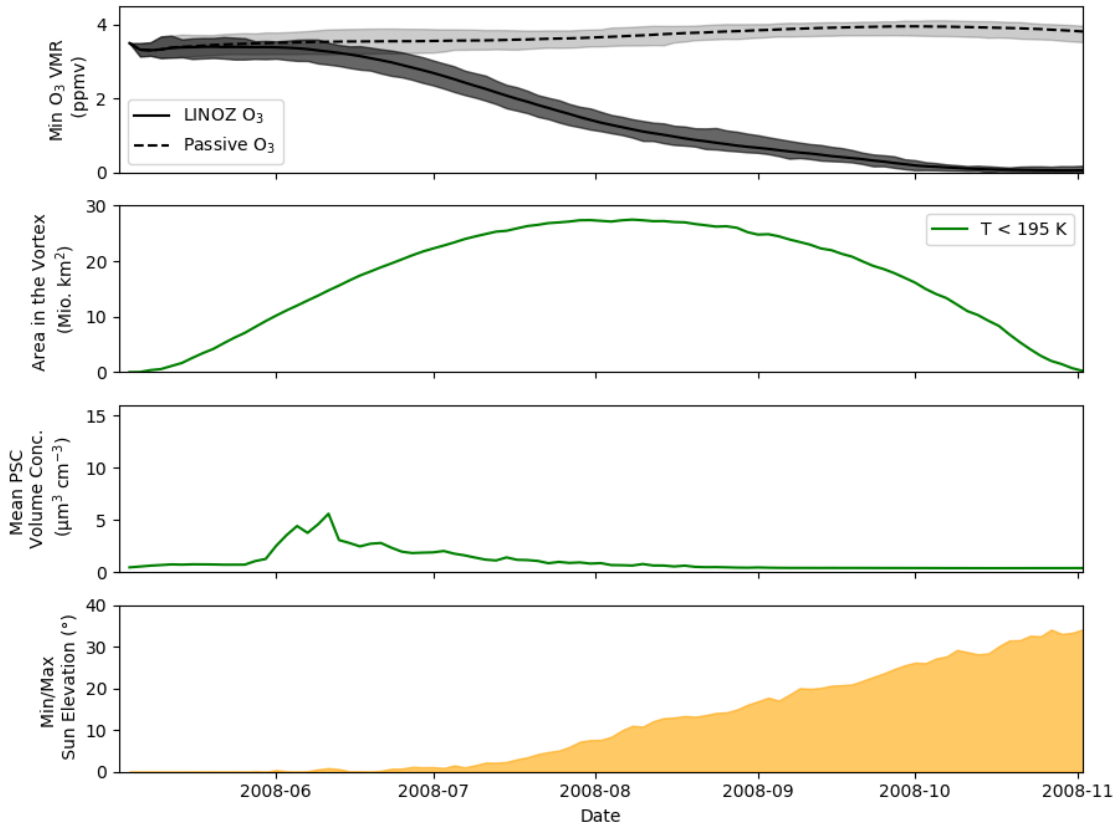

Figure 5.25: Comparison of linearised ozone with the PSC scheme in ICON-ART within the polar vortex. Results of the time slice experiment are shown. The polar vortex is defined for PV of $PV < -50$ PVU at $\theta = 475$ K where the ICON-ART data is vertically linearly interpolated. The uppermost panel shows the minimum ozone within the vortex for the chemically active and passive tracers as ranges in the time slice experiment. The second panel shows the time slice-averaged number of cells with temperature lower than the typical formation temperatures of the PSC types relative to the total number of grid cells in the vortex. The third panel shows the time slice-averaged vortex-mean PSC volume concentration within the vortex. The lowermost panel illustrates the time slice-averaged minimum and maximum of the solar elevation angle in the vortex.

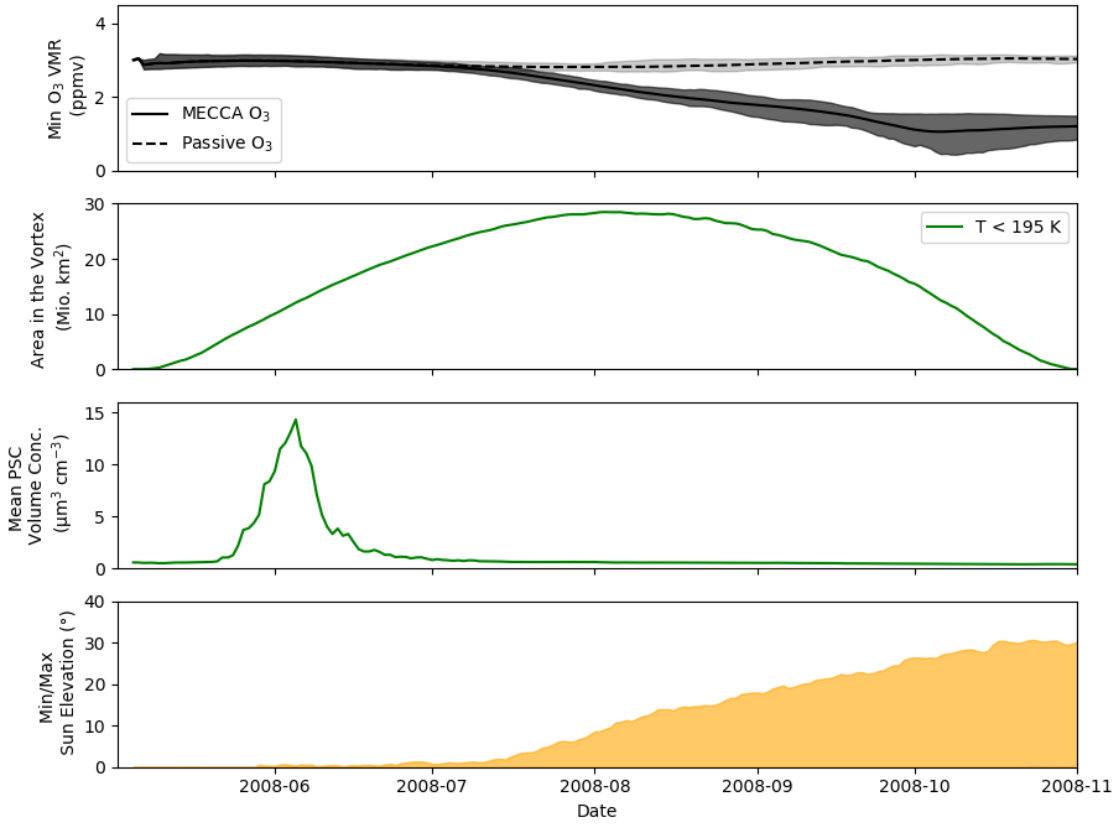

Figure 5.26: Comparison of gas phase chemistry with the PSC scheme in ICON-ART within the polar vortex. Same figure as Fig. 5.25 but for the ensemble simulation and ozone calculated as part of the stratospheric gas phase chemistry.

Fig. 5.26 but for the ensemble simulation and using ozone as result of the stratospheric chemistry instead of LINOZ ozone.

Passive and active ozone in both simulations first coincide during May 2008. While the area with $T < 195$ K increases, the minimum value of LINOZ ozone in Fig. 5.25 also begins to differ from the passive tracer, thus showing the heterogeneous depletion of ozone during the polar night. In contrast to this, the depletion should start not before the sun rises. During the begin of June, the solar elevation angle is nearly zero in the maximum so that the photolysis rates are not large enough to lead to ozone depletion. This is shown in the ensemble simulation in Fig. 5.26 where the two ozone time series start to differ after begin of July when also the sun rises. In addition, the decrease of ozone in the ensemble simulation follows after the peak of the PSC volume concentration whereas LINOZ ozone is already depleted when the PSC formation is at its maximum, i.e. when the coldest temperatures occur in the polar vortex.

Ozone of the linearised scheme in Fig. 5.25 is depleted until the temperature increases to values larger than 195 K. Thus, there are regions in the polar vortex where ozone is depleted completely with the LINOZ scheme. This is not the case for ozone using the stratospheric chemistry. A fraction of at least 0.2 ppmv of ozone remains in the polar vortex in the ensemble simulation. The time series of ozone will be evaluated with satellite data in Sect. 5.7.3.

In summary, this section demonstrated the differences of the linearised ozone scheme LINOZ and ozone as result of the stratospheric chemistry. Ozone as result of the stratospheric chemistry includes all relevant processes for a realistic representation in the model. In the LINOZ scheme, the effect of PSCs is parametrised which leads to an ozone depletion that starts too early at the coldest temperatures in the vortex and holds on until ozone is depleted completely at least at some grid points.

5.7 Evaluation of the PSC Scheme with Satellite Measurements

The goal of this chapter is the evaluation of the PSC scheme with reference data. So far, the size of the polar vortex was compared with ERA5 data and denitrification was evaluated with results of airborne measurements. In this section, the PSC scheme itself and the time evolution of trace gases closely connected to the presence of PSCs are compared to satellite data.

First, the PSC development is compared to MIPAS and CALIOP data (Sect. 5.7.1). Then, the trace gases HNO_3, N_2O, H_2O, ClO and HCl are evaluated with MLS measurements (Sect. 5.7.2). Finally, the evolution of ozone in the model in comparison to OMI measurements is investigated (Sect. 5.7.3).

5.7.1 Comparison of PSCs with MIPAS and CALIOP Measurements

The PSC measurements of MIPAS and CALIOP are used for a detailed comparison with ICON-ART. Figure 5.27 shows the sum of STS, NAT and ice particle volume concentrations of ICON-ART on the vertical axis and the MIPAS measurements of the total PSC volume concentration on the horizontal axis. The ICON-ART data is the average of all ensemble members and the MIPAS data

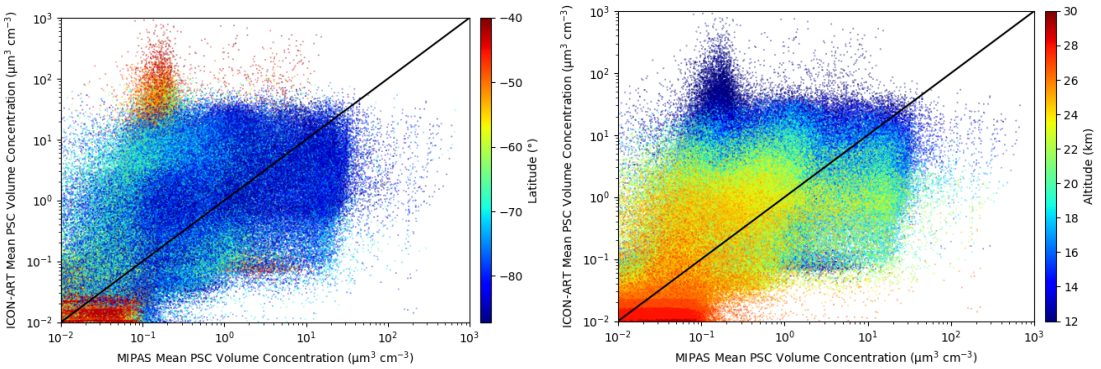

(a) Latitude colour-coded (b) Altitude colour-coded

Figure 5.27: ICON-ART total PSC volume concentration compared to MIPAS measurements. The average of all members of the ensemble simulation is shown colour-coded with (a) latitude and (b) altitude. The MIPAS data are the average between maximum and minimum approach.

is the average between maximum and minimum assumptions, as already used by Höpfner et al. (2018).

In the latitude regions between 50°S to 40°S (red colours in Fig. 5.27(a)) clouds are detected by ICON-ART at an altitude lower than 16 km (blue colours in Fig. 5.27(b)) and with particle volume concentrations higher than 300 $\mu m^3\ cm^{-3}$. These clouds can be explained by tropospheric ice clouds which have not been observed by MIPAS. At altitudes above 26 km (red colours in Fig. 5.27(b)), the PSC volume concentration decreases to values lower than 0.1 $\mu m^3\ cm^{-3}$, thus corresponding to the background sulphate aerosol, see Sect. 5.3.2. Apart from some outliers in both measurements and model simulation, they agree in the maximum PSC volume concentration of around 300 $\mu m^3\ cm^{-3}$.

The quantitative comparison between MIPAS and ICON-ART differs in up to three orders of magnitude. There are some possible reasons for this. First, the dynamics between model and measurements differ. This is shown in Fig. 5.28(a) where the temperature values between ICON-ART and MIPAS are illustrated. The temperature values differ by up to 20 K which could explain the different development of PSCs in the model and the MIPAS measurements.

To investigate this further, the values where the absolute value of the temperature difference between MIPAS and ICON-ART is higher than 1 K are eliminated in Fig. 5.28(b). This assumes that PSCs are instantaneously formed in thermodynamic equilibrium. The differences between MIPAS and ICON-ART are still in the order of two orders of magnitude and thus suggesting that the PSC types between model and MIPAS differ. In the region where differences in Fig. 5.28(b) are largest (1 to 10 $\mu m^3\ cm^{-3}$ for ICON-ART and MIPAS) NAT particles have a large fraction of the total PSC volume concentration (not shown). As shown in Sect. 5.3.3, the NAT volume concentration is underestimated in the model which could also explain the differences between measurements and model output. These differences should be investigated further in the future, especially for the application of the PSC scheme in the Arctic where the interaction of PSCs and the chemistry is more sensitive to small-scale temperature fluctuations (e.g., Eckermann et al., 2009).

Horizontal structures in Figs. 5.27(b) and 5.28(b) could indicate that the PSC volume concentration

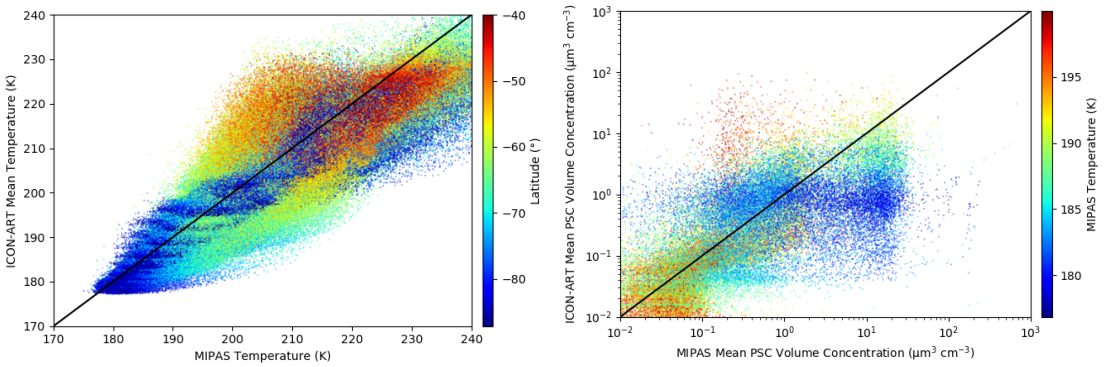

(a) Temperature

(b) PSC volume concentration for $|\Delta T| < 1$ K

Figure 5.28: Temperature and PSC volume concentration at the same temperature for MIPAS and ICON-ART. The temperature in panel (a) is colour-coded by the latitude. For the PSC volume concentration, only values are shown where the temperature is lower than 200 K and where the temperature difference is lower than 1 K.

saturates a value of about 3 µm^3 cm^{-3} at altitudes from 20 to 22 km and at temperatures lower than 188 K. This temperature can be assumed as the ice formation threshold at these altitudes (see Sect. 5.1). Thus, an underestimation of the ice volume concentration could be the reason for these horizontal structures in the figures.

The comparison of the PSC types to CALIOP measurements is shown in Fig. 5.29. As mentioned above, the CALIOP PSC type is derived from the measured backscatter coefficient of the particles. It is assumed that NAT particles are always in mixture with STS particles. Three mixture types (Mix1, Mix2, Mix-enh) are defined for CALIOP that correspond to different assumptions about particle number concentration of NAT and STS (Pitts et al., 2018). This is why Fig. 5.29 shows the sum of STS and NAT for both CALIOP and ICON-ART data. In addition, the wave-ice type of CALIOP is attributed to ice in the CALIOP data.

From a theoretical point of view, the backscatter coefficient of a particle depends on the differential cross section of the particle (Wandinger, 2005). Thus, it depends on the surface of the particle which is why the particle surface concentration is chosen for the comparison of ICON-ART with the CALIOP PSC types. In addition, the comparison with the PSC volume concentration is shown in Fig. 5.29(b). For this, the ICON-ART major PSC type is determined as the PSC type of which the particle surface (volume) concentration is larger than 50 % of the total particle surface (volume) concentration:

$$S_c > 0.5\,(S_{\mathrm{STS+NAT}} + S_{\mathrm{ice}}), \quad c \in \{\mathrm{STS} + \mathrm{NAT}, \mathrm{ice}\} \tag{5.35}$$

In addition, STS in ICON-ART also accounts for binary solution droplets which is not the case in the CALIOP data. To avoid binary solution droplets, a threshold of 0.1 µm^3 cm^{-3} in the particle volume concentration of STS is used to distinguish between binary and ternary solution droplets, cf. Fig. 5.12.

In order to compare the CALIOP measurements with ICON-ART, it is investigated which major type of PSCs occurs in ICON-ART if a specific type was measured by CALIOP. For this, Figure

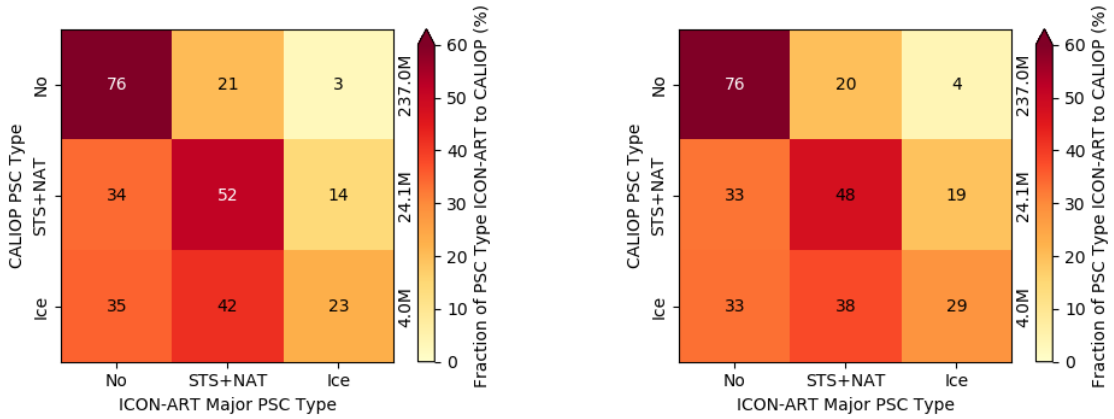

(a) Surface Concentration

(b) Volume Concentration

Figure 5.29: CALIOP PSC types compared to ICON-ART. Results of the base run of the ensemble simulation are shown. The major PSC type in ICON-ART is derived (a) from the PSC surface concentration, see Eq. (5.35), and (b) from the PSC volume concentration with the same algorithm. The vertical range from 12 to 30 km is used for the comparison. The total number of measurement points in 10^6 points is denoted on the right hand side of each row.

5.29 illustrates the distribution of PSC types in ICON-ART for no cloud, STS+NAT and ice PSCs in the observations. Thus, each row in Fig. 5.29 sums up to 100 %.

The best agreement between CALIOP and ICON-ART can be found for no PSCs: 76 % of the measured "No" PSCs are also determined as such in ICON-ART in both panels of Fig. 5.29. The selected data covers areas up to mid-latitudinal 50°S where no PSCs occur anymore. In this general sense, this result shows that the PSC scheme forms PSCs in similar areas of the Earth as in the CALIOP measurements. Uncertainties remain in the determination of no PSCs in ICON-ART, as mentioned above.

The observed and modelled mixture type STS+NAT coincide with a fraction of 52 % and 48 % for the particle surface and volume concentration, respectively. Thus, the coincident PSC types have largest fraction but this also means that nearly half of the measurements of STS+NAT particles do not fit to the ICON-ART data.

For ice, the smallest fraction is also determined as ice PSC in ICON-ART with values of 23 % and 29 %. Thus, this suggests that the dynamics in the model differs to that in the measurements.

Spang et al. (2016) derived a PSC classifier for MIPAS and compared coincident MIPAS and CALIOP PSC type measurements with each other. They demonstrated that also differences between the classification methods between both instruments exist which can be attributed to different instrument sensitivities. Thus, the classification of PSCs by satellite instruments includes an uncertainty. An investigation of the area covered by PSCs as shown by Spang et al. (2018) could help to get a global picture of PSC occurrence with respect to both satellite measurements.

The time series of the PSC types in comparison to CALIOP is shown in Fig. 5.30. In ICON-ART, the formation of PSCs starts in the mid of May 2008 in contrast to CALIOP where PSCs occur first at the beginning of June. In comparison to MIPAS measurements, this start of the formation of PSCs is too late (not shown, Höpfner, 2019, pers. communication) which indicates that start and

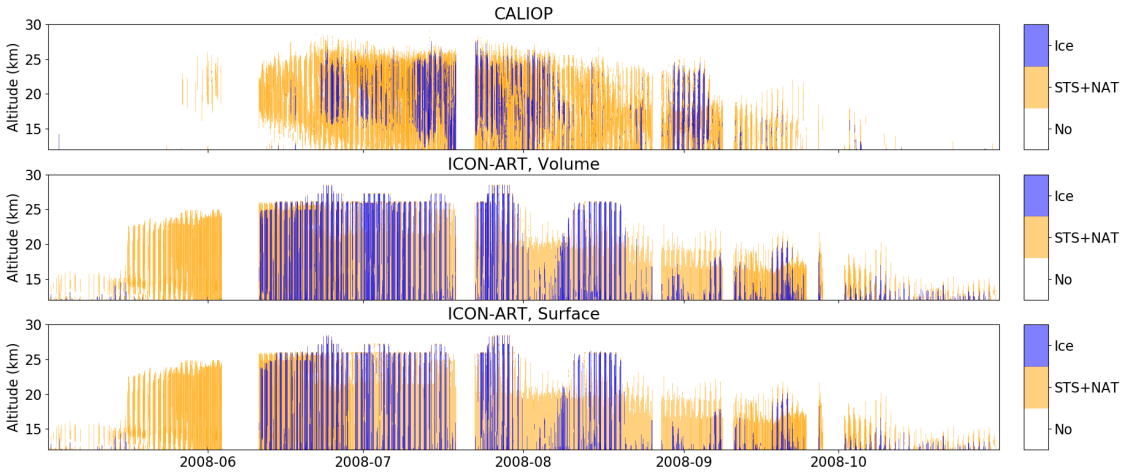

Figure 5.30: Time series of polar stratospheric clouds in CALIOP and ICON-ART. Results of the ensemble base run are shown. The CALIOP mixture types are summarised as STS+NAT. The two lower panels show the ICON-ART PSC type with volume and surface concentration as basic quantities, respectively. The data points of neighboured profiles overlap in the figures. At the dates where both types occur in neighboured profiles, the colour merges to violet.

end of the PSC period in ICON-ART are in agreement with the measurements. The maximum height of PSCs of about 28 km of the CALIOP data is reflected in the ICON-ART simulation. In addition, the decrease in the maximum PSC height after begin of September is in agreement with the measurements. Generally, the time period of the occurrence of PSCs is consistent to the measurements, demonstrating that the yearly cycle of PSCs is reflected in the simulations of ICON-ART.

In total, the detailed method for comparison of the PSC volume concentration and PSC types to the satellite observations is uncertain and a comparison using the radiative quantities derived from the model data as mentioned by Engel et al. (2013) would be highly appreciated. Apart from these uncertainties, the PSC scheme generally produces PSCs in ICON-ART in a similar area like in the measurements. The yearly cycle of PSCs is consistent to the measurements.

To summarise both comparisons of this section, the composition of PSCs differs probably either because of different dynamics in the model compared to the measurements or because of incomplete nucleation mechanisms of the PSCs. As mentioned in Sect. 2.5, especially the nucleation of NAT on other pre-existing PSCs that work as nuclei for NAT is current issue of research. In the configuration of ICON-ART, NAT is formed independently of other aerosols in the atmosphere which could be improved in the future. The comparison to MIPAS showed that the particle volume concentration of the PSCs is in the correct order of magnitude but it also suggested that the type of the PSCs does not match. This is confirmed by the CALIOP comparison where still uncertainties remain in the composition of PSCs in ICON-ART. In addition, the daily model output interval as well as the horizontal resolution of around 160 km in the ICON-ART simulations might limit these detailed comparisons to the satellite data.

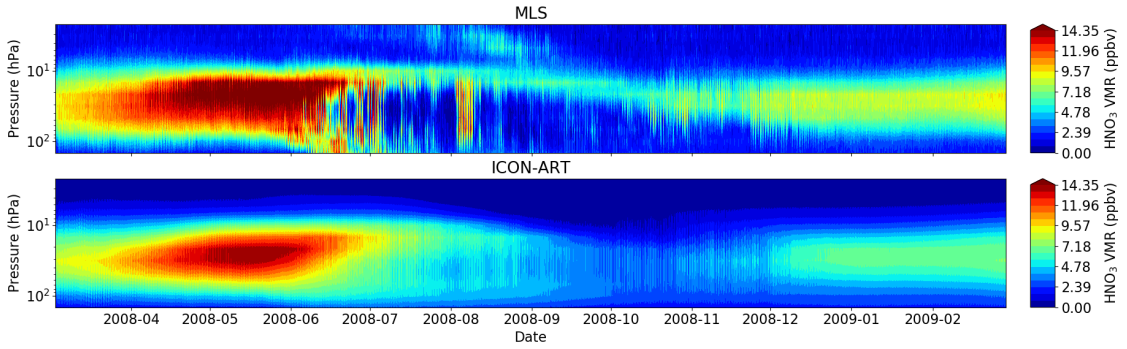

(a) HNO_3

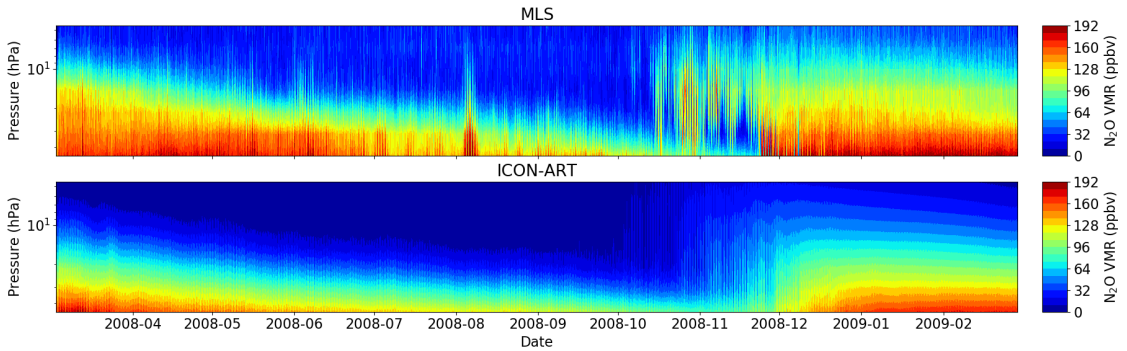

(b) N_2O

Figure 5.31: ICON-ART time series of (a) HNO_3 and (b) N_2O compared to MLS measurements. ICON-ART values are the ensemble mean. Data is selected for the southern high latitudes (75°S to 82°S).

5.7.2 Comparison of Relevant Trace Gases with MLS Measurements

In this section, some trace gases related to the heterogeneous chemistry are compared with MLS measurements. Figure 5.31 shows time series HNO_3 in Fig. 5.31(a) and nitrous oxide (N_2O) in Fig. 5.31(b) for the southern high latitudes from 75°S down to 82°S for the year 2008. The average of all ensemble members of ICON-ART is shown in the lower panels of the figures. In the early time of the polar night between April and May 2008, the photochemistry of the active nitrogen-containing species gets less efficient so that the reservoir gas HNO_3 is formed with volume mixing ratios up to 18 ppbv in the MLS measurements, see Fig. 5.31(a), upper panel. From June until September, dentrification takes place so that HNO_3 decreases to values below 2 ppbv. When the vortex dissipates in November to December 2008, air from mid-latitudes increases the HNO_3 mixing ratio again with values up to 9 ppbv in the pressure region from 50 to 10 hPa.

All these general features are represented in the ensemble simulation of ICON-ART using the stratospheric chemistry, see lower panel of Fig. 5.31(a) but the absolute volume mixing ratios of HNO_3 are lower than in the MLS measurements. In ICON-ART, the HNO_3 volume mixing ratio peaks at around 14 ppbv whereas the maximum in the MLS measurements is at about 18 ppbv (not shown). In addition, HNO_3 is also underestimated after the dissipation of the polar vortex in November to December where the volume mixing ratio in ICON-ART is about 7 ppbv compared to the measured 9 ppbv mentioned above.

In the MLS measurements, enhanced HNO_3 mixing ratios up to 5 ppbv occur in August within the pressure range from 7 to 1 hPa. Most probably, these originate from nitrogen-containing species being intruded from higher altitudes which is a current issue of research (see, e.g., Bender et al., 2019) and which cannot be represented in the current state of ICON-ART.

Denitrification is weaker in the model than in the measurements which was also shown in several previous sections of this chapter. The comparison of the thermodynamic and the kinetic NAT parametrisation already suggested that the kinetic approach underestimates denitrification. In the measurements, obviously larger NAT particles form that lead to a denitrification between 20 and 100 hPa and a renitrification at lower altitudes. In ICON-ART, the general shape of denitrification can also be found in the time series: the volume mixing ratio is enhanced at a pressure value of about 10 hPa and at lower altitudes at about 100 hPa. In between, the HNO_3 volume mixing ratio decreases to values of 4 ppbv. The presence of denitrification in the simulations was already demonstrated in Sect. 5.4, and more specifically in Fig. 5.21. Thus, the denitrification in the model is weaker than in the MLS measurements, most probably because of a general underestimation of HNO_3 in the model and the general underestimation of NAT particles with the kinetic approach in ICON-ART so that NAT particles form that are smaller than in the measurements.

HNO_3 in the model is produced by the reaction NO_2 + OH and the active nitrogen-containing species, such as NO and NO_2, are produced by N_2O. This is why Fig. 5.31(b) shows the time series of N_2O for MLS and ICON-ART. In the shown southern high latitudes, N_2O decreases with time as a result of the downwelling in the polar vortex. After its dissipation in December 2008, mid-latitudinal values are mixed into this region so that the N_2O volume mixing ratio increases back to values up to 192 ppbv in the shown pressure range in the MLS measurements.

In ICON-ART, the N_2O volume mixing ratio is also underestimated by a factor of about 2 from the beginning of the simulation compared to the MLS measurements. Thus, the time series of N_2O could explain the general underestimation of HNO_3 in the model. The general features, like the large-scale downwelling and the subsequent decrease of N_2O as well as the increase of N_2O after the dissipation of the polar vortex are represented in ICON-ART.

N_2O is a trace gas which has no chemical sources in the troposphere and stratosphere, see Appendix C. The only source of atmospheric N_2O are emissions at the Earth's surface. Thus, two possible reasons can result in the underestimation of N_2O in ICON-ART which are discussed in the following: either the initialisation of N_2O already contains too low values or the emissions of N_2O are not well represented in the model.

In the time series shown in Fig. 5.31(b), the differences start at the beginning of the simulation in March 2008. Therefore, the initialisation of N_2O could already involve an underestimation of N_2O. It is initialised from an EMAC simulation where the setup was validated in several studies with measurements in the stratosphere (e.g., Jöckel et al., 2006; Kirner, 2008). Thus, it is improbable that the EMAC model includes these underestimated values. Nevertheless, an initialisation with assimilated MLS measurements could be checked in the future.

In addition, the impact of the interpolation on the ICON-ART grid with the nearest neighbour method is negligible (not shown). Thus, the initialisation of N_2O in ICON-ART seems to be consistent with EMAC which is validated with measurements. On the other hand, emissions of N_2O by the EDGAR inventory include an uncertainty in the order of 100 % (Olivier et al., 1999) which could explain the discrepancies between N_2O in the model and in the measurements.

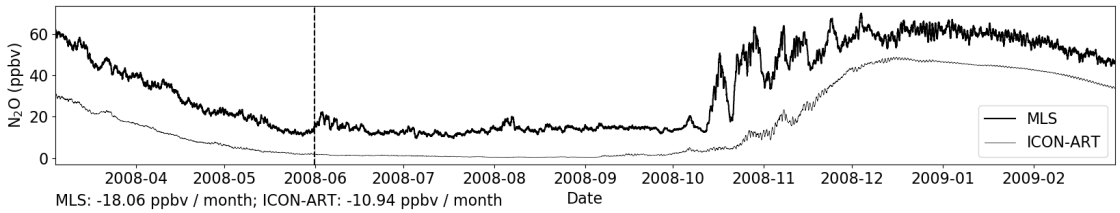

Figure 5.32: N_2O time series at an altitude of 10 hPa in MLS and ICON-ART. A moving average with a time window of 1 d is applied to the data to suppress small-scale fluctuations. The trends denoted at the right bottom of the figure are linear regressions of the time series until begin of June where the dashed vertical line is included. Data is selected for the southern high latitudes (75°S to 82°S).

N_2O can be used as proxy for the transport in atmospheric chemistry models (e.g., Kirner et al., 2015a) which is additionally shown in Fig. 5.32 where the time series of N_2O is depicted at an altitude of 10 hPa for MLS (thick line) and ICON-ART (thin line). A moving average with a time window of 1 d is applied to the data in order to suppress small-scale fluctuations in the data that originate from the different longitudes which the satellite covers during the day. The time series show the decrease due to the large-scale downwelling in the polar vortex until begin of June 2008. During June to September, the N_2O volume mixing ratio saturates at about 20 ppbv for MLS and at lower than 1 ppbv for ICON-ART. In the mid of October, the N_2O volume mixing ratio increases again due to the mixing of mid-latitudinal air.

The volume mixing ratio of N_2O in ICON-ART at the altitude of 10 hPa already differs by a factor of 2 at the beginning of the simulation compared to the MLS measurements. This is why the linear trend in the first months, depicted in the lower left corner of Fig. 5.32, is smaller in ICON-ART than in the measurements. The trend in the MLS observations is -18 ppbv month^{-1} whereas it is about -11 ppbv month^{-1} in the ICON-ART simulation. As already suggested by Fig. 5.31(b), this indicates a slower downwelling in ICON-ART than in the MLS measurements.

In summary of Fig. 5.31 and Fig. 5.32, the volume mixing ratios of HNO_3 and N_2O are underestimated in ICON-ART with respect to the MLS measurements. With the PSC scheme in ICON-ART, denitrification occurs in the model, but is underestimated. Possible reasons could be too low values in the initialisation and the limits of the kinetic NAT parametrisation.

The sedimentation of ice particles in the stratosphere leads to dehydration in the model which is shown in Fig. 5.33. In both the measurements (upper panel) and the ICON-ART simulation (middle panel), the H_2O volume mixing ratio decreases in July to values down to 2 ppmv for MLS and lower than 1 ppmv for ICON-ART within the pressure range from 100 to 10 hPa. Larger mixing ratios advected from higher altitudes within the polar vortex gradually increase the H_2O volume mixing ratio again until end of December 2008.

Comparing the ICON-ART time series in the middle panel of Fig. 5.33 with the MLS measurements, the H_2O volume mixing ratio is by a factor of about 0.3 smaller. The middle panel shows water vapour as computed in the ICON microphysics which misses one of the major stratospheric sources: the production due to the reaction CH_4 + OH where two molecules of H_2O are produced in a reaction chain (ECMWF, 2003). This is why the increase in H_2O can be estimated as follows as post-processing:

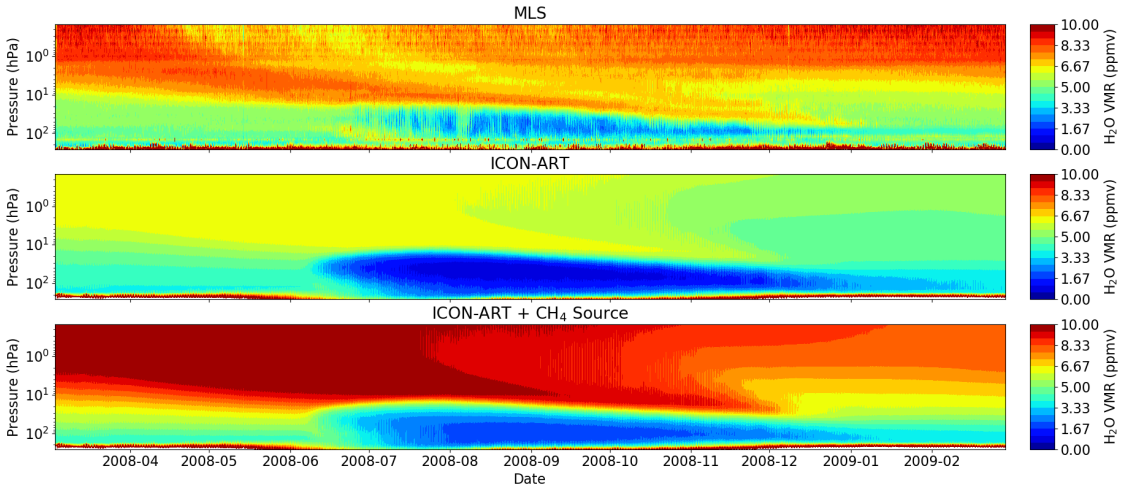

Figure 5.33: ICON-ART time series of H_2O compared to MLS measurements. ICON-ART values are the ensemble mean. The lowermost panel shows the H_2O volume mixing ratio increased by Eq. (5.36). Data is selected for the southern high latitudes (75°S to 82°S).

$$\Delta X_{\mathrm{H_2O}}(\mathbf{x}) \approx 2\left(\overline{X}_{\mathrm{CH_4,trop}} - X_{\mathrm{CH_4}}(\mathbf{x})\right) \tag{5.36}$$

The increase of the H_2O volume mixing ratio at the stratospheric location $\mathbf{x}$ is twice the difference between the average tropospheric CH_4 volume mixing ratio and the value at the location $\mathbf{x}$. In ICON-ART, the tropospheric average is calculated as global average of all tropospheric model layers. The given $\Delta X_{\mathrm{H_2O}}(\mathbf{x})$ by Eq. (5.36) is then added to the water vapour volume mixing ratio of the middle panel in Fig. 5.33. The resulting H_2O time series is shown in the lowermost panel of this figure.

As can be seen, the H_2O volume mixing ratio is improved in the pressure range between 100 and 10 hPa where the ice PSCs occur in model and measurements. The minimum value of $X_{\mathrm{H_2O}}$ is increased with values around 1 ppmv which coincides with the MLS measurements. For lower pressure values, the H_2O volume mixing ratio is by 2 ppmv larger than the measured one suggesting that the parametrisation of Eq. (5.36) misses some relevant processes at these altitudes. The production of other substances due to the oxidation of CH_4 leads to a factor lower than 2 in Eq. (5.36). One example is the production of molecular hydrogen (ECMWF, 2003) with volume mixing ratios around 0.5 ppbv in the atmosphere (Brasseur and Solomon, 1986).

On the other hand, the overestimation of H_2O at high altitudes after applying Eq. (5.36) could indicate that the volume mixing ratio of CH_4 is too low compared to the measurements at these altitudes. This would be in agreement with the results of N_2O which was discussed previously in this section (Fig. 5.31(b)).

In summary, the dehydration due to ice PSCs in the model occurs at the same time spans and altitude regions as in the MLS measurements. Underestimation of the minimum values can be explained by the missing CH_4 source of water vapour in the lower stratosphere.

With the previous figures, denitrification and dehydration as integrated in ICON-ART have been shown. In Figures 5.34 and 5.35, time series of the active chlorine species ClO and HCl are illustrated

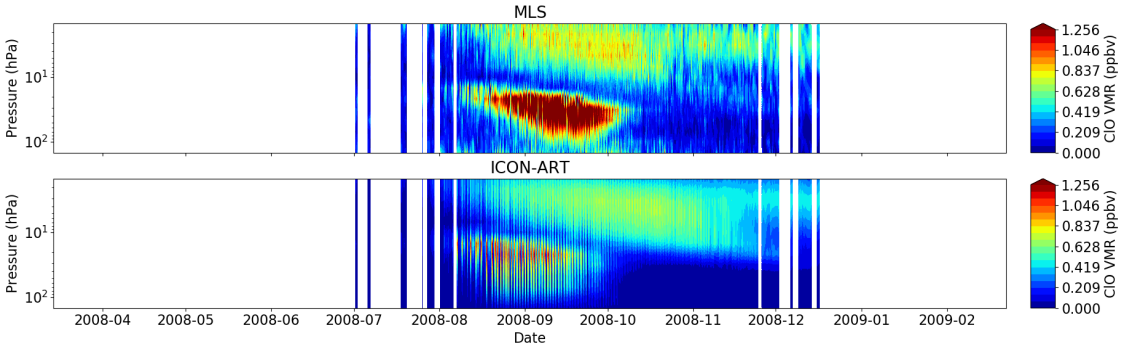

Figure 5.34: ICON-ART time series of ClO compared to MLS measurements. ICON-ART values are the ensemble mean. In the time series of ClO negative values in the volume mixing ratio occurred in the edge months of this figure and within the recommended pressure range so that these profiles have been deleted. Data is selected for the southern high latitudes (75°S to 82°S).

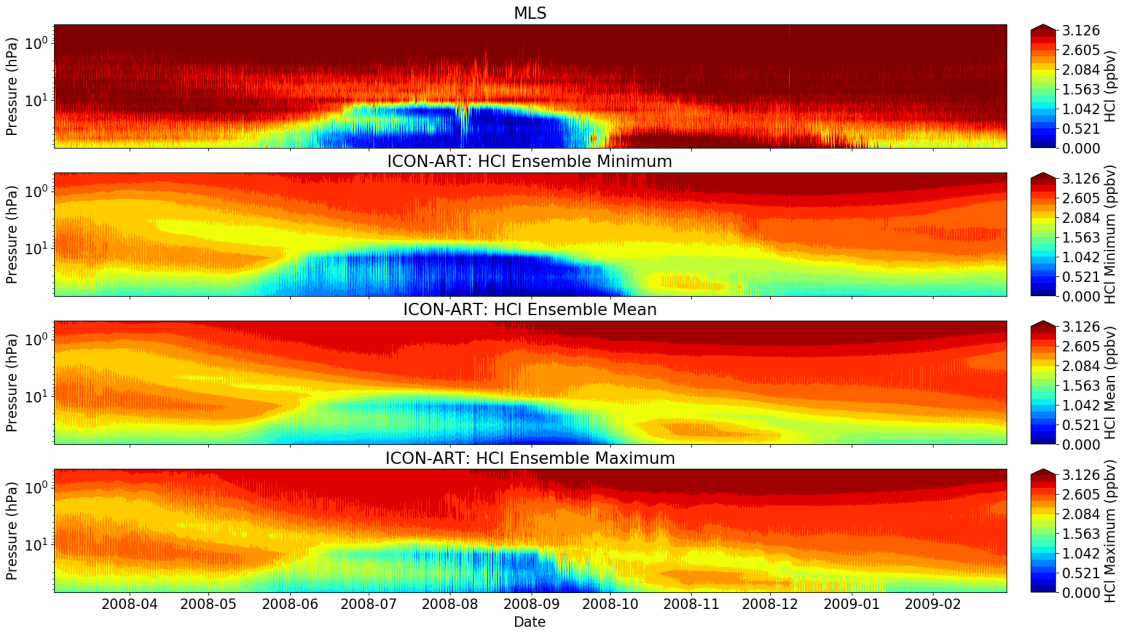

Figure 5.35: ICON-ART time series of HCl compared to MLS measurements. ICON-ART values are the ensemble minimum (second panel), mean (third panel) and maximum (last panel). Data is selected for the southern high latitudes (75°S to 82°S).

for MLS and ICON-ART. These time series demonstrate that chlorine activation is included in the model but with underestimation of the absolute volume mixing ratios.

In the pressure range from 10 to 1 hPa of Fig. 5.34, the ClO volume mixing ratio is in the order of 1 ppbv in both the ICON-ART simulation and the MLS measurements. For higher pressure values, the global maximum of about 1.2 ppbv occurs around the beginning of September which agrees with the minimum values in HCl in both ICON-ART and MLS (Fig. 5.35).

HCl is depleted almost completely with volume mixing ratios close to zero due to the heterogeneous chemistry on the surface of PSCs in the MLS measurements, see Fig. 5.35. This is reflected in the ensemble minimum which is shown in the second panel of the figure. Higher values around 2 ppbv, which are advected from higher altitudes, are also represented in all ensemble simulations which is shown by the same structures in the ensemble minimum, mean and maximum.

In addition, the time range as well as the pressure range of the depletion of HCl coincides with the measurements which demonstrates that chlorine is activated in the model on the surface of PSCs. In contrast to Grooß et al. (2018) who showed that the chlorine activation with HCl starts too late in several atmospheric chemistry models, there are members of the ensemble simulation that can reflect the early start of chlorine activation. Thus, this shows that the chlorine activation in the MLS measurements is within the range of the ICON-ART ensemble simulation so that it can be stated that it is in the correct order of magnitude, at least for some members of the ensemble simulation.

Altogether, this section showed that with introduction of the PSC scheme all relevant processes for the realistic representation of ozone are included in ICON-ART: formation of the polar vortex with subsequent downwelling, denitrification (although too weak), dehydration and chlorine activation. No fundamental process is missing as the maximum and minimum values in all figures occur at similar times and altitudes. Thus, ozone can now be evaluated with satellite measurements which is demonstrated in the following section.

5.7.3 Comparison of Ozone with OMI Measurements

The major goal of any PSC scheme in atmospheric chemistry models is the representation of denitrification and chlorine activation in order to achieve a realistic ozone depletion in the model. As mentioned in Sect. 4.7.3, ozone satellite measurements have a long history and these measurements are compared to the ICON-ART ensemble simulation in this section. In addition, the simulation without PSCs is used in order to investigate the influence of PSCs on the development of ozone in the model.

Figure 5.36 shows the southern hemispheric minimum ozone column time series for both measurements and ICON-ART simulations. The measurements of minimum ozone are illustrated as blue shade for the time period 1979 to 2017, which illustrates the range of all measurements since begin of the measurements. The blue line represents the measured minimum ozone for the year 2008. The range of the ICON-ART ensemble simulation minimum ozone is orange-shaded whereas the minimum ozone of the simulation without PSCs is illustrated by the green line in the figure.

The simulation without PSCs is within the range of the measurements during autumn and winter (January to July). During spring, however, when the sun rises over the Antarctica the minimum

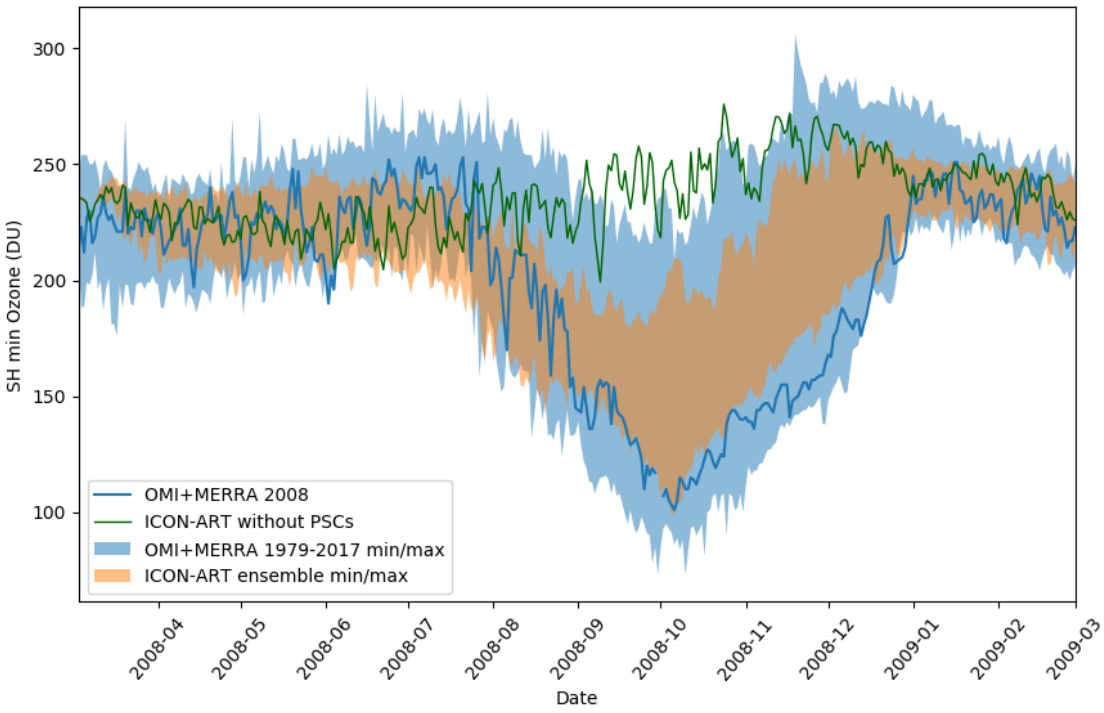

Figure 5.36: Southern hemispheric minimum ozone column in OMI measurements and ICON-ART simulations. The blue line corresponds to the OMI measurements of 2008, the green line depicts the minimum ozone in the simulation without PSCs. The blue range illustrates the range of southern hemispheric minimum ozone measurements between 1979 to 2017. The orange range corresponds to the range of the ensemble simulation.

ozone value is larger than any measured minimum ozone column since 1979. It is in the order of 250 DU which has never been measured in the past decades.

In contrast to this, all members of the ensemble simulation are within the range of the measurements apart from some underestimations during June and July. Thus, the general progress of the minimum ozone column is realistic in the sense that ozone values in the order of magnitude were already measured in the past. Some ensemble members reach the minimum around 100 DU which was also measured in October 2008. In comparison to the measurements for 2008, the ensemble simulation is larger than the measured ozone values between October and December 2008. The general time evolution with nearly constant values from March to July, decreasing values during August and September, minimum in October and increasing values in November and December is within the range of the measurements.

Thus, this figure demonstrates the importance of heterogeneous processes on the surface of PSCs in atmospheric chemistry models. Without PSCs, ozone loss is missing in the model while the PSC scheme in ICON-ART leads to a realistic ozone loss in the model.

6

Interaction between Mountain Waves and Polar Stratospheric Clouds

This chapter demonstrates that the two-way nesting enables ICON-ART to represent mountain-wave induced PSCs in coarse resolutions where this process cannot be simulated otherwise. In addition, the formation of directly simulated mountain-wave induced PSCs leads to chlorine activation that is not represented in the model without the nesting technique. A specific mountain wave event around the Antarctic Peninsula is investigated which began on 20 July 2008 and lasted for more than 10 days (Noel and Pitts, 2012).

In the first section, the dynamical structure of the mountain wave on 21 July 2008 is shown (Sect. 6.1), followed by the influence of the mountain wave on H_2SO_4, HNO_3 and H_2O (Sect. 6.2). Then, the formation of PSCs in the mountain wave is demonstrated (Sect. 6.3). The impact of mountain-wave induced PSCs on chlorine activation during this mountain wave event is shown in the subsequent section (Sect. 6.4). Finally, the impact on ozone is analysed for the first ten days after begin of the mountain wave event (Sect. 6.5).

6.1 Dynamical Structure of the Mountain Wave on 21 July 2008

In this section, the dynamical structure of the mountain wave event is analysed with ICON-ART on 21 July 2008. The Antarctic Peninsula as a relatively far north reaching mountain ridge is in the west wind drift of the southern hemisphere, as shown e.g. by Wessem et al. (2015) and Zhang and Zhang (2018). Thus, mountain waves mainly occur eastward in the lee of the mountain which is also the case of this specific event and in the nest simulation of this thesis.

Figure 6.1 shows the horizontal temperature structure around the Antarctic Peninsula for the simulation without nests (Fig. 6.1(a)) and with the nests described in Sect. 4.4 at an altitude of 23.9 km. Temperature values below the typical formation threshold of 195 K occur all over the Antarctica in both simulations.

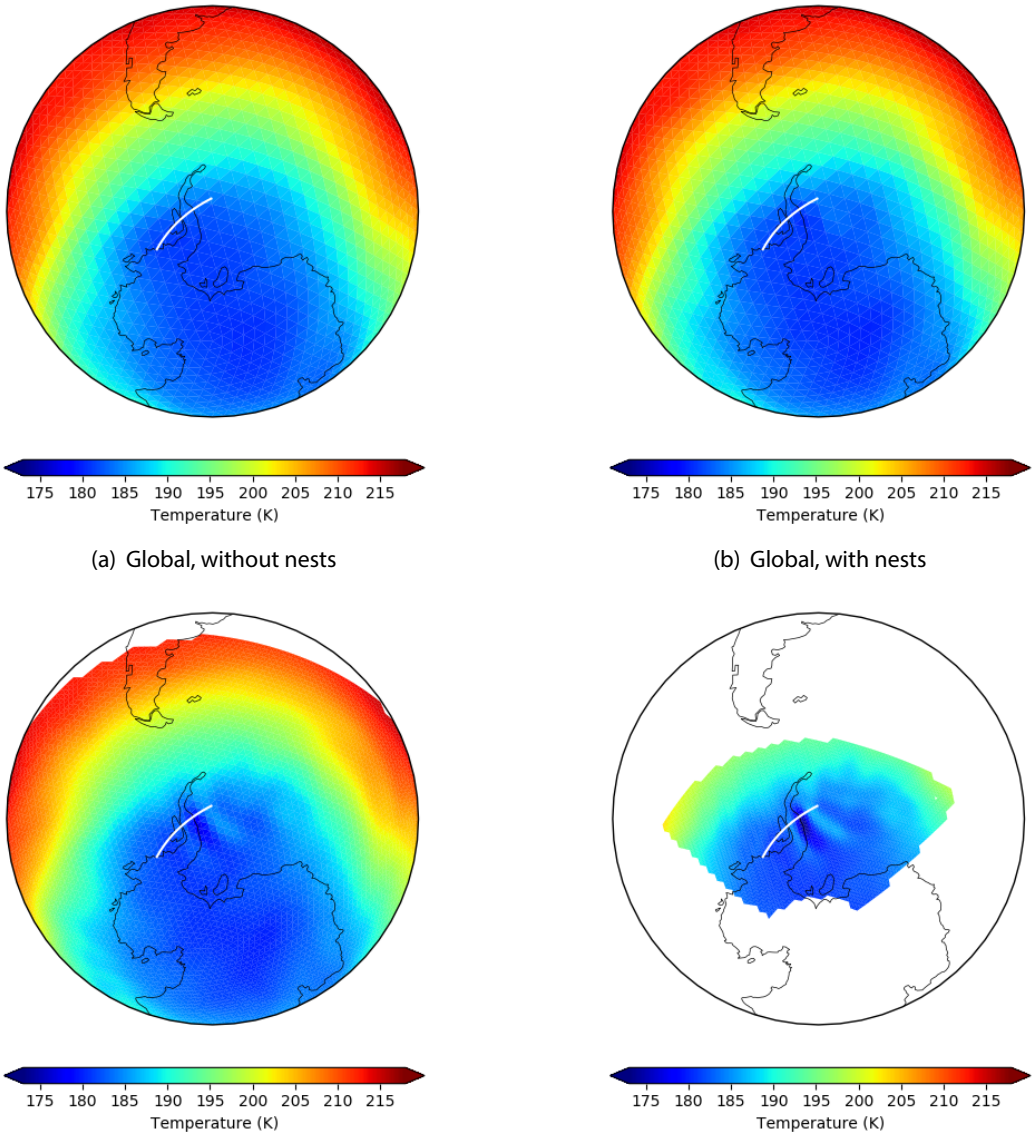

(a) Global, without nests

(b) Global, with nests

(c) Antarctica

(d) Antarctic Peninsula

Figure 6.1: Horizontal temperature structure at an altitude of 23.9 km around the Antarctic Peninsula. The temperature distribution is shown (a) for the simulation without nest, (b) for the global domain including two-way nesting around the Antarctic Peninsula, and for (c) and (d) in the nests. White areas show the edges of the nests. The date of this snap shot is 21 July 2008 at 14 UTC. The white line depicts the location of the cross section, that is used in the remaining figures of this chapter.

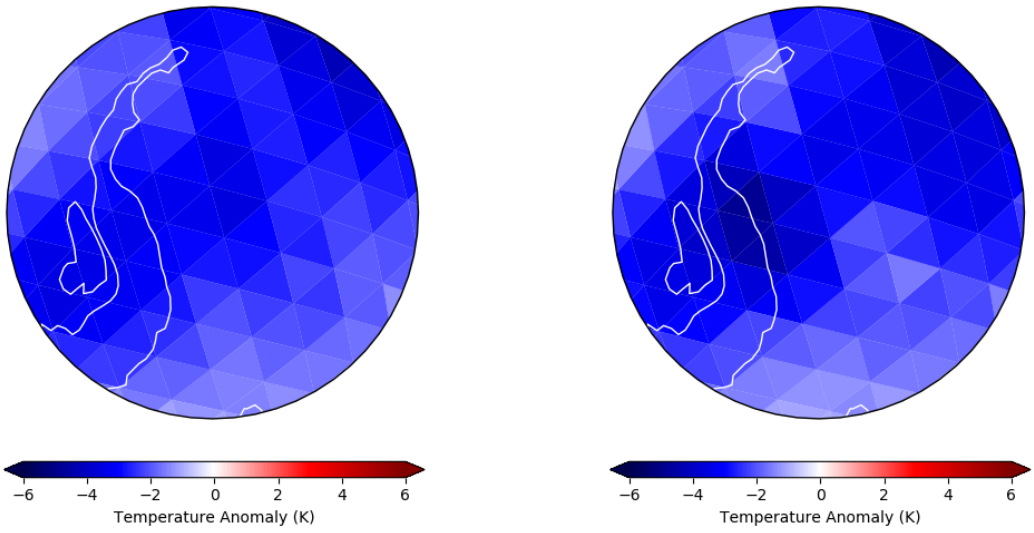

(a) Global, without nests (b) Global, with nests

Figure 6.2: Temperature deviation from zonal mean around the Antarctic Peninsula. Results from the global domains (a) without and (b) with nests are shown for the same date and altitude as in Fig. 6.1.

In the global simulation without nests, no indication of a mountain wave occurs at the Antarctic Peninsula. With the horizontal resolution of R2B04 (approx. 160 km), the mountain wave cannot be represented by the model because of the coarse resolution of the underlying orography.

In the simulation including the two nests with the horizontal resolutions of R2B05 and R2B06 (approx. 80 and 40 km), respectively, variations in the temperature occur that are a result of the two-way nesting technique. Wave-like patterns occur in the east (i.e. downstream) of the Antarctic Peninsula with a horizontal wavelength of about 450 km and an amplitude of about 5 K in the global domain (Fig. 6.1(b)). These wave-like patterns originate from the higher resolved nested domains where the mountain wave is amplified with temperature minimum values below 175 K and maximum values around 190 K at this altitude of 23.9 km (Fig. 6.1(d)).

The impact of the two-way nesting in the global domain is also shown in Fig. 6.2 where the deviation of the zonal mean temperature is shown around the Antarctic Peninsula. Deviations down to −6 K occur in the simulation in the east of the Peninsula which cannot be simulated without the nests. This can be attributed to the lower temperature in the nests as will be also demonstrated in the following.

Cross sections along the white lines of Fig. 6.1 of temperature, horizontal wind and potential temperature are shown in Fig. 6.3. The cross section is defined for latitudes increasing linearly from 73.5°S to 65°S and for longitudes from 84.5°W to 54.5°W. The ICON-ART data is interpolated by an inverse distance method as used for the interpolation to the satellites (Eq. (4.1)). Therefore, this method shows the variables in the model by the same algorithm in each domain so that it is independent of the resolution of the model.

The bottom row of Fig. 6.3 shows the surface altitude for each domain with the global resolutions of 160 km without and with nests in the two left columns and the higher resolved nested domains in the two right columns. The Antarctic Peninsula is barely represented in the global resolution

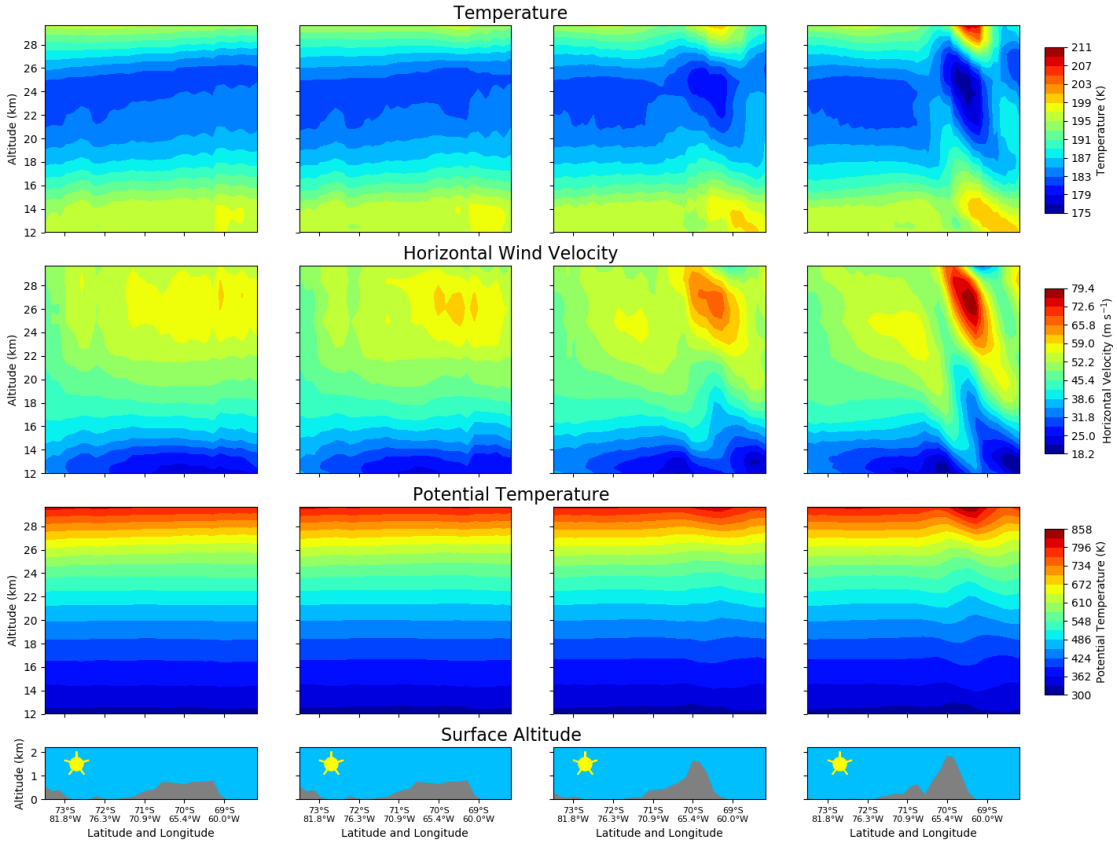

Figure 6.3: Temperature, horizontal wind and potential temperature around the Antarctic Peninsula. The cross section along the white line in Fig. 6.1 is shown (latitudes from 73.5°S to 65°S and longitudes from 84.5°W to 54.5°W). Each row represents different variables in the model. The bottom row shows the surface altitude with the Antarctic Peninsula at around 65°W. The columns represent the different simulations and domains: The first column is the simulation without nest, the second one is the global domain including two-way nesting and the two right columns represent the Antarctica and Antarctic Peninsula nests, respectively.

with a maximum altitude of less than 1 km. Thus, the mountain wave cannot be represented in the simulation without the nests (leftmost column in Fig. 6.3). The temperature increases by around 2 K in the whole altitude range from 12 to 24 km in the lee of the mountain.

This changes if the refined grids around the Antarctic Peninsula are included. Within the innermost nest (right column in Fig. 6.3), the Antarctic Peninsula is better resolved with altitudes up to 2 km. The subsequent lifting and downwelling of the air leads to a temperature decrease down to values around 175 K at the altitude of 24 km in the lee (east side) of the mountain. This is in accordance to the literature where temperature perturbations up to ±10 K have been observed (e.g., Meilinger et al., 1995).

Because of the two-way nesting in ICON-ART, the temperature values in the Antarctic Peninsula nest influence both the Antarctica nest and the global domain. Temperature values down to 183 K occur in the lee of the mountain in the global domain that are not represented in the simulation without nests.

Gradients in temperature induce changes in the streamlines of the flow and thus in the wind velocity. This is shown in the second row of Fig. 6.3 where a maximum in the horizontal wind speed of about 79 m s^{-1} in the Antarctic Peninsula nest occurs at an altitude of 26 km, i.e. above the minimum value of temperature. The wave-like pattern with alternating minimum (18 m s^{-1}) and maximum (40 m s^{-1}) values also occurs at the lower altitudes between 12 and 20 km beyond the mountain.

These features are again led back to the global domain (second column, second row in Fig. 6.3) where the wave-like pattern is also amplified in comparison to the simulation without the nests. Maximum values up to about 62 m s^{-1} occur from longitudes of 65°W to 60°W at an altitude of 26 km which is not represented in the simulation without nests. In addition, changes in the horizontal wind velocity with two-way nesting occur at the lower altitudes where maximum and minimum values alternate like in the nested domains.

The wave-like patterns in all three variables in the Antarctica and Antarctic Peninsula nests (two right columns of Fig. 6.3) are shifted upstream with increasing altitude. This is a result of the upward propagating mountain wave and is in correspondence with the theory of mountain waves, as shown e.g. in Fig. 2.3.

Altogether, the results described above demonstrate that the typical patterns of mountain waves in the lee of the Antarctic Peninsula can be simulated in the innermost nest. Due to the two-way nesting in ICON-ART, these patterns can also be represented in the global domain where the Antarctic Peninsula is barely resolved.

The potential temperature in the third row of Fig. 6.3 is an indicator for the flow in terms of lifting and downwelling because the flow in the stratosphere is isentropic as a first approximation, see also Sect. 2.2. Therefore, the flow follows the lines of constant potential temperature.

The influence of the two-way nesting on the potential temperature is negligible due to the pressure dependence of the potential temperature (see Eq. (2.8)) and the lower influence of the mountain wave on the absolute values of the potential temperature. In both global domains in the two left columns in Fig. 6.3, the potential temperature shows an altitude dependence but is horizontally nearly constant. In the nested domains, the vertical displacement of the potential temperature is amplified. In the Antarctic Peninsula nest (right column), the vertical displacement is in the order of 1 km within the whole shown altitude range from 12 to 30 km. Thus, air parcels at these altitudes are lifted by 1 km with corresponding influence on the dynamics in the model which was already demonstrated previously in this section.

The fact that the interaction back to the global domain has negligible influence on the potential temperature in the model emphasises that it is the two-way interaction which impacts the temperature and horizontal velocity. An artificial mountain wave is explicitly not induced in the global domain but the effect of the mountain wave can be represented in the global resolution of 160 km using the local grid refinement with two-way interaction. This is the general idea of parametrisations of subgrid-scale processes in atmospheric models and thus these results could be used to parametrise the effect of mountain-wave induced PSCs in the model as shown in the following sections.

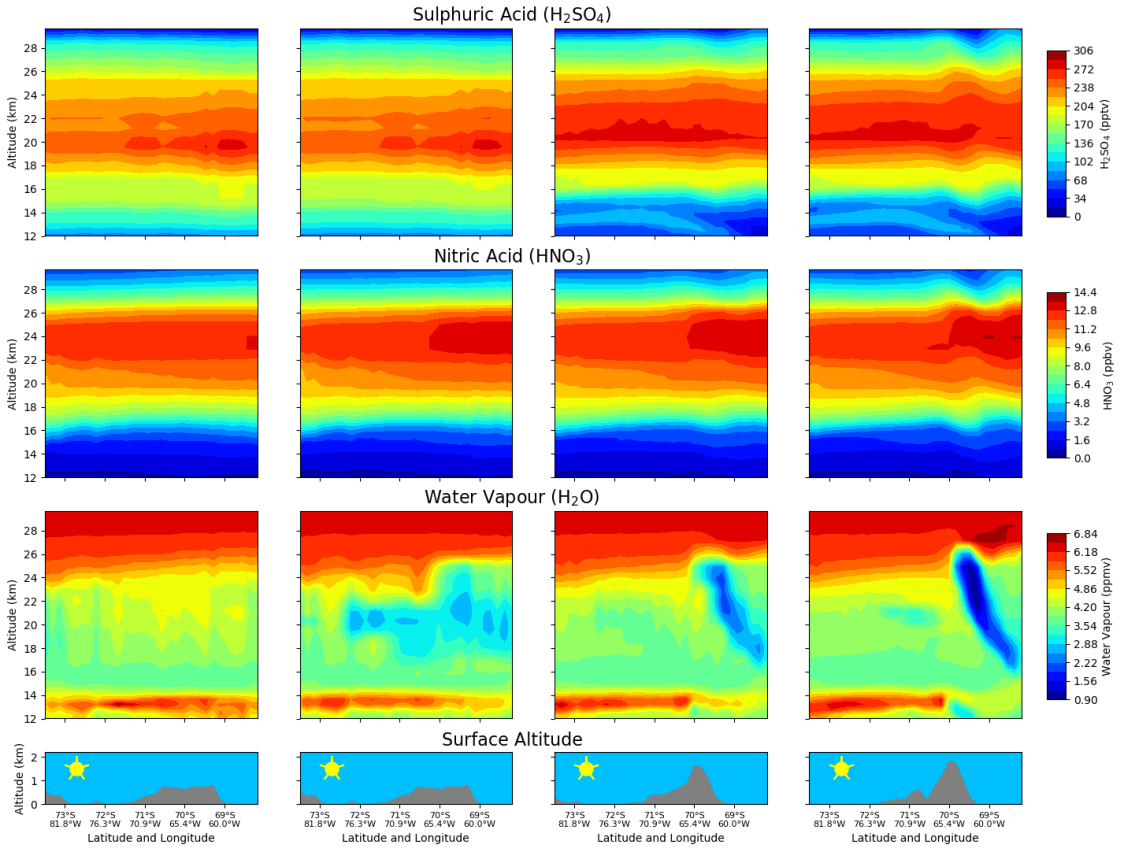

Figure 6.4: Sulphuric acid, nitric acid and water vapour volume mixing ratios around the Antarctic Peninsula. Figure concept as in Fig. 6.3.

6.2 Influence of the Mountain Wave on Long-lived Trace Gases

The different dynamics in the mountain wave, which was discussed in the previous section, also influence the chemistry in the model. In this section, the long-lived tracers H_2SO_4, HNO_3 and H_2O are investigated around the Antarctic Peninsula. They additionally interact with the composition of PSCs.

The influence of the mountain wave on these tracers can be found in Fig. 6.4 which has the same concept as Fig. 6.3 but with H_2SO_4 in the first row, HNO_3 in the second row and H_2O in the third row.

The volume mixing ratio of H_2SO_4 is prescribed in the global domains of the simulations. The prescribing is included at the very beginning of the ICON-ART time integration so that the influence of two-way nesting can be seen only within one time step of ICON-ART. This is why the difference between the panels in the two left columns are negligible for H_2SO_4.

In the nested domains of Fig. 6.4, H_2SO_4 runs freely. In the altitude range from 18 to 26 km, the volume mixing ratio of H_2SO_4 is by about 15 pptv larger than in the global domain. On the other hand, it is by factor of two lower at altitudes below 16 km. H_2SO_4 has no chemical sink in the atmosphere and the sedimentation of H_2SO_4 absorbed in aerosols is missing in the model. Thus,

these changes can only be explained by vertical or horizontal advection. The horizontal wind speed is larger around the Antarctic Peninsula than in other regions (not shown) which could indicate a divergent flow around the Antarctic Peninsula and at least partly explain the low H_2SO_4 values at altitudes below 16 km.

The mountain wave induces wave-like patterns also in H_2SO_4 in the two nested domains (right two columns in Fig. 6.4) that correspond to the patterns of the potential temperature (Fig. 6.3). As a long-lived tracer, H_2SO_4 is mainly changed by advection in the model. Thus, this demonstrates that the flow in the mountain wave is isentropic as already mentioned above.

Similar patterns also occur for HNO_3 (second row of Fig. 6.4) in the nested domains within the altitude range from 16 to 29 km. In contrast to H_2SO_4, HNO_3 is not prescribed so that the feedback processes due to the two-way nesting can be analysed with HNO_3.

In the global domain including the nests (second column), the HNO_3 volume mixing ratio in the altitude range from 23 to 25 km is by 1 ppbv larger than in the simulation without the nests (first column). This is a result of higher values in both nests in this altitude range. The reason for these enhanced values in HNO_3 are heterogeneous processes on the surface of mountain-wave induced PSCs which will be further discussed in the next sections.

Differences between the simulations with and without nests can be seen in gaseous H_2O in the model (third row in Fig. 6.4). In the lee of the mountain, the H_2O volume mixing ratio decreases to values lower than 2.8 ppmv where it is larger than 4 ppmv in the simulation without the nests. Due to the locally low temperatures in the mountain wave (Fig. 6.3), a large fraction of H_2O is converted to ice particles. This is shown in the right column of Fig. 6.4 where the H_2O volume mixing ratio is decreased to values lower than 1.3 ppmv in the mountain wave. The feedback due to the two-way nesting explains the reduced volume mixing ratios of H_2O in the global domain compared to the simulation without the nests.

In summary, the long-lived species, which are dominated by advection in the model, show similar patterns like the potential temperature in the mountain wave, i.e. showing the property of isentropic flow in the mountain wave. This is in accordance to the theory of mountain waves, as described in Sect. 2.2. In addition, the impact of mountain-wave induced PSCs on the shown species has been demonstrated: HNO_3 is formed by the heterogeneous reactions on PSCs and H_2O is converted to ice in the mountain wave. These processes are further discussed in the next sections.

6.3 The Formation of Polar Stratospheric Clouds in the Mountain Wave

The analysis of the trace gases, that are important for the formation of PSCs, in the last section already indicated that PSCs are formed in the mountain wave including a feedback to the global domain. The particle volume concentrations of STS, NAT and ice PSCs are illustrated in the three rows of Fig. 6.5.

STS droplets are calculated by a diagnostic parametrisation (first row of Fig. 6.5). Therefore, the STS particles in the nested domains are influenced by the changes of the related trace gases and the temperature in the mountain wave. As can be seen in comparison of the two global domains (two left columns in Fig. 6.5), the STS volume concentration is lower in the lee of the mountain in the

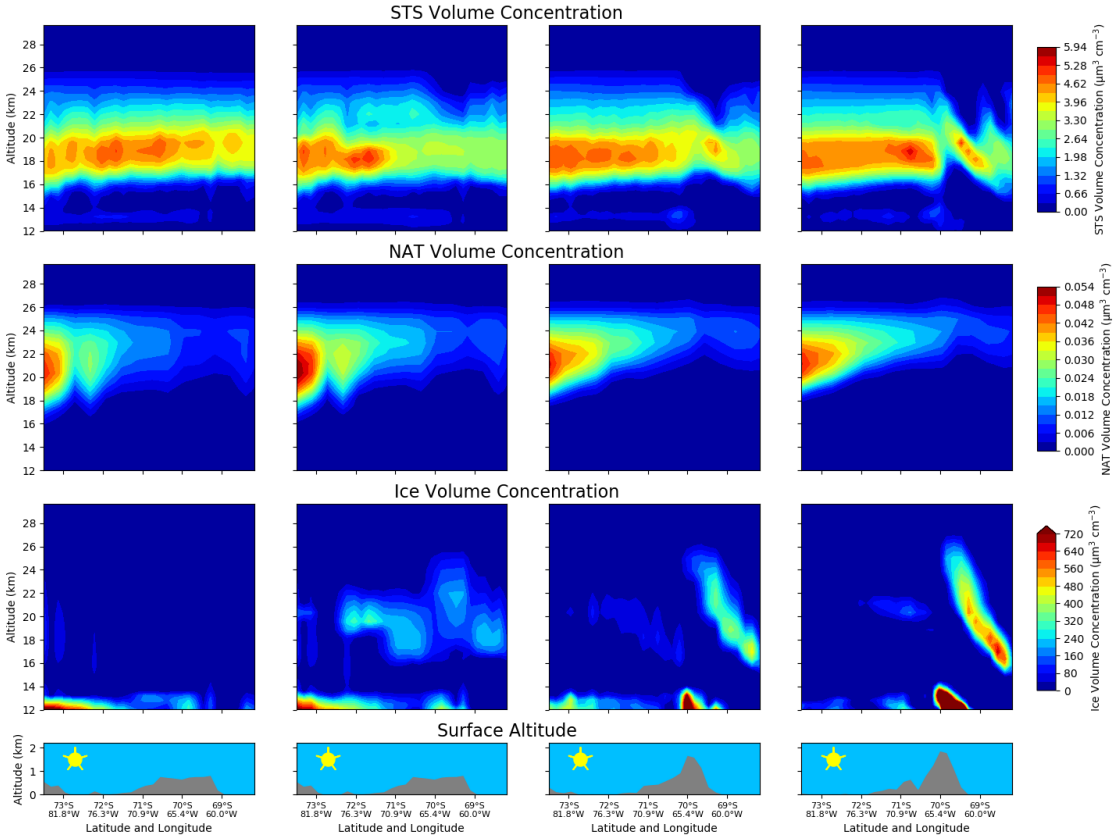

Figure 6.5: Particle volume concentrations of the three PSC types around the Antarctic Peninsula. Figure concept as in Fig. 6.3.

simulation with the nests than in the simulation without the nests. This is a result of the reduced fraction of H_2O that remains in the gas phase as discussed in the previous section. Confirmed by box model studies (not shown), the formation of STS particles is suppressed if water vapour is lower than 2 ppmv. Thus, STS particles with particle volume concentrations larger than 3 $\mu m^3\ cm^{-3}$ are formed in regions where the water vapour volume mixing ratio is above this limit.

The STS volume concentration in the global domain with nests is influenced by the mountain wave, especially at altitudes higher than 22 km where particle volume concentrations close to zero occur in the global domain which do not occur without the nesting technique. The influence of the mountain wave on STS is amplified within the nests. The STS particles are assumed to freeze at temperatures 3 K below the frost point (Engel et al., 2013) so that STS particles are formed in the mountain wave where the temperature is larger than this threshold.

The formation of NAT, shown in the second row of Fig. 6.5, demonstrates that the two-way nesting principally works for the NAT size bins of the kinetic parametrisation which are treated as passive tracers in the model. Apart from the general underestimation of the NAT volume concentration, which was already discussed in the previous chapter, the NAT volume concentration in the global domain with nests is by 0.02 $\mu m^3\ cm^{-3}$ larger than without nests in the longitude range from 76°W to 65°W where also these larger values occur in the nested domains (two right columns).

In contrast to the literature, the NAT volume concentration decreases when the air masses approach

the mountain wave. Since the NAT size bins are advected with the general air masses, the wave-like patterns occur in both nests. Most probably due to the missing gaseous H_2O (see Fig. 6.4), NAT cannot be formed in the mountain wave. In addition, NAT PSCs are formed by freezing STS particles in the mountain wave, as shown e.g. by Bertram et al. (2000) and Salcedo et al. (2001). This is not integrated in the model so far and should be considered in the future.

As already suggested by H_2O in Fig. 6.4, a large fraction of water vapour is resublimed in the ice phase in the mountain wave. This is shown in the third row of Fig. 6.5 where the ice volume concentration is depicted. Particle volume concentrations up to 720 $\mu m^3\ cm^{-3}$ occur at altitudes above 16 km in the Antarctic Peninsula nest, by two orders of magnitude larger than that of STS. These values are correlated with the temperatures lower than 185 K in the mountain wave and explain the descrease in water vapour in this region.

The two-way nesting in ICON-ART leads to increased ice volume concentrations in the global domain (second column) up to 200 $\mu m^3\ cm^{-3}$ in the lee of the mountain. The enhanced ice volume concentrations on the luv side (i.e. west side) of the mountain are remnants of previously formed ice clouds as shown in the nested domains. In the global domain without the nests (first column), no ice PSCs are formed.

This demonstrates that the two-way nesting in ICON-ART leads to formation of ice PSCs in the global domain where they cannot be simulated without the nests. In addition, this shows that the ice volume concentration can be at least locally larger in the nested domains in contrast to the global simulations of the previous chapter where the ice volume concentration was partly underestimated. The total PSC volume concentration in the mountain wave is dominated by ice particles which has been observed (e.g., Höpfner et al., 2018). Thus, a higher global resolution could help to improve the existence of ice particles in the lower stratosphere.

Altogether, this section showed that mountain-wave induced PSCs can be simulated with ICON-ART including the two-way nesting technique. Ice particles dominate the particle volume concentration of the PSCs in the mountain wave which is consistent with observations. The large fraction of water that is removed from the gas phase to form the ice particles leads to underrepresented STS and NAT particles. Thus, the interaction between the three PSC types, such as the formation of NAT by freezing of STS, should be considered in the future. The chlorine activation due to the simulated mountain-wave induced PSCs is investigated in the following section.

6.4 Impact of Mountain-Wave Induced Polar Stratospheric Clouds on Chlorine Activation

In the previous section, it was shown that ice PSCs with particle volume concentrations up to 720 $\mu m^3\ cm^{-3}$ form in the mountain wave around the Antarctic Peninsula. As mentioned in Sect. 6.1, the horizontal wavelength of the simulated mountain wave is in the oder of 450 km. In combination with horizontal velocities of around 60 $m\ s^{-1}$, this results in a residence time of air parcels in the cold part of the mountain wave of about 1 h. The large surfaces of the ice particles lead to an increased efficiency of the heterogeneous reactions in the mountain wave. The impact on chlorine activation is demonstrated in this section.

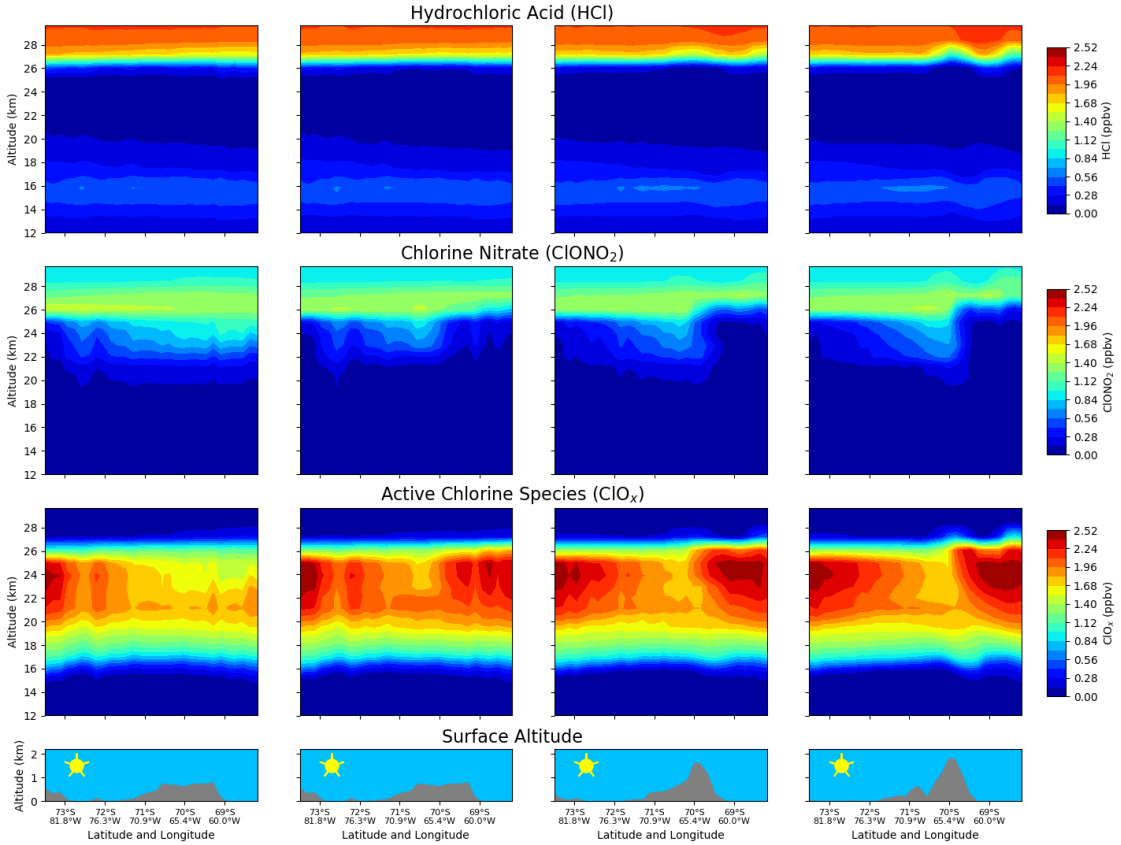

Figure 6.6: Chlorine species around the Antarctic Peninsula. Figure concept as in Fig. 6.3. ClO_x is calculated as defined in Eq. (5.32).

The volume mixing ratios of HCl, $ClONO_2$ and ClO_x around the Antarctic Peninsula are shown in the different rows of Fig. 6.6. The mountain wave in the end of July 2008 occurred close to the date of largest extent of the polar vortex, see Sect. 5.1. Thus, the major fraction of the chlorine reservoir species is already activated at this state of the polar vortex. This is shown in HCl where volume mixing ratios lower than 0.5 ppbv arise within the whole altitude range from 16 to 26 km of the mountain wave in all domains. Wave-like perturbations in the nested domains (two right panels) demonstrate that HCl is a relatively long-lived species transported with the background flow.

In contrast to HCl, which is already depleted in the altitude range of the mountain wave, remnant mixing ratios in the order of 1 ppbv occur for $ClONO_2$ in the simulation without the nests in 22 to 26 km (left column of Fig. 6.6). Due to the mountain-wave induced PSCs and the efficient heterogeneous reactions on their surface, the residence time of about 1 h in the cold part of the mountain wave suffices that $ClONO_2$ is nearly completely activated in the lee of the mountain resulting in values lower than 0.2 ppbv. In combination with the feedback of the mountain-wave induced ice PSCs, described in the previous section, and the feedback of $ClONO_2$ itself, the depletion of $ClONO_2$ is also represented in the global domain of the simulation including the nests (second column).

A corresponding increase of about 1 ppbv can be found in the volume mixing ratio of ClO_x in the lee of the mountain in all domains of the simulations with the nests. In the simulation without nests,

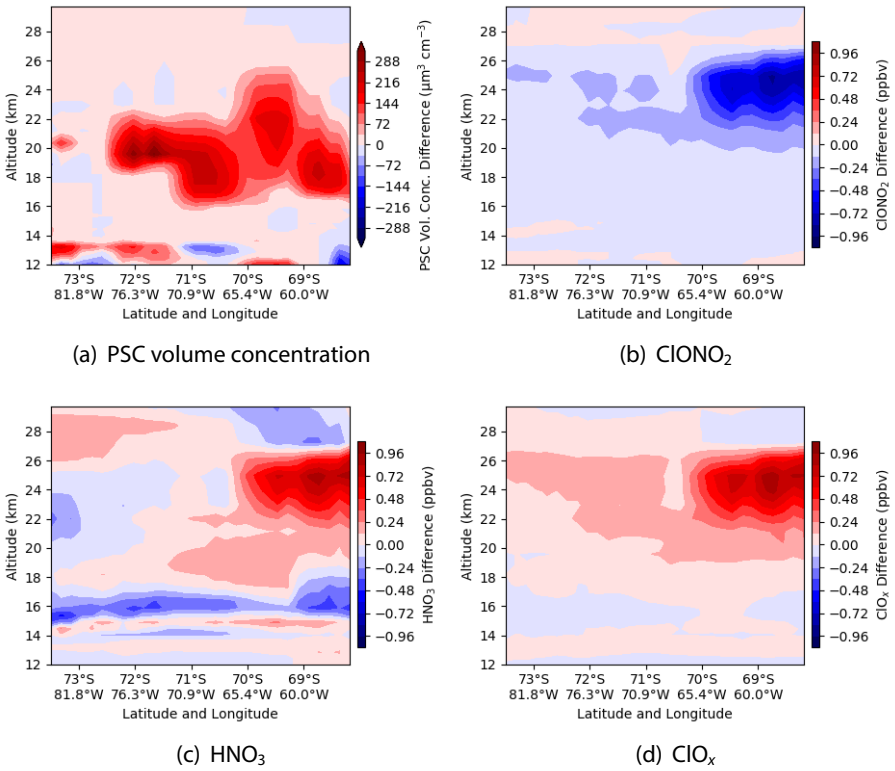

Figure 6.7: Difference in global domain between with and without nest around the Antarctic Peninsula. The difference is shown (a) for the total PSC volume concentration, and for the volume mixing ratios of (b) $ClONO_2$, (c) HNO_3 and (d) ClO_x. ClO_x is calculated as defined in Eq. (5.32). The same colour bars are used for the chemical species.

the volume mixing ratio of ClO_x decreases at altitudes from 24 to 26 km in the lee of the Antarctic Peninsula from 2.2 down to 1.6 ppbv. Thus, this demonstrates that with the two-way nesting in ICON-ART both PSCs and heterogeneous chemistry in the mountain wave can be represented in the global resolution of 160 km where this process cannot be simulated without the nests.

The impact of the two-way nesting is summarised in Fig. 6.7 where the difference of the global domains with and without nests of PSCs, $ClONO_2$, HNO_3 and ClO_x are depicted around the Antarctic Peninsula. For the total PSC volume concentration in Fig. 6.7(a), the particle volume concentrations of STS, NAT and ice are summed up in the global domains of the simulations with and without nests and subtracted subsequently. The total PSC volume concentration is dominated by ice originating from the flow around the mountain ridge of the Antarctic Peninsula. Therefore, differences in the order of 200 $\mu m^3\ cm^{-3}$ occur in the PSC volume concentration in the lee of the Antarctic Peninsula up to altitudes of 26 km.

At these altitudes, $ClONO_2$ is depleted (Fig. 6.7(b)) so that it is by 1 ppbv lower in the simulation with nests than without the nests in the altitude range from 24 to 26 km. $ClONO_2$ is heterogeneously depleted by Reacts. (R2.29) to (R2.31). In each reaction, HNO_3 is produced along with one active chlorine species. This is why both HNO_3 (Fig. 6.7(c)) and ClO_x (Fig. 6.7(d)) are increased in this altitude range by 1 ppbv.

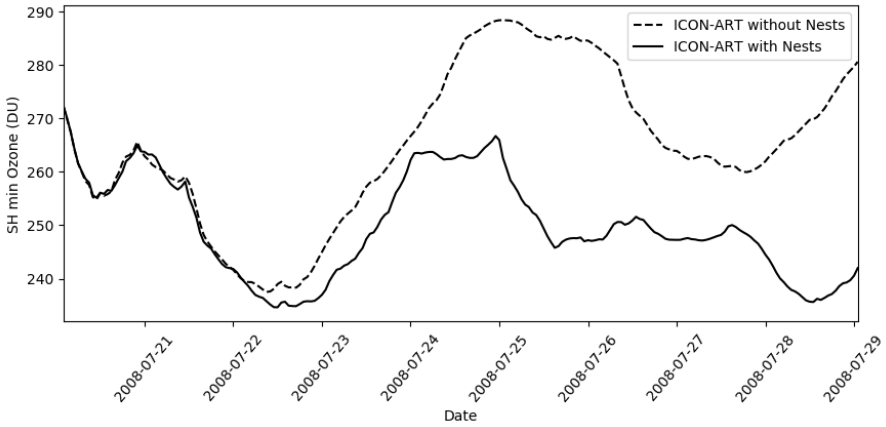

Figure 6.8: Time series of total column ozone in the global domain with and without nests. The southern hemispheric minimum total colum ozone in the global domain with and without the nests is shown, calculated by the same method as in Fig. 5.36.

As indicated by the subscript (a) in the heterogeneous reactions (R2.29) to (R2.39), the produced HNO_3 should be adsorbed on the surface of the particle. In the MECCA module, used to calculate the gas phase chemistry in ICON-ART including the heterogeneous chemistry, the produced HNO_3 is treated as gaseous compound. From a theoretical point of view, the HNO_3 should be evaporated from the particle with a time lag or it should be absorbed in the bulk of the particle after being produced heterogeneously. In the second case, it would influence the composition of the PSC particles. This is reflected indirectly in the model because higher volume mixing ratios of HNO_3 lead to larger PSC particles in the next time step. The integration of this process could be discussed in the future.

6.5 Impact of Mountain-Wave Induced Polar Stratospheric Clouds on Ozone

The mountain wave event at the Antarctic Peninsula took place in the end of July 2008. Thus, the polar vortex is at its maximum size during the event, as shown in Fig. 5.1. The simulation with nests lasts 10 days so that the impact on ozone is expected to be small since the activated chlorine species remain in the polar vortex until the radiation of the sun splits them up.

On the other hand, the Antarctic Peninsula reaches to latitudes as low as 69°S which most probably is at the edge of the polar vortex. Therefore, the activated chlorine species due to the mountain wave around the Antarctic Peninsula could affect ozone which is shown in Fig. 6.8. In this figure, the southern hemispheric minimum total ozone colum is shown as time series for the global domains with and without nests for the whole time period of the nest simulation.

Both time series in Fig. 6.8 coincide until 22 July. Then, the southern hemispheric minimum ozone of the simulation with nests is lower than without the nests until the end of the simulation. Differences up to 40 DU between the simulation appear during the progress of the simulation. This is an indication for higher activated chlorine species in this region, especially at the edge of the polar vortex where the sun is already elevated.

The Antarctic Peninsula is predestined to explain this higher burden of ClO_x in the atmosphere because the mountain wave is resolved in this region. Chlorine activation takes place in the mountain wave, as shown above. On the other hand, the attribution of the Antarctic Peninsula to the chlorine activation cannot be verified in this simulation because the Antarctic nest covers most of the southern hemisphere including other mountains. This has to be verified in future simulations, e.g. by a simulation with two nests close to the Antarctic Peninsula.

In summary, this section demonstrated that the chlorine activation due to the two-way nesting in ICON-ART has an impact on ozone in the global resolution. Most probably at the edge of the polar vortex, where the mountain wave around the Antarctic Peninsula could be simulated with ICON-ART, the rising sun and the higher burden of active chlorine lead to a decrease in ozone with respect to the simulation without the nests. The attribution of the Antarctic Peninsula should be further analysed in the future. In addition, the impact after the southern hemispheric winter should be investigated by simulations that cover longer time periods until at least begin of October.

Altogether, this chapter showed for the example of a mountain wave event in the end of July 2008 that mountain-wave induced PSCs can be directly simulated with ICON-ART. By using the two-way nesting technique of ICON-ART, the effects of the generated PSCs can be transferred back to the global domain where they cannot be represented without the refined grids. These effects include the formation of mountain-wave induced PSCs in the global domain as well as the heterogeneous chemistry on their surface which was shown to be consistently integrated in the model. In addition, the higher burden of activated chlorine leads to an ozone depletion in the model that is not represented in the simulation without the nests.

Further analysis of this event should include its comparison to measurement data such as satellite data. The dynamical structure of the mountain wave could be compared to measurements of the Atmospheric Infrared Sounder (AIRS, Hoffmann et al., 2017). Noel and Pitts (2012) characterised the mountain wave event in July 2008 with vertical wind speeds up to 7.8 m s^{-1} which should be verified in the ICON-ART simulations. The highly resolved CALIOP dataset is able to capture mountain-wave induced PSCs at the Antarctic Peninsula so that it could be used for a comparison of the structure of PSCs in the mountain wave.

7

Conclusions and Outlook

In this thesis, a scheme for polar stratospheric clouds (PSCs) has been implemented into the atmospheric chemistry model ICON-ART. Now, a comprehensive process chain for the realistic and interactive representation of stratospheric ozone are included in the model: the radiation-driven stratospheric ozone chemistry, emissions of chlorofluorocarbons and greenhouse gases (Weimer et al., 2017), their photolysis in the lower stratosphere and transport towards the poles due to the Brewer-Dobson circulation, heterogeneous reactions on the surface of PSCs during the polar night and the catalytic ozone depletion after sunrise. In contrast to the linearised ozone scheme, where ozone is depleted for temperatures smaller than 195 K and solar zenith angles larger than 92°, i.e. during the polar night, the interactive calculation is consistent with observed southern hemispheric ozone development.

ICON-ART is able to directly resolve mountain-wave induced PSCs with a feedback to a coarse resolution where this process cannot be represented. The limitation of horizontal resolution was one of the main constraints in recent studies of mountain-wave induced PSCs although it is known from observations and box model studies that they have a significant effect on the ozone depletion (e.g., Orr et al., 2015; Zhu et al., 2017).

In the PSC scheme of ICON-ART, the three known types of PSCs are represented: it was shown that ice PSCs can be simulated with the microphysics of the base model up to the lower stratosphere, especially in the mountain wave where large particles could be simulated. In climate configuration, uncertainties remain about the assumed size distribution of the cloud ice particles. Supercooled ternary solution droplets (STS) were demonstrated to be consistently integrated in the model because they showed the observed features of binary as well as ternary solution droplets. For nitric acid trihydrate (NAT) particles two parametrisations can be chosen: an approach in thermodynamic equilibrium and a non-equilibrium kinetic approach with a flexible size distribution so that denitrification can be adapted and investigated easily with the model.

This thesis showed the first example of the transition from horizontal resolutions used in current chemistry climate models towards the resolution necessary for the direct simulation of mountain-wave induced PSCs. For an exemplary mountain wave event in July 2008, it was demonstrated that mountain-wave induced PSCs can be directly simulated downstream of the Antarctic Peninsula.

This includes a two-way interaction with a coarse global resolution where the mountain-wave induced PSCs then have an impact on the ozone chemistry due to a higher burden of activated chlorine in the polar vortex. This could lead to a parametrisation of mountain-wave induced PSCs and their effect on the chemistry.

A time slice experiment as well as an ensemble simulation with 30 and 31 realisations of the year 2008 were conducted, respectively, and compared to reanalysis and observational data for a general evaluation of the PSC scheme in ICON-ART. By generating different realisations of the same year, the uncertainty range of the model dynamics can be derived and compared to reference data. It was shown that both time slice and ensemble experiments are able to simulate the dynamics of the polar vortex in comparison to ERA5 reanalysis data apart from the late spring where the polar vortex of 2008 showed exceptional features compared to other years. This also showed that ICON-ART can be used for detailed studies of one event as well as to large-scale multi-year simulations.

Polar stratospheric clouds lead to denitrification and chlorine activation, both influencing the polar ozone chemistry. The simulated dentrification was compared to flight measurements (Waibel et al., 1999) and it could be demonstrated that denitrification is captured by the model. Comparisons between the thermodynamic and kinetic NAT parametrisations showed that the thermodynamic NAT parametrisation suppresses the formation of STS particles. In comparison to MLS satellite data, it was shown that the denitrification due to the kinetic approach is too weak. Problems could be a general underestimation of gaseous HNO_3 and N_2O or limitations in the kinetic NAT parametrisation. In addition, it was shown that the HCl MLS measurements are within the uncertainty range of the ensemble simulation with ICON-ART in the time period of its minimum values. Thus, this demonstrated that chlorine activation is realistically represented by the model.

As a result, the southern hemispheric minimum ozone column of the ensemble simulation is within the range of the historical product of OMI satellite measurements assimilated into the MERRA reanalysis. In addition, some ensemble members are able to reflect the minimum ozone value of the specific year 2008 which could be traced back to the heterogeneous processes on PSCs.

Nevertheless, the NAT volume concentration is by at least one order of magnitude too small. Possible reasons could be the hard limits in the kinetic NAT parametrisations, as already mentioned above: NAT is sublimated for temperatures higher than 200 K and a minimum number of particles has to be generated to be really treated as NAT particles by the module. These limits should be reconsidered in the future as well as the initialisation of the relevant gases.

The underestimation of the NAT volume concentration in the model is one possible reason why the comparison to the MIPAS and CALIOP satellite instruments showed that the prevalent PSC types between model and measurements differ. In comparison to MIPAS measurements, the total PSC volume concentration in ICON-ART saturated at a specific value in high latitudes for temperatures lower than the typical PSC formation threshold. The underestimated NAT volume concentration could explain this difference. Another possible reason could be the different temperatures in the model compared to the measurements since the formation of PSCs is highly sensitive to the temperature. Local temperature deviations of up to 20 K between MIPAS and the ICON-ART simulation confirmed this assumption. Although the prevalent types differ, the yearly cycle of Antarctic PSCs is similar in comparison to the CALIOP measurements.

The ice number concentration should be set consistently to the microphysics of the model. In NWP configuration, it is set to a tropospheric value of 250 000 m^{-3} which is too large in comparison to measurements. In climate configuration, it is set to 10^4 m^{-3} which was measured before but most

probably is not consistent to the ice microphysics. Changes of these values mean changes in one the core modules of the dynamical model so that this should be discussed in the future.

In ICON-ART, the three PSC types are formed independently. Future developments with the PSC scheme in ICON-ART could involve the interaction of the formation between the three PSC types as well as the formation of the PSCs due to foreign nuclei. Hoyle et al. (2013) showed a parametrisation for NAT formation due to meteoric dust which has been implemented in CLaMS by Grooß et al. (2014). Its implementation in ICON-ART could improve the nucleation processes for NAT.

In addition, the heterogeneous nucleation of NAT and ice PSCs due to the existence of other PSCs could be considered in the future. Freezing STS droplets can result in NAT particles (e.g. Peter and Grooß, 2011). Due to the uptake of HNO_3 in ice particles, NAT particles can be formed (Iannarelli and Rossi, 2015). In addition, the heterogeneous reactions lead to gaseous HNO_3 but should be absorbed at least partly by the particle. In the model, this is reflected indirectly because higher HNO_3 lead to larger particles in the next time step. Its direct implementation could be discussed in the future. On the other hand, ice nucleation can be initiated by STS and NAT PSCs (e.g., Engel et al., 2013). The implementation of these processes could result in a more realistic distribution of the PSC types which was shown to differ from the MIPAS and CALIOP measurements in the ensemble simulation.

Although the different PSC types in ICON-ART are formed independently, they depend on the partitioning of the gaseous species H_2O and HNO_3 in the PSCs. Thus, the order of nucleation of the different PSC types should be further analysed in the future. In the model, ice nucleation is calculated before NAT and finally, STS is formed. This issue could be one explanation why NAT is not formed in the mountain wave: The uptake of gaseous water in ice results in low water vapour mixing ratios so that supersaturation with respect to NAT may not occur anymore. It could be investigated if an earlier start of the nests improves the NAT formation since NAT nucleation starts at higher temperatures. The issue with too low water vapour also holds for STS in the model which is calculated with a diagnostic parametrisation. Non-equilibrium processes, as suggested e.g. by Zhu et al. (2015), could be of importance especially in the mountain wave where STS particles take up large fractions of HNO_3 (e.g. Bertram et al., 2000). A parametrisation based on fluxes as suggested by Khosrawi (2001) for sulphate aerosols could be included in the future.

In comparison to MLS measurements, it was shown that long-lived trace gases such as N_2O are underestimated by a factor of up to two in southern high latitudes from 75°S to 90°S and within the pressure range from 46 to 4.6 hPa at the beginning of the simulation. With the implementation of the initialisation of these gases with MLS data, as used e.g. in CLaMS, the influence of this underestimation could be investigated further. In addition, H_2SO_4 is prescribed in the simulations by a climatology because of the missing sedimentation sink in the stratosphere. The STS module also covers binary solution droplets so that either a module like ISORROPIA (Fountoukis and Nenes, 2007) or the sedimentation of H_2SO_4 in the binary droplets could help to calculate H_2SO_4 interactively within the model.

This thesis presented the PSC occurrence and their interaction with the chemistry for the example of a southern hemispheric winter. In the northern hemisphere, the dynamics of PSCs and their influence highly depend on small-scale temperature fluctuations and thus on the correctly generated PSC types. Investigations including the two-way nesting technique could help to understand the processes that lead to Arctic ozone loss. This could be compared to Arctic measurement campaigns, such as Polar Stratosphere in a Changing Climate (POLSTRACC, e.g., Johansson et al., 2019).

In addition, the radiation feedback of ozone and its impact on the dynamics of the polar vortex could be further investigated in the future. This is one difference between the simulations performed in this thesis and which could be part of the explanation why the size of the polar vortex is lower than in ERA5 for the ensemble simulation in contrast to the other simulations.

In this context, the linearised ozone scheme used for simplified ozone simulations could be improved with respect to its calculation of the heterogeneous ozone depletion which occurs already during the polar night as mentioned above. The seasonal total amount of PSCs could be derived from temperature thresholds as shown in Fig. 5.3 for each grid point as sum over the winter period. This amount then could be used to calculate the lifetime of ozone after the sunrise.

Further investigations of the specific mountain wave event, especially its comparison to measurements, are needed to establish a parametrisation for mountain-wave induced PSCs in the coarser global resolution. This could include the comparison of the mountain wave to AIRS measurements, as shown e.g. by Hoffmann et al. (2017). The fine structures of mountain-wave induced PSCs during that event could be analysed with CALIOP measurements. The vertical wind speed of $7.2\,\mathrm{m\,s^{-1}}$ as mentioned by Noel and Pitts (2012) should be verified in the model. The radius and sedimentation velocity of the mountain-wave induced ice particles should be analysed in the future to get information about their impact on dehydration of the lower stratosphere.

In addition, the parametrisation of non-resolved mountain waves is switched on also in the nest around the Antarctic Peninsula with horizontal resolution of approx. 40 km because mountain waves with wavelengths smaller than about six times of this resolution cannot be resolved (e.g., Vosper et al., 2016). The difference between parametrised and not parametrised mountain waves could be investigated in the future.

Finally, the nesting used in this thesis could be adapted in sensitivity simulations. The ICON-ART nesting technique provides the possibility of nesting not only horizontally but also vertically. The impact of higher vertical resolution around the Antarctic Peninsula for this mountain wave event could be investigated. The influence of the two-way nesting outside the boundaries of the nests in the global domain could be examined. In addition, the horizontal nests could be adapted because the impact of the nests on chlorine activation could not definitely be traced back to the Antarctic Peninsula in this thesis. In order to investigate this, the two nests could be setup closely around the Antarctic Peninsula so that every change in the chemistry due to the nests could be traced back to this region.

Altogether, this thesis showed that PSCs can be simulated with ICON-ART and are in general agreement with observations, apart from the underestimation of NAT particles in the model which should be reconsidered in the future. Mountain-wave induced PSCs and their impact on the chemistry in the lower stratosphere could be consistently simulated with the model with a feedback to the global resolution. Thus, this thesis bridges the gap between directly simulated mountain-wave induced PSCs and their representation in coarse global resolutions which has been a challenge in the past.

Appendix

A

Unit Conversions

In this chapter, several unit conversion algorithms are described that are used in this thesis. Units where constant factors have to applied to get it in SI units are summarised in Table A.1.

A.1 Ozone Volume Mixing Ratio to Dobson Unit

For the transport in ICON-ART, all chemical tracers are treated as volume mixing ratios in mol mol^{-1}. Ozone is usually given as vertically integrated column values in Dobson units (DU). To convert the volume mixing ratio to DU it has to be converted to number concentration:

$$[\mathrm{O_3}]_m = X_{\mathrm{O_3},m} \frac{p_m N_\mathrm{A}}{R^* T_m} \tag{A.1}$$

In this equation, the index m depicts the height dependence of the respective variables. The number concentration is then integrated vertically to get the number of molecules above an area unit:

$$C_{\mathrm{O_3}} = \sum_{m=1}^{n_\mathrm{lev}} [\mathrm{O_3}]_m \Delta z_m \tag{A.2}$$

Table A.1: Conversion of units to SI units if constant factor can be applied.

Unit	SI Unit	Description
1 torr	133.322 Pa	Pressure
1 PVU	10^{-6} K m^2 kg^{-1} s^{-1}	Potential vorticity
1 ppmv	10^{-6} mol mol^{-1}	Volume mixing ratio
1 ppbv	10^{-9} mol mol^{-1}	Volume mixing ratio
1 pptv	10^{-12} mol mol^{-1}	Volume mixing ratio
1 ppmm	10^{-6} kg kg^{-1}	Mass mixing ratio

One Dobson unit is defined as the thickness of the ozone layer in 10^{-2} mm at the surface. Therefore, the ozone column of Eq. (A.2) has to be multiplied by the volume of a molecule at standard conditions ($T_0 = 273.15\,\mathrm{K}$ and $p_0 = 101\,325\,\mathrm{Pa}$):

$$V_{\mathrm{molecule},0} = \frac{R^* T_0}{N_\mathrm{A} p_0} \tag{A.3}$$

In the equations above, all variables have to be given in SI units. Therefore, the unit of the product of C_{O_3} and $V_{\mathrm{molecule},0}$ is metre. To get it in 10^{-2} mm (i.e. DU) it has to be multiplied by 10^5 accordingly:

$$C_{\mathrm{O}_3,\mathrm{DU}} = 10^5 V_{\mathrm{molecule},0} C_{\mathrm{O}_3} \overset{(A.3)}{=} 10^5 \frac{R^* T_0}{N_\mathrm{A} p_0} C_{\mathrm{O}_3} \approx 3.72 \times 10^{-21}\, C_{\mathrm{O}_3} \tag{A.4}$$

A.2 PSC Concentrations to Particle Volume Concentration

From satellites, PSC volume concentrations are measured (e.g., Höpfner et al., 2002). In ICON-ART, the particle volume concentration of STS particles is calculated internally, see Eq. (3.42). Ice and NAT PSCs are represented by the particle number concentration and the particle radius. In order to get the particle volume concentration, the particle number concentration has to be multiplied by the volume of each particle. By assuming spherical particles, this yields:

$$V_c = N_c \frac{4\pi r_c^3}{3}, \quad c \in \{\mathrm{ice}, \mathrm{NAT}\} \tag{A.5}$$

In case of the kinetic NAT parametrisation, NAT in each size bin is given as volume mixing ratio of HNO_3 in NAT. To get the total particle volume concentration of NAT PSCs from the volume mixing ratio of HNO_3 in NAT, it has to be divided by the molar volume of air $R^* T/p$ (in $\mathrm{m^3\,mol^{-1}}$) as well as by the density of NAT ρ_{NAT} (in $\mathrm{kg\,m^{-3}}$) and multiplied by the molar mass of NAT M_{NAT} (in $\mathrm{kg\,mol^{-1}}$):

$$V_{\mathrm{NAT}} = \frac{p}{R^* T} \frac{M_{\mathrm{NAT}}}{\rho_{\mathrm{NAT}}} \sum_{b=1}^{n_{\mathrm{bin}}} X_{\mathrm{HNO_3(NAT)},b} \tag{A.6}$$

This assumes that the number of moles of HNO_3 in NAT equals the number of moles of NAT. Since NAT (i.e. $HNO_3(H_2O)_3$) contains one HNO_3 molecule this assumption holds for a trihydrate particle.

B

The Diffusion Coefficient of HNO_3 in Air

For the sedimentation of PSCs, the diffusion coefficient of HNO_3 in air is one input parameter, see Eq. (3.23). The diffusion coefficient d_{12} of a dilute gas (gas 1 in gas 2) in $m^2\,s^{-1}$ can be calculated according to the following formula (e.g., Mason and Monchick, 1962; Reif, 1965):

$$d_{12} = \frac{0.002628 \times T^{\frac{3}{2}}}{p\,\sigma_{12}^2\,\Omega_{12}} \sqrt{\frac{M_1 + M_2}{M_1\,M_2}} \tag{B.1}$$

where T is temperature in K, p is pressure in mbar, σ_{12} is the characteristic length calculated by the Lennard-Jones potential to be given in Å and M_x are the molar masses of the two gases.

The collision integral Ω_{12} depends on temperature in a non-linear manner as well as on the gases (see e.g., Poling et al., 2001). This is why the temperature dependence of d_{12} differs from the given $T^{\frac{3}{2}}$ when Eq. (B.1) is used for two specified gases.

σ_{12} and Ω_{12} have not been measured yet for the mixture of HNO_3 in air. Therefore, it is assumed that the diffusion coefficient of water vapour can be transferred to that of HNO_3 so that the formula by Hall and Pruppacher (1976) can be applied:

$$d_{H_2O} = 0.211 \times 10^{-4} \left(\frac{T}{273.15}\right)^{1.94} \frac{101325}{p} \tag{B.2}$$

where temperature T and pressure p have to be given in K and Pa, respectively, to get d_{H_2O} in $m^2\,s^{-1}$. According to Hall and Pruppacher (1976), this equation is valid within the temperature range 193.15 K < T < 313.15 K. Pruppacher and Klett (1997), however, published its validity range as 233.15 K < T < 313.15 K referring to the same equation. With the range in Pruppacher and Klett (1997), PSCs as well as clouds in the upper troposphere could not be calculated by Eq. (B.2).

To derive Eq. (B.2), Hall and Pruppacher (1976) extrapolated measurements to temperatures below 273.15 K where no measurements are available. Equation (B.2) is the parametrisation used in other models for the diffusion coefficient of water vapour in air (e.g., Larsen, 2000; Zhu et al., 2015;

Eidhammer et al., 2017). Therefore, it is also calculated by Eq. (B.2) for temperatures of PSC occurrence in ICON-ART.

In order to transfer the diffusion coefficient of water vapour to that of HNO_3 the molar mass of water has to be replaced by the molar mass of HNO_3 in Eq. (B.1). This neglects the dependencies of σ_{12} and Ω_{12} on the mixture, resulting in the following equation:

$$d_{\mathrm{HNO_3}} = d_{\mathrm{H_2O}} \sqrt{\frac{\frac{M_{\mathrm{HNO_3}}+M_{\mathrm{air}}}{M_{\mathrm{HNO_3}}\,M_{\mathrm{air}}}}{\frac{M_{\mathrm{H_2O}}+M_{\mathrm{air}}}{M_{\mathrm{H_2O}}\,M_{\mathrm{air}}}}} = d_{\mathrm{H_2O}} \sqrt{\frac{M_{\mathrm{H_2O}}}{M_{\mathrm{HNO_3}}} \frac{M_{\mathrm{HNO_3}} + M_{\mathrm{air}}}{M_{\mathrm{H_2O}} + M_{\mathrm{air}}}} \tag{B.3}$$

By using the molar mass of dry air ($M_{\mathrm{air}} \approx 29.8\,\mathrm{g\,mol^{-1}}$) this results in a factor of 0.748 between $d_{\mathrm{HNO_3}}$ and $d_{\mathrm{H_2O}}$:

$$d_{\mathrm{HNO_3}} \approx 0.748\, d_{\mathrm{H_2O}} \tag{B.4}$$

Larsen (2000) calculated a relation between the diffusion coefficients of 0.559. This value, though, is the result if the square root in Eq. (B.3) is left out. On the other hand, Zhu et al. (2015) tuned Eq. (B.2) to measurements by Tang et al. (2014) which resulted in a factor of 0.466:

$$d_{\mathrm{HNO_3}} = 0.466\, d_{\mathrm{H_2O}} \tag{B.5}$$

Concluding, the diffusion coefficient of HNO_3 is uncertain because no measurements have been made so far for stratospheric conditions. As an appropriate estimation, the diffusion coefficient of H_2O is transferred to that of HNO_3. The factors between $d_{\mathrm{H_2O}}$ and $d_{\mathrm{HNO_3}}$ range from 0.748 down to 0.466. In ICON-ART, Equation (B.5) is used.

C

Stratospheric Chemistry Mechanism

In this appendix, the chemistry mechanism selected in MECCA and used for the ensemble and nest simulations is illustrated. This mechanism includes 142 reactions including 93 gas phase reactions (Table C.1), 38 photolysis reactions (Table C.2) and 11 heterogeneous reactions (Table C.3).

As mentioned in Sect. 2.1, atomic oxygen can exist in the atmosphere in two different states: the ground state and the excited state. The background of these states is briefly discussed in this appendix.

On atomic scales, quantum mechanics apply where properties such as orbital angular momentum (spin) are quantised. Electrons of atoms have a specific region where they stay most probably which are called orbitals. They can be expressed by the main and spin quantum number and usually are abbreviated by the letters s,p,d,f etc. Pauli's exclusion principle (Pauli, 1925) states that free electrons with same spin cannot share a subshell and must have a different spin number, i.e. 1/2 or −1/2 (up and down). This is why the configuration of electrons in an atom can be schematically illustrated by the rectangles and spin arrows as shown in Fig. C.1.

For the example of atomic oxygen, the first rule by Hund (1927) says that the lowest energy of the atom is the state where the multiplicity maximises. The multiplicity is given by $2s + 1$ where s is the sum of all electron spins. In Figure C.1(a), the multiplicity is 3 whereas in Fig. C.1(b) the multiplicity

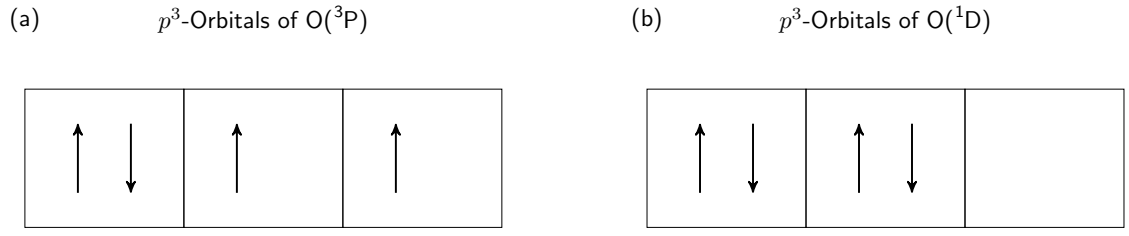

Figure C.1: Spin illustration of atomic oxygen. For atomic oxygen in ground state (panel a), all p orbitals are filled with at least one electron whereas the third orbital is empty in case of the excited state (panel b).

is 1. Thus, the spin configuration of Fig. C.1(a) represents the ground state, which is called triplet according to its multiplicity, written as $O(^3P)$.

If the oxygen atom is excited e.g. by a photon of correct energy (i.e. frequency), an electron can get a spin quantum number that differs from that corresponding to the lowest energy. Schematically, the electron fills the second p-orbital but with spin down of –1/2 according to Pauli's exclusion principle. According to Hund's rule, it has a higher energy than the ground state of oxygen and because of its multiplicity of 1 it is called singlet and written as $O(^1D)$.

Table C.1: Gas phase reactions. References for the formulae of the rate constants can be found in the MECCA description.

Reaction	Rate Constant
$O_2 + O(^1D) \rightarrow O(^3P) + O_2$	`3.3E-11*EXP(55./temp)`
$O_2 + O(^3P) \rightarrow O_3$	`6.E-34*((temp/300.)**(-2.4))*cair`
$O_3 + O(^1D) \rightarrow 2\ O_2$	`1.2E-10`
$O_3 + O(^3P) \rightarrow 2\ O_2$	`8.E-12*EXP(-2060./temp)`
$H + O_2 \rightarrow HO_2$	`k_3rd(temp,cair,4.4E-32,1.3,7.5E-11, -0.2,0.6)`
$H + O_3 \rightarrow OH + O_2$	`1.4E-10*EXP(-470./temp)`
$H_2 + O(^1D) \rightarrow H + OH$	`1.2E-10`
$OH + O(^3P) \rightarrow H + O_2$	`1.8E-11*EXP(180./temp)`
$OH + O_3 \rightarrow HO_2 + O_2$	`1.7E-12*EXP(-940./temp)`
$OH + H_2 \rightarrow H_2O + H$	`2.8E-12*EXP(-1800./temp)`
$HO_2 + O(^3P) \rightarrow OH + O_2$	`3.E-11*EXP(200./temp)`
$HO_2 + O_3 \rightarrow OH + 2\ O_2$	`1.E-14*EXP(-490./temp)`
$HO_2 + H \rightarrow 2\ OH$	`7.2E-11`
$HO_2 + H \rightarrow H_2 + O_2$	`6.9E-12`
$HO_2 + H \rightarrow O(^3P) + H_2O$	`1.6E-12`
$HO_2 + OH \rightarrow H_2O + O_2$	`4.8E-11*EXP(250./temp)`
$HO_2 + HO_2 \rightarrow H_2O_2 + O_2$	`k_HO2_HO2`
$H_2O + O(^1D) \rightarrow 2\ OH$	`1.63E-10*EXP(60./temp)`
$H_2O_2 + OH \rightarrow H_2O + HO_2$	`1.8E-12`
$N + O_2 \rightarrow NO + O(^3P)$	`1.5E-11*EXP(-3600./temp)`
$N_2 + O(^1D) \rightarrow O(^3P) + N_2$	`2.15E-11*EXP(110./temp)`
$N_2O + O(^1D) \rightarrow 2\ NO$	`7.25E-11*EXP(20./temp)`
$N_2O + O(^1D) \rightarrow N_2 + O_2$	`4.63E-11*EXP(20./temp)`
$NO + O_3 \rightarrow NO_2 + O_2$	`3.E-12*EXP(-1500./temp)`
$NO + N \rightarrow O(^3P) + N_2$	`2.1E-11*EXP(100./temp)`
$NO_2 + O(^3P) \rightarrow NO + O_2$	`5.1E-12*EXP(210./temp)`
$NO_2 + O_3 \rightarrow NO_3 + O_2$	`1.2E-13*EXP(-2450./temp)`
$NO_2 + N \rightarrow N_2O + O(^3P)$	`5.8E-12*EXP(220./temp)`
$NO_3 + NO \rightarrow 2\ NO_2$	`1.5E-11*EXP(170./temp)`
$NO_3 + NO_2 \rightarrow N_2O_5$	`k_NO3_NO2`
$N_2O_5 \rightarrow NO_2 + NO_3$	`k_NO3_NO2/(2.7E-27*EXP(11000./temp))`
$NO + HO_2 \rightarrow NO_2 + OH$	`3.3E-12*EXP(270./temp)`
$NO_2 + OH \rightarrow HNO_3$	`k_3rd(temp,cair,1.8E-30,3.0, 2.8E-11,0.,0.6)`

Table C.1: Gas phase reactions (... continued).

Reaction	Rate Constant
$NO_2 + HO_2 \rightarrow HNO_4$	k_NO2_HO2
$HNO_3 + OH \rightarrow H_2O + NO_3$	k_HNO3_OH
$HNO_4 \rightarrow NO_2 + HO_2$	k_NO2_HO2/(2.1E-27*EXP(10900./temp))
$HNO_4 + OH \rightarrow NO_2 + H_2O$	1.3E-12*EXP(380./temp)
$CH_4 + O(^1D) \rightarrow .75\ CH_3O_2 + .75\ OH + .25\ HCHO + .4\ H + .05\ H_2$	1.75E-10
$CH_4 + OH \rightarrow CH_3O_2 + H_2O$	1.85E-20* EXP(2.82*log(temp)-987./temp)
$CH_3O_2 + HO_2 \rightarrow CH_3OOH + O_2$	4.1E-13*EXP(750./temp)
$CH_3O_2 + NO \rightarrow HCHO + NO_2 + HO_2$	2.8E-12*EXP(300./temp)
$CH_3O_2 \rightarrow HCHO + HO_2$	2.*RO2*9.5E-14*EXP(390./temp)/ (1.+1./26.2*EXP(1130./temp))
$CH_3O_2 \rightarrow .5\ HCHO + .5\ CH_3OH + .5\ O_2$	2.*RO2*9.5E-14*EXP(390./temp)/ (1.+26.2*EXP(-1130./temp))
$CH_3OOH + OH \rightarrow .7\ CH_3O_2 + .3\ HCHO + .3\ OH + H_2O$	k_CH3OOH_OH
$HCHO + OH \rightarrow CO + H_2O + HO_2$	9.52E-18*EXP(2.03*log(temp) +636./temp)
$CO + OH \rightarrow H + CO_2$	(1.57E-13+cair*3.54E-33)
$Cl + O_3 \rightarrow ClO + O_2$	2.8E-11*EXP(-250./temp)
$ClO + O(^3P) \rightarrow Cl + O_2$	2.5E-11*EXP(110./temp)
$ClO + ClO \rightarrow Cl_2 + O_2$	1.0E-12*EXP(-1590./temp)
$ClO + ClO \rightarrow 2\ Cl + O_2$	3.0E-11*EXP(-2450./temp)
$ClO + ClO \rightarrow Cl + OClO$	3.5E-13*EXP(-1370./temp)
$ClO + ClO \rightarrow Cl_2O_2$	k_ClO_ClO
$Cl_2O_2 \rightarrow ClO + ClO$	k_ClO_ClO/(1.72E-27*EXP(8649./temp))
$Cl + H_2 \rightarrow HCl + H$	3.9E-11*EXP(-2310./temp)
$Cl + HO_2 \rightarrow HCl + O_2$	4.4E-11-7.5E-11*EXP(-620./temp)
$Cl + HO_2 \rightarrow ClO + OH$	7.5E-11*EXP(-620./temp)
$Cl + H_2O_2 \rightarrow HCl + HO_2$	1.1E-11*EXP(-980./temp)
$ClO + OH \rightarrow .94\ Cl + .94\ HO_2 + .06\ HCl + .06\ O_2$	7.3E-12*EXP(300./temp)
$ClO + HO_2 \rightarrow HOCl + O_2$	2.2E-12*EXP(340./temp)
$HCl + OH \rightarrow Cl + H_2O$	1.7E-12*EXP(-230./temp)
$HOCl + OH \rightarrow ClO + H_2O$	3.0E-12*EXP(-500./temp)
$ClO + NO \rightarrow NO_2 + Cl$	6.2E-12*EXP(295./temp)
$ClO + NO_2 \rightarrow ClNO_3$	k_3rd_iupac(temp,cair,1.6E-31,3.4, 7.E-11,0.,0.4)
$ClNO_3 + O(^3P) \rightarrow ClO + NO_3$	4.5E-12*EXP(-900./temp)
$ClNO_3 + Cl \rightarrow Cl_2 + NO_3$	6.2E-12*EXP(145./temp)
$Cl + CH_4 \rightarrow HCl + CH_3O_2$	6.6E-12*EXP(-1240./temp)
$Cl + HCHO \rightarrow HCl + CO + HO_2$	8.1E-11*EXP(-34./temp)
$Cl + CH_3OOH \rightarrow HCHO + HCl + OH$	5.9E-11
$ClO + CH_3O_2 \rightarrow HO_2 + Cl + HCHO$	3.3E-12*EXP(-115./temp)

Table C.1: Gas phase reactions (... continued).

Reaction	Rate Constant
$CCl_4 + O(^1D) \rightarrow ClO + 3\ Cl$	`3.3E-10`
$CH_3Cl + O(^1D) \rightarrow OH + Cl$	`1.65E-10`
$CH_3Cl + OH \rightarrow H_2O + Cl$	`2.4E-12*EXP(-1250./temp)`
$CH_3CCl_3 + O(^1D) \rightarrow OH + 3\ Cl$	`3.E-10`
$CH_3CCl_3 + OH \rightarrow H_2O + 3\ Cl$	`1.64E-12*EXP(-1520./temp)`
$CF_2Cl_2 + O(^1D) \rightarrow ClO + Cl$	`1.4E-10`
$CFCl_3 + O(^1D) \rightarrow ClO + 2\ Cl$	`2.3E-10`
$Br + O_3 \rightarrow BrO + O_2$	`1.7E-11*EXP(-800./temp)`
$BrO + O(^3P) \rightarrow Br + O_2$	`1.9E-11*EXP(230./temp)`
$BrO + BrO \rightarrow 2\ Br + O_2$	`2.7E-12`
$BrO + BrO \rightarrow Br_2 + O_2$	`2.9E-14*EXP(840./temp)`
$Br + HO_2 \rightarrow HBr + O_2$	`7.7E-12*EXP(-450./temp)`
$BrO + HO_2 \rightarrow HOBr + O_2$	`4.5E-12*EXP(500./temp)`
$HBr + OH \rightarrow Br + H_2O$	`6.7E-12*EXP(155./temp)`
$HOBr + O(^3P) \rightarrow OH + BrO$	`1.2E-10*EXP(-430./temp)`
$Br_2 + OH \rightarrow HOBr + Br$	`2.0E-11*EXP(240./temp)`
$BrO + NO \rightarrow Br + NO_2$	`8.7E-12*EXP(260./temp)`
$BrO + NO_2 \rightarrow BrNO_3$	`k_BrO_NO2`
$Br + HCHO \rightarrow HBr + CO + HO_2$	`7.7E-12*EXP(-580./temp)`
$CH_3Br + OH \rightarrow H_2O + Br$	`2.35E-12*EXP(-1300./temp)`
$BrO + ClO \rightarrow Br + OClO$	`1.6E-12*EXP(430./temp)`
$BrO + ClO \rightarrow Br + Cl + O_2$	`2.9E-12*EXP(220./temp)`
$BrO + ClO \rightarrow BrCl + O_2$	`5.8E-13*EXP(170./temp)`
$SO_2 + OH \rightarrow H_2SO_4 + HO_2$	`k_3rd(temp,cair,3.3E-31,4.3,1.6E-12, 0.,0.6)`

Table C.2: Photolysis reactions. Photolysis rates are computed by the Cloud-J module (Prather, 2015).

Reaction
$O_2 + h\nu \rightarrow O(^3P) + O(^3P)$
$O_3 + h\nu \rightarrow O(^1D) + O_2$
$O_3 + h\nu \rightarrow O(^3P) + O_2$
$H_2O + h\nu \rightarrow H + OH$
$H_2O_2 + h\nu \rightarrow 2\ OH$
$N_2O + h\nu \rightarrow O(^1D) + N_2$
$NO_2 + h\nu \rightarrow NO + O(^3P)$
$NO + h\nu \rightarrow N + O(^3P)$
$NO_3 + h\nu \rightarrow NO_2 + O(^3P)$
$NO_3 + h\nu \rightarrow NO + O_2$
$N_2O_5 + h\nu \rightarrow NO_2 + NO_3$
$HNO_3 + h\nu \rightarrow NO_2 + OH$
$HNO_4 + h\nu \rightarrow .667\ NO_2 + .667\ HO_2 + .333\ NO_3 + .333\ OH$

Table C.2: Photolysis reactions (... continued).

Reaction
$CH_3OOH + h\nu \rightarrow HCHO + OH + HO_2$
$HCHO + h\nu \rightarrow H_2 + CO$
$HCHO + h\nu \rightarrow H + CO + HO_2$
$CO_2 + h\nu \rightarrow CO + O(^3P)$
$CH_4 + h\nu \rightarrow CO + 0.31\ H + 0.69\ H_2 + 1.155\ H_2O$
$Cl_2 + h\nu \rightarrow Cl + Cl$
$Cl_2O_2 + h\nu \rightarrow 2\ Cl$
$OClO + h\nu \rightarrow ClO + O(^3P)$
$HOCl + h\nu \rightarrow OH + Cl$
$ClNO_2 + h\nu \rightarrow Cl + NO_2$
$ClNO_3 + h\nu \rightarrow Cl + NO_3$
$ClNO_3 + h\nu \rightarrow ClO + NO_2$
$CH_3Cl + h\nu \rightarrow Cl + CH_3O_2$
$CCl_4 + h\nu \rightarrow 4\ Cl$
$CH_3CCl_3 + h\nu \rightarrow 3\ Cl$
$CFCl_3 + h\nu \rightarrow 3\ Cl$
$CF_2Cl_2 + h\nu \rightarrow 2\ Cl$
$Br_2 + h\nu \rightarrow Br + Br$
$BrO + h\nu \rightarrow Br + O(^3P)$
$HOBr + h\nu \rightarrow Br + OH$
$BrNO_3 + h\nu \rightarrow 0.85\ Br + 0.85\ NO_3 + 0.15\ BrO + 0.15\ NO_2$
$CH_3Br + h\nu \rightarrow Br + CH_3O_2$
$CF_3Br + h\nu \rightarrow Br$
$BrCl + h\nu \rightarrow Br + Cl$
$CF_2ClBr + h\nu \rightarrow Br + Cl$

Table C.3: Heterogeneous reactions. The rate constants are calculated by the PSC scheme in ICON-ART as described in Sect. 3.5.

Reaction
$N_2O_5 + H_2O \rightarrow 2\ HNO_3$
$HOCl + HCl \rightarrow Cl_2 + H_2O$
$ClNO_3 + HCl \rightarrow Cl_2 + HNO_3$
$ClNO_3 + H_2O \rightarrow HOCl + HNO_3$
$N_2O_5 + HCl \rightarrow ClNO_2 + HNO_3$
$HOBr + HBr \rightarrow Br_2 + H_2O$
$BrNO_3 + H_2O \rightarrow HOBr + HNO_3$
$ClNO_3 + HBr \rightarrow BrCl + HNO_3$
$BrNO_3 + HCl \rightarrow BrCl + HNO_3$
$HOCl + HBr \rightarrow BrCl + H_2O$
$HOBr + HCl \rightarrow BrCl + H_2O$

List of Symbols and Abbreviations

Variables, Latin Letters

ΔA	m^2	Area of a triangle of the ICON grid, Eq. (3.32) 46
C_C	–	Cunningham factor for slip flow correction between continuum and kinetic regime, Eq. (2.24) 15
C_{O_3}	m^{-2}	Column ozone concentration, Eq. (A.2) 129
$d^*_{HNO_3,b}$	$m^2\,s^{-1}$	Diffusion coefficient of HNO_3 in air accounting for non-continuum effects, Eq. (3.23) 43
D_c	m	Collision diameter of molecules in a binary gas mixture, Eq. (2.28) 23
D_g	m	Median diameter of the particle size distribution, Eq. (2.16) 13
D_c	m	Diameter D of particle c, Eq. (2.16) 13
d_i	$m^2\,s^{-1}$	Diffusion coefficient of gaseous species i in air, Eq. (2.23) 14
d_{12}	$m^2\,s^{-1}$	Diffusion coefficient of gas 1 in gas 2 , Eq. (B.1) 131
$\mathbf{f}$	$N\,kg^{-1}$	Sum of mass specific external forces, Eq. (2.5) 6
$\mathbf{f}_F$	$N\,kg^{-1}$	Frictional forces on the Earth, Eq. (2.6) 7
f	s^{-1}	Absolute vorticity of the air, Eq. (3.4) 27
G_b	$m^2\,s^{-1}$	Growth factor for a growing NAT particle in size bin b, Eq. (3.21) . 43
h_{top}	m	Top altitude of ICON NWP microphysics 36
J	s^{-1}	Photolysis rate 12
Kn	–	Knudsen number, Eq. (2.20) 14
k	s^{-1} or cm^3s^{-1}	Reaction rate constant, Eq. (2.14) 12
K_h	$m^2\,s^{-2}$	Horizontal component of the specific kinetic energy, Eq. (3.4) 27
$k_{het,r,c}$	$cm^3\,s^{-1}$	Heterog. reaction rate const. of PSC type c and reaction r, Eq. (2.26)22
m_c	kg	Particle mass of PSC type c, Eq. (2.23) 14
M_i	$kg\,mol^{-1}$	Molar mass of gaseous species i, Eq. (2.23) 14
Δn_{NAT}	mol	Number of moles of HNO_3 in NAT that are subtracted from level above, Eq. (3.30) 46
$N(D_c)$	$m^{-3}\,\mu m^{-1}$	Infinitesimal particle number conc. at diameter D_c, Eq. (2.16) 13
$N_{NAT,cur}$	m^{-3}	Particle number conc. of NAT using the minimum radius, Eq. (3.17)42
$N_{NAT,max,0}$	m^{-3}	Maximum particle number conc. of original size bin, Eq. (5.6) 82
$N_{NAT,max,1}$	m^{-3}	Max. particle number conc. of the new smaller size bin, Eq. (5.9) . 82
$N_{NAT,max,2}$	m^{-3}	Max. particle number conc. of the new larger size bin, Eq. (5.9) . . . 82
$N_{NAT,max}$	m^{-3}	Maximum particle number concentration of NAT 42
N_t	m^{-3}	Total particle number conc. of the size distribution, Eq. (2.16) 13

N_c	m^{-3}	Particle number concentration of particle c, Eq. (2.19) 13
$n_{air,m}$	mol	Number of moles of air at level m, Eq. (3.30) 46
$n_{falling,m}$	mol	Fraction of NAT particles that sediment from vertical level m into vertical level $m+1$, Eq. (3.30) 46
$N_{j(r)}$	m^{-3}	Number conc. of gaseous reactant in heterog. reaction r, Eq. (2.26) 22
p	Pa	Air pressure, Eq. (2.5) 6
p_i	Pa	Partial pressure of gaseous species i, Eq. (2.21) 14
$p_{sat,i}$	Pa	Saturation vapour pressure of species i, Eq. (2.21) 14
PV	PVU	Potential vorticity of the air, Eq. (2.9) 8
Q	s^{-1}	Source and sink term for temperature, Eq. (3.4) 27
Q_I	$K\,s^{-1}$	Source term for temperature due to radiation of the sun, Eq. (2.5) . . 6
Q_w	$K\,s^{-1}$	Source term for temperature due to water change of state, Eq. (2.5) . 6
r_0	m	Mean radius of original size bin, Eq. (5.6) 82
r_1	m	Mean radius of the new smaller size bin, Eq. (5.9) 82
r_2	m	Mean radius of the new larger size bin, Eq. (5.9) 82
r_l	m	Lower boundary radius of original size bin, Eq. (5.12) 82
r_r	m	Upper boundary radius of original size bin, Eq. (5.12) 82
r_b	m	NAT particle radius in size bin b, Eq. (3.22) 43
r_c	m	Radius of particle c, Eq. (2.20) 14
R_{532}	–	Ratio of total and molecular backscatter coefficient at 532 nm 62
$\Delta s_{NAT,m}$	m	Distance how far NAT particles sediment within Δt, Eq. (3.30) . . . 46
S_{STS}	$\mu m^2\,cm^{-3}$	Liquid particle surface concentration of STS, Eq. (2.29) 23
S_c	$m^2\,m^{-3}$	Particle surface concentration of particle c, Eq. (2.19) 13
s_p	m	Distance to the neighbour grid point p, Eq. (4.1) 64
Δt	s	Advective model time step, Eq. (3.25) 44
Δt_{start}	s	Time lag of nest to start after the parent domain 29
T	K	Air temperature, Eq. (2.1) 5
t	s	Time, Eq. (2.5) 6
$\mathbf{v}$	$m\,s^{-1}$	Three-dimensional air velocity, Eq. (2.5) 6
$\overline{v}_i$	$m\,s^{-1}$	Expected value of Maxwell-Boltzmann distributed thermal velocities of air molecules, Eq. (2.27) 23
v_n	$m\,s^{-1}$	Horizontal air velocity perpendicular to triangle edge, Eq. (3.4) . . . 27
V_{STS}	$\mu m^3\,cm^{-3}$	Liquid particle volume concentration on STS, Eq. (3.36) 48
v_t	$m\,s^{-1}$	Horizontal air velocity tangential to triangle edge , Eq. (3.4) 27
V_c	$m^3\,m^{-3}$	Particle volume concentration of particle c, Eq. (2.19) 13
$v_{t,c}$	$m\,s^{-1}$	Terminal sedimentation velocity of PSC type c, Eq. (2.24) 15
$v_{b,m}$	$m\,s^{-1}$	Sedimentation velocity of NAT particles in size bin b and at the vertical level m, Eq. (3.28) 45
w	$m\,s^{-1}$	Vertical wind velocity of the air, Eq. (3.4) 27
W_0	$kg\,m^{-3}$	Particle mass concentration of original size bin, Eq. (5.6) 82

W_1	$\mathrm{kg\,m^{-3}}$	Particle mass conc. of the new smaller size bin, Eq. (5.9) 82
W_2	$\mathrm{kg\,m^{-3}}$	Particle mass conc. of the new larger size bin, Eq. (5.9) 82
W_{ice}	$\mathrm{kg\,kg^{-1}}$	Water mass mixing ratio in cloud ice, Eq. (3.9) 39
$W_{\mathrm{STS,tot}}$	$\mathrm{kg\,m^{-3}}$	Liquid particle mass concentration, Eq. (3.41) 50
x	$\mathrm{m^2\,s^{-1}}$	Summary of variables that do not depend on the radius in the growth factor, Eq. (5.23) 85
x_1	–	Fraction of $N_{\mathrm{NAT,max,1}}/N_{\mathrm{NAT,max,0}}$, Eq. (5.9) 82
x_2	–	Fraction of $N_{\mathrm{NAT,max,2}}/N_{\mathrm{NAT,max,0}}$, Eq. (5.9) 82
X_i	$\mathrm{mol\,mol^{-1}}$	Volume mixing ratio of gaseous species i in air 87
$X_{i(c)}$	$\mathrm{mol\,mol^{-1}}$	Volume mixing ratio of gasous species i partitioned in PSC type c with respect to the air, Eq. (3.7) 35
Δz_m	m	Distance between vertical model levels m and $m+1$, Eq. (3.30) . . . 46
z	m	Geometric altitude, Eq. (2.1) 5

Variables, Greek Letters

α	–	Accommodation coefficient, Eq. (2.23) 14
β	$\mathrm{m^{-1}}$	Absorption or extinction coefficient, Eq. (3.38) 48
$\beta_{\perp,532}$	$\mathrm{m^{-1}}$	Backscatter coeff. with perpendicular polarisation at 532 nm 62
ε	differs	Generalised vertical coordinate (p or z), Eq. (4.3) 64
η	$\mathrm{kg\,m^{-1}\,s^{-1}}$	Dynamic viscosity of the air, Eq. (2.24) 15
$\gamma_{r,c}$	–	Uptake coefficient or reaction probability on PSC type c in heterogeneous reaction r, Eq. (2.26) 22
λ	m	Wave length, Eq. (2.25) 16
λ_{mfp}	m	Mean free path of air, Eq. (2.28) 23
λ_p	rad	Longitude of the grid point p, Eq. (4.1) 64
ν	$\mathrm{s^{-1}}$	Frequency of the light 12
ν_{B}	$\mathrm{s^{-1}}$	Brunt-Väisälä frequency, Eq. (2.11) 10
Ω_{12}	–	Collision integral for the diffusion coefficient, Eq. (B.1) 131
φ_p	rad	Latitude of the grid point p, Eq. (4.1) 64
π	–	Exner function, Eq. (3.5) 27
ψ	differs	ICON-ART variable to be interpolated, Eq. (4.1) 64
ρ	$\mathrm{kg\,m^{-3}}$	Air density, Eq. (2.5) 6
ρ_c	$\mathrm{kg\,m^{-3}}$	Particle density of PSC type c, Eq. (2.24) 15
σ_{g}	–	Standard deviation of the particle size distribution, Eq. (2.16) 13
σ_{12}	Å	Characteristic length for the diffusion coefficient , Eq. (B.1) 131
τ	s	Tracer lifetime, Eq. (2.13) 11
θ	K	Potential temperature, Eq. (2.8) 7
θ_{v}	K	Virtual potential temperature, Eq. (3.4) 27
$\boldsymbol{\zeta}$	$\mathrm{s^{-1}}$	Three-dimensional relative vorticity of the air, Eq. (2.10) 8

ζ	s^{-1}	Relative vorticity of the air, Eq. (3.4) 27

Subscripts and Counters

b	Counter of size bins in kinetic NAT parametrisation, Eq. (3.21) 43
c	PSC type specifier, Eq. (2.23) 14
i	Gaseous species identifier, Eq. (2.23) 14
$i(r)$	Gaseous reactant in heterogeneous reaction r, Eq. (2.26) 22
$j(r)$	Adsorbed reactant in heterogeneous reaction r, Eq. (2.26) 22
$\mathbf{k}$	Local vertical unity vector, Eq. (2.6) 7
m	Vertical level specifier, Eq. (3.28) 45
n	Direction perpendicular to triangle edge (m), Eq. (3.4) 27
n_{bin}	Number of size bins in kinetic NAT parametrisation, Eq. (3.26) 44
n_{lev}	Number of model levels, Eq. (A.2) 129
p	Index of the neighbour grid point, Eq. (4.1) 64
r	Reaction number of heterogeneous reaction, Eq. (2.26) 22
s	Total spin quantum number of an atom 134

Constants

A	Factor in Arrhenius equation ($cm^3\ s^{-1}$), Eq. (2.15) 12
a^*	Derived parameter for getting the particle surface number concentration from the particle volume concentration, Eq. (3.39) 50
A_{ice}	Factor in ice parametrisation (2663.5), Eq. (3.6) 35
a_{NAT}	Parameter in calculation of the saturation vapour pressure over NAT, Eq. (3.15) . 41
a_{SV}	Parameter for derivation of the particle surface number concentration from the particle volume concentration, Eq. (3.36) 48
a_S	Parameter for derivation of the particle surface number concentration from the extinction coefficient, Eq. (3.38) 48
a_V	Parameter for derivation of the particle volume number concentration from the extinction coefficient, Eq. (3.38) 48
b^*	Derived parameter for getting the particle surface number concentration from the particle volume concentration, Eq. (3.39) 50
B_{ice}	Summand in ice parametrisation (12.537), Eq. (3.6) 35
b_{NAT}	Parameter in calculation of the saturation vapour pressure over NAT, Eq. (3.15) . 41
b_{SV}	Parameter for derivation of the particle surface number concentration from the particle volume concentration, Eq. (3.36) 48
b_S	Parameter for derivation of the particle surface number concentration from the extinction coefficient, Eq. (3.38) 48
b_V	Parameter for derivation of the particle volume number concentration from the extinction coefficient, Eq. (3.38) 48
c_{pd}	Specific heat capacity of dry air for constant pressure ($1004.64\ J\,kg^{-1}\,K^{-1}$), Eq. (2.8)7
c_{vd}	Specific heat capacity of dry air for constant volume ($717.60\ J\,kg^{-1}\,K^{-1}$), Eq. (3.4) 27

$\hat{E}$	Activation energy in Arrhenius equation (J mol^{-1}), Eq. (2.15) 12
g	Graviational acceleration on Earth (9.806 65 m s^{-2}), Eq. (2.6) 7
h	Planck's constant (6.626×10^{-23} J s) 12
M_{air}	Molar mass of dry air (0.028 970 kg mol^{-1}), Eq. (3.17) 42
M_{NAT}	Molar mass of NAT (0.117 059 kg mol^{-1}), Eq. (3.21) 43
$M_{\mathrm{H_2O}}$	Molar mass of H_2O (0.018 015 4 kg mol^{-1}), Eq. (3.41) 50
$M_{\mathrm{H_2SO_4}}$	Molar mass of H_2SO_4 (0.098 078 kg mol^{-1}), Eq. (3.41) 50
N_{A}	Avogadro constant ($6.022\,141\,79 \times 10^{23}$ mol^{-1}), Eq. (2.28) 23
$\mathbf{\Omega}$	Angular velocity vector of the Earth (abs. value 7.29 rad s^{-1}), Eq. (2.6) 7
p_0	Pressure at standard conditions (101 325 Pa), Eq. (A.3) 130
p_{00}	Standard pressure for potential temperature (1000 hPa), Eq. (2.8) 7
ρ_{NAT}	Crystal mass density of NAT (1.626×10^3 kg m^{-3}), Eq. (3.21) 43
R^*	Universal constant of an ideal gas (8.314 472 J mol^{-1} K^{-1}), Eq. (2.15) 12
R_{d}	Gas constant of dry air (287.04 J kg^{-1} K), Eq. (2.5) 6
r_{min}	Minimum radius of NAT particles in thermodynamic parametrisation (0.1 µm), Eq. (3.17) 42
T_0	Temperature at standard conditions (273.15 K), Eq. (A.3) 130
$V_{\mathrm{molecule,0}}$	Volume of an air molecule at standard conditions (m^3), Eq. (A.3) 130

Abbreviations

AIRS	Atmospheric infrared sounder 121
AMIP	Atmospheric model intercomparison project 53
ART	Aerosols and reactive trace gases 3
CALIOP	Cloud-aerosol lidar with orthogonal polarisation 62
CALIPSO	Cloud-aerosol lidar and infrared pathfinder satellite observation 62
CFCs	Chlorofluorocarbons 17
CLaMS	Chemical lagrangian model of the stratosphere 47
CMIP	Coupled model intercomparison project 32
COSMO	Consortium for small-scale modeling 47
DWD	Deutscher Wetterdienst (German Weather Service) 25
ECCAD	Emissions of atmospheric compounds & compilation of ancillary data 33
ECHAM	ECMWF and Hamburg 33
ECMWF	European Centre for Medium-Range Weather Forecasts 32
EDGAR	Emissions database for global atmospheric research 32
EMAC	ECHAM/MESSy atmospheric chemistry 33
Envisat	Environmental satellite 61
ERA	ECMWF reanalysis 59
ESA	European Space Agency 61
GEIA	Global emissions initiative 32

GEMS	Global and regional earth-system (atmosphere) monitoring using satellite and in-situ data . . . 55
GEOS	Goddard earth observing system . . . 60
GFED	Global fire emissions database . . . 32
GMI	Global modeling initiative . . . 33
ICON	Icosahedral non-hydrostatic modelling framework . . . 3
IFS	Integrated forecasting system . . . 32
KASIMA	Karlsruhe simulation model of the middle atmosphere . . . 47
KPP	Kinetic preprocessor . . . 32
LES	Large eddy simulation . . . 25
LINOZ	Linearised ozone . . . 55
MACC	Monitoring atmospheric composition and climate . . . 32
MACCity	MACC/CityZEN EU projects . . . 32
MECCA	Module efficiently calculating the chemistry of the atmosphere . . . 29
MEGAN	Model of emissions of gases and aerosols from nature . . . 32
MERRA	Modern-era retrospective analysis for research and applications . . . 60
MESSy	Modular earth submodel system . . . 33
MIPAS	Michelson interferometer for passive atmospheric sounding . . . 61
MLS	Microwave limb sounder . . . 62
MPI	Message passing interface . . . 28
MPI-M	Max-Planck-Institute for Meteorology . . . 25
NAD	Nitric acid dihydrate . . . 21
NAT	Nitric acid trihydrate . . . 20
NWP	Numerical weather prediction . . . 25
ODE	Ordinary differential equation . . . 32
OMI	Ozone monitoring instrument . . . 62
PSCs	Polar stratospheric clouds . . . 1
SAGE	Stratospheric aerosol and gas experiment . . . 32
SI	Système international d'unités . . . 129
SIC	Sea ice cover . . . 54
SPARC	Stratosphere-troposphere processes and their role in climate . . . 68
SST	Sea surface temperature . . . 54
STS	Supercooled ternary solution . . . 20
TOMS	Total ozone mapping spectrometer . . . 63
UNEP	United Nations Environment Programme . . . 1
UV	Ultra-violet . . . 1
WACCM	Whole atmosphere community climate model . . . 47
XML	Extensible markup language . . . 28

Acknowledgements

Mein herzlicher Dank gilt zunächst Prof. Dr. Peter Braesicke für die Übernahme des Referats dieser Arbeit, sowie PD Dr. Michael Höpfner für die Übernahme des Korreferats. Ich habe mich zu jeder Zeit sehr gut durch euch betreut gefühlt und eure Rückmeldungen zu meiner Arbeit waren immer eine Bereicherung. Außerdem bedanke ich mich bei Prof. Dr. Martin Frank und Prof. Dr. Achim Streit für die sehr gute Arbeitsatmosphäre am SCC.

Des Weiteren möchte ich mich bei Dr. Ole Kirner, Dr. Roland Ruhnke und Dr. Jennifer Schröter ganz herzlich für das Korrekturlesen und die konstruktive Kritik an meiner Arbeit bedanken, die mir immer geholfen hat, die Arbeit zu überdenken und zu verbessern. Insbesondere möchte ich mich bei dir, Roland, für das Ausleihen von Kugelschreibern und Schmierblättern bedanken, die ich nach unseren zahlreichen Gesprächen mitnehmen durfte, meist gefüllt mit vielen weiteren Ideen. Vielen Dank auch an Dr. Marco Berghoff, der mir die LaTeX-Vorlage für diese Arbeit zur Verfügung gestellt hat! Damit hat mir das Schreiben zu jeder Zeit Freude bereitet und mir die Arbeit deutlich erleichtert.

Bedanken möchte ich mich auch bei Dr. Andrew Orr vom British Antarctic Survey für das Organisieren eines Workshops genau zu dem Thema dieser Doktorarbeit. Auch bei Dr. Lars Hoffmann vom Forschungszentrum Jülich möchte ich mich bedanken, mit dem ich bei dem Workshop insbesondere über das untersuchte Schwerewellen-Ereignis reden konnte. Der Workshop hat mir die Relevanz meiner Arbeit noch einmal verdeutlicht und mich in den letzten Monaten zusätzlich motiviert. Ich hoffe, dass diese Arbeit unsere Kooperation stärkt und Anhaltspunkte für eine weitere Zusammenarbeit bietet.

Große Teile dieser Arbeit wurden auf dem Supercomputer ForHLR II ausgeführt, der vom Ministerium für Wissenschaft, Forschung und Kunst Baden-Württemberg und vom Bundesministerium für Bildung und Forschung gefördert wird. Außerdem bedanke ich mich für den Beitrag des Bundeslandes Baden-Württemberg durch bwHPC und der dadurch möglichen Nutzung des bwUniClusters. Ich bedanke mich bei der ECCAD Datenbank für die Archivierung und Verteilung der Emissionsdaten.

Die Auswertungen in dieser Arbeit wurden mit Hilfe der Programmiersprache Python erstellt. Deren intuitive Bedienung und als trotzdem umfassende Programmiersprache sowie die große Nutzer-Community im Internet ermöglichten erst die schnelle Auswertung der Daten, speziell gegen Ende dieser Arbeit. Im Speziellen möchte ich mich bei Uğur Çayoğlu und Dr. Jennifer Schröter bedanken, die mir mit ihrem großen Vorwissen bei Problemen verschiedenster Art immer wieder geholfen haben.

Des Weiteren bedanke ich mich bei allen Kollegen des Simlabs Klima und Umwelt am Steinbuch Centre for Computing und der MOD-Gruppe des Instituts für Meteorologie und Klimaforschung, insbesondere bei Dr. Roland Ruhnke, Dr. Ole Kirner, Dr. Björn-Martin Sinnhuber, Dr. Thomas Reddmann, Dr. Jennifer Schröter, Dr. Johannes Eckstein, Christian Scharun, Carmen Ullwer

und Hanna Guggenberger. Euer Feedback und eure Erfahrung haben mich immer wieder in meiner Arbeit weitergebracht. Bedanken möchte ich mich auch bei Christopher Diekmann für das Bereitstellen einer seiner Abbildungen aus seiner Masterarbeit.

Meinen Kollegen hier am SCC möchte ich auch meinen ganz persönlichen Dank aussprechen. Mit dir, Thorsten Zirwes, konnte ich viel über Chemie und deren numerische Implementierung diskutieren. Daneben haben auch unsere gemeinsamen Kinobesuche meinen Horizont immer wieder erweitert. Das Diskutieren mit dir, Maren Hattebuhr, über die Einflussgrößen des Klimawandels und auch über meine Arbeit haben mir sehr geholfen, die komplexen Fragestellungen meiner Arbeit herunterzubrechen. Dies war auch in den beiden Science Slams möglich, die Dr. Eileen Kühn und Dr. Marco Berghoff organisiert hatten. Dadurch habe auch ich ein besseres Verständnis meiner Arbeit gefunden, was mir sehr geholfen hat. Die fachlichen Gresprächе mit dir, Dr. Marco Berghoff, haben mir zusätzlich ein allgemeineres Verständnis der mathematischen Modellierung gegeben. Außerdem warst du in Sachen MPI mein erster Anprechpartner. Bei euch, Dr. Marco Berghoff, Mehmet Soysal, Dr. Marcus Strobl und Maren Hattebuhr, möchte ich mich sehr für die schöne gemeinsame Zeit bedanken, in der wir viel miteinander erlebt haben. Durch euch habe ich das Bouldern und Klettern kennen gelernt und bei vielen Ausflügen und gemeinsamen Abenden hatten wir viel Spaß miteinander.

Dir, Dr. Jennifer Schröter, gebührt auch mein ganz besonderer Dank. Du hattest immer ein offenes Ohr für mich und konntest mir bei Problemen in vielerlei Hinsicht weiterhelfen. Bei Fragen, was das Modell anging, die python betrafen, die mit Fortran und Vim zu tun hatten, aber auch in generellen Fragen zu Promotion und und und ... warst du mir eine große Hilfe. Auch die nahezu täglichen Spaziergänge auf dem Campus Nord gegen Ende der Doktorarbeit haben mir sehr gut getan.

Dass ich in den vergangenen Jahren auch Musik machen konnte, hat meinen Alltag sehr bereichert. Dazu möchte ich mich bei meinem Orgellehrer Christian-Markus Raiser bedanken, der mich in den Jahren meiner Doktorarbeit geduldig in das Orgelspielen eingeführt hat, sowie beim Uni-Orchester Collegium Musicum des KIT unter der Leitung von Hubert Heitz, in dem ich mich neben der Doktorarbeit auch immer ausleben und Ausgleich finden konnte. Das Spielen mit Dr. Sebastian Rast vom Max-Planck-Institut für Meteorologie begeistert mich auch immer wieder. Vielen Dank dafür! Es freut mich ebenfalls, dass ich in diesen Jahren meine kompositorische Kreativität ausleben konnte und diese inzwischen nicht nur mir Freude bereitet.

Meinen Eltern, Andrea und Peter, und meinem Bruder Tobias gilt ebenfalls mein besonderer Dank. Mit euch konnte ich immer über alles reden, in schwierigeren wie in guten Zeiten. Das hat mich immer motiviert und gestärkt.

Die Begleitung von dir, Katharina Müller, in der Endphase der Doktorarbeit war für mich von unschätzbarem Wert. Du hattest immer das richtige Gefühl, was gerade gut für mich war, und warst immer für mich da. Es ist so schön, dass wir uns kennen gelernt haben, und wir schon so viel gemeinsam erleben durften.

Bibliography

Alexander, M. J., M. Geller, C. McLandress, S. Polavarapu, P. Preusse, F. Sassi, K. Sato, S. Eckermann, M. Ern, A. Hertzog, Y. Kawatani, M. Pulido, T. A. Shaw, M. Sigmond, R. Vincent, and S. Watanabe (2010). *Recent developments in gravity-wave effects in climate models and the global distribution of gravity-wave momentum flux from observations and models*. Quarterly Journal of the Royal Meteorological Society 136 (650), 1103–1124. DOI: 10.1002/qj.637 (cit. on p. 11).

Alexander, S. P., A. R. Klekociuk, M. C. Pitts, A. J. McDonald, and A. Arevalo-Torres (2011). *The effect of orographic gravity waves on Antarctic polar stratospheric cloud occurrence and composition*. Journal of Geophysical Research: Atmospheres 116 (D6). DOI: 10.1029/2010JD015184 (cit. on pp. 2, 11).

Arnold, F. (1992). *Stratospheric Aerosol Increases and Ozone Destruction: Implications from Mass Spectrometer Measurements*. Berichte der Bunsengesellschaft für physikalische Chemie 96 (3), 339–350. DOI: 10.1002/bbpc.19920960321 (cit. on p. 20).

Arrhenius, S (1889). *Über die Reaktionsgeschwindigkeit bei der Inversion von Rohrzucker durch Säuren*. Zeitschrift für Physikalische Chemie 4U (1), 226–248. DOI: 10.1515/zpch-1889-0416 (cit. on p. 12).

Austin, J., D. Shindell, S. R. Beagley, C. Brühl, M. Dameris, E. Manzini, T. Nagashima, P. Newman, S. Pawson, G. Pitari, E. Rozanov, C. Schnadt, and T. G. Shepherd (2003). *Uncertainties and assessments of chemistry-climate models of the stratosphere*. Atmospheric Chemistry and Physics 3 (1), 1–27. DOI: 10.5194/acp-3-1-2003 (cit. on p. 68).

Bacmeister, J. (1993). *Mountain-Wave Drag in the Stratosphere and Mesosphere Inferred from Observed Winds and a Simple Mountain-Wave Parameterization Scheme*. Journal of the Atmospheric Sciences 50 (3), 377–399. DOI: 10.1175/1520-0469(1993)050<0377:MWDITS>2.0.CO;2 (cit. on p. 2).

Bacmeister, J. T., P. A. Newman, B. L. Gary, and K. R. Chan (1994). *An Algorithm for Forecasting Mountain Wave-Related Turbulence in the Stratosphere*. Weather and Forecasting 9 (2), 241–253. DOI: 10.1175/1520-0434(1994)009<0241:AAFFMW>2.0.CO;2 (cit. on p. 2).

Barton, R. A., R. A. Cox, and T. J. Wallington (1984). *Novel ultraviolet product spectra in the photolysis of chlorine dioxide*. J. Chem. Soc., Faraday Trans. 1 80 (10), 2737–2743. DOI: 10.1039/F19848002737 (cit. on p. 17).

Bates, D. and M. Nicolet (1965). *Atmospheric hydrogen*. Planetary and Space Science 13 (9), 905 –909. DOI: https://doi.org/10.1016/0032-0633(65)90175-3 (cit. on p. 16).

Beckert, M., E. R. Wouters, M. N. R. Ashfold, and E. Wrede (2003). *High resolution ion imaging study of BrCl photolysis in the wavelength range 330–570 nm*. The Journal of Chemical Physics 119 (18), 9576–9589. DOI: 10.1063/1.1615951 (cit. on p. 17).

Bender, S., M. Sinnhuber, P. J. Espy, and J. P. Burrows (2019). *Mesospheric nitric oxide model from SCIAMACHY data*. Atmospheric Chemistry and Physics 19 (4), 2135–2147. DOI: 10.5194/acp-19-2135-2019 (cit. on p. 103).

Bertram, A. K., D. B. Dickens, and J. J. Sloan (2000). *Supercooling of type 1 polar stratospheric clouds: The freezing of submicron nitric acid aerosols having HNO_3 mol fractions less than 0.5*. Journal of Geophysical Research: Atmospheres 105 (D7), 9283–9290. DOI: 10.1029/1999JD901174 (cit. on pp. 21, 117, 125).

Bevilacqua, R. M., M. D. Fromm, J. M. Alfred, J. S. Hornstein, G. E. Nedoluha, K. W. Hoppel, J. D. Lumpe, C. E. Randall, E. P. Shettle, E. V. Browell, C. Butler, A. Dörnbrack, and A. W. Strawa (2002). *Observations and analysis of polar stratospheric clouds detected by POAM III during the 1999/2000 Northern Hemisphere winter*. Journal of Geophysical Research: Atmospheres 107 (D20). 8281, SOL 24–1–SOL 24–18. DOI: 10.1029/2001JD000477 (cit. on pp. 19, 22).

Biele, J., A. Tsias, B. P. Luo, K. S. Carslaw, R. Neuber, G. Beyerle, and T. Peter (2001). *Nonequilibrium coexistence of solid and liquid particles in Arctic stratospheric clouds*. Journal of Geophysical Research: Atmospheres 106 (D19), 22991–23007. DOI: 10.1029/2001JD900188 (cit. on p. 20).

Bönisch, H., A. Engel, T. Birner, P. Hoor, D. W. Tarasick, and E. A. Ray (2011). *On the structural changes in the Brewer-Dobson circulation after 2000*. Atmospheric Chemistry and Physics 11 (8), 3937–3948. DOI: 10.5194/acp-11-3937-2011 (cit. on pp. 7, 8).

Borchert, S., G. Zhou, M. Baldauf, H. Schmidt, G. Zängl, and D. Reinert (2019). *The upper-atmosphere extension of the ICON general circulation model (version: ua-icon-1.0)*. Geoscientific Model Development 12 (8), 3541–3569. DOI: 10.5194/gmd-12-3541-2019 (cit. on p. 26).

Braathen, G and M. Proffitt (2000). *Polar vortex climatology from the ECMWF ERA-15 data*. In: *SPARC 2nd General Assembly, At Mar del Plata, Argentina*. DOI: 10.13140/RG.2.1.2344.4640 (cit. on p. 66).

Braesicke, P., J. Neu, V. Fioletov, S. Godin-Beekmann, D. Hubert, I. Petropavlovskikh, M. Shiotani, and B.-M. Sinnhuber (2018). "Chapter 3: Update on Global Ozone: Past, Present, and Future". In: *Scientific Assessment of Ozone Depletion: 2018*. Ed. by D. W. Fahey, P. A. Newman, J. A. Pyle, and B. Safari. World Meteorological Organization, Geneva, Switzerland: Global Ozone Research and Monitoring Project – Report No. 58 (cit. on p. 1).

Brasseur, G. and S. Solomon (1986). *Aeronomy of the Middle Atmosphere*. Second edition. Atmospheric sciences library. Dordrecht: D. Reidel Publishing Company (cit. on p. 105).

Brewer, A. W. (1949). *Evidence for a world circulation provided by the measurements of helium and water vapour distribution in the stratosphere*. Quarterly Journal of the Royal Meteorological Society 75 (326), 351–363. DOI: 10.1002/qj.49707532603 (cit. on p. 7).

Buchholz, J. (2005). *Simulations of Physics and Chemistry of Polar Stratospheric Clouds with a General Circulation Model*. PhD thesis. Mainz, Germany: Johannes-Gutenberg University (cit. on pp. 35, 40, 42, 45, 47).

Butchart, N. and A. J. Charlton-Perez (2010). "Stratospheric Dynamics". In: *SPARC CCMVal Report on the Evaluation of Chemistry-Climate Models*. Ed. by V. Eyring, T. Shepherd, and D. Waugh. Vol. No. 5. SPARC Office, 426 pp. (Cit. on p. 68).

Cariolle, D. (1983). *The ozone budget in the stratosphere: Results of a one-dimensional photochemical model*. Planetary and Space Science 31 (9), 1033 –1052. DOI: https://doi.org/10.1016/0032-0633(83)90093-4 (cit. on p. 16).

Carslaw, K. S., B. P. Luo, S. L. Clegg, T. Peter, P. Brimblecombe, and P. J. Crutzen (1994). *Stratospheric aerosol growth and HNO_3 gas phase depletion from coupled HNO_3 and water uptake by liquid particles*. Geophysical Research Letters 21 (23), 2479–2482. DOI: 10.1029/94GL02799 (cit. on pp. 19, 20, 48, 49, 50, 77).

Carslaw, K. S., S. L. Clegg, and P. Brimblecombe (1995a). *A Thermodynamic Model of the System HCl-HNO_3-H_2SO_4-H_2O, Including Solubilities of HBr, from < 200 to 328 K*. J. Phys. Chem. 99 (29), 11557–11574. DOI: 10.1021/j100029a039 (cit. on pp. 20, 47).

Carslaw, K. S., B. Luo, and T. Peter (1995b). *An analytic expression for the composition of aqueous HNO_3-H_2SO_4 stratospheric aerosols including gas phase removal of HNO_3*. Geophys. Res. Lett. 22 (14), 1877–1880. DOI: 10.1029/95GL01668 (cit. on pp. 20, 47, 48, 51, 79).

Carslaw, K. S., M. Wirth, A. Tsias, B. P. Luo, A. Dörnbrack, M. Leutbecher, H. Volkert, W. Renger, J. T. Bacmeister, and T. Peter (1998). *Particle microphysics and chemistry in remotely observed mountain polar stratospheric clouds*. Journal of Geophysical Research: Atmospheres 103 (D5), 5785–5796. DOI: 10.1029/97JD03626 (cit. on pp. 2, 19, 21).

Carslaw, K. S., J. A. Kettleborough, M. J. Northway, S. Davies, R.-S. Gao, D. W. Fahey, D. G. Baumgardner, M. P. Chipperfield, and A. Kleinböhl (2002). *A vortex-scale simulation of the growth and sedimentation of large nitric acid hydrate particles*. Journal of Geophysical Research: Atmospheres 107 (D20). 8300, SOL 43–1–SOL 43–16. DOI: 10.1029/2001JD000467 (cit. on pp. 21, 42, 43, 44, 45, 85).

Chapman, S. (1930). *A Theory of Upper-Atmospheric Ozone*. Memoirs of the Royal Meteorological Society 3, 103–125 (cit. on pp. 1, 15, 16).

Chipperfield, M. P., S. S. Dhomse, W. Feng, R. McKenzie, G. J. Velders, and J. A. Pyle (2015). *Quantifying the ozone and ultraviolet benefits already achieved by the Montreal Protocol*. Nature communications 6, 7233 (cit. on p. 19).

Cionni, I., V. Eyring, J. F. Lamarque, W. J. Randel, D. S. Stevenson, F. Wu, G. E. Bodeker, T. G. Shepherd, D. T. Shindell, and D. W. Waugh (2011). *Ozone database in support of CMIP5 simulations: results and corresponding radiative forcing*. Atmospheric Chemistry and Physics 11 (21), 11267–11292. DOI: 10.5194/acp-11-11267-2011 (cit. on p. 56).

Considine, D. B., A. R. Douglass, P. S. Connell, D. E. Kinnison, and D. A. Rotman (2000). *A polar stratospheric cloud parameterization for the global modeling initiative three-dimensional model and its response to stratospheric aircraft*.

Journal of Geophysical Research: Atmospheres 105 (D3), 3955–3973. DOI: 10.1029/1999JD900932 (cit. on pp. 20, 21, 33, 40, 43, 47).

Cooper, W. A. (1986). *Ice Initiation in Natural Clouds*. Meteorological Monographs 43, 29–32. DOI: 10.1175/0065-9401-21.43.29 (cit. on pp. 35, 36).

Crutzen, P. J. (1970). *The influence of nitrogen oxides on the atmospheric ozone content*. Quarterly Journal of the Royal Meteorological Society 96 (408), 320–325. DOI: 10.1002/qj.49709640815 (cit. on pp. 1, 16).

– (1971). *Ozone production rates in an oxygen-hydrogen-nitrogen oxide atmosphere*. Journal of Geophysical Research 76 (30), 7311–7327. DOI: 10.1029/JC076i030p07311 (cit. on p. 16).

Crutzen, P. and F Arnold (1986). *Nitric acid cloud formation in the cold Antarctic stratosphere: a major cause for the springtime 'ozone hole'*. Nature 324, 651–655. DOI: 10.1038/324651a0 (cit. on p. 21).

Cunningham, E. M. (1910). *On the velocity of steady fall of spherical particles through fluid medium*. Proceedings of the Royal Society of London A: Mathematical, Physical and Engineering Sciences 83 (563), 357–365. DOI: 10.1098/rspa.1910.0024 (cit. on pp. 14, 15).

Cunnold, D. M., P. J. Fraser, R. F. Weiss, R. G. Prinn, P. G. Simmonds, B. R. Miller, F. N. Alyea, and A. J. Crawford (1994). *Global trends and annual releases of CCl_3F and CCl_2F_2 estimated from ALE/GAGE and other measurements from July 1978 to June 1991*. Journal of Geophysical Research: Atmospheres 99 (D1), 1107–1126. DOI: 10.1029/93JD02715 (cit. on p. 33).

Dalton, J. (1802). "On the expansion of elastic fluids by heat". In: *Memoirs of the Literary and Philosophical Society of Manchester*. Vol. 5. 2. Princeton University: The Society (cit. on p. 14).

Damian, V., A. Sandu, M. Damian, F. Potra, and G. R. Carmichael (2002). *The kinetic preprocessor KPP-a software environment for solving chemical kinetics*. Computers & Chemical Engineering 26 (11), 1567 –1579. DOI: 10.1016/S0098-1354(02)00128-X (cit. on p. 32).

Danilin, M. Y. and J. C. McConnell (1995). *Stratospheric effects of bromine activation on/in sulfate aerosol*. Journal of Geophysical Research: Atmospheres 100 (D6), 11237–11243. DOI: 10.1029/95JD00999 (cit. on p. 22).

Davies, S., M. P. Chipperfield, K. S. Carslaw, B.-M. Sinnhuber, J. G. Anderson, R. M. Stimpfle, D. M. Wilmouth, D. W. Fahey, P. J. Popp, E. C. Richard, P. von der Gathen, H. Jost, and C. R. Webster (2002). *Modeling the effect of denitrification on Arctic ozone depletion during winter 1999/2000*. Journal of Geophysical Research: Atmospheres 107 (D5), SOL 65–1–SOL 65–18. DOI: 10.1029/2001JD000445 (cit. on p. 42).

Davies, S., G. W. Mann, K. S. Carslaw, M. P. Chipperfield, J. A. Kettleborough, M. L. Santee, H. Oelhaf, G. Wetzel, Y. Sasano, and T. Sugita (2005). *3-D microphysical model studies of Arctic denitrification: comparison with observations*. Atmospheric Chemistry and Physics 5 (11), 3093–3109. DOI: 10.5194/acp-5-3093-2005 (cit. on p. 42).

Davison, C. (1886). *Iridescent Clouds*. Nature 33, 220 (cit. on pp. 2, 19).

Dee, D. P., S. M. Uppala, A. J. Simmons, P. Berrisford, P. Poli, S. Kobayashi, U. Andrae, M. A. Balmaseda, G. Balsamo, P. Bauer, P. Bechtold, A. C. M. Beljaars, L. van de Berg, J. Bidlot, N. Bormann, C. Delsol, R. Dragani, M. Fuentes, A. J. Geer, L. Haimberger, S. B. Healy, H. Hersbach, E. V. Hólm, L. Isaksen, P. Kållberg, M. Köhler, M. Matricardi, A. P. McNally, B. M. Monge-Sanz, J.-J. Morcrette, B.-K. Park, C. Peubey, P. de Rosnay, C. Tavolato, J.-N. Thépaut, and F. Vitart (2011). *The ERA-Interim reanalysis: configuration and performance of the data assimilation system*. Quarterly Journal of the Royal Meteorological Society 137 (656), 553–597. DOI: 10.1002/qj.828 (cit. on pp. 54, 59).

Deshler, T., M. E. Hervig, D. J. Hofmann, J. M. Rosen, and J. B. Liley (2003). *Thirty years of in situ stratospheric aerosol size distribution measurements from Laramie, Wyoming (41°N), using balloon-borne instruments*. Journal of Geophysical Research: Atmospheres 108 (D5). DOI: 10.1029/2002JD002514 (cit. on p. 13).

Dhaniyala, S., K. A. Mckinney, and P. O. Wennberg (2002). *Lee-wave clouds and denitrification of the polar stratosphere*. Geophysical Research Letters 29 (9), 36–1–36–4. DOI: 10.1029/2001GL013900 (cit. on p. 2).

Dhomse, S. S., D. Kinnison, M. P. Chipperfield, R. J. Salawitch, I. Cionni, M. I. Hegglin, N. L. Abraham, H. Akiyoshi, A. T. Archibald, E. M. Bednarz, S. Bekki, P. Braesicke, N. Butchart, M. Dameris, M. Deushi, S. Frith, S. C. Hardiman, B. Hassler, L. W. Horowitz, R.-M. Hu, P. Jöckel, B. Josse, O. Kirner, S. Kremser, U. Langematz, J. Lewis, M. Marchand, M. Lin, E. Mancini, V. Marécal, M. Michou, O. Morgenstern, F. M. O'Connor, L. Oman, G. Pitari, D. A. Plummer, J. A. Pyle, L. E. Revell, E. Rozanov, R. Schofield, A. Stenke, K. Stone, K. Sudo, S. Tilmes, D. Visioni, Y. Yamashita, and G. Zeng (2018). *Estimates of ozone return dates from Chemistry-Climate Model Initiative simulations*. Atmospheric Chemistry and Physics 18 (11), 8409–8438. DOI: 10.5194/acp-18-8409-2018 (cit. on p. 1).

Diehl, T., A. Heil, M. Chin, X. Pan, D. Streets, M. Schultz, and S. Kinne (2012). *Anthropogenic, biomass burning, and volcanic emissions of black carbon, organic carbon, and SO_2 from 1980 to 2010 for hindcast model experiments*. Atmos. Chem. Phys. Discuss. 12 (9), 24895–24954. DOI: 10.5194/acpd-12-24895-2012 (cit. on p. 33).

Diekmann, C. (2017). *Simulation der polaren UT/LS im Winter 2015/16 mit ICON-ART*. Master's Thesis. Germany: Karlsruhe Institute of Technology (KIT) (cit. on pp. 19, 29, 58).

Dipankar, A., B. Stevens, R. Heinze, C. Moseley, G. Zängl, M. Giorgetta, and S. Brdar (2015). *Large eddy simulation using the general circulation model ICON*. Journal of Advances in Modeling Earth Systems 7 (3), 963–986. DOI: 10.1002/2015MS000431 (cit. on p. 25).

Dobson, G. M. B., D. N. Harrison, and J. Lawrence (1929). *Measurements of the amount of ozone in the Earth's atmosphere and its relation to other geophysical conditions. – Part III*. Proceedings of the Royal Society of London. Series A, Containing Papers of a Mathematical and Physical Character 122 (790), 456–486. DOI: 10.1098/rspa.1929.0034 (cit. on p. 7).

Doms, G., J. Förstner, E. Heise, H.-J. Herzog, D. Mironov, M. Raschendorfer, T. Reinhardt, B. Ritter, R. Schrodin, J.-P. Schulz, and G. Vogel (2011). *A Description of the Nonhydrostatic Regional COSMO Model. Part II: Physical Parametrization*. Tech. rep. Offenbach: Deutscher Wetterdienst (cit. on pp. 35, 39, 75, 77).

Dörnbrack, A., S. Gisinger, M. C. Pitts, L. R. Poole, and M. Maturilli (2017). *Multilevel Cloud Structures over Svalbard*. Monthly Weather Review 145 (4), 1149–1159. DOI: 10.1175/MWR-D-16-0214.1 (cit. on p. 9).

Drdla, K., R. P. Turco, and S. Elliott (1993). *Heterogeneous chemistry on Antarctic polar stratospheric clouds: A microphysical estimate of the extent of chemical processing*. Journal of Geophysical Research: Atmospheres 98 (D5), 8965–8981. DOI: 10.1029/93JD00164 (cit. on pp. 22, 23, 43, 47).

Dye, J. E., D. Baumgardner, B. W. Gandrud, S. R. Kawa, K. K. Kelly, M. Loewenstein, G. V. Ferry, K. R. Chan, and B. L. Gary (1992). *Particle size distributions in Arctic polar stratospheric clouds, growth and freezing of sulfuric acid droplets, and implications for cloud formation*. Journal of Geophysical Research: Atmospheres 97 (D8), 8015–8034. DOI: 10.1029/91JD02740 (cit. on pp. 20, 48, 50, 80).

Eckermann, S. D., L. Hoffmann, M. Höpfner, D. L. Wu, and M. J. Alexander (2009). *Antarctic NAT PSC belt of June 2003: Observational validation of the mountain wave seeding hypothesis*. Geophysical Research Letters 36 (2). DOI: 10.1029/2008GL036629 (cit. on pp. 2, 98).

Eckermann, S. D., A. Dörnbrack, H. Flentje, S. B. Vosper, M. J. Mahoney, T. P. Bui, and K. S. Carslaw (2006). *Mountain Wave-Induced Polar Stratospheric Cloud Forecasts for Aircraft Science Flights during SOLVE/THESEO 2000*. Weather and Forecasting 21 (1), 42–68. DOI: 10.1175/WAF901.1 (cit. on p. 2).

Eckstein, J., R. Ruhnke, S. Pfahl, E. Christner, C. Diekmann, C. Dyroff, D. Reinert, D. Rieger, M. Schneider, J. Schröter, A. Zahn, and P. Braesicke (2018). *From climatological to small-scale applications: simulating water isotopologues with ICON-ART-Iso (version 2.3)*. Geoscientific Model Development 11 (12), 5113–5133. DOI: 10.5194/gmd-11-5113-2018 (cit. on p. 29).

Eckstein, J. (2013). *Simulation der polaren unteren Stratosphäre mit dem regionalen Chemie-Transport Modell COSMO-ART*. Master's Thesis. Germany: Karlsruhe Institute of Technology (KIT) (cit. on p. 47).

ECMWF (2003). "Part IV: Physical Processes". In: *IFS Documentation CY23R4*. Ed. by P White. Reading, United Kingdom: ECMWF (cit. on pp. 104, 105).

Eidhammer, T., H. Morrison, D. Mitchell, A. Gettelman, and E. Erfani (2017). *Improvements in Global Climate Model Microphysics Using a Consistent Representation of Ice Particle Properties*. Journal of Climate 30 (2), 609–629. DOI: 10.1175/JCLI-D-16-0050.1 (cit. on p. 131).

Elliott, S., R. J. Cicerone, R. P. Turco, K. Drdla, and A. Tabazadeh (1994). *Influence of the heterogeneous reaction HCl + HOCl on an ozone hole model with hydrocarbon additions*. Journal of Geophysical Research: Atmospheres 99 (D2), 3497–3508. DOI: 10.1029/93JD03089 (cit. on p. 22).

Engel, I., B. P. Luo, M. C. Pitts, L. R. Poole, C. R. Hoyle, J.-U. Grooß, A. Dörnbrack, and T. Peter (2013). *Heterogeneous formation of polar stratospheric clouds – Part 2: Nucleation of ice on synoptic scales*. Atmospheric Chemistry and Physics 13 (21), 10769–10785. DOI: 10.5194/acp-13-10769-2013 (cit. on pp. 21, 101, 116, 125).

Engel, I., B. P. Luo, S. M. Khaykin, F. G. Wienhold, H. Vömel, R. Kivi, C. R. Hoyle, J.-U. Grooß, M. C. Pitts, and T. Peter (2014). *Arctic stratospheric dehydration – Part 2: Microphysical modeling*. Atmospheric Chemistry and Physics 14 (7), 3231–3246. DOI: 10.5194/acp-14-3231-2014 (cit. on p. 21).

Ern, M., Q. T. Trinh, P. Preusse, J. C. Gille, M. G. Mlynczak, J. M. Russell III, and M. Riese (2018). *GRACILE: a comprehensive climatology of atmospheric gravity wave parameters based on satellite limb soundings*. Earth System Science Data 10 (2), 857–892. DOI: 10.5194/essd-10-857-2018 (cit. on p. 61).

Fabry, C. and H. Buisson (1921). *A Study of the Ultra-Violet End of the Solar Spectrum*. Astrophysical Journal 54, 297–323. DOI: 10.1086/142647 (cit. on p. 1).

Fahey, D. W., K. K. Kelly, G. V. Ferry, L. R. Poole, J. C. Wilson, D. M. Murphy, M. Loewenstein, and K. R. Chan (1989). *In situ measurements of total reactive nitrogen, total water, and aerosol in a polar stratospheric cloud in the Antarctic*. Journal of Geophysical Research: Atmospheres 94 (D9), 11299–11315. DOI: 10.1029/JD094iD09p11299 (cit. on p. 20).

Fahey, D. W., R. S. Gao, K. S. Carslaw, J. Kettleborough, P. J. Popp, M. J. Northway, J. C. Holecek, S. C. Ciciora, R. J. McLaughlin, T. L. Thompson, R. H. Winkler, D. G. Baumgardner, B. Gandrud, P. O. Wennberg, S. Dhaniyala, K. McKinney, T. Peter, R. J. Salawitch, T. P. Bui, J. W. Elkins, C. R. Webster, E. L. Atlas, H. Jost, J. C. Wilson, R. L. Herman, A. Kleinböhl, and M. von König (2001). *The Detection of Large HNO_3-Containing Particles in the Winter Arctic Stratosphere*. Science 291 (5506), 1026–1031. DOI: 10.1126/science.1057265 (cit. on pp. 20, 21, 42, 44, 55).

Fang, X., J. A. Pyle, M. P. Chipperfield, J. S. Daniel, S. Park, and R. G. Prinn (2019). *Challenges for the recovery of the ozone layer*. Nature Geoscience 12 (8), 592–596. DOI: 10.1038/s41561-019-0422-7 (cit. on p. 1).

Farman, J., W. Gardiner, and J. Shanklin (1985). *Large losses of total ozone in Antarctic reveal seasonal ClO_x/NO_x interaction*. Nature 315, 207–210. DOI: 10.1038/315207a0 (cit. on pp. 1, 17, 19).

Finlayson-Pitts, B. J. and J. N. Pitts (2000). "CHAPTER 4 - Photochemistry of Important Atmospheric Species". In: *Chemistry of the Upper and Lower Atmosphere*. Ed. by B. J. Finlayson-Pitts and J. N. Pitts. San Diego: Academic Press, 86 –129. DOI: https://doi.org/10.1016/B978-012257060-5/50006-X (cit. on p. 19).

Fischer, H., M. Birk, C. Blom, B. Carli, M. Carlotti, T. von Clarmann, L. Delbouille, A. Dudhia, D. Ehhalt, M. Endemann, J. M. Flaud, R. Gessner, A. Kleinert, R. Koopman, J. Langen, M. López-Puertas, P. Mosner, H. Nett, H. Oelhaf, G. Perron, J. Remedios, M. Ridolfi, G. Stiller, and R. Zander (2008). *MIPAS: an instrument for atmospheric and climate research*. Atmos. Chem. Phys. 8 (8), 2151–2188. DOI: 10.5194/acp-8-2151-2008 (cit. on p. 61).

Flentje, H., A. Dörnbrack, A. Fix, A. Meister, H. Schmid, S. Füglistaler, B. Luo, and T. Peter (2002). *Denitrification inside the stratospheric vortex in the winter of 1999–2000 by sedimentation of large nitric acid trihydrate particles*. Journal of Geophysical Research: Atmospheres 107 (D16). DOI: 10.1029/2001JD001015 (cit. on p. 21).

Forster, P., V. Ramaswamy, P. Artaxo, T. Berntsen, R. Betts, D. W. Fahey, J. Haywood, J. Lean, D. C. Lowe, G. Myhre, J. Nganga, R. Prinn, G. Raga, M. Schulz, and R. V. Dorland (2007). "Changes in Atmospheric Constituents and in Radiative Forcing". In: *Climate Change 2007: The Physical Science Basis. Contribution of Working Group I to the Fourth Assessment Report of the Intergovernmental Panel on Climate Change*. Ed. by S. Solomon, D. Qin, M. Manning, Z. Chen, M. Marquis, K. B. Averyt, M. Tignor, and H. L. Miller. Cambridge, United Kingdom and New York, NY, USA: Cambridge University Press (cit. on p. 1).

Fountoukis, C. and A. Nenes (2007). *ISORROPIA II: a computationally efficient thermodynamic equilibrium model for K^+–Ca^{2+}–Mg^{2+}–$NH_4{}^+$–Na^+–$SO_4{}^{2-}$–$NO_3{}^-$–Cl^-–H_2O aerosols*. Atmospheric Chemistry and Physics 7 (17), 4639–4659. DOI: 10.5194/acp-7-4639-2007 (cit. on p. 125).

Fritts, D. C. (1984). *Gravity wave saturation in the middle atmosphere: A review of theory and observations*. Reviews of Geophysics 22 (3), 275–308. DOI: 10.1029/RG022i003p00275 (cit. on p. 10).

Fritts, D. C. and M. J. Alexander (2003). *Gravity wave dynamics and effects in the middle atmosphere*. Reviews of Geophysics 41 (1). DOI: 10.1029/2001RG000106 (cit. on pp. 9, 10, 11).

Fuchs, N. and A. Sutugin (1971). "High-Dispersed Aerosols". In: *Topics in Current Aerosol Research*. Ed. by G. Hidy and J. Brock. International Reviews in Aerosol Physics and Chemistry. Pergamon, 1. DOI: 10.1016/B978-0-08-016674-2.50006-6 (cit. on p. 23).

Fueglistaler, S., S. Buss, B. P. Luo, H. Wernli, H. Flentje, C. A. Hostetler, L. R. Poole, K. S. Carslaw, and T. Peter (2003). *Detailed modeling of mountain wave PSCs*. Atmospheric Chemistry and Physics 3 (3), 697–712. DOI: 10.5194/acp-3-697-2003 (cit. on p. 2).

Ganske, J. A., H. N. Berko, and B. J. Finlayson-Pitts (1992). *Absorption cross sections for gaseous $ClNO_2$ and Cl_2 at 298 K: Potential organic oxidant source in the marine troposphere*. Journal of Geophysical Research: Atmospheres 97 (D7), 7651–7656. DOI: 10.1029/92JD00414 (cit. on p. 19).

Gates, W. L., J. S. Boyle, C. Covey, C. G. Dease, C. M. Doutriaux, R. S. Drach, M. Fiorino, P. J. Gleckler, J. J. Hnilo, S. M. Marlais, T. J. Phillips, G. L. Potter, B. D. Santer, K. R. Sperber, K. E. Taylor, and D. N. Williams (1999). *An Overview of the Results of the Atmospheric Model Intercomparison Project (AMIP I)*. Bulletin of the American Meteorological Society 80 (1), 29–56. DOI: 10.1175/1520-0477(1999)080<0029:AOOTRO>2.0.CO;2 (cit. on p. 56).

Gelaro, R., W. McCarty, M. J. Suárez, R. Todling, A. Molod, L. Takacs, C. A. Randles, A. Darmenov, M. G. Bosilovich, R. Reichle, K. Wargan, L. Coy, R. Cullather, C. Draper, S. Akella, V. Buchard, A. Conaty, A. M. da Silva, W. Gu, G.-K. Kim, R. Koster, R. Lucchesi, D. Merkova, J. E. Nielsen, G. Partyka, S. Pawson, W. Putman, M. Rienecker, S. D. Schubert, M. Sienkiewicz, and B. Zhao (2017). *The Modern-Era Retrospective Analysis for Research and Applications, Version 2 (MERRA-2)*. Journal of Climate 30 (14), 5419–5454. DOI: 10.1175/JCLI-D-16-0758.1 (cit. on p. 60).

Giorgetta, M. A., E. Roeckner, T. Mauritsen, J. Bader, T. Crueger, M. Esch, S. Rast, L. Kornblueh, H. Schmidt, S. Kinne, C. Hohenegger, B. Möbis, T. Krismer, K.-H. Wieners, and B. Stevens (2013). *The atmospheric general circulation model ECHAM6 – Model description*. Tech. rep. 135. Berichte zur Erdsystemforschung/Max-Planck-Institut für Meteorologie (cit. on pp. 39, 40).

Giorgetta, M. A., R. Brokopf, T. Crueger, M. Esch, S. Fiedler, J. Helmert, C. Hohenegger, L. Kornblueh, M. Köhler, E. Manzini, T. Mauritsen, C. Nam, T. Raddatz, S. Rast, D. Reinert, M. Sakradzija, H. Schmidt, R. Schneck, R. Schnur, L. Silvers, H. Wan, G. Zängl, and B. Stevens (2018). *ICON-A, the Atmosphere Component of the ICON Earth System Model: I. Model Description*. Journal of Advances in Modeling Earth Systems 18. DOI: 10.1029/2017MS001242 (cit. on pp. 25, 32, 39).

GLOBE Task Team (1999). *The Global Land One-kilometer Base Elevation (GLOBE) Digital Elevation Model, Version 1.0*. Ed. by D. A. Hastings, P. K. Dunbar, G. M. Elphingstone, M. Bootz, H. Murakami, H. Maruyama, H. Masaharu, P. Holland, J. Payne, N. A. Bryant, T. L. Logan, J.-P. Muller, G. Schreier, and J. S. MacDonald. Digital data base on the World Wide Web and CD-ROMs. National Oceanic and Atmospheric Administration, National Geophysical Data Center, 325 Broadway, Boulder, Colorado 80305 – 3328, U.S.A (cit. on p. 31).

Grainger, R. G., A. Lambert, C. D. Rodgers, F. W. Taylor, and T. Deshler (1995). *Stratospheric aerosol effective radius, surface area and volume estimated from infrared measurements*. Journal of Geophysical Research: Atmospheres 100 (D8), 16507–16518. DOI: 10.1029/95JD00988 (cit. on pp. 13, 48, 49, 50).

Granier, C., B. Bessagnet, T. Bond, A. D'Angiola, H. Denier van der Gon, G. Frost, A. Heil, J. Kaiser, S. Kinne, Z. Klimont, S. Kloster, J.-F. Lamarque, C. Liousse, T. Masui, F. Meleux, A. Mieville, T. Ohara, J.-C. Raut, K. Riahi, M. Schultz, S. Smith, A. Thompson, J. van Aardenne, G. van der Werf, and D. van Vuuren (2011). *Evolution of anthropogenic and biomass burning emissions of air pollutants at global and regional scales during the 1980-2010 period*. English. Climatic Change 109 (1-2), 163–190. DOI: 10.1007/s10584-011-0154-1 (cit. on p. 33).

Grooß, J.-U., G. Günther, P. Konopka, R. Müller, D. S. McKenna, F. Stroh, B. Vogel, A. Engel, M. Müller, K. Hoppel, R. Bevilacqua, E. Richard, C. R. Webster, J. W. Elkins, D. F. Hurst, P. A. Romashkin, and D. G. Baumgardner (2002). *Simulation of ozone depletion in spring 2000 with the Chemical Lagrangian Model of the Stratosphere (CLaMS)*. Journal of Geophysical Research: Atmospheres 107 (D20), SOL 38–1–SOL 38–13. DOI: 10.1029/2001JD000456 (cit. on pp. 21, 43).

Grooß, J.-U., G. Günther, R. Müller, P. Konopka, S. Bausch, H. Schlager, C. Voigt, C. M. Volk, and G. C. Toon (2005). *Simulation of denitrification and ozone loss for the Arctic winter 2002/2003*. Atmospheric Chemistry and Physics 5 (6), 1437–1448. DOI: 10.5194/acp-5-1437-2005 (cit. on p. 42).

Grooß, J.-U., I. Engel, S. Borrmann, W. Frey, G. Günther, C. R. Hoyle, R. Kivi, B. P. Luo, S. Molleker, T. Peter, M. C. Pitts, H. Schlager, G. Stiller, H. Vömel, K. A. Walker, and R. Müller (2014). *Nitric acid trihydrate nucleation and denitrification in the Arctic stratosphere*. Atmospheric Chemistry and Physics 14 (2), 1055–1073. DOI: 10.5194/acp-14-1055-2014 (cit. on p. 125).

Grooß, J.-U., R. Müller, R. Spang, I. Tritscher, T. Wegner, M. P. Chipperfield, W. Feng, D. E. Kinnison, and S. Madronich (2018). *On the discrepancy of HCl processing in the core of the wintertime polar vortices*. Atmospheric Chemistry and Physics 18 (12), 8647–8666. DOI: 10.5194/acp-18-8647-2018 (cit. on p. 107).

Gruber, S. (2019). *Contrails and Climate Engineering - Process Studies on Natural and Artificial High-Level Clouds and Their Impact on the Radiative Fluxes*. PhD thesis. Germany: Karlsruher Institut für Technologie (KIT). 251 pp. DOI: 10.5445/IR/1000089933 (cit. on p. 29).

Guggenberger, H. (2018). *Investigation of atmospheric methane trends using ICON-ART simulations*. Master's Thesis. Germany: Karlsruhe Institute of Technology (KIT) (cit. on p. 29).

Haagen-Smit, A. J., C. E. Bradley, and M. M. Fox (1953). *Ozone Formation in Photochemical Oxidation of Organic Substances*. Industrial & Engineering Chemistry 45 (9), 2086–2089. DOI: 10.1021/ie50525a044 (cit. on p. 1).

Hall, W. D. and H. R. Pruppacher (1976). *The Survival of Ice Particles Falling from Cirrus Clouds in Subsaturated Air*. Journal of the Atmospheric Sciences 33 (10), 1995–2006. DOI: 10.1175/1520-0469(1976)033<1995:TSOIPF>2.0.CO;2 (cit. on pp. 44, 131).

Hamill, P. and O. B. Toon (1991). *Polar Stratospheric Clouds and the Ozone Hole*. Physics Today 44 (12), 34–42. DOI: 10.1063/1.881277 (cit. on p. 15).

Hancock, G. and P. L. Tyley (2001). *The near-uv photolysis of ozone: quantum yields of $O(^1D)$ between 305 and 329 nm at temperatures from 227-298 K, and the room temperature quantum yield of $O(^3P_2)$ between 303 and 310 nm, measured by resonance enhanced multiphoton ionisation*. Phys. Chem. Chem. Phys. 3 (22), 4984–4990. DOI: 10.1039/B107018P (cit. on p. 12).

Hanson, D. R. and K. Mauersberger (1988). *Laboratory studies of the nitric acid trihydrate: Implications for the south polar stratosphere*. Geophysical Research Letters 15 (8), 855–858. DOI: 10.1029/GL015i008p00855 (cit. on pp. 19, 20, 40, 41, 43).

Hanson, D. R. and A. R. Ravishankara (1994). *Reactive Uptake of $ClONO_2$ onto Sulfuric Acid Due to Reaction with HCl and H_2O*. The Journal of Physical Chemistry 98 (22), 5728–5735. DOI: 10.1021/j100073a026 (cit. on p. 48).

– (1995). *Heterogeneous chemistry of bromine species in sulfuric acid under stratospheric conditions*. Geophysical Research Letters 22 (4), 385–388. DOI: 10.1029/94GL03379 (cit. on pp. 22, 48).

Hanson, D. R., A. R. Ravishankara, and E. R. Lovejoy (1996). *Reaction of $BrONO_2$ with H_2O on submicron sulfuric acid aerosol and the implications for the lower stratosphere*. Journal of Geophysical Research: Atmospheres 101 (D4), 9063–9069. DOI: 10.1029/96JD00347 (cit. on pp. 23, 48).

Hersbach, H., P. de Rosnay, B. Bell, D. Schepers, A. Simmons, C. Soci, S. Abdalla, M. Alonso-Balmaseda, G. Balsamo, P. Bechtold, P. Berrisford, J.-R. Bidlot, E. de Boisséson, M. Bonavita, P. Browne, R. Buizza, P. Dahlgren, D. Dee, R. Dragani, M. Diamantakis, J. Flemming, R. Forbes, A. J. Geer, T. Haiden, E. Hólm, L. Haimberger, R. Hogan, A. Horányi, M. Janiskova, P. Laloyaux, P. Lopez, J. Munoz-Sabater, C. Peubey, R. Radu, D. Richardson, J.-N. Thépaut, F. Vitart, X Yang, E. Zsótér, and H. Zuo (2018). *Operational global reanalysis: progress, future directions and synergies with NWP*. (27). DOI: 10.21957/tkic6g3wm (cit. on p. 59).

Hervig, M. E. and T. Deshler (1998). *Stratospheric aerosol surface area and volume inferred from HALOE, CLAES, and ILAS measurements*. Journal of Geophysical Research: Atmospheres 103 (D19), 25345–25352. DOI: 10.1029/98JD01962 (cit. on pp. 13, 48, 49, 50).

Hines, C. O. (1997). *Doppler-spread parameterization of gravity-wave momentum deposition in the middle atmosphere. Part 1: Basic formulation*. Journal of Atmospheric and Solar-Terrestrial Physics 59 (4), 371 –386. DOI: 10.1016/S1364-6826(96)00079-X (cit. on pp. 11, 32).

Hoffmann, L., R. Spang, A. Orr, M. J. Alexander, L. A. Holt, and O. Stein (2017). *A decadal satellite record of gravity wave activity in the lower stratosphere to study polar stratospheric cloud formation*. Atmospheric Chemistry and Physics 17 (4), 2901–2920. DOI: 10.5194/acp-17-2901-2017 (cit. on pp. 2, 11, 53, 121, 126).

Hoffmann, L., G. Günther, D. Li, O. Stein, X. Wu, S. Griessbach, Y. Heng, P. Konopka, R. Müller, B. Vogel, and J. S. Wright (2019). *From ERA-Interim to ERA5: the considerable impact of ECMWF's next-generation reanalysis on Lagrangian transport simulations*. Atmospheric Chemistry and Physics 19 (5), 3097–3124. DOI: 10.5194/acp-19-3097-2019 (cit. on p. 59).

Hofmann, D. J., J. M. Rosen, T. J. Pepin, and R. G. Pinnick (1975). *Stratospheric Aerosol Measurements I: Time Variations at Northern Midlatitudes*. Journal of the Atmospheric Sciences 32 (7), 1446–1456. DOI: 10.1175/1520-0469(1975)032<1446:SAMITV>2.0.CO;2 (cit. on p. 13).

Hollingsworth, A., R. J. Engelen, C. Textor, A. Benedetti, O. Boucher, F. Chevallier, A. Dethof, H. Elbern, H. Eskes, J. Flemming, C. Granier, J. W. Kaiser, J.-J. Morcrette, P. Rayner, V.-H. Peuch, L. Rouil, M. G. Schultz, and A. J. a. Simmons (2008). *Toward a monitoring and forecasting system for atmospheric composition*. Bulletin of the American Meteorological Society 89 (8), 1147–1164. DOI: 10.1175/2008BAMS2355.1 (cit. on p. 55).

Höpfner, M., H. Oelhaf, G. Wetzel, F. Friedl-Vallon, A. Kleinert, A. Lengel, G. Maucher, H. Nordmeyer, N. Glatthor, G. Stiller, T. v. Clarmann, H. Fischer, C. Kröger, and T. Deshler (2002). *Evidence of scattering of tropospheric radiation*

by PSCs in mid-IR limb emission spectra: MIPAS-B observations and KOPRA simulations. Geophysical Research Letters 29 (8), 119–1–119–4. DOI: 10.1029/2001GL014443 (cit. on pp. 13, 130).

Höpfner, M., N. Larsen, R. Spang, B. P. Luo, J. Ma, S. H. Svendsen, S. D. Eckermann, B. Knudsen, P. Massoli, F. Cairo, G. Stiller, T. v. Clarmann, and H. Fischer (2006a). *MIPAS detects Antarctic stratospheric belt of NAT PSCs caused by mountain waves*. Atmospheric Chemistry and Physics 6 (5), 1221–1230. DOI: 10.5194/acp-6-1221-2006 (cit. on p. 2).

Höpfner, M., B. P. Luo, P. Massoli, F. Cairo, R. Spang, M. Snels, G. Di Donfrancesco, G. Stiller, T. von Clarmann, H. Fischer, and U. Biermann (2006b). *Spectroscopic evidence for NAT, STS, and ice in MIPAS infrared limb emission measurements of polar stratospheric clouds*. Atmos. Chem. Phys. 6 (5), 1201–1219. DOI: 10.5194/acp-6-1201-2006 (cit. on pp. 20, 61).

Höpfner, M., M. C. Pitts, and L. R. Poole (2009). *Comparison between CALIPSO and MIPAS observations of polar stratospheric clouds*. Journal of Geophysical Research: Atmospheres 114 (D4). D00H05, n/a–n/a. DOI: 10.1029/2009JD012114 (cit. on p. 62).

Höpfner, M., T. Deshler, M. Pitts, L. Poole, R. Spang, G. Stiller, and T. von Clarmann (2018). *The MIPAS/Envisat climatology (2002–2012) of polar stratospheric cloud volume density profiles*. Atmospheric Measurement Techniques 11 (10), 5901–5923. DOI: 10.5194/amt-11-5901-2018 (cit. on pp. 61, 70, 98, 117).

Horný, Ľuboš, M. Quack, H. F. S. III, and M. Willeke (2016). *Chlorine peroxide (Cl_2O_2) and its isomers: structures, spectroscopy, formation and thermochemistry*. Molecular Physics 114 (7-8), 1135–1147. DOI: 10.1080/00268976.2016.1143984 (cit. on p. 16).

Hoskins, B. J. (2014). *Fluid dynamics of the midlatitude atmosphere*. Ed. by I. N. James. Advancing weather and climate science series. Chicester: Wiley Blackwell. DOI: 10.1002/9781118526002 (cit. on p. 8).

Hoyle, C. R., I. Engel, B. P. Luo, M. C. Pitts, L. R. Poole, J.-U. Grooß, and T. Peter (2013). *Heterogeneous formation of polar stratospheric clouds – Part 1: Nucleation of nitric acid trihydrate (NAT)*. Atmos. Chem. Phys. 13 (18), 9577–9595. DOI: 10.5194/acp-13-9577-2013 (cit. on pp. 21, 35, 125).

Hsu, J. and M. J. Prather (2009). *Stratospheric variability and tropospheric ozone*. Journal of Geophysical Research: Atmospheres 114 (D6). DOI: 10.1029/2008JD010942 (cit. on p. 54).

Hund, F. (1927). *Zur Deutung der Molekelspektren. I*. Zeitschrift für Physik 40 (10), 742–764. DOI: 10.1007/BF01400234 (cit. on p. 133).

Huthwelker, T., T. Peter, B. P. Luo, S. L. Clegg, K. S. Carslaw, and P. Brimblecombe (1995). *Solubility of HOCl in water and aqueous H_2SO_4 to stratospheric temperatures*. Journal of Atmospheric Chemistry 21 (1), 81–95. DOI: 10.1007/BF00712439 (cit. on p. 48).

Iannarelli, R. and M. J. Rossi (2015). *The mid-IR Absorption Cross Sections of α- and β-NAT ($HNO_3 \cdot 3H_2O$) in the range 170 to 185 K and of metastable NAD ($HNO_3 \cdot 2H_2O$) in the range 172 to 182 K*. Journal of Geophysical Research: Atmospheres 120 (22), 11,707–11,727. DOI: 10.1002/2015JD023903 (cit. on pp. 21, 125).

Ingham, T., D. Bauer, J. Landgraf, and J. N. Crowley (1998). *Ultraviolet-Visible Absorption Cross Sections of Gaseous HOBr*. The Journal of Physical Chemistry A 102 (19), 3293–3298. DOI: 10.1021/jp980272c (cit. on p. 19).

Innis, J. L. and A. R. Klekociuk (2006). *Planetary wave and gravity wave influence on the occurrence of polar stratospheric clouds over Davis Station, Antarctica, seen in lidar and radiosonde observations*. Journal of Geophysical Research: Atmospheres 111 (D22). DOI: 10.1029/2006JD007629 (cit. on p. 11).

Ivy, D. J., S. Solomon, D. Kinnison, M. J. Mills, A. Schmidt, and R. R. Neely (2017). *The influence of the Calbuco eruption on the 2015 Antarctic ozone hole in a fully coupled chemistry-climate model*. Geophysical Research Letters 44 (5), 2556–2561. DOI: 10.1002/2016GL071925 (cit. on p. 19).

James, A. D., J. S. A. Brooke, T. P. Mangan, T. F. Whale, J. M. C. Plane, and B. J. Murray (2018). *Nucleation of nitric acid hydrates in polar stratospheric clouds by meteoric material*. Atmospheric Chemistry and Physics 18 (7), 4519–4531. DOI: 10.5194/acp-18-4519-2018 (cit. on p. 21).

Janssens-Maenhout, G., A. M. Petrescu, M. Muntean, and V. Blujdea (2011). *Verifying Greenhouse Gas Emissions: Methods to Support International Climate Agreements*. Greenhouse Gas Measurement and Management 1 (2), 132–133. DOI: 10.1080/20430779.2011.579358 (cit. on p. 33).

Janssens-Maenhout, G., V. Diego, and G Marilena Muntean (2013). *Global emission inventories in the Emission Database for Global Atmospheric Research (EDGAR)–Manual (I)*. Gridding: EDGAR emissions distribution on global gridmaps, Publications Office of the European Union, Luxembourg (cit. on p. 33).

Jeuken, A. B. M., P. C. Siegmund, L. C. Heijboer, J. Feichter, and L. Bengtsson (1996). *On the potential of assimilating meteorological analyses in a global climate model for the purpose of model validation*. Journal of Geophysical Research: Atmospheres 101 (D12), 16939–16950. DOI: 10.1029/96JD01218 (cit. on p. 58).

Jöckel, P., H. Tost, A. Pozzer, C. Brühl, J. Buchholz, L. Ganzeveld, P. Hoor, A. Kerkweg, M.-G. Lawrence, R. Sander, B. Steil, G. Stiller, M. Tanarhte, D. Taraborrelli, J. van Aardenne, and J. Lelieveld (2006). *The atmospheric chemistry general circulation model ECHAM5/MESSy1: consistent simulation of ozone from the surface to the mesosphere*. Atmos. Chem. Phys. 6 (12), 5067–5104. DOI: 10.5194/acp-6-5067-2006 (cit. on pp. 33, 103).

Jöckel, P., A. Kerkweg, A. Pozzer, R. Sander, H. Tost, H. Riede, A. Baumgaertner, S. Gromov, and B. Kern (2010). *Development cycle 2 of the Modular Earth Submodel System (MESSy2)*. Geoscientific Model Development 3 (2), 717–752. DOI: 10.5194/gmd-3-717-2010 (cit. on p. 54).

Johansson, S., M. L. Santee, J.-U. Grooß, M. Höpfner, M. Braun, F. Friedl-Vallon, F. Khosrawi, O. Kirner, E. Kretschmer, H. Oelhaf, J. Orphal, B.-M. Sinnhuber, I. Tritscher, J. Ungermann, K. A. Walker, and W. Woiwode (2019). *Unusual chlorine partitioning in the 2015/16 Arctic winter lowermost stratosphere: observations and simulations*. Atmospheric Chemistry and Physics 19 (12), 8311–8338. DOI: 10.5194/acp-19-8311-2019 (cit. on p. 125).

Junge, C. E., C. W. Chagnon, and J. E. Manson (1961). *Stratospheric Aerosols*. J. Meteor. 18 (1), 81–108. DOI: 10.1175/1520-0469(1961)018<0081:SA>2.0.CO;2 (cit. on p. 13).

Keeble, J., P. Braesicke, N. L. Abraham, H. K. Roscoe, and J. A. Pyle (2014). *The impact of polar stratospheric ozone loss on Southern Hemisphere stratospheric circulation and climate*. Atmospheric Chemistry and Physics 14 (24), 13705–13717. DOI: 10.5194/acp-14-13705-2014 (cit. on p. 1).

Kelly, K. K., A. F. Tuck, D. M. Murphy, M. H. Proffitt, D. W. Fahey, R. L. Jones, D. S. McKenna, M. Loewenstein, J. R. Podolske, S. E. Strahan, G. V. Ferry, K. R. Chan, J. F. Vedder, G. L. Gregory, W. D. Hypes, M. P. McCormick, E. V. Browell, and L. E. Heidt (1989). *Dehydration in the lower Antarctic stratosphere during late winter and early spring, 1987*. Journal of Geophysical Research: Atmospheres 94 (D9), 11317–11357. DOI: 10.1029/JD094iD09p11317 (cit. on p. 21).

Kennard, E. H. (1938). *Kinetic theory of gases, with an introduction to statistical mechanics*. New York and London: McGraw-Hill Book Company (cit. on p. 23).

Khaykin, S. M., I. Engel, H. Vömel, I. M. Formanyuk, R. Kivi, L. I. Korshunov, M. Krämer, A. D. Lykov, S. Meier, T. Naebert, M. C. Pitts, M. L. Santee, N. Spelten, F. G. Wienhold, V. A. Yushkov, and T. Peter (2013). *Arctic stratospheric dehydration – Part 1: Unprecedented observation of vertical redistribution of water*. Atmospheric Chemistry and Physics 13 (22), 11503–11517. DOI: 10.5194/acp-13-11503-2013 (cit. on p. 21).

Khosrawi, F., O. Kirner, G. Stiller, M. Höpfner, M. L. Santee, S. Kellmann, and P. Braesicke (2018). *Comparison of ECHAM5/MESSy Atmospheric Chemistry (EMAC) simulations of the Arctic winter 2009/2010 and 2010/2011 with Envisat/MIPAS and Aura/MLS observations*. Atmospheric Chemistry and Physics 18 (12), 8873–8892. DOI: 10.5194/acp-18-8873-2018 (cit. on p. 81).

Khosrawi, F. (2001). *Modellierung der Bildung und des Wachstums von H_2SO_4/H_2O Aerosolen in der Stratosphäre und oberen Troposphäre*. PhD thesis. Forschungszentrum Jülich. 117 pp. (cit. on p. 125).

Kim, Y.-J., S. D. Eckermann, and H.-Y. Chun (2003). *An overview of the past, present and future of gravity-wave drag parametrization for numerical climate and weather prediction models*. Atmosphere-Ocean 41 (1), 65–98. DOI: 10.3137/ao.410105 (cit. on p. 11).

Kirner, O., R. Ruhnke, J. Buchholz-Dietsch, P. Jöckel, C. Brühl, and B. Steil (2011). *Simulation of polar stratospheric clouds in the chemistry-climate-model EMAC via the submodel PSC*. Geoscientific Model Development 4 (1), 169–182. DOI: 10.5194/gmd-4-169-2011 (cit. on pp. 35, 40, 42, 47).

Kirner, O., R. Ruhnke, and B.-M. Sinnhuber (2015a). *Chemistry–Climate Interactions of Stratospheric and Mesospheric Ozone in EMAC Long-Term Simulations with Different Boundary Conditions for CO_2, CH_4, N_2O, and ODS*. Atmosphere-Ocean 53 (1), 140–152. DOI: 10.1080/07055900.2014.980718 (cit. on p. 104).

Kirner, O., R. Müller, R. Ruhnke, and H. Fischer (2015b). *Contribution of liquid, NAT and ice particles to chlorine activation and ozone depletion in Antarctic winter and spring.* Atmospheric Chemistry and Physics 15 (4), 2019–2030. DOI: 10.5194/acp-15-2019-2015 (cit. on p. 20).

Kirner, O. (2008). *Prozessstudien der stratosphärischen Chemie und Dynamik mit Hilfe des Chemie-Klima-Modells ECHAM5/MESSy1.* PhD thesis. Universität Karlsruhe (cit. on p. 103).

Köhler, H. (1936). *The nucleus in and the growth of hygroscopic droplets.* Trans. Faraday Soc. 32 (0), 1152–1161. DOI: 10.1039/TF9363201152 (cit. on p. 14).

Kohma, M. and K. Sato (2011). *The effects of atmospheric waves on the amounts of polar stratospheric clouds.* Atmospheric Chemistry and Physics 11 (22), 11535–11552. DOI: 10.5194/acp-11-11535-2011 (cit. on pp. 2, 53).

Koop, T., U. M. Biermann, W. Raber, B. P. Luo, P. J. Crutzen, and T. Peter (1995). *Do stratospheric aerosol droplets freeze above the ice frost point?* Geophysical Research Letters 22 (8), 917–920. DOI: 10.1029/95GL00814 (cit. on p. 21).

Koop, T., B. Luo, A. Tsias, and T. Peter (2000). *Water activity as the determinant for homogeneous ice nucleation in aqueous solutions.* Nature 406 (611). DOI: 10.1038/35020537 (cit. on p. 21).

Kouker, W., D. Offermann, V. Küll, T. Reddmann, R. Ruhnke, and A. Franzen (1999). *Streamers observed by the CRISTA experiment and simulated in the KASIMA model.* J. Geophys. Res.: Atmospheres 104 (D13), 16405–16418. DOI: 10.1029/1999JD900177 (cit. on p. 47).

Kremser, S., L. W. Thomason, M. Hobe, M. Hermann, T. Deshler, C. Timmreck, M. Toohey, A. Stenke, J. P. Schwarz, R. Weigel, S. Fueglistaler, F. J. Prata, J.-P. Vernier, H. Schlager, J. E. Barnes, J.-C. Antuña Marrero, D. Fairlie, M. Palm, E. Mahieu, J. Notholt, M. Rex, C. Bingen, F. Vanhellemont, A. Bourassa, J. M. C. Plane, D. Klocke, S. A. Carn, L. Clarisse, T. Trickl, R. Neely, A. D. James, L. Rieger, J. C. Wilson, and B. Meland (2016). *Stratospheric aerosol – Observations, processes, and impact on climate.* Reviews of Geophysics 54 (2), 278–335. DOI: 10.1002/2015RG000511 (cit. on pp. 13, 14).

Lamarque, J.-F., T. C. Bond, V. Eyring, C. Granier, A. Heil, Z. Klimont, D. Lee, C. Liousse, A. Mieville, B. Owen, M. G. Schultz, D. Shindell, S. J. Smith, E. Stehfest, J. Van Aardenne, O. R. Cooper, M. Kainuma, N. Mahowald, J. R. McConnell, V. Naik, K. Riahi, and D. P. van Vuuren (2010). *Historical (1850-2000) gridded anthropogenic and biomass burning emissions of reactive gases and aerosols: methodology and application.* Atmos. Chem. Phys. 10 (15), 7017–7039. DOI: 10.5194/acp-10-7017-2010 (cit. on p. 33).

Larsen, N. (2000). *Polar Stratospheric Clouds Microphysical and optical models.* Tech. rep. Report 00 – 06. Danish Meteorological Institute, Copenhagen (cit. on pp. 131, 132).

Lean, J., G. Rottman, J. Harder, and G. Kopp (2005). *SORCE Contributions to New Understanding of Global Change and Solar Variability.* Solar Physics 230 (1), 27–53. DOI: 10.1007/s11207-005-1527-2 (cit. on p. 56).

Lelieveld, J., S. Gromov, A. Pozzer, and D. Taraborrelli (2016). *Global tropospheric hydroxyl distribution, budget and reactivity.* Atmospheric Chemistry and Physics 16 (19), 12477–12493. DOI: 10.5194/acp-16-12477-2016 (cit. on p. 12).

Leuenberger, D., M. Koller, O. Fuhrer, and C. Schär (2010). *A Generalization of the SLEVE Vertical Coordinate.* Monthly Weather Review 138 (9), 3683–3689. DOI: 10.1175/2010MWR3307.1 (cit. on p. 27).

Levelt, P. F., E. Hilsenrath, G. W. Leppelmeier, G. H. J. van den Oord, P. K. Bhartia, J. Tamminen, J. F. de Haan, and J. P. Veefkind (2006a). *Science objectives of the ozone monitoring instrument.* IEEE Transactions on Geoscience and Remote Sensing 44 (5), 1199–1208. DOI: 10.1109/TGRS.2006.872336 (cit. on p. 63).

Levelt, P. F., G. H. J. van den Oord, M. R. Dobber, A. Malkki, Huib Visser, Johan de Vries, P. Stammes, J. O. V. Lundell, and H. Saari (2006b). *The ozone monitoring instrument.* IEEE Transactions on Geoscience and Remote Sensing 44 (5), 1093–1101. DOI: 10.1109/TGRS.2006.872333 (cit. on pp. 62, 63).

Liu, Y., J. P. Cain, H. Wang, and A. Laskin (2007). *Kinetic Study of Heterogeneous Reaction of Deliquesced NaCl Particles with Gaseous HNO_3 Using Particle-on-Substrate Stagnation Flow Reactor Approach.* J. Phys. Chem. A 111 (40). PMID: 17850118, 10026–10043. DOI: 10.1021/jp072005p (cit. on p. 45).

Loewenstein, M., J. R. Podolske, D. W. Fahey, E. L. Woodbridge, P. Tin, A. Weaver, P. A. Newman, S. E. Strahan, S. R. Kawa, M. R. Schoeberl, and L. R. Lait (1993). *NEw observations of the NOy/N2O correlation in the lower stratosphere.* Geophysical Research Letters 20 (22), 2531–2534. DOI: 10.1029/93GL03004 (cit. on p. 87).

Lohmann, U. and E. Roeckner (1996). *Design and performance of a new cloud microphysics scheme developed for the ECHAM general circulation model.* Climate Dynamics 12 (8), 557–572. DOI: 10.1007/BF00207939 (cit. on p. 39).

Lorenz, E. N. (1963). *Deterministic Nonperiodic Flow.* Journal of the Atmospheric Sciences 20 (2), 130–141. DOI: 10.1175/1520-0469(1963)020<0130:DNF>2.0.CO;2 (cit. on p. 57).

Lott, F. (1999). *Alleviation of Stationary Biases in a GCM through a Mountain Drag Parameterization Scheme and a Simple Representation of Mountain Lift Forces.* Monthly Weather Review 127 (5), 788–801. DOI: 10.1175/1520-0493(1999)127<0788:AOSBIA>2.0.CO;2 (cit. on p. 31).

Lott, F. and M. J. Miller (1997). *A new subgrid-scale orographic drag parametrization: Its formulation and testing.* Quarterly Journal of the Royal Meteorological Society 123 (537), 101–127. DOI: 10.1002/qj.49712353704 (cit. on pp. 11, 31).

Lovejoy, E. R. and D. R. Hanson (1995). *Measurement of the Kinetics of Reactive Uptake by Submicron Sulfuric Acid Particles.* The Journal of Physical Chemistry 99 (7), 2080–2087. DOI: 10.1021/j100007a043 (cit. on p. 23).

Luo, B. P., S. L. Clegg, T. Peter, R. Müller, and P. J. Crutzen (1994). *HCl solubility and liquid diffusion in aqueous sulfuric acid under stratospheric conditions.* Geophysical Research Letters 21 (1), 49–52. DOI: 10.1029/93GL02956 (cit. on p. 48).

Luo, B., U. K. Krieger, and T. Peter (1996). *Densities and refractive indices of $H_2SO_4/HNO_3/H_2O$ solutions to stratospheric temperatures.* Geophysical Research Letters 23 (25), 3707–3710. DOI: 10.1029/96GL03581 (cit. on p. 50).

Lyman, J. L., B. E. Newnam, J. W. Early, and A. F. G. van der Meer (1997). *Infrared Free-Electron-Laser Photolysis of $CFCl_3$ and CF_2Cl_2.* The Journal of Physical Chemistry A 101 (1), 49–54. DOI: 10.1021/jp961739r (cit. on p. 17).

Mann, G. W., S. Davies, K. S. Carslaw, M. P. Chipperfield, and J. Kettleborough (2002). *Polar vortex concentricity as a controlling factor in Arctic denitrification.* Journal of Geophysical Research: Atmospheres 107 (D22). 4663, 1–11. DOI: 10.1029/2002JD002102 (cit. on p. 21).

Mann, G. W., K. S. Carslaw, M. P. Chipperfield, S. Davies, and S. D. Eckermann (2005). *Large nitric acid trihydrate particles and denitrification caused by mountain waves in the Arctic stratosphere.* Journal of Geophysical Research: Atmospheres 110 (D8). D08202. DOI: 10.1029/2004JD005271 (cit. on pp. 2, 22, 42).

Marti, J. and K. Mauersberger (1993). *A survey and new measurements of ice vapor pressure at temperatures between 170 and 250K.* Geophysical Research Letters 20 (5), 363–366. DOI: 10.1029/93GL00105 (cit. on pp. 19, 21, 33, 36, 38, 72, 75, 76, 77).

Mason, E. A. and L. Monchick (1962). *Transport Properties of Polar–Gas Mixtures.* The Journal of Chemical Physics 36 (10), 2746–2757. DOI: 10.1063/1.1732363 (cit. on p. 131).

Massie, S. T., J. C. Gille, D. P. Edwards, P. L. Bailey, L. V. Lyjak, C. A. Craig, C. P. Cavanaugh, J. L. Mergenthaler, A. E. Roche, J. B. Kumer, A. Lambert, R. G. Grainger, C. D. Rodgers, F. W. Taylor, J. M. Russell, J. H. Park, T. Deshler, M. E. Hervig, E. F. Fishbein, J. W. Waters, and W. A. Lahoz (1996). *Validation studies using multiwavelength Cryogenic Limb Array Etalon Spectrometer (CLAES) observations of stratospheric aerosol.* Journal of Geophysical Research: Atmospheres 101 (D6), 9757–9773. DOI: 10.1029/95JD03225 (cit. on p. 50).

McDonald, A. J., S. E. George, and R. M. Woollands (2009). *Can gravity waves significantly impact PSC occurrence in the Antarctic?* Atmospheric Chemistry and Physics 9 (22), 8825–8840. DOI: 10.5194/acp-9-8825-2009 (cit. on p. 2).

McElroy, M. B., R. J. Salawitch, S. C. Wofsy, and J. A. Logan (1986). *Reductions of Antarctic ozone due to synergistic interactions of chlorine and bromine.* Nature 321, 759–762. DOI: 10.1038/321759a0 (cit. on p. 17).

McKenna, D. S., J.-U. Grooß, G. Günther, P. Konopka, R. Müller, G. Carver, and Y. Sasano (2002). *A new Chemical Lagrangian Model of the Stratosphere (CLaMS) 2. Formulation of chemistry scheme and initialization.* Journal of Geophysical Research: Atmospheres 107 (D15), 1–14. DOI: 10.1029/2000JD000113 (cit. on p. 47).

McLandress, C. and J. F. Scinocca (2005). *The GCM Response to Current Parameterizations of Nonorographic Gravity Wave Drag.* Journal of the Atmospheric Sciences 62 (7), 2394–2413. DOI: 10.1175/JAS3483.1 (cit. on p. 11).

Meilinger, S. K., T. Koop, B. P. Luo, T. Huthwelker, K. S. Carslaw, U. Krieger, P. J. Crutzen, and T. Peter (1995). *Size-dependent stratospheric droplet composition in Lee wave temperature fluctuations and their potential role in PSC freezing.* Geophysical Research Letters 22 (22), 3031–3034. DOI: 10.1029/95GL03056 (cit. on pp. 2, 21, 112).

Miura, H. (2007). *An Upwind-Biased Conservative Advection Scheme for Spherical Hexagonal–Pentagonal Grids.* Monthly Weather Review 135 (12), 4038–4044. DOI: 10.1175/2007MWR2101.1 (cit. on p. 27).

Möhler, O., H. Bunz, and O. Stetzer (2006). *Homogeneous nucleation rates of nitric acid dihydrate (NAD) at simulated stratospheric conditions – Part II: Modelling.* Atmospheric Chemistry and Physics 6 (10), 3035–3047. DOI: 10.5194/acp-6-3035-2006 (cit. on p. 20).

Molina, L. T. and M. J. Molina (1987). *Production of chlorine oxide (Cl_2O_2) from the self-reaction of the chlorine oxide (ClO) radical.* The Journal of Physical Chemistry 91 (2), 433–436. DOI: 10.1021/j100286a035 (cit. on pp. 16, 22).

Molina, M. J. and F. Rowland (1974). *Stratospheric sink for chlorofluoromethanes: chlorine atom-catalysed destruction of ozone.* Nature 249, 810 –812. DOI: 10.1038/249810a0 (cit. on pp. 16, 17).

Molina, M. J., T. Ishiwata, and L. T. Molina (1980). *Production of hydroxyl from photolysis of hypochlorous acid at 307-309 nm.* The Journal of Physical Chemistry 84 (8), 821–826. DOI: 10.1021/j100445a004 (cit. on p. 19).

Molleker, S., S. Borrmann, H. Schlager, B. Luo, W. Frey, M. Klingebiel, R. Weigel, M. Ebert, V. Mitev, R. Matthey, W. Woiwode, H. Oelhaf, A. Dörnbrack, G. Stratmann, J.-U. Grooß, G. Günther, B. Vogel, R. Müller, M. Krämer, J. Meyer, and F. Cairo (2014). *Microphysical properties of synoptic-scale polar stratospheric clouds: in situ measurements of unexpectedly large HNO_3-containing particles in the Arctic vortex.* Atmospheric Chemistry and Physics 14 (19), 10785–10801. DOI: 10.5194/acp-14-10785-2014 (cit. on pp. 20, 21).

MPI Forum (2015). *A Message-Passing Interface Standard Version 3.1.* Knoxville, Tennesse: University of Tennessee (cit. on p. 28).

Murphy, D. M. and B. L. Gary (1995). *Mesoscale Temperature Fluctuations and Polar Stratospheric Clouds.* Journal of the Atmospheric Sciences 52 (10), 1753–1760. DOI: 10.1175/1520-0469(1995)052<1753:MTFAPS>2.0.CO;2 (cit. on p. 21).

NASA (1976). *U.S. Standard Atmosphere.* Tech. rep. Washington, DC, United States: National Oceanic and Atmospheric Administration (cit. on pp. 5, 6).

Nedoluha, G. E., R. M. Bevilacqua, K. W. Hoppel, M. Daehler, E. P. Shettle, J. H. Hornstein, M. D. Fromm, J. D. Lumpe, and J. E. Rosenfield (2000). *POAM III measurements of dehydration in the Antarctic lower stratosphere.* Geophysical Research Letters 27 (12), 1683–1686. DOI: 10.1029/1999GL011087 (cit. on p. 21).

Newell, R. E. (1963). *Transfer through the tropopause and within the stratosphere.* Quarterly Journal of the Royal Meteorological Society 89 (380), 167–204. DOI: 10.1002/qj.49708938002 (cit. on p. 7).

Newman, P. A., S. R. Kawa, and E. R. Nash (2004). *On the size of the Antarctic ozone hole.* Geophysical Research Letters 31 (21). DOI: 10.1029/2004GL020596 (cit. on p. 19).

Noel, V. and M. Pitts (2012). *Gravity wave events from mesoscale simulations, compared to polar stratospheric clouds observed from spaceborne lidar over the Antarctic Peninsula.* Journal of Geophysical Research: Atmospheres (1984–2012) 117 (D11). DOI: 10.1029/2011JD017318 (cit. on pp. 2, 53, 58, 109, 121, 126).

Nowack, P., P. Braesicke, J. Haigh, N. L. Abraham, J. Pyle, and A. Voulgarakis (2018). *Using machine learning to build temperature-based ozone parameterizations for climate sensitivity simulations.* Environmental Research Letters 13 (10), 104016. DOI: 10.1088/1748-9326/aae2be (cit. on p. 1).

Olivier, J., A. Bouwman, J. Berdowski, C. Veldt, J. Bloos, A. Visschedijk, C. van der Maas, and P. Zandveld (1999). *Sectoral emission inventories of greenhouse gases for 1990 on a per country basis as well as on 1°×1°.* Environmental Science & Policy 2 (3), 241 –263. DOI: https://doi.org/10.1016/S1462-9011(99)00027-1 (cit. on p. 103).

Orr, A., J. S. Hosking, L. Hoffmann, J. Keeble, S. M. Dean, H. K. Roscoe, N. L. Abraham, S. Vosper, and P. Braesicke (2015). *Inclusion of mountain-wave-induced cooling for the formation of PSCs over the Antarctic Peninsula in a chemistry–climate model.* Atmospheric Chemistry and Physics 15 (2), 1071–1086. DOI: 10.5194/acp-15-1071-2015 (cit. on pp. 2, 123).

Orr, A., P. Bechtold, J. Scinocca, M. Ern, and M. Janiskova (2010). *Improved Middle Atmosphere Climate and Forecasts in the ECMWF Model through a Nonorographic Gravity Wave Drag Parameterization.* Journal of Climate 23 (22), 5905–5926. DOI: 10.1175/2010JCLI3490.1 (cit. on pp. 9, 11, 31, 32).

Pauli, W. (1925). *Über den Zusammenhang des Abschlusses der Elektronengruppen im Atom mit der Komplexstruktur der Spektren.* Z. Physik 31 (765) (cit. on p. 133).

Pawson, S., K. Krüger, R. Swinbank, M. Bailey, and A. O'Neill (1999). *Intercomparison of two stratospheric analyses: Temperatures relevant to polar stratospheric cloud formation.* Journal of Geophysical Research: Atmospheres 104 (D2), 2041–2050. DOI: 10.1029/98JD02279 (cit. on p. 68).

Peter, T. (1997). *Microphysics and heterogeneous chemistry of polar stratospheric clouds*. Annual Review of Physical Chemistry 48 (1). PMID: 15012456, 785–822. DOI: 10.1146/annurev.physchem.48.1.785 (cit. on pp. 20, 48).

Peter, T. and J.-U. Grooß (2011). "Chapter 4: Polar Stratospheric Clouds and Sulfate Aerosol Particles: Microphysics, Denitrification and Heterogeneous Chemistry". In: *Stratospheric Ozone Depletion and Climate Change*. Ed. by R. Müller. The Royal Society of Chemistry. DOI: 10.1039/9781849733182 (cit. on pp. 1, 20, 21, 125).

Peter, T., C. Brühl, and P. J. Crutzen (1991). *Increase in the PSC-formation probability caused by high-flying aircraft*. Geophysical Research Letters 18 (8), 1465–1468. DOI: 10.1029/91GL01562 (cit. on pp. 21, 43).

Piazzi-Smyth, C (1886). *Iridescent Clouds*. Nature 33, 219–220 (cit. on p. 19).

Pitts, M. C., L. R. Poole, and L. W. Thomason (2009). *CALIPSO polar stratospheric cloud observations: second-generation detection algorithm and composition discrimination*. Atmospheric Chemistry and Physics 9 (19), 7577–7589. DOI: 10.5194/acp-9-7577-2009 (cit. on p. 62).

Pitts, M. C., L. R. Poole, and R. Gonzalez (2018). *Polar stratospheric cloud climatology based on CALIPSO spaceborne lidar measurements from 2006 to 2017*. Atmospheric Chemistry and Physics 18 (15), 10881–10913. DOI: 10.5194/acp-18-10881-2018 (cit. on pp. 19, 38, 62, 99).

Plumb, R. A. (1996). *A "tropical pipe" model of stratospheric transport*. Journal of Geophysical Research: Atmospheres 101 (D2), 3957–3972. DOI: 10.1029/95JD03002 (cit. on p. 11).

Poling, B. E., J. M. Prausnitz, and J. P. OConnell (2001). *The properties of gases and liquids*. 5th edition. New York: McGraw-Hill (cit. on p. 131).

Poole, L. R. and M. P. McCormick (1988). *Airborne lidar observations of Arctic polar stratospheric clouds: Indications of two distinct growth stages*. Geophysical Research Letters 15 (1), 21–23. DOI: 10.1029/GL015i001p00021 (cit. on p. 20).

Prather, M. J. (2015). *Photolysis rates in correlated overlapping cloud fields: Cloud-J 7.3c*. Geoscientific Model Development 8 (8), 2587–2595. DOI: 10.5194/gmd-8-2587-2015 (cit. on pp. 29, 136).

Pruppacher, H. R. and J. D. Klett (1997). *Microphysics of clouds and precipitation*. 2nd, rev. and enl. ed. Atmospheric and oceanographic sciences library ; 18. Dordrecht: Kluwer (cit. on pp. 45, 131).

Queney, P. (1948). *The Problem of Air Flow Over Mountains: A Summary of Theoretical Studies*. Bulletin of the American Meteorological Society 29 (1), 16–26. DOI: 10.1175/1520-0477-29.1.16 (cit. on p. 9).

Raoult, F.-M. (1886). *Loi générale des tensions de vapeur des dissolvants*. C.R. Acad. Sci. Paris 104, 1430–1433 (cit. on p. 14).

Reif, F. (1965). *Fundamentals of statistical and thermal physics*. internat. student ed. McGraw-Hill series in fundamentals of physics. New York: McGraw-Hill (cit. on p. 131).

Reinert, D., F. Prill, G. Zängl, D. Rieger, J. Schröter, J. Förstner, S. Werchner, M. Weimer, R. Ruhnke, and B. Vogel (2019). *Working with the ICON Model*. Tech. rep. https://code.mpimet.mpg.de/attachments/download/19568/ICON_tutorial_2019.pdf. Offenbach: Deutscher Wetterdienst (cit. on p. 29).

Riahi, K., A. Grübler, and N. Nakicenovic (2007). *Scenarios of long-term socio-economic and environmental development under climate stabilization*. Technological Forecasting and Social Change 74 (7). Greenhouse Gases - Integrated Assessment, 887 –935. DOI: https://doi.org/10.1016/j.techfore.2006.05.026 (cit. on p. 56).

Rieckh, T., B. Scherllin-Pirscher, F. Ladstädter, and U. Foelsche (2014). *Characteristics of tropopause parameters as observed with GPS radio occultation*. Atmospheric Measurement Techniques 7 (11), 3947–3958. DOI: 10.5194/amt-7-3947-2014 (cit. on p. 74).

Rieger, D., M. Bangert, I. Bischoff-Gauss, J. Förstner, K. Lundgren, D. Reinert, J. Schröter, H. Vogel, G. Zängl, R. Ruhnke, and B. Vogel (2015). *ICON-ART 1.0 - a new online-coupled model system from the global to regional scale*. Geosci. Model Dev. 8 (6), 1659–1676. DOI: 10.5194/gmd-8-1659-2015 (cit. on pp. 3, 28, 39).

Rienecker, M. M., M. J. Suarez, R. Gelaro, R. Todling, J. Bacmeister, E. Liu, M. G. Bosilovich, S. D. Schubert, L. Takacs, G.-K. Kim, S. Bloom, J. Chen, D. Collins, A. Conaty, A. da Silva, W. Gu, J. Joiner, R. D. Koster, R. Lucchesi, A. Molod, T. Owens, S. Pawson, P. Pegion, C. R. Redder, R. Reichle, F. R. Robertson, A. G. Ruddick, M. Sienkiewicz, and J. Woollen (2011). *MERRA: NASA's Modern-Era Retrospective Analysis for Research and Applications*. Journal of Climate 24 (14), 3624–3648. DOI: 10.1175/JCLI-D-11-00015.1 (cit. on p. 60).

Rinsland, C. P., M. R. Gunson, R. J. Salawitch, M. J. Newchurch, R. Zander, M. M. Abbas, M. C. Abrams, G. L. Manney, H. A. Michelsen, A. Y. Chang, and A. Goldman (1996). *ATMOS measurements of H_2O+2CH_4 and total reactive nitrogen in the November 1994 Antarctic stratosphere: Dehydration and denitrification in the vortex*. Geophysical Research Letters 23 (17), 2397–2400. DOI: 10.1029/96GL00048 (cit. on pp. 87, 88, 90).

Roche, A. E., J. B. Kumer, J. L. Mergenthaler, G. A. Ely, W. G. Uplinger, J. F. Potter, T. C. James, and L. W. Sterritt (1993). *The cryogenic limb array etalon spectrometer (CLAES) on UARS: Experiment description and performance*. Journal of Geophysical Research: Atmospheres 98 (D6), 10763–10775. DOI: 10.1029/93JD00800 (cit. on p. 50).

Romakkaniemi, S., H. Kokkola, K. E. J. Lehtinen, and A. Laaksonen (2006). *The influence of nitric acid on the cloud processing of aerosol particles*. Atmospheric Chemistry and Physics 6 (6), 1627–1634. DOI: 10.5194/acp-6-1627-2006 (cit. on p. 20).

Ruhnke, R., W. Kouker, and T. Reddmann (1999). *The influence of the* OH + NO_2 + M *reaction on the* NO_y*, partitioning in the late Arctic winter 1992/1993 as studied with KASIMA*. J. Geophys. Res.: Atmospheres 104 (D3), 3755–3772. DOI: 10.1029/1998JD100062 (cit. on p. 47).

Salawitch, R., G. Gobbi, S. Wofsy, and M. McElroy (1989). *Denitrification in the Antarctic stratosphere*. Nature 339, 525–527. DOI: 10.1038/339525a0 (cit. on p. 21).

Salcedo, D., L. T. Molina, and M. J. Molina (2001). *Homogeneous Freezing of Concentrated Aqueous Nitric Acid Solutions at Polar Stratospheric Temperatures*. The Journal of Physical Chemistry A 105 (9), 1433–1439. DOI: 10.1021/jp001639s (cit. on pp. 21, 117).

Sander, R., A. Baumgaertner, S. Gromov, H. Harder, P. Jöckel, A. Kerkweg, D. Kubistin, E. Regelin, H. Riede, A. Sandu, D. Taraborrelli, H. Tost, and Z.-Q. Xie (2011a). *The atmospheric chemistry box model CAABA/MECCA-3.0*. Geoscientific Model Development 4 (2), 373–380. DOI: 10.5194/gmd-4-373-2011 (cit. on pp. 29, 32).

Sander, S., J Abbatt, J. Barker, J. Burkholder, R. Friedl, D. Golden, R. Huie, C. Kolb, M. Kurylo, K Moortgat, V. Orkin, and P. Wine (2011b). *Chemical Kinetics and Photochemical Data for Use in Atmospheric Studies, Evaluation No. 17*. JPL Publication 10-6 (cit. on pp. 12, 51).

Sandu, A. and R. Sander (2006). *Technical note: Simulating chemical systems in Fortran90 and Matlab with the Kinetic PreProcessor KPP-2.1*. Atmospheric Chemistry and Physics 6 (1), 187–195. DOI: 10.5194/acp-6-187-2006 (cit. on p. 32).

Sandu, A., J. Verwer, J. Blom, E. Spee, G. Carmichael, and F. Potra (1997). *Benchmarking stiff ode solvers for atmospheric chemistry problems II: Rosenbrock solvers*. Atmospheric Environment 31 (20), 3459 –3472. DOI: 10.1016/S1352-2310(97)83212-8 (cit. on p. 32).

Schär, C., D. Leuenberger, O. Fuhrer, D. Lüthi, and C. Girard (2002). *A New Terrain-Following Vertical Coordinate Formulation for Atmospheric Prediction Models*. Monthly Weather Review 130 (10), 2459–2480. DOI: 10.1175/1520-0493(2002)130<2459:ANTFVC>2.0.CO;2 (cit. on p. 27).

Schoeberl, M. R., A. R. Douglass, E. Hilsenrath, P. K. Bhartia, R. Beer, J. W. Waters, M. R. Gunson, L. Froidevaux, J. C. Gille, J. J. Barnett, P. F. Levelt, and P. DeCola (2006). *Overview of the EOS aura mission*. IEEE Transactions on Geoscience and Remote Sensing 44 (5), 1066–1074. DOI: 10.1109/TGRS.2005.861950 (cit. on p. 62).

Schoeberl, M. R. and D. L. Hartmann (1991). *The Dynamics of the Stratospheric Polar Vortex and Its Relation to Springtime Ozone Depletions*. Science 251 (4989), 46–52. DOI: 10.1126/science.251.4989.46 (cit. on p. 7).

Schreiner, J., C. Voigt, C. Weisser, A. Kohlmann, K. Mauersberger, T. Deshler, C. Kröger, J. Rosen, N. Kjome, N. Larsen, A. Adriani, F. Cairo, G. Di Donfrancesco, J. Ovarlez, H. Ovarlez, and A. Dörnbrack (2002). *Chemical, microphysical, and optical properties of polar stratospheric clouds*. Journal of Geophysical Research: Atmospheres 107 (D5). 8313, SOL 56–1–SOL 56–10. DOI: 10.1029/2001JD000825 (cit. on p. 21).

Schröter, J., D. Rieger, C. Stassen, H. Vogel, M. Weimer, S. Werchner, J. Förstner, F. Prill, D. Reinert, G. Zängl, M. Giorgetta, R. Ruhnke, B. Vogel, and P. Braesicke (2018). *ICON-ART 2.1: a flexible tracer framework and its application for composition studies in numerical weather forecasting and climate simulations*. Geoscientific Model Development 11 (10), 4043–4068. DOI: 10.5194/gmd-11-4043-2018 (cit. on pp. 3, 28, 29, 32, 39, 43, 55, 94).

Schröter, J. (2018). *Modelling of the interaction between radiation and the atmospheric composition with ICON-ART*. 12.04.03; LK 01. PhD thesis. Karlsruher Institut für Technologie (KIT). 150 pp. DOI: 10.5445/IR/1000080647 (cit. on pp. 27, 29, 56, 94).

Scinocca, J. F. (2003). *An Accurate Spectral Nonorographic Gravity Wave Drag Parameterization for General Circulation Models*. Journal of the Atmospheric Sciences 60 (4), 667–682. DOI: 10.1175/1520-0469(2003)060<0667:AASNGW>2.0.CO;2 (cit. on p. 31).

Seinfeld, J. H. and S. N. Pandis (2006). *Atmospheric Chemistry and Physics : from Air Pollution to Climate Change*. 2. ed. Previous ed.: 1998. Hoboken, NJ: Wiley (cit. on pp. 1, 5, 12, 13, 14, 15, 17, 18).

Selz, T. (2019). "Calculation of Potential Vorticity on the ICON Grid". In: *Reports on ICON*. Ed. by S. Rast, R. Redler, D. Reinert, D. Rieger, and F. Prill. Offenbach, Germany: Deutscher Wetterdienst. DOI: 10.5676/DWD_pub/nwv/icon_002 (cit. on p. 66).

Serra, M., P. Sathe, F. Beron-Vera, and G. Haller (2017). *Uncovering the Edge of the Polar Vortex*. Journal of the Atmospheric Sciences 74 (11), 3871–3885. DOI: 10.1175/JAS-D-17-0052.1 (cit. on p. 66).

Shi, Q., J. T. Jayne, C. E. Kolb, D. R. Worsnop, and P. Davidovits (2001). *Kinetic model for reaction of $ClONO_2$ with H_2O and HCl and HOCl with HCl in sulfuric acid solutions*. Journal of Geophysical Research: Atmospheres 106 (D20), 24259–24274. DOI: 10.1029/2000JD000181 (cit. on p. 23).

Simmons, A. J., D. M. Burridge, M. Jarraud, C. Girard, and W. Wergen (1989). *The ECMWF medium-range prediction models development of the numerical formulations and the impact of increased resolution*. Meteorology and Atmospheric Physics 40 (1), 28–60. DOI: 10.1007/BF01027467 (cit. on pp. 31, 59).

Sindelarova, K., C. Granier, I. Bouarar, A. Guenther, S. Tilmes, T. Stavrakou, J.-F. Müller, U. Kuhn, P. Stefani, and W. Knorr (2014). *Global data set of biogenic VOC emissions calculated by the MEGAN model over the last 30 years*. Atmos. Chem. Phys. 14 (17), 9317–9341. DOI: 10.5194/acp-14-9317-2014 (cit. on p. 33).

Smiatek, G., B. Rockel, and U. Schättler (2008). *Time invariant data preprocessor for the climate version of the COSMO model (COSMO-CLM)*. Meteorologische Zeitschrift 17 (4), 395–405. DOI: 10.1127/0941-2948/2008/0302 (cit. on pp. 29, 31).

Solomon, S, R. Garcia, F. Rowland, and Wuebbles (1986). *On the depletion of Antarctic ozone*. Nature 321, 755–758. DOI: 10.1038/321755a0 (cit. on pp. 1, 19, 22).

Solomon, S. (1999). *Stratospheric ozone depletion: A review of concepts and history*. Reviews of Geophysics 37 (3), 275–316. DOI: 10.1029/1999RG900008 (cit. on p. 22).

Spang, R., L. Hoffmann, M. Höpfner, S. Griessbach, R. Müller, M. C. Pitts, A. M. W. Orr, and M. Riese (2016). *A multi-wavelength classification method for polar stratospheric cloud types using infrared limb spectra*. Atmospheric Measurement Techniques 9 (8), 3619–3639. DOI: 10.5194/amt-9-3619-2016 (cit. on p. 100).

Spang, R., L. Hoffmann, R. Müller, J.-U. Grooß, I. Tritscher, M. Höpfner, M. Pitts, A. Orr, and M. Riese (2018). *A climatology of polar stratospheric cloud composition between 2002 and 2012 based on MIPAS/Envisat observations*. Atmospheric Chemistry and Physics 18 (7), 5089–5113. DOI: 10.5194/acp-18-5089-2018 (cit. on p. 100).

SPARC (2013). *SPARC Newsletter No. 40*. available at http://www.sparc-climate.org/publications/newsletter. 68 pp. (Cit. on p. 32).

Staniforth, A. and J. Thuburn (2012). *Horizontal grids for global weather and climate prediction models: a review*. Quarterly Journal of the Royal Meteorological Society 138 (662), 1–26. DOI: 10.1002/qj.958 (cit. on p. 25).

Stassen, C. (2015). *Simulation von chemischen Tracern mit ICON-ART*. Master's Thesis. Germany: Karlsruhe Institute of Technology (KIT) (cit. on p. 29).

Stenchikov, G. L., I. Kirchner, A. Robock, H.-F. Graf, J. C. Antuña, R. G. Grainger, A. Lambert, and L. Thomason (1998). *Radiative forcing from the 1991 Mount Pinatubo volcanic eruption*. Journal of Geophysical Research: Atmospheres 103 (D12), 13837–13857. DOI: 10.1029/98JD00693 (cit. on p. 56).

Stenchikov, G. L., K. Hamilton, A. Robock, V. Ramaswamy, and M. D. Schwarzkopf (2004). *Arctic oscillation response to the 1991 Pinatubo eruption in the SKYHI general circulation model with a realistic quasi-biennial oscillation*. Journal of Geophysical Research: Atmospheres 109 (D3). DOI: 10.1029/2003JD003699 (cit. on p. 56).

Stenchikov, G. L., T. L. Delworth, V. Ramaswamy, R. J. Stouffer, A. Wittenberg, and F. Zeng (2009). *Volcanic signals in oceans*. Journal of Geophysical Research: Atmospheres 114 (D16). DOI: 10.1029/2008JD011673 (cit. on p. 56).

Stephens, G. L., D. G. Vane, R. J. Boain, G. G. Mace, K. Sassen, Z. Wang, A. J. Illingworth, E. J. O'connor, W. B. Rossow, S. L. Durden, S. D. Miller, R. T. Austin, A. Benedetti, and C. a. Mitrescu (2002). *The CloudSat Mission and the*

A-Train. Bulletin of the American Meteorological Society 83 (12), 1771–1790. DOI: 10.1175/BAMS-83-12-1771 (cit. on pp. 60, 62).

Stevenson, J. (1886). *Iridescent Clouds*. Nature 33, 220 (cit. on p. 19).

Stohl, A., P. Bonasoni, P. Cristofanelli, W. Collins, J. Feichter, A. Frank, C. Forster, E. Gerasopoulos, H. Gäggeler, P. James, T. Kentarchos, H. Kromp-Kolb, B. Krüger, C. Land, J. Meloen, A. Papayannis, A. Priller, P. Seibert, M. Sprenger, G. J. Roelofs, H. E. Scheel, C. Schnabel, P. Siegmund, L. Tobler, T. Trickl, H. Wernli, V. Wirth, P. Zanis, and C. Zerefos (2003). *Stratosphere-troposphere exchange: A review, and what we have learned from STACCATO*. Journal of Geophysical Research: Atmospheres 108 (D12). DOI: 10.1029/2002JD002490 (cit. on p. 8).

Stokes, G. G. (1851). *On the Effect of the Internal Friction of Fluids on the Motion of Pendulums*. Transactions of the Cambridge Philosophical Society Part II (9), 8 –106 (cit. on p. 15).

Størmer, C. (1929). *Remarkable Clouds at High Altitudes*. Nature 123, 260–261 (cit. on p. 19).

Sutherland, W. (1893). *The Viscosity of Gases and Molecular Force*. Philos. Mag. Series 5 (36), 507–531. DOI: 10.1080/14786449308620508 (cit. on p. 15).

Tabazadeh, A., M. L. Santee, M. Y. Danilin, H. C. Pumphrey, P. A. Newman, P. J. Hamill, and J. L. Mergenthaler (2000). *Quantifying Denitrification and Its Effect on Ozone Recovery*. Science 288 (5470), 1407–1411. DOI: 10.1126/science.288.5470.1407 (cit. on pp. 2, 20, 21).

Tabazadeh, A., E. J. Jensen, O. B. Toon, K. Drdla, and M. R. Schoeberl (2001). *Role of the Stratospheric Polar Freezing Belt in Denitrification*. Science 291 (5513), 2591–2594. DOI: 10.1126/science.1057228 (cit. on p. 19).

Tabazadeh, A., Y. S. Djikaev, P. Hamill, and H. Reiss (2002). *Laboratory Evidence for Surface Nucleation of Solid Polar Stratospheric Cloud Particles*. The Journal of Physical Chemistry A 106 (43), 10238–10246. DOI: 10.1021/jp021045k (cit. on p. 20).

Tang, M. J., R. A. Cox, and M. Kalberer (2014). *Compilation and evaluation of gas phase diffusion coefficients of reactive trace gases in the atmosphere: volume 1. Inorganic compounds*. Atmospheric Chemistry and Physics 14 (17), 9233–9247. DOI: 10.5194/acp-14-9233-2014 (cit. on p. 132).

Taylor, K., D. Williamson, and F. Zwiers (2000). *The Sea Surface Temperature and Sea-ice Concentration Boundary Conditions for AMIP II Simulations*. PCMDI report. Program for Climate Model Diagnosis and Intercomparison, Lawrence Livermore National Laboratory (cit. on pp. 54, 56).

Thomason, L. W., S. P. Burton, B.-P. Luo, and T. Peter (2008). *SAGE II measurements of stratospheric aerosol properties at non-volcanic levels*. Atmospheric Chemistry and Physics 8 (4), 983–995. DOI: 10.5194/acp-8-983-2008 (cit. on p. 32).

Thomson, S. W. F. (1871). *LX. On the equilibrium of vapour at a curved surface of liquid*. The London, Edinburgh, and Dublin Philosophical Magazine and Journal of Science 42 (282), 448–452. DOI: 10.1080/14786447108640606 (cit. on p. 14).

Thornton, J. A., P. J. Wooldridge, R. C. Cohen, M. Martinez, H. Harder, W. H. Brune, E. J. Williams, J. M. Roberts, F. C. Fehsenfeld, S. R. Hall, R. E. Shetter, B. P. Wert, and A. Fried (2002). *Ozone production rates as a function of NO_x abundances and HO_x production rates in the Nashville urban plume*. Journal of Geophysical Research: Atmospheres 107 (D12), 1–17. DOI: 10.1029/2001JD000932 (cit. on p. 1).

Tolbert, M. A., M. J. Rossi, and D. M. Golden (1988). *Antarctic Ozone Depletion Chemistry: Reactions of N_2O_5 with H_2O and HCl on Ice Surfaces*. Science 240 (4855), 1018–1021. DOI: 10.1126/science.240.4855.1018 (cit. on p. 22).

Tomita, H., M. Tsugawa, M. Satoh, and K. Goto (2001). *Shallow Water Model on a Modified Icosahedral Geodesic Grid by Using Spring Dynamics*. Journal of Computational Physics 174 (2), 579 –613. DOI: 10.1006/jcph.2001.6897 (cit. on p. 27).

Toon, O. B., P. Hamill, R. P. Turco, and J. Pinto (1986). *Condensation of HNO_3 and HCl in the winter polar stratospheres*. Geophysical Research Letters 13 (12), 1284–1287. DOI: 10.1029/GL013i012p01284 (cit. on pp. 20, 21).

Toon, O. B., E. V. Browell, S. Kinne, and J. Jordan (1990). *An analysis of lidar observations of polar stratospheric clouds*. Geophysical Research Letters 17 (4), 393–396. DOI: 10.1029/GL017i004p00393 (cit. on p. 20).

Turco, R. P., O. B. Toon, and P. Hamill (1989). *Heterogeneous physicochemistry of the polar ozone hole*. Journal of Geophysical Research: Atmospheres 94 (D14), 16493–16510. DOI: 10.1029/JD094iD14p16493 (cit. on pp. 20, 22).

Ullwer, C. (2018). *Untersuchung der Verteilung von aerosolbildenden Spurengasen mit ICON-ART*. Master's Thesis. Germany: Karlsruhe Institute of Technology (KIT) (cit. on p. 29).

UNEP (1987). *Montreal protocol on substances that deplete the ozone layer*. Final Act (cit. on p. 1).

van den Broek, M. M. P., J. E. Williams, and A. Bregman (2004). *Implementing growth and sedimentation of NAT particles in a global Eulerian model*. Atmospheric Chemistry and Physics 4 (7), 1869–1883. DOI: 10.5194/acp-4-1869-2004 (cit. on pp. 42, 43, 44, 55, 81).

van der Werf, G. R., J. T. Randerson, L. Giglio, G. J. Collatz, P. S. Kasibhatla, and A. F. Arellano Jr. (2006). *Interannual variability in global biomass burning emissions from 1997 to 2004*. Atmos. Chem. Phys. 6 (11), 3423–3441. DOI: 10.5194/acp-6-3423-2006 (cit. on p. 33).

van der Werf, G. R., J. T. Randerson, L. Giglio, G. J. Collatz, M. Mu, P. S. Kasibhatla, D. C. Morton, R. S. DeFries, Y. Jin, and T. T. van Leeuwen (2010). *Global fire emissions and the contribution of deforestation, savanna, forest, agricultural, and peat fires (1997-2009)*. Atmos. Chem. Phys. 10 (23), 11707–11735. DOI: 10.5194/acp-10-11707-2010 (cit. on p. 33).

Voigt, C., H. Schlager, A. Roiger, A. Stenke, M. de Reus, S. Borrmann, E. Jensen, C. Schiller, P. Konopka, and N. Sitnikov (2008). *Detection of reactive nitrogen containing particles in the tropopause region – evidence for a tropical nitric acid trihydrate (NAT) belt*. Atmospheric Chemistry and Physics 8 (24), 7421–7430. DOI: 10.5194/acp-8-7421-2008 (cit. on p. 20).

Voigt, C., A. Dörnbrack, M. Wirth, S. M. Groß, M. C. Pitts, L. R. Poole, R. Baumann, B. Ehard, B.-M. Sinnhuber, W. Woiwode, and H. Oelhaf (2018). *Widespread polar stratospheric ice clouds in the 2015–2016 Arctic winter – implications for ice nucleation*. Atmospheric Chemistry and Physics 18 (21), 15623–15641. DOI: 10.5194/acp-18-15623-2018 (cit. on pp. 2, 21).

Voigt, C., J. Schreiner, A. Kohlmann, P. Zink, K. Mauersberger, N. Larsen, T. Deshler, C. Kröger, J. Rosen, A. Adriani, F. Cairo, G. D. Donfrancesco, M. Viterbini, J. Ovarlez, H. Ovarlez, C. David, and A. Dörnbrack (2000). *Nitric Acid Trihydrate (NAT) in Polar Stratospheric Clouds*. Science 290 (5497), 1756–1758. DOI: 10.1126/science.290.5497.1756 (cit. on p. 20).

Vömel, H., S. J. Oltmans, D. J. Hofmann, T. Deshler, and J. M. Rosen (1995). *The evolution of the dehydration in the Antarctic stratospheric vortex*. Journal of Geophysical Research: Atmospheres 100 (D7), 13919–13926. DOI: 10.1029/95JD01000 (cit. on p. 21).

Vosper, S. B., A. R. Brown, and S. Webster (2016). *Orographic drag on islands in the NWP mountain grey zone*. Quarterly Journal of the Royal Meteorological Society 142 (701), 3128–3137. DOI: 10.1002/qj.2894 (cit. on p. 126).

Waibel, A. E., T. Peter, K. S. Carslaw, H. Oelhaf, G. Wetzel, P. J. Crutzen, U. Pöschl, A. Tsias, E. Reimer, and H. Fischer (1999). *Arctic Ozone Loss Due to Denitrification*. Science 283 (5410), 2064–2069. DOI: 10.1126/science.283.5410.2064 (cit. on pp. 87, 88, 90, 124).

Wan, H., M. A. Giorgetta, G. Zängl, M. Restelli, D. Majewski, L. Bonaventura, K. Fröhlich, D. Reinert, P. Rípodas, L. Kornblueh, and J. Förstner (2013). *The ICON-1.2 hydrostatic atmospheric dynamical core on triangular grids – Part 1: Formulation and performance of the baseline version*. Geoscientific Model Development 6 (3), 735–763. DOI: 10.5194/gmd-6-735-2013 (cit. on p. 27).

Wandinger, U. (2005). "Introduction to Lidar". In: *Lidar: Range-Resolved Optical Remote Sensing of the Atmosphere*. Ed. by C. Weitkamp. New York, NY, USA: Springer (cit. on p. 99).

Waters, J. W., L. Froidevaux, R. S. Harwood, R. F. Jarnot, H. M. Pickett, W. G. Read, P. H. Siegel, R. E. Cofield, M. J. Filipiak, D. A. Flower, J. R. Holden, G. K. Lau, N. J. Livesey, G. L. Manney, H. C. Pumphrey, M. L. Santee, D. L. Wu, D. T. Cuddy, R. R. Lay, M. S. Loo, V. S. Perun, M. J. Schwartz, P. C. Stek, R. P. Thurstans, M. A. Boyles, K. M. Chandra, M. C. Chavez, G.-S. Chen, B. V. Chudasama, R. Dodge, R. A. Fuller, M. A. Girard, J. H. Jiang, Y. Jiang, B. W. Knosp, R. C. LaBelle, J. C. Lam, K. A. Lee, D. Miller, J. E. Oswald, N. C. Patel, D. M. Pukala, O. Quintero, D. M. Scaff, W. V. Snyder, M. C. Tope, P. A. Wagner, and M. J. Walch (2006). *The Earth observing system microwave limb sounder (EOS MLS) on the Aura Satellite*. IEEE Trans. Geosci. Remote Sens. 44 (5), 1075–1092. DOI: 10.1109/TGRS.2006.873771 (cit. on pp. 62, 63).

Waters, J. (1989). *Microwave limb-sounding of earth's upper atmosphere*. Atmospheric Research 23 (3), 391 –410. DOI: https://doi.org/10.1016/0169-8095(89)90028-8 (cit. on p. 62).

Weimer, M., J. Schröter, J. Eckstein, K. Deetz, M. Neumaier, G. Fischbeck, L. Hu, D. B. Millet, D. Rieger, H. Vogel, B. Vogel, T. Reddmann, O. Kirner, R. Ruhnke, and P. Braesicke (2017). *An emission module for ICON-ART 2.0: implementation and simulations of acetone*. Geosci. Model Dev. 10 (6), 2471–2494. DOI: 10.5194/gmd-10-2471-2017 (cit. on pp. 26, 28, 29, 32, 33, 38, 94, 123).

Weimer, M. (2015). *Simulation of volatile organic compounds with ICON-ART*. Master's Thesis. Germany: Karlsruhe Institute of Technology (KIT) (cit. on p. 26).

Wessem, J. M. van, C. H. Reijmer, W. J. van de Berg, M. R. van den Broeke, A. J. Cook, L. H. van Ulft, and E. van Meijgaard (2015). *Temperature and Wind Climate of the Antarctic Peninsula as Simulated by a High-Resolution Regional Atmospheric Climate Model*. Journal of Climate 28 (18), 7306–7326. DOI: 10.1175/JCLI-D-15-0060.1 (cit. on p. 109).

Winker, D. M., W. H. Hunt, and M. J. McGill (2007). *Initial performance assessment of CALIOP*. Geophysical Research Letters 34 (19). DOI: 10.1029/2007GL030135 (cit. on p. 62).

WMO (1957). *Meteorology A Three-Dimensional Science: Second Session of the Commission for Aerology*. WMO Bulletin IV. Geneva: WMO, 134–138 (cit. on pp. 74, 75, 76).

Wofsy, S. C., M. B. McElroy, and Y. L. Yung (1975). *The chemistry of atmospheric bromine*. Geophysical Research Letters 2 (6), 215–218. DOI: 10.1029/GL002i006p00215 (cit. on p. 16).

Wohltmann, I., R. Lehmann, and M. Rex (2010). *The Lagrangian chemistry and transport model ATLAS: simulation and validation of stratospheric chemistry and ozone loss in the winter 1999/2000*. Geoscientific Model Development 3 (2), 585–601. DOI: 10.5194/gmd-3-585-2010 (cit. on p. 42).

Wohltmann, I., T. Wegner, R. Müller, R. Lehmann, M. Rex, G. L. Manney, M. L. Santee, P. Bernath, O. Sumińska-Ebersoldt, F. Stroh, M. von Hobe, C. M. Volk, E. Hösen, F. Ravegnani, A. Ulanovsky, and V. Yushkov (2013). *Uncertainties in modelling heterogeneous chemistry and Arctic ozone depletion in the winter 2009/2010*. Atmos. Chem. Phys. 13 (8), 3909–3929. DOI: 10.5194/acp-13-3909-2013 (cit. on pp. 20, 77).

Woiwode, W., J.-U. Grooß, H. Oelhaf, S. Molleker, S. Borrmann, A. Ebersoldt, W. Frey, T. Gulde, S. Khaykin, G. Maucher, C. Piesch, and J. Orphal (2014). *Denitrification by large NAT particles: the impact of reduced settling velocities and hints on particle characteristics*. Atmospheric Chemistry and Physics 14 (20), 11525–11544. DOI: 10.5194/acp-14-11525-2014 (cit. on p. 21).

Woiwode, W., M. Höpfner, L. Bi, M. C. Pitts, L. R. Poole, H. Oelhaf, S. Molleker, S. Borrmann, M. Klingebiel, G. Belyaev, A. Ebersoldt, S. Griessbach, J.-U. Grooß, T. Gulde, M. Krämer, G. Maucher, C. Piesch, C. Rolf, C. Sartorius, R. Spang, and J. Orphal (2016). *Spectroscopic evidence of large aspherical β-NAT particles involved in denitrification in the December 2011 Arctic stratosphere*. Atmospheric Chemistry and Physics 16 (14), 9505–9532. DOI: 10.5194/acp-16-9505-2016 (cit. on pp. 20, 21).

Worsnop, D. R., M. S. Zahniser, L. E. Fox, and S. C. Wofsy (1993). *Vapor Pressures of Solid Hydrates of Nitric Acid: Implications for Polar Stratospheric Clouds*. Science 259 (5091), 71–74. DOI: 10.1126/science.259.5091.71 (cit. on p. 20).

Wright, C. J., N. P. Hindley, L. Hoffmann, M. J. Alexander, and N. J. Mitchell (2017). *Exploring gravity wave characteristics in 3-D using a novel S-transform technique: AIRS/Aqua measurements over the Southern Andes and Drake Passage*. Atmospheric Chemistry and Physics 17 (13), 8553–8575. DOI: 10.5194/acp-17-8553-2017 (cit. on p. 10).

Xu, X., J. Song, Y. Wang, and M. Xue (2017). *Quantifying the Effect of Horizontal Propagation of Three-Dimensional Mountain Waves on the Wave Momentum Flux Using Gaussian Beam Approximation*. Journal of the Atmospheric Sciences 74 (6), 1783–1798. DOI: 10.1175/JAS-D-16-0275.1 (cit. on p. 11).

Yu, F. (2004). *Formation of large NAT particles and denitrification in polar stratosphere: possible role of cosmic rays and effect of solar activity*. Atmospheric Chemistry and Physics 4 (9/10), 2273–2283. DOI: 10.5194/acp-4-2273-2004 (cit. on p. 21).

Zängl, G., D. Reinert, P. Rípodas, and M. Baldauf (2015). *The ICON (ICOsahedral Non-hydrostatic) modelling framework of DWD and MPI-M: Description of the non-hydrostatic dynamical core*. Quart. J. Roy. Meteor. Soc. 141 (687), 563–579. DOI: 10.1002/qj.2378 (cit. on pp. 3, 7, 25, 27).

Zhang, C. and J. Zhang (2018). *Modeling Study of Foehn Wind Events in Antarctic Peninsula with WRF Forced by CCSM*. Journal of Meteorological Research 32 (6), 909–922. DOI: 10.1007/s13351-018-8067-9 (cit. on p. 109).

Zhang, F., Y. Q. Sun, L. Magnusson, R. Buizza, S.-J. Lin, J.-H. Chen, and K. Emanuel (2019). *What Is the Predictability Limit of Midlatitude Weather?* Journal of the Atmospheric Sciences 76 (4), 1077–1091. DOI: 10.1175/JAS-D-18-0269.1 (cit. on p. 56).

Zhu, Y., O. B. Toon, A. Lambert, D. E. Kinnison, M. Brakebusch, C. G. Bardeen, M. J. Mills, and J. M. English (2015). *Development of a Polar Stratospheric Cloud Model within the Community Earth System Model using constraints on Type I PSCs from the 2010-2011 Arctic winter.* Journal of Advances in Modeling Earth Systems 7 (2), 551–585. DOI: 10.1002/2015MS000427 (cit. on pp. 2, 15, 20, 47, 125, 131, 132).

Zhu, Y., O. B. Toon, M. C. Pitts, A. Lambert, C. Bardeen, and D. E. Kinnison (2017). *Comparing simulated PSC optical properties with CALIPSO observations during the 2010 Antarctic winter.* Journal of Geophysical Research: Atmospheres 122 (2), 1175–1202. DOI: 10.1002/2016JD025191 (cit. on pp. 2, 38, 123).